UNIVERSITY OF CALIFORNIA

Los Angeles

Initiation Mechanisms, Comfort Level, and Magnitude Control of Vortex-induced Vibration for Long-span Box Girder Suspension Bridge

A dissertation submitted in partial satisfaction of the

requirements for the degree Doctor of Philosophy

in Civil Engineering

by

Jingxi Qin

2023

ABSTRACT OF THE DISSERTATION

Initiation Mechanisms, Comfort Level, and Magnitude Control of Vortex-induced Vibration for Long-span Box Girder Suspension Bridge

by

Jingxi Qin

Doctor of Philosophy in Civil Engineering

University of California, Los Angeles, 2023

Professor Jiann-Wen Ju, Chair

Vortex-induced Vibrations (VIV) on long-span suspension bridges have become increasingly prevalent in recent years. The specific mechanisms of VIV on box girder bridges and efficient counter-measures for the VIV that are practical for bridge engineering applications have yet to be proposed. This research focuses on exploring the initiation mechanisms of the VIV on long-span box girder suspension bridges, determining how the VIV affects the comfort level for drivers and passengers in vehicles traveling on bridges with VIV, and proposing measures that can effectively detect and mitigate the VIV on long-span box girder suspension bridges. The

overarching goal is to amplify the mechanistic understanding of VIV on long-span suspension bridges and inform the optimization of structural design to advance driving safety and passenger comfort subjected to VIV. A prototypical box girder suspension bridge with a main span of 1760 m is used as the engineering background for this research, and the dynamic characteristics of the bridge are analyzed with the Finite Element Method (FEM) and wind tunnel experiments to set as the foundation for the rest of the research. Three topics are investigated:

1) To elucidate the VIV initiation mechanism for long-span suspension bridges, several box girder sections, including the rectangular girder sections, the rectangular girder sections with wind noses, and the streamlined box girder section of the prototypical bridge are tested in wind tunnel laboratories to observe their respective VIV performances and the effectiveness of various aerodynamic VIV mitigation measures. VIV initiation mechanisms of the box girder sections are explored in CFD analysis by recognizing vortexes and tracking their paths around the girder sections using two different methods. The influence of the Reynolds number effect is discussed with experimental results from wind tunnel experiments of girder sections with different scaling factors.

2) To characterize the driving and riding comfort level on bridge with VIV, a wind-traffic-vehicle coupled vibration model is established to determine the accelerations experienced by drivers and passengers in moving vehicles traveling on bridges with VIV, the comfort level is evaluated using two indices, including the Overall Vibration Total Value (OVTV) and the Motion

Sickness Index (MSI).

3) Several mechanical VIV mitigation measures are proposed and tested on girder section models in the FEM model of the prototypical bridge. An effective mitigation measure consisting of a V-shaped damping cable connecting the main cables on the main span and side span with a rotational damping device at the tower-girder intersection is tested and validated. The equivalent damping capability of girder-end bearing support friction force is analyzed and its potential in mitigating VIV is discussed. A VIV dynamic characteristics detection method based on machine learning and visual recognition is developed, and the functionalities are tested with a video of a bridge vibrating under the influence of VIV as well as a simulation animation of bridge with VIV.

The dissertation of Jingxi Qin is approved.

Ajit K. Mal

Scott Joseph Brandenberg

Idil Deniz Akin

Jiann-Wen Ju, Committee Chair

University of California, Los Angeles

2023

Table of Contents

Acknowledgment

I would like to first express my gratitude to my Ph.D. advisor, Professor Jiann-Wen Woody Ju, for generously providing me with his kind support and guidance throughout my academic career at UCLA and my life. My Ph.D. study and this research would not have become a reality without Professor Ju's continuous support and advising. I would also like to express my gratefulness to Professor Ajit Mal, Professor Scott Brandenberg, Professor Idil Akin, Professor Jian Zhang, and Professor Henry Burton for participating in my doctoral committee. Each committee member has provided me with extensive guidance and valuable knowledge in structural and mechanical engineering in the classroom and for my Ph.D. research.

Due to the Covid-19 pandemic, some of the experiments in this research were conducted at the Southwest Jiaotong University (SWJTU) in Chengdu, China. I want to thank Professor Yongle Li, Professor Kai Wei, and Professor Mingjin Zhang of SWJTU for supporting my experiments by providing laboratories and sharing their expertise in wind engineering. I would also like to thank Doctor Zilong Ti, Doctor Lianhuo Wu, and Ph.D. candidate Fanying Jiang of SWJTU for assisting me with the experiments.

I want to thank Mr. Dyab Khazem of Parsons Transportation Group for mentoring me during my three years of professional engineering career and supporting my decision when I decided to pursue my Ph.D.

I want to thank Professor John Ma of the University of Tennessee, Knoxville, for enlightening me as an engineering student and offering his valuable insight and unconditional help during the highs and lows of my academic career.

I would like to thank Professor Gilbert Gee of the University of California, Los Angeles, for providing his valuable insights into my Doctoral study and kindly including me in his research, which expanded my vision beyond Civil Engineering.

Last but not least, I would like to thank my family for supporting me throughout my life. I want to share how grateful I am to have such a caring and compassionate family whom I can always count on.

Vita

Jingxi Qin attended the University of California, Los Angeles, from 2010 to 2016 and received his Bachelor's Degree and Master's Degree in Civil Engineering. After graduation, Jingxi worked as a Bridge Engineer at Parsons Transportation Group in New York City from 2016 to 2019. Jingxi is currently a Ph.D. candidate in Civil Engineering at the University of California, Los Angeles. His doctoral research focuses on the vortex-induced vibration on long-span suspension bridges. Jingxi is registered as a Professional Engineer in Civil Engineering in the state of California.

Chapter 1 Background and Introduction

1.1 Introduction

Modern long-span bridges are trending toward longer spans, thinner structure components, lighter self-weight, lower girder stiffness, and lower damping ratio. They are becoming significantly more sensitive to wind-induced effects. For long-span suspension bridges, stability and reliability in wind load design are two of the most critical limiting factors for their design and construction. Generally speaking, bridges tend to be more susceptible to the influence of wind when their main spans increase. It is particularly true for lightweight bridges with low damping ratios, which are prone to vortex-induced vibration (VIV) under low wind speed. The VIV is a self-inducing and self-limiting phenomenon caused by vortex-induced forces (VIF) due to periodically shedding vortexes when air flows around surfaces of structures and detaches from them. Unlike other wind-induced vibrations, such as flutter vibration and galloping vibration, the VIV generally will not cause catastrophic destruction for bridges and structures due to its self-limiting characteristics. However, the VIV usually occurs under low wind speed conditions, has a high probability of occurrence, and interferes with the serviceability of bridges and the comfort of drivers and passengers in vehicles on bridges [1]. It could also cause fatigue on structural components, decreasing reliability and structural service life. To this day, more than 30 bridges around the world have been observed to experience VIV phenomena. In 2020 alone, the VIV

happened on at least five long-span suspension bridges and attracted significant public attention and media coverage across the globe. Bridge vibration incidents are believed to have been prevalent in recent years due to climate change [2], increasing numbers of long-span bridges being constructed, growing focus on structural safety, and more intensive media coverage [3].

The 1940 Tacoma Narrows Bridge was a suspension bridge in Tacoma, Washington. It was opened to traffic on July 1st, 1940. It had a main span of 853 m and a clearance of 59.4 m. A picture of the bridge is shown in Figure 1-1-1. Since the completion of the superstructure before the bridge's official opening, vertical bending mode vibration and rotational mode vibration had been observed on the bridge despite several damping measures being applied to the bridge. Because of its frequent vibration, the bridge was nicknamed "The Galloping Gertie". The bridge experienced almost daily VIV. Figure 1-1-2 shows significant rotational mode deformation of the main girder under wind-induced vibration.

Figure 1-1-1: Tacoma Narrows Bridge on opening day

(https://www.vice.com/en/article/kb78w3/the-myth-of-galloping-gertie)

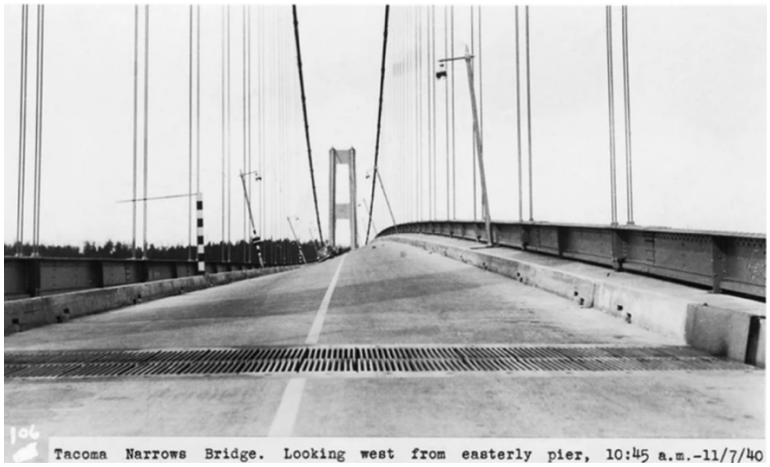

Figure 1-1-2: Tacoma narrows bridge under wind-induced vibration

(https://www.vice.com/en/article/kb78w3/the-myth-of-galloping-gertie)

The Humen Bridge is a suspension bridge in Guangdong, China, as shown in Figure 1-1-3. It spans 888 m and was opened to traffic in 1997. In May 2020, a significant VIV phenomenon was observed on the bridge, and the bridge was closed for more than a week before it was reopened to traffic. Investigation suspected that the temporary barriers on top of the bridge and the then recently installed maintenance vehicle tracks at the bottom of the bridge changed the aerodynamic shape of the girder section and caused the resonance between the main girder and wind-induced vortex shedding, which led to the VIV phenomenon [3] [4].

Figure 1-1-3: Humen Bridge

(https://wikipedia.org/wiki/humenbridge)

The Xihoumen Bridge, shown in Figure 1-1-4, is a suspension bridge with a 1650 m main span that opened in 2009. The bridge appeared to be prone to VIV since its completion. Monitoring systems for wind-induced vibrations were installed on the bridge before completion due to concerns about its low stiffness and high wind environment on the bridge site [4]. On average, wind-induced vibration happens 20-30 times yearly on the Xihoumen Bridge.

Figure 1-1-4: Xihoumen Bridge

(https://www.sohu.com/a/279718525_100160593)

The Verrazano Narrows Bridge is a truss girder suspension bridge in New York City that connects Brooklyn and Staten Island. The earliest reports of bridge vibration under extreme weather conditions date back to 2006. A recent incident happened in November 2020. A video taken during the recent wind-induced vibration on the Verrazano Narrows Bridge shows that loud noises were heard during the incident. It was suspected that the friction from the relative movements between the truss members of the main girder produced such sound. A screenshot of the forementioned video is shown in Figure 1-1-5.

Figure 1-1-5: Verrazano Narrows Bridge under wind-induced vibration

(https://secretnyc.co/video-verrazano-bridge-sway/)

The Yingwuzhou Bridge, shown in Figure 1-1-6, is a suspension bridge located in Wuhan, China. It has a main span of 850 m. The bridge had been open for more than six years before its first significant wind-induced vibration that attracted public attention. In May 2020, a VIV phenomenon with a magnitude of more than 50 cm was observed on the bridge, which was closed for two days for traffic safety concerns. It was suspected that the change in its wind environment

near the bridge site and the decrease in structural damping capability caused by wear and tear from normal operation led to a delay in observing the vibration for the first time after six years in operation [5].

Figure 1-1-6: Yingwuzhou Yangtze River Bridge

(https://finance.sina.com.cn/wm/2020-04-26/doc-iirczymi8517062.shtml)

As reflected in the above incidents, the VIV phenomenon has become a prevalent and severe threat to traffic safety and structural integrity and has emerged as a social welfare liability. Therefore, it is necessary to conduct further study on such matter. This research explores the initiation mechanisms, comfort level, and magnitude control of the VIV phenomenon of long-span suspension box girder bridges through theoretical analysis, wind tunnel experiments, CFD simulations, and numerical analysis.

1.2 Literature review and status quo on vortex-induced force (VIF) models and vortex-induced vibration (VIV) related research

1.2.1 VIV mechanism of box girders

Existing research reveals that the VIV response of structures is highly sensitive to aerodynamic shapes. The shapes of the girder section and installed accessory non-structural components are two of the determining factors of its VIV response. The aerodynamic shape influences the separation point of the incoming flow, the amount of separation, the location of reattachment, and the characteristics of the vortex shedding phenomenon. There are several ways to modify the aerodynamic shape of structures. Some existing research focuses on considering the location, shape, size, and ventilation rate of barriers and the set-up and width of the central opening on the girder. Some scholars have done early research on the mechanisms of the VIV with various girder section shapes and methods. Nakamura [6] experimented with girder sections with different aspect ratios and found that vortexes do not reattach to the original section when the aspect ratio is around 1:1 and 1:2, and the reattachment starts to become evident when the aspect ratio is about 1:4. Fail et al. [7] found that when the aspect ratio becomes smaller, the VIF experienced by the girder section becomes smaller. Komatsu et al. [8] experimented with girders with an L-shape, H-shape, and T-shape and found that the Karman vortex street that appears downstream of the section is the main factor that induced VIV. Shiraishi et al. [9] did testings on girders with different rotation-vertical bending frequency ratios. They found that there are three types of mechanisms

that induce VIV on box girders: vortex generated at the top of the girder induced by structural movement, Karman vortex street downstream of the girder, and small vortexes downstream of the girder due to structural movement. On the foundation of the early research, scholars have since expanded the research on bridge VIV in more systematic and innovative approaches, categorizing different types of box girder sections, distinguishing the effects of different influencing factors, and utilizing more advanced research methods.

To provide generality and comparability to the research projects on the topic of VIV of box girder bridges, many studies simplified girder sections to the more general rectangular sections to help understand the mechanisms of box girder VIV, which in turn became a major topic in the VIV mechanism research. Some scholars have done extensive studies comparing VIV mechanisms of rectangular sections with different aspect ratios using numerical simulation methods. Welsh et al. [10] studied the flow field characteristics, such as the initiation of vortex street and its re-attachment around rectangular sections. Nakamura et al. [11] analyzed the Strouhal numbers and predominant frequencies of different rectangular sections. Paidoussis et al. [12] did research based on Shiraishi's findings and proposed a new mechanism, which is based on vortexes generated upstream of the girder by the dull wind nose shape and proposed several typical aspect ratios of the girder where the four types of vortex shedding mechanisms are prevalent. These research projects compared the flow field characteristics between different rectangular sections in detail and laid solid foundations for future research on this topic. A Benchmark on the Aerodynamics of a Rectangular 1:5 Cylinder (BARC) [13] was proposed at the 6th International Colloquia on Bluff

Body and Aerodynamics and Its Application (BBAA6). Since then, scholars have carried out extensive research on the aerodynamics of the 1:5 rectangular sections [14] [15] [16] [17] [18] [19] [20] [21]. Bruno [22] reviewed 70 BARC-related projects and concluded that the accuracy of the results and the time-average characteristics of the flow field in these studies vary as the flow fields are sensitive to the configurations and parameter settings of the simulation. Some research projects extended their applicability from two-dimensional to three-dimensional space and explored the longitudinal characteristics of rectangular box girder VIV [23] [24]. These research projects presented a more realistic perspective on the mechanisms of the VIV.

On the basis of the rectangular box girder sections, more streamlined box girder sections are studied for their VIV mechanisms. Larsen et al. [25] compared the intensities of each vortex shedding mechanism and discussed the scenarios where each of these mechanisms would become dominant and applied the finding to the design of the Halogaland bridge in Norway and the Izmit bridge in Turkey. Larsen et al. [26] also explored how the spoilers would interfere with generating vortexes and designed spoilers that reduce VIV on the Angchuanzhou bridge. Li et al. [27] did wind tunnel experiments for the Xihoumen bridge with a central opening and found that the central opening of the girder did not generate any significant vortexes when VIV was not activated, and the Karman vortex street that appeared downstream of the upstream half girder during the VIV impacted the downstream half girder and helped creating a stronger VIV downstream of the entire girder section. Kwok et al. [28] explored how the width of the girder's central opening would influence the girder section's VIV performance and found that the VIV would increase as the

central opening increases. Hu et al. [29] explored how the VIF was distributed across the surface of the streamlined box girder section experimentally and studied the influence of VIF from different surface locations of the girder on the overall VIF of the girder section.

Structural and non-structural components on bridges can affect the bridge VIV as well. Nagao [30] found that the VIV response of box girder sections is affected by the crash barriers on top of the girder. Removal of the barriers reduces the magnitude of the VIV response. Guan et al. [31] found that the barriers turn the girder section into more of a bluff body under the influence of horizontal incoming wind and, therefore, magnify the effect of flow separation, which would, in turn, magnify the vortex-shedding phenomenon. Studies by Laima et al. [32] and Yang et al. [33] showed that the wider central opening on the girder section contributes to a lower VIV wind speed range and lower vertical bending mode shape response but lightly increases the VIV magnitude for rotational mode. Hallak et al. [34] studied the influence of large vehicles on the VIV response of box girder bridges and found that the existence of these vehicles would significantly increase the magnitude of the VIV response of the girder section. Larsen et al. [35] studied the effect of box girder bottom surface angles on the VIV response of the girder section. It was concluded that the best VIV performance occurs when the angle is around 15 degrees.

For bridge structures, the model used in wind tunnel experiments is required to be scaled according to the dimensions of the wind tunnel to obtain proper flow field simulation. It creates a difference in the real bridge Reynolds number and wind tunnel Reynolds number. Previous research believed that the sharp wind nose of box girders separates incoming wind flow very

efficiently and quickly. The differences in Reynolds numbers can hence be ignored. However, the actual bridge observations contradicted the belief. In 1998, the Great Belt bridge observed a significant VIV phenomenon under a wind speed of 18 m/s, with a Strouhal number of 0.21. The two values differed from the result of the wind tunnel experiment conducted during the design phase of the bridge, which yielded a VIV wind speed of 23 m/s and a Strouhal number of 0.16. Schewe et al. [36] researched such differences with wind tunnel experiments, which focused on the flow field consistency. It was concluded that the difference between the real bridge VIV performance and previous wind tunnel experiments is due to the Reynolds number effect, which affects the flow field around the girder section and the Strouhal number for the section. The results obtained by Schewe et al. showed that the Strouhal number increases as the Reynolds number increases, which directly results from how the flow is separated at the upstream wind nose. With a higher Reynolds number, the VIV wind speed range would become lower, the VIV magnitude would become higher, and the lock-in wind speed range would be widened.

The characteristic of incoming flow has significantly affected the VIV response of the box girder sections, as Kawatani et al. [37] studied turbulence intensity for the VIV response on several rectangular box girder sections with different aspect ratios. The results showed that the VIV magnitude would decrease or even approach zero as turbulence intensity increases. Matsumoto et al. [38] studied the VIV response on the box girder section and found that the separation point would move further in the upstream direction under higher turbulence intensity. The VIV magnitude would increase as well.

The structural damping ratio of the bridges also plays an important role in the VIV performance. Manzoor et al. [39] conducted wind tunnel experiments and the result showed that the effect of the damping ratio has a higher impact on the VIV response of the box rectangular girder section than the mass of the girder does. Zhu [40] and Xian et al. [41] also studied the effect of mass and damping ratio on the VIV response of structures. Zhu found that when the VIF experienced by the girder section fits the linear empirical model by Scanlan, the magnitude of the VIV response appears to have a reverse linear relationship with mass and damping ratio. However, no specific theoretically proven relationship was proposed by scholars.

Many research performed wind tunnel experiments and numerical analysis on box girders have observed multi-order lock-in ranges in the VIV response of girder sections [9] [29] [32] [42] [43] [44]. Tamura et al. [45] proposed a wake oscillator model that describes the bluff body VIV response as a two-degree-of-freedom system to describe the multi-order lock-in ranges. Matsumoto [46] performed experiments in water flumes and wind tunnels and concluded that the coupling effect between the motion-induced vortexes and the Karman vortexes of the girder section causes such a phenomenon. Wu et al. [47]attributed such a phenomenon to the principle of frequency de-multiplication. Huang et al. [48] proposed that Karman vortexes induce the first lock-in range and the second lock-in range is caused by the swaying motion of the flow field at the rear of the girder section since little to no Karman vortex characteristics were found. Hu et al. [49] performed wind tunnel experiments for a girder section embedded with static pressure monitors and proposed a simplified vortex model that explains the multi-order lock-in ranges based on the

data obtained. The model reveals that the first lock-in range is excited and sustained by the separate vortexes formed at the trailing edge, and the others are excited and sustained by the separate vortexes formed at the leading edge.

Some scholars incorporated machine learning techniques into the research of VIV mechanisms. Li et al. [50] proposed a machine-learning-based method that analyzes on-site monitoring data to simulate the vortex shedding phenomenon, establishing the relationship between wind field characteristics and structural response. Raissi et al. [51] established and deep-learning method that links wind flow data and structural response with VIF. Li et al. [52] explored increasing the calculation efficiency of the N-S equation by machine learning. Such research on machine learning is still on a preliminary level, but it provides a new path for the research of the VIV and the VIF. Therefore, it is worth exploring.

Scholars have made noticeable progress on the topic of full bridge VIV analysis. The popular method for full bridge VIV response analysis is to establish a wind-structure coupling model with data obtained from girder section wind tunnel analysis that is then input into FEM models to calculate full bridge VIV response, which considers spanwise effects. The FEM method applies wind loads from the girder section wind tunnel experiment onto full bridge FEM models as nodal loads, then calculates the full bridge structural response time histories with aerodynamic damping and stiffness matrices. On this topic, Barhoush et al. [53] derived the unit aerodynamic damping matrix on 2D girder sections based on the nonlinear empirical model by Scanlan. They extended the application of this method to a 3D domain by assigning a zero value to the remaining

degrees of freedom. The limitation of this method is that it ignores the effect of forced vibration. To solve this problem, Lewandowski et al. [54] reproduced vortex shedding-induced vibration time history using the harmonic wave method, which considers the wind speed variance in the vertical direction of the girder section. Ehsan et al. [55] proposed a calculation method considering the VIF distribution on the longitudinal direction based on the nonlinear empirical model by Scanlan by measuring the longitudinal distribution factor of VIF on a stationary girder model and applying the factor to the model. This method by Ehsan is proven to be applicable and relatively accurate. Zhu et al. [40] derived the conversion method between the girder section model and full bridge response in terms of displacement magnitude based on the linear empirical mode proposed by Scanlan. Zhang et al. [56] extended this conversion to the nonlinear empirical model by Scanlan. The previous two conversion methods are based solely on the modal analysis and left out the effect of the distribution of VIF on the longitudinal direction of the bridge. Xian et al. [57] and Sun et al. [58] improved the accuracy of the spanwise distribution factor of VIF. Meng [59] reveals that the self-induced terms in the VIF modal are entirely associated with the spanwise distribution of the VIF. Meng also found that the forced vibration terms are partially associated and, therefore, do not significantly influence the modal results. The method is yet to be adequately verified on real bridge structures and requires further investigation to validate its applicability.

1.2.2 Theoretical models for VIF and VIV

Typical VIF models are usually based on classic single-degree vibration theories with additional terms specific to VIV response and forces. To research VIF girder section models, Scanlan et al. [36] proposed that it is appropriate to describe the coupling effect during the VIV process by putting an additional aeroelastic effect into the equations. Vickery et al. [37] made it possible to consider the aerodynamic damping effects in the VIF models by establishing a VIV response spectrum based on random vibration theory. The terms that describe the aeroelastic and aerodynamic damping effects are measured empirically in the wind tunnels. The related parameters are obtained by fitting parameters based on how well they match the behaviors of the wind tunnel models. Several classic models are introduced below.

a) Empirical linear VIF model proposed by Scanlan et al. [60].

$$f_v = \frac{1}{2}\rho U^z B[Y_1(K_1)\frac{\dot{y}}{U} + Y_z(K_1)\frac{y}{B} + \frac{1}{2}C_L(K_1)\sin(\omega_1 t + \phi)] \quad \textbf{(Eq. 1-2-1)}$$

where f_v is the linear VIF, ρ is the air density, U is the wind speed, B is the dimension of the section facing the incoming flow, y is the vertical displacement, and ω_1 is the vortex shedding frequency. K_1 is the modified vortex shedding frequency, and equals to $\omega_1 * B/U$. Y_1, Y_2, and C_L are functions that are left to be empirically determined.

With the above VIF model, the displacement of the VIV can be calculated.

$$my'' + c_v y' + k_v y = r(x)f_v = \frac{1}{2}r(x)\rho U^2 D[Y_{1,v}(K_v)\frac{y'}{U} + Y_{2,v}(K_v)\frac{y}{D} + \frac{1}{2}C_{l,v}(K_v)\sin(\omega_v t + \theta_v)] \quad \textbf{(Eq. 1-2-2)}$$

The longitudinal relationship function *r(x)* can be measured by the girder section model experiment in wind tunnels coupled with the girder VIV response equation along with the vibration mode parameters. The longitudinal VIV response can be calculated with the following formula.

$$y_v = \frac{\rho B^3 r(x) C_\phi \phi_v(x) C_L(K_1)}{4 m_{eq} K_0^2} \frac{\sin(Ks - \theta)}{[(1-\beta^2)^2 - (2\gamma\beta)^2)]^{0.5}} \quad \textbf{(Eq. 1-2-3)}$$

The maximum response is calculated with the following formula.

$$y_{v.max} = \phi_{v.max} \eta_{\max} B = \frac{\phi_{v.max} \rho B^3 C_\phi C_{\mathrm{rv}} C_L(K_1)}{4 m_{eq} K_0^2 (2\gamma\sqrt{1-\gamma^2})} \quad \textbf{(Eq. 1-2-4)}$$

In this empirical model, all parameters are obtained from analyzing data from wind tunnel experiments.

b) Empirical nonlinear VIF model by Scanlan and Ehsan [55].

Based on the linear VIF model mentioned above, Scanlan and Ehsan proposed the nonlinear model by introducing nonlinear aerodynamic damping terms into the equation. The equation is given below:

$$m(\ddot{y} + 2\xi\omega_0\dot{y} + \omega_0^2 y) = \frac{1}{2}\rho U^2 (2D)(Y_t(K_t)[1 - \varepsilon\frac{y^2}{D^2}]\frac{\dot{y}}{U} + Y_z(K_t)\frac{y}{D} + \frac{1}{2}C_t(K_t)\sin(\omega t + \theta)(1) \quad \textbf{(Eq. 1-2-5)}$$

where m is the mass, ω_0 is the vortex shedding frequency, ρ is the air density, U is the incoming wind speed, D is the structural dimension facing the incoming wind, y is the vertical displacement, K_v is the modified vortex shedding frequency, and C_L are functions left to be determined empirically.

With parameters obtained from analyzing data from wind tunnel experiments, the VIV

response of the model can be calculated as follows:

$$A = A_0 \Big/ \sqrt{\frac{C_2^*}{C_1^*}A_0^2 + \left(1 - \frac{C_2^*}{C_1^*}A_0^2\right)\mathrm{e}^{-2C_0^* C_2^* s}} \quad \textbf{(Eq. 1-2-6)}$$

where,

$$\begin{cases} C_0^* = 1/(8K \cdot \Delta K) \\ C_1^* = 6K \cdot \Delta\bar{K}\bar{\varepsilon}C_1 + (\bar{\varepsilon}\sigma - \bar{\varepsilon}C_3)C_1 \\ C_2^* = \dfrac{\bar{\varepsilon}C_2}{16}[10K \cdot \Delta K + 3(\bar{\varepsilon}\sigma - \bar{\bar{\varepsilon}}C_3)] \end{cases} \quad \textbf{(Eq. 1-2-7)}$$

c) General empirical nonlinear VIF model proposed by Larsen [61].

The model proposed by Larsen is given below:

$$\begin{aligned} my'' + c_v y' + k_v y &= r(x) f_v \\ &= r(x)\rho D^3 \omega_v C_{av}(1 - \epsilon_v \mid y/D \mid^{2\delta_v}) y'/2\pi \end{aligned} \quad \textbf{(Eq. 1-2-8)}$$

The expression can be re-written by considering it as a function of several factors:

$$F_{VI} = f(y,\ \dot{y},\ \ddot{y},\ \alpha,\ \dot{\alpha},\ \ddot{\alpha},\ U,\ I,\ t) \quad \textbf{(Eq. 1-2-9)}$$

By splitting up the expression with the Taylor expansion, the following expression is obtained.

$$\begin{aligned} F_{VI}^v \approx \frac{1}{2}\rho U^2(2D)\,[\,&P_{10}\,y + P_{01}\dot{y} + P_{20}\dot{y}^2 + P_{11}\dot{y}y + P_{02}\dot{y}^2] \cdots \\ &+ P_{ij} y^i \dot{y}^j + \frac{1}{2} C_{\mathrm{L}} \sin(\omega t + \phi)] \end{aligned} \quad \textbf{(Eq. 1-2-10)}$$

The above expression includes linear stiffness terms, linear aerodynamic damping terms, and several high-order terms. By reorganizing the expression in terms of linear and nonlinear Van Der Pol vibration terms and through high-order term elimination, the expression can be simplified

to the following shape:

$$F_{VI}^{v} = \frac{1}{2}\rho U^2 (2D)(P_{10}y + P_{01}\dot{y} + P_{20}y^2 + P_{11}y\dot{y} + P_{02}\dot{y}^2 . P_{30}y^3 + P_{21}y^2\dot{y} + P_{12}y\dot{y}^2 + P_{03}\dot{y}^3) \quad \textbf{(Eq. 1-2-11)}$$

Further simplification yields the final equation for VIF:

$$F_{\mathrm{VI}}^{v} = \frac{1}{2}\rho U^2(2D)(Q_{01}\dot{y} + Q_{21}y^2\dot{y} + Q_{12}y\dot{y}^2 + Q_{03}\dot{y}^3) \quad \textbf{(Eq. 1-2-12)}$$

Other terms can be obtained by analyzing data from wind tunnel experiments.

d) Other models

The harmonic oscillator model is a simplified model that assumes the structure to be stationary and ignores the coupling effect between wind flow and the structure. Additionally, this model treats the lift force factor as a constant value. Therefore, the model only applies to calculating lift force but not the rotational moments on the structure. The model is defined as follows.

$$F_v = \frac{1}{2}\,\rho\, U^2 B C_L \sin(\omega_s + \phi) \quad \textbf{(Eq. 1-2-13)}$$

where F_v is the linear VIF, ρ is the air density, U is the wind speed, B is the dimension of the section facing the incoming flow, y is the vertical displacement, *and* ω_s is the vortex shedding frequency. C_L is a function left to be determined empirically.

The lift oscillator model [62] is another simplified model. The expression is shown below.

$$F_v = \frac{1}{2}\rho \boldsymbol{U}^2 B C_L(t)$$
$$\ddot{C}_L + a_1\dot{C}_L + a_2\dot{C}_L^3 + a_3 C_L = a_4 y \quad \textbf{(Eq. 1-2-14)}$$

where a_1, a_2, a_3, and a_4 are model parameters obtained by analyzing data from wind tunnel experiments. The lift force factor is a function of time instead of a constant value in the Harmonic oscillator model discussed above and is related to the magnitude of the VIV response. It can be determined by measuring the structure's air pressure and wind load time history. Although this model took a step forward compared to the Harmonic oscillator model in terms of model comprehensiveness, there are still many unknowns left to be determined from empirical data, and it is, therefore, not very accurate.

The models introduced above have their respective pros and cons. The linear empirical model proposed by Scanlan can only describe the stable state of the VIV response, it does not provide any information regarding the development and decay of the response. The nonlinear empirical model proposed by Scanlan fixes the problem, but its sensitivity toward different parameters of the VIF varies, and the model's reliability is unstable.

The nonlinear empirical model proposed by Scanlan derives several high-order harmonic wave terms that sometimes overlap with lower-order harmonic wave terms, producing additional vortex-shedding frequencies that do not exist in real VIV. As a comparison, the general nonlinear model proposed by Larsen does not have this problem, as the model only consists of linear and nonlinear terms specific to wind speed. It does not have the high-order harmonic wave terms that appear to be the nonlinear empirical model proposed by Scanlan.

Based on research by Scanlan et al., Goswami et al. [63] introduced forced vibration onto the nonlinear empirical model and improved it to a model with a parameter that considers the

nonlinear damping effect. Xu et al. [64] researched and proposed a method that measures how the aerodynamic damping and aerodynamic stiffness change as the magnitude of the VIV response changes and proposed a model for aerodynamic damping and stiffness by fitting data from wind tunnel experiments based on recognizing the transient state of the structure. Xu's method improves the accuracy in determining the aerodynamic damping and introduces the aerodynamic stiffness term. Mashnad et al. [65] introduced the aerodynamic damping and stiffness terms into nonlinear function and related these two terms with the vibration displacement equation. With Mashnad's method, the determination of parameters of the nonlinear empirical model no longer solely relies on fitting data from experiments. Marra et al. [14] proposed a fitting method for parameters based on numerical optimization, increasing the accuracy of parameter data fitting. Meng et al. [59] proposed a similar model to the Scanlan nonlinear empirical model with a nonlinear 3rd order term depending on wind speed and a 2nd order term that depends on aerodynamic stiffness. Meng's model consistently predicts the VIF and VIV response under different mass/damping scenarios, but it only applies to conditions with fixed wind speed due to its time history/frequency domain hybrid nature. Diana et al. [66] explored the relationship between the VIF and VIV response of the structure by observing the forced vibration of wind tunnel models and found that the lock-in wind range of the VIV changes with wind speed and VIV response magnitude. Diana proposed to simulate the nonlinear aeroelastic effect by adding equivalent nonlinear oscillators onto FEM models. The limitation of Diana's model is that it only applies to conditions with fixed wind speed due to its time history/frequency domain hybrid nature, the same as the method proposed by Meng.

Zhu et al. [67] proposed a parameter fitting method for the nonlinear empirical model by Scanlan based on displacement measurement of the VIV response, the parameter obtained from this method works well in predicting rotational mode response. Larsen [68] improved on his general nonlinear empirical model by making the highest order term of the nonlinear oscillator a user-defined value and it predicts how the magnitude changes with the varying Scruton number more accurately.

1.2.3 Numerical simulation analysis of VIV

The numerical simulation method is frequently adopted in VIV studies because it allows direct observation and monitoring of the flow field characteristics around girder sections. For the flow field simulation, unstructured meshing is usually used to accommodate the surface layout of the girder sections, and structured meshing is used for portions of the flow field not directly adjacent to the girders for better simulation efficiency. For dynamic girder models, dynamic meshing that utilizes mesh deforming techniques allows girder movement. The commonly used mesh deforming methods include layering, spring smoothing, overset mesh, sliding mesh, etc., [69] [70]. The Reynolds-Averaged Navier-Stokes (RANS) model and the Large Eddy Simulation (LES) model are two of VIV simulation's most adopted turbulence models. The RANS model is commonly used for locations near the structure surface, and the LES model is typically used for portions of mesh away from the structure [71]. The Detached-Eddy Simulation (DES) model and Delayed Detached-Eddy Simulation (DDES) model combine the RANS model with the LES

model and designate the two models to appropriate portions of the simulated flow field for a more efficient solution process [72] [73].

To analyze the simulated flow field, scholars have proposed various methods. The Proper Orthogonal Decomposition (POD) method and the Dynamic Model Decomposition (DMD) method are the two promising and frequently used methods [74] [75]. These methods and their derivations provide accurate and reliable modal decompositions of two-dimensional spaces as well as descriptions of the growth and decay rate of the flow field during the simulation process. On the topic of vortex recognition, many scholars have made significant progress and proposed various methods. Wang et al. [76] categorized the progress in vortex recognition into three generations. The first generation is based on directly recognizing the vorticity distribution of the flow field in two-dimensional space. However, this method cannot distinguish the natural vortex from the vorticity of the non-vortex shear layer disturbance near the surface of the girder. To fix the shortcomings mentioned above, Liu et al. [77] proposed the second and third generations, which filtered the non-vortex shear layer disturbance near the girder for better recognition accuracy near the girder section surface and expanded the vortex recognition from two-dimensional space to three-dimensional space.

1.2.4 The comfort level for drivers, passengers, and pedestrians on a bridge under VIV

The inherent design characteristics of high flexibility and low structural damping render the cable-supported bridge susceptible to aeroelastic phenomena, such as vortex-induced

vibrations (VIVs), coupled flutter, torsional flutter, and galloping [78]. The VIVs of long-span bridges usually take place at low wind speeds, and the nature of the resulting aerodynamic forces acting on the deck makes VIV self-limited in amplitude. For the other three wind aerodynamic phenomena, the vibration amplitude tends to increase continuously, categorized as aeroelastic instabilities [79]. As a result, the VIV is less destructive than the other three wind aerodynamic phenomena and usually serves as an indicator of serviceability [80] [81]. Nevertheless, VIVs can cause discomfort to the users of a bridge or even failure by fatigue in the long term. In addition, the amplitude can become of concern when the bridge has low damping and the frequency of vortex trails is close to or coincides with the natural frequency of the girder [78].

The above discussions indicate that the VIVs may impact the serviceability and the safety of long-span bridges when the amplitude of the girder's motion is too large and lasts for a long time. In fact, VIVs have been observed in many long-span bridges worldwide, some of which caused significant serviceability issues by interrupting the traffic or resulting in modification costs. The Rio-Niterói Bridge in Brazil is a steel-box-girder pillar-supported bridge with a central span of 300 m at 72 m high. Since its opening to traffic in 1974, the bridge has frequently suffered from VIVs at low wind speeds, resulting in bridge closure to traffic for user comfort and safety concerns [82]. The other example of VIVs is the Great Belt East Bridge in Denmark, a suspension bridge with a main span of 1624 m that opened to traffic in 1998. During the final phases of construction, low-frequency vortex-induced vertical oscillations of the girder were observed in the wind speed range of 5 m/s to 10 m/s [83]. The oscillations were mitigated after implementing the guide vanes

at the bottom edges of the girder. Examples of actual long-span bridges experiencing VIVs also include the Trans-Tokyo Bay crossing bridge in Japan [84], the Ewijk bridge in the Netherlands [85], the Second Severn crossing cable-stayed bridge in Great Britain [86], the Volgograd continuous bridge in Russia [87], etc. More recently, two VIV events of long-span suspension bridges occurred successively one week apart on the Yingwuzhou Yangtze River Bridge [88] and Humen Bridge [89]. The field inspection and theoretical analysis suggested that the structural impact of the oscillations on the above two bridges was trivial. However, since the oscillations convey a sense of unsafe, widespread public concerns were raised, worrying that the oscillations could deteriorate the vehicle ride comfort [90] [91]. For the Humen Bridge in particular, the amplitude of VIV was so noticeable that the traffic on the bridge was closed for ten days shortly after the occurrence of VIVs on May 5, 2020, for the sake of the comfort of bridge users [92].

Therefore, quantifying the comfort of bridge users, e.g., pedestrians, workers, and vehicle users, is critical to reducing the risk of human discomfort and improving the serviceability of long-span bridges in wind-prone regions. To ensure human comfort, various design criteria are defined in many codes and specifications for the serviceability limit state of vibrations, in which the analysis procedures are categorized into two groups, i.e., deflection and acceleration based methods. The deflection-based method aims to control the bridge vibration via a prescribed deflection limit, such as an allowable span-to-depth ratio [93] or a value calculated from the fundamental frequency of bridges [94] [95] [96]. Nevertheless, the deflection limits only consider one parameter and fail to account for the effect of dynamic excitations on the human body and are

not appropriate for controlling bridge vibrations [97] [98]. From the point of view of human comfort, the acceleration-based method is more rational than the deflection-based method because the human response strongly depends on the characteristics of the excitation, e.g., the exposure time, magnitude, direction, and frequent content of the excitation [99]. The peak value and the root mean square (RMS) value of the acceleration are recommended in most of the current codes and specifications as the indices for human comfort evaluation. However, the use of peak acceleration could be questionable in some cases. For example, the peak acceleration of the bridge deck near the abutments could far exceed the allowable limit when the vehicle enters and leaves the bridge [100]. This also applies to situations where significant pavement irregularities are considered, and the limit can be easily exceeded by the peak acceleration at any girder location [101]. The RMS acceleration may be the most appropriate index for human comfort evaluation. In fact, the frequency-weighted RMS acceleration is proposed in codes such as ISO 2631 [102] and BS 6841 [103], which consider the effect of direction and frequency content of the excitation on human comfort. This is achieved by applying frequency-weighing curves and multiplying factors to each direction of excitation.

Over the past few decades, there have been many comprehensive studies about the human comfort evaluation of bridge users in the context of wind-traffic-bridge (WTB) coupled vibration. Xu and Guo [104] explored the ride comfort of high-sided road vehicles running on a long-span cable-stayed bridge under a crosswind, in which the lateral and vertical directions of vehicle ride comfort were found to be affected by the crosswind and bridge motion, respectively. Nguyen et al.

[98] also pointed out that strong crosswinds can significantly deteriorate the comfort of both vehicle drivers and pedestrians on a slender arch bridge. Zhu et al. [105] analyzed the ride comfort of vehicles crossing a coastal cable-stayed bridge subjected to correlated wind and wave loads via the overall vibration total value (OVTV) calculated from frequency-weighted RMS acceleration. The OVTV was first proposed by Griffin [99] and later recommended in ISO 2631 [102]. Recently, Camara et al. [106] evaluated the driver's ride comfort when crossing a long-span cable-stayed bridge, and the results showed that the strong gust wind and large-amplitude pavement irregularities could result in severe discomfort. It is noted that the above studies mainly focus on the ride comfort of a single vehicle or simplified vehicle queues, which ignores the realistic behavior of traffic flow crossing long-span bridges. This could result in inaccurate ride comfort assessment. To overcome this issue, further endeavors have been made by many researchers to incorporate real-world vehicle behavior into the ride comfort evaluation. Chen and Wu [107] introduced the microscopic cellular automaton (CA) traffic model into wind-traffic-bridge (WTB) analysis for the first time, which enables the simulation of real-world vehicle behavior such as acceleration, deceleration, and lane-changing. The CA-based stochastic traffic flow model was later proved by a range of analyses to be able to accurately predict the realistic traffic loading scenario [108] [109] [110].

Although the studies mentioned above and discoveries have contributed significantly to understanding vehicle ride comfort, they all consider only the normal wind conditions, while the effect of adverse wind conditions such as VIV on ride comfort remains unclear. Recently, scholars

have begun to pay attention to the ride comfort of traffic flow crossing the long-span bridges experiencing VIV. Yu et al. [111] examined the influence of VIV-induced bridge vibration on ride comfort, which showed that the VIV could aggravate the dynamic responses of road vehicles and thereby cause severe ride discomfort issues. Dan et al. [92] explored the impact mechanism of traffic loads on the dynamic behavior of a suspension bridge subjected to VIV, and the results showed that the traffic flow on the bridge could result in a remarkable increase in the structural damping ratio, which helps to mitigate the VIV response. Zhu et al. [91] assessed the drivers' ride comfort in different traffic flows crossing a long-span suspension bridge under VIV through the criteria recommended in the ISO 2631 standard based on OVTV. The effects of several key factors, such as traffic density, traffic proportion, and road roughness, on drivers' ride comfort were studied. When VIVs already occur in long-span bridges, it would take a while for structural engineers to identify the mechanism of the VIVs and find the appropriate vibration mitigation measures. Under such circumstances, priority shall be given to undertaking timely traffic management strategies to ensure ride comfort without causing too much traffic inconvenience. However, there is currently little existing study related to optimal or reasonable traffic management strategy for bridge management departments to refer to when the VIV event of long-span bridges occurs, making it a research topic worth exploring.

1.2.5 Mitigation measures of VIV on long-span suspension bridges

With different bridge spans and girder aerodynamic shapes for different bridges, although effective, it is difficult for aerodynamic measures to mitigate the VIV of suspension bridges completely. Therefore, effective VIV mitigation counter-measures have become a coveted topic in bridge wind engineering [112].

In addition to aerodynamic measures, the VIV of long-span suspension bridges can be further suppressed by installing mechanical VIV mitigation devices. Researchers and engineers have done extensive studies on mechanical VIV mitigation measures, some options for mitigation measures are summarized in Table 1-2-1, and three popular mitigation measures are discussed below.

Table 1-2-1: popular mechanical VIV mitigation measures

Mechanical VIV mitigation measures for long-span suspension bridges	Energy dissipation devices	Friction energy dissipation devices
		Elastic energy dissipation devices
		Lead extrusion energy dissipation devices
	Damping devices	Dynamic dampers
		Viscous dampers
		Magnetorheological dampers
		Tuned mass dampers

1.2.5.1 Tuned mass damper (TMD)

Tuned Mass Dampers (TMD) are widely used in bridge wind engineering, especially for active structural vibration mitigation. TMD is reliable and effective but is relatively less cost-effective and adds considerable additional weight to bridge structures.

By installing TMDs on bridge structures, the external excitation of structures can be effectively transferred to the TMD system, decreasing the structure's vibration. TMDs are widely utilized in wind design for tall buildings and vibration control for pedestrian and rail bridges. The TMD system reduces the vibration of structures when being tuned to the resonance frequency of the structure and “absorbs” the vibration. Its main components include springs, mass blocks, and dampers. Figure 1-2-1 shows the TMD system installed on the steel box girder of the Cumberland Bridge. Figure 1-2-2 shows a schematic of the components of the TMD system.

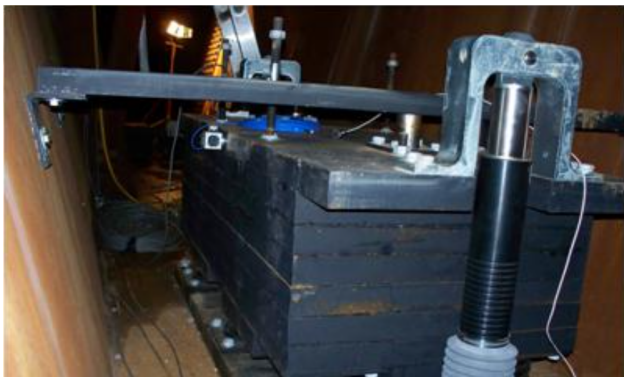

Figure 1-2-1: TMD device in the Cumberland bridge

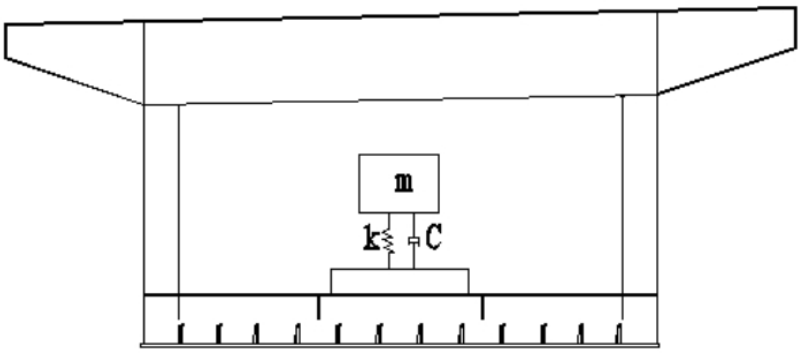

Figure 1-2-2: Schematic of the TMD in the Cumberland Bridge

The TMD system includes the following advantages compared to other mechanical structural vibration mitigation measures:

a) Casts little influence on the dynamic characteristics of structures and has modifiable frequency ranges, which enables flexible modification based on on-site measurements that increase mitigation reliability.

b) Has a multi-axis degree of freedom, capable of mitigating vibration in various directions.

c) Mechanical characteristics are controllable and reliable, long-term use is possible.

1.2.5.2 Viscous dampers

Structural vibration of multiple modes with different frequencies could appear for long-span suspension bridges. Although TMDs have modifiable frequency ranges, the ranges could not possibly include all potential vibration frequencies. Viscous dampers, on the other hand, could supplement such disadvantage. Zhu et al. [125] studied the application of viscous dampers on a cable-stayed bridge under the influence of combination loads from wind and vehicles. In this study,

spring/damper elements were used to simulate viscous dampers of various parameters, and their performances were tested under the influence of wind and vehicle loads. It was found that for wind loads, the vibration mitigation efficiency of viscous dampers on the longitudinal displacement of the main girder, the main tower, and at the tower-girder intersections increase as the velocity coefficients decrease and as the damping coefficients increase. The longitudinal displacement at these three locations can be as high as 94.8%, 77.2%, and 95.2%, respectively.

1.2.5.3 Magnetorheological (MRF) damping devices

Some scholars explored the applicability of other damping devices on bridges and made concrete progress. Wang and Chen [126] tested the application of Magnetorheological damping devices on cables of cable-stayed bridges. It was found that the modal frequency of the cable system increased by 3%-4% after installing the MRF damping devices, and the modal damping ratio increased by 3-6 times. The vibration amplitude was decreased by 20-30 times during vibration events. MRF has proven effective in mitigating cable vibration and is worth exploring in other vibration control efforts of bridges.

1.3 Objectives and structure of this dissertation

This research seeks to explore the initiation mechanism, comfort level, and magnitude control of VIV on box girder suspension bridges using girder section wind tunnel experiment,

bridge FEM modeling in ANSYS Workbench [113], flow field CFD analysis in ANSYS Fluent [113], and data analysis using MATLAB [114] and Pycharm [115] (a Python-based IDE). A prototypical long-span suspension bridge with a 1760 m main span is used as the engineering background for this research. The Chapters are structured as follows.

In Chapter 2, generic-shaped girder sections such as rectangular girder sections and rectangular girder sections with wind noses are tested in wind tunnel experiments and analyzed in CFD analysis to monitor the girder sections' dynamic VIV responses and flow field characteristics. A two-dimensional vortex recognition and tracking method based on mass monitoring point setup is proposed to track the development of individual vortexes around rectangular girder sections with or without wind noses.

In Chapter 3, a streamlined box girder section from the prototypical bridge is tested in wind tunnel experiments and CFD analysis. Several aerodynamic mitigation measures of VIV are tested for their effectiveness. The influence of Reynolds number and scaling factor are discussed based on wind tunnel experiment results. A computer vision vortex recognition and tracking method based on machine learning and Convolutional Neural Network (CNN) is proposed, which is suitable for the complex flow field around the streamlined girder section.

Chapter 4 proposes a methodology for determining the comfort level of drivers and passengers on suspension bridges under VIV based on the vibrational serviceability of the human body via wind-traffic-bridge (WTB) coupled vibration analysis. First, the proposed methodology is introduced. Subsequently, the proposed methodology is applied to the 1760 m prototypical long-

span suspension bridge for demonstration. Finally, the comfort level of drivers and passengers in vehicles on the prototypical long-span suspension bridge under VIV is determined.

In Chapter 5, several mechanical VIV mitigation counter-measures are proposed and tested in the FEM model of the prototypical suspension bridge. A V-shaped damping cable that connects the main cables on the main span and the side span with a rotational damping device located at the tower-girder intersection is the most effective. The V-shaped damping cable is tested on a higher order mode of VIV on the bridge, and its effectiveness increases as the order of the vibration mode increases. The equivalent damping effect of the girder-end bearing supports friction force is discussed. The friction force is verified to improve the damping capability of the bridge and could potentially be an effective mitigation VIV measure as well. An innovative framework for bridge VIV dynamic characteristics monitoring with AI-based machine-learning target object detection and tracking with keypoint detection is proposed. Accurate frequency, amplitude, and mode shapes of the bridge VIV are achieved with a video of a bridge VIV event and a simulation animation video of bridge VIV.

Figure 1-3-1 shows a flow chart that introduces the structure of this dissertation.

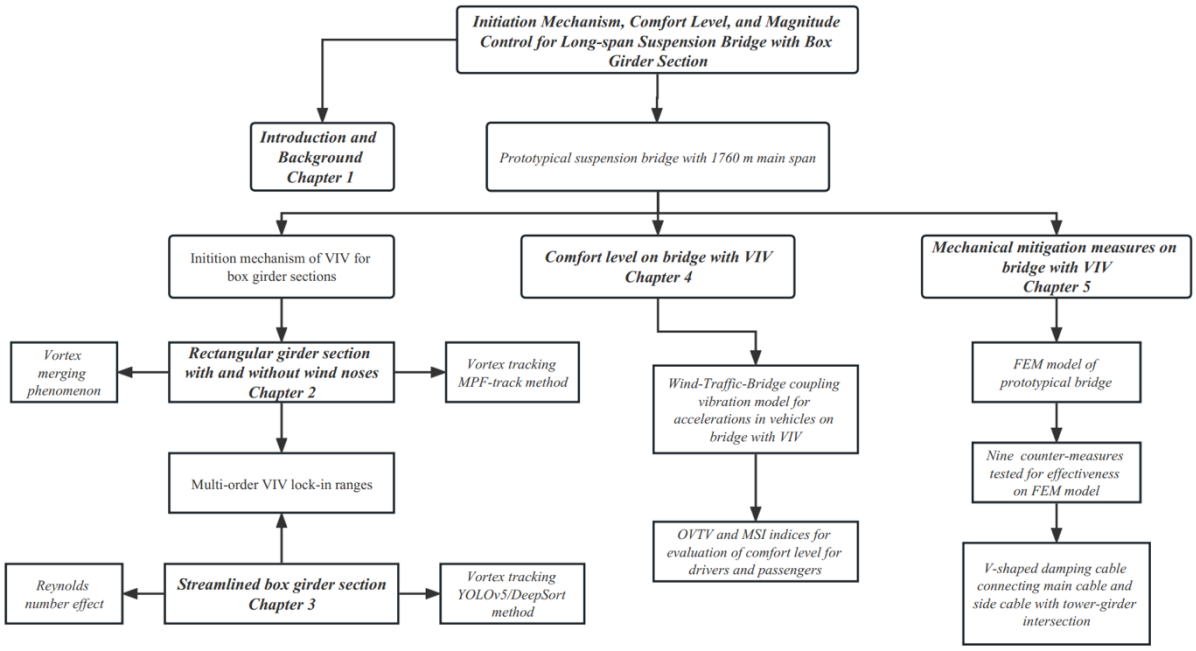

Figure 1-3-1: Chapter structure of this dissertation

Chapter 2 Initiation mechanisms of VIV for rectangular box girder sections

To explore the mechanism of VIV of box girder sections on long-span bridges, it is effective to conduct two-dimensional wind tunnel experiments and CFD analysis for the box girder sections. This chapter starts its analysis with VIV mechanisms of rectangular box girder sections, then extends the analysis to rectangular girder sections with triangular wind noses installed, setting up a stepping stone for the research into the streamlined girder section VIV mechanisms in the following Chapter.

2.1 VIV response for rectangular box girder sections based on wind tunnel experiments

The research lays its background on a prototypical long-span suspension bridge currently under construction. The prototypical bridge is a single-span suspension bridge, of which the entire span is 580+1760+580m. Its girder width is 31.5 m, with two main cables supporting it. The span/width ratio of the bridge is 56:1. The fundamental frequency of the bridge is lower than most of the suspension bridges built. Therefore, the bridge is extremely sensitive to wind loads. As a result, it is an excellent platform to research mechanisms of the VIV phenomenon and measures to control and mitigate such phenomenon on this bridge. The elevation view of the bridge's main span is shown in Figure 2-1-1.

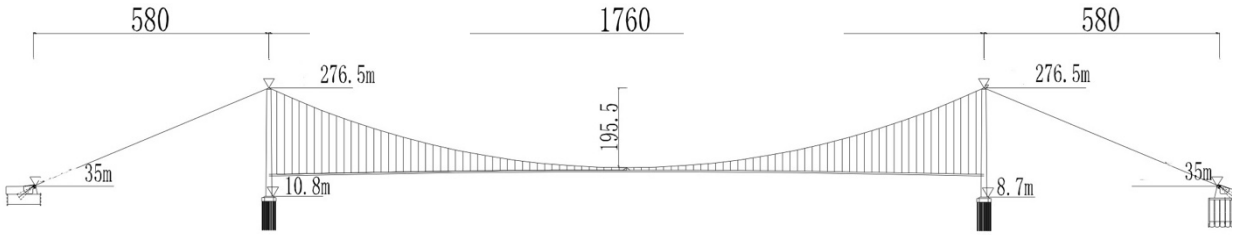

Figure 2-1-1: Elevation view of the bridge main span

The main girder is a prefabricated steel streamlined box girder with a height of 4.005 m and a width of 31.5 m. Suspension hangers are located on the two sides of the bridge, and the pavement thickness is 75 mm. The maintenance walkways and crash barriers are located on top of the girder and the side and center of the driveway. The typical streamlined cross-section of the bridge girder is shown in Figure 2-1-2.

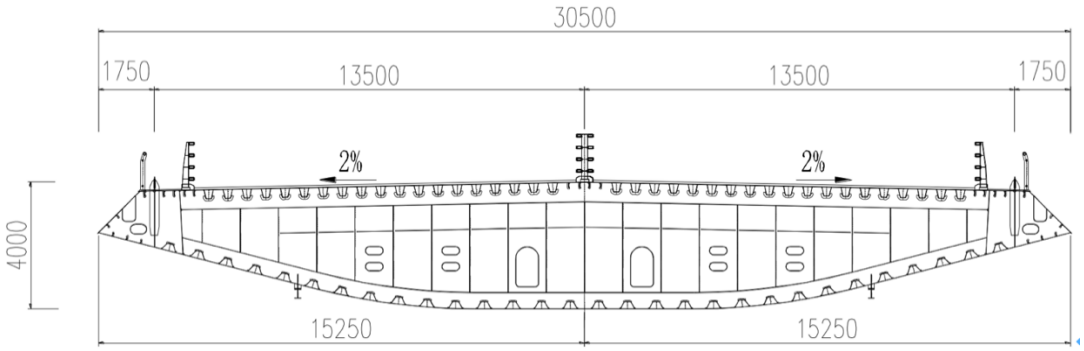

Figure 2-1-2: Elevation view of the girder section

For research on the rectangular girder sections with or without wind noses, the streamlined girder section of the original design is directly replaced by sections of interest with the same weight, stiffness, damping ratio, and height, while all other designs of the bridge remain the same for comparison purposes. The rectangular box girder sections tested have aspect ratios of 1:6 and 1:7.875. The 1:7.875 section has the same height and aspect ratio as the streamlined box girder

section of the original design. The 1:6 section has the same height and aspect ratio as the streamlined box girder section of the original design when wind noses are installed.

2.1.1 Experimental preparation and setup

2.1.1.1 Dynamic characteristic analysis

The dynamic characteristics analysis is the premise of VIV and other wind-induced vibration analyses. Structural modal frequencies, structural modal shapes, and equivalent damping ratio of the main girder can be obtained through the modal analysis and later used as the foundation for wind tunnel experiments and the CFD analysis. The analysis is conducted for a FEM model constructed based on the original design of the prototypical bridge with the streamlined box girder section. As mentioned previously, for research on the rectangular box girder sections with or without wind noses in this chapter, the original design of the girder section is directly replaced by sections of interest with the same weight, longitudinal stiffness, damping ratio, and height, while all other designs of the bridge remain the same for comparison purposes. Therefore, the dynamic analysis result applies to the wind tunnel experiment of not only the streamlined box girder section of the original design, which will be discussed in the following chapter, but also to the rectangular girder sections with or without wind noses discussed in this chapter.

The dynamic characteristics analysis in this experiment utilizes ANSYS Workbench, a widely used finite element analysis software for structural engineering and research in fields such as mechanical engineering, electrical engineering, and the aviation industry. It has proven to be

reliable and efficient after years of industrial adoption.

The main tower for the prototypical bridge is made of reinforced concrete, with one cross beam under the main girder and one at the top of the tower. The towers and cross beams adopt hollow cross-sections. The towers have a 7.5-10.5 m dimension in the transverse direction from bottom to top. In the longitudinal direction, the towers have a dimension of 11.0-14.0 m. Typical sections of bridge towers are shown in Figure 2-1-3:

Tower cross sections

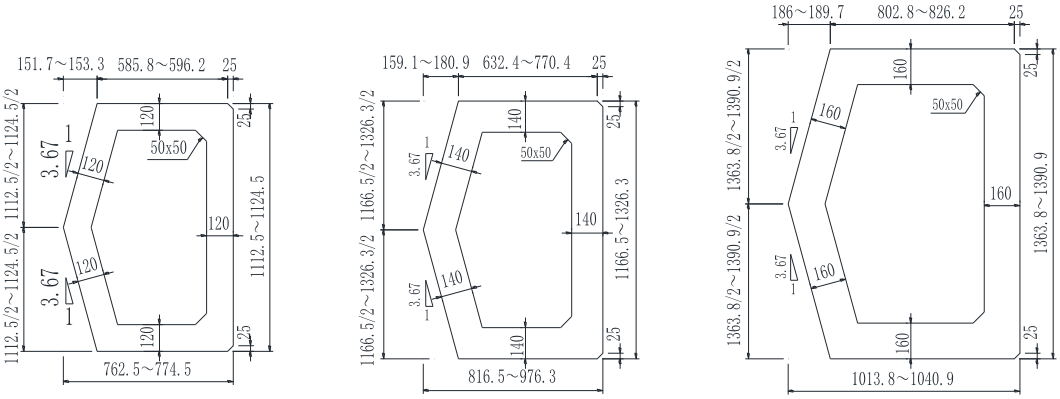

Lower cross beam and upper cross beam cross sections

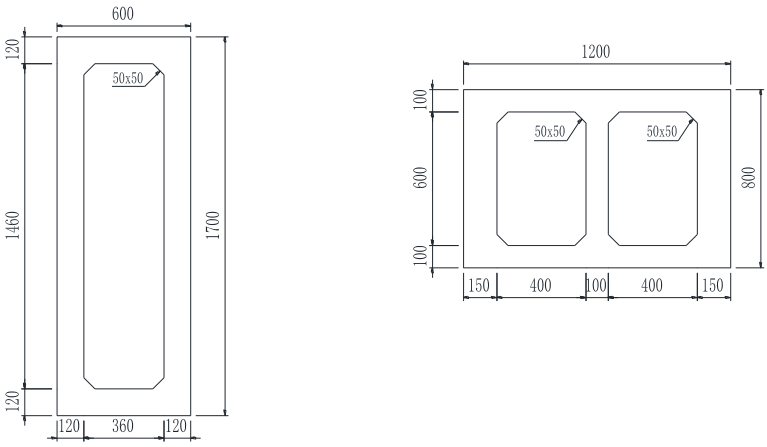

Figure2-1-3: Typical cross-section of main towers

In the finite element model used to determine the structural dynamic characteristics in ANSYS, the main girder and main towers are modeled as spatial beam elements. Main cables and hangers are modeled as spatial bar elements, and cable sockets and hangers connectors are modeled as mass units. The Young's modulus for the main girder is 2.06×10^5 MPa, the Poisson ratio is 0.3, and the density of the materials is 15240.461 kg/m^3. The Young's modulus for main towers is 3.6×10^4 MPa, the Poisson ratio is 0.2, density is 2600 kg/m^3. The Young's modulus for the main cable is 2.05×10^5 MPa, the Poisson ratio is 0.3, density is 7989.012 kg/m^3. The Young's modulus for hangers is 2.05×10^5 MPa, the Poisson ratio is 0.3, density is 8600 kg/m^3. The ANSYS finite element model is shown in Figure 2-1-4 and Figure 2-1-5.

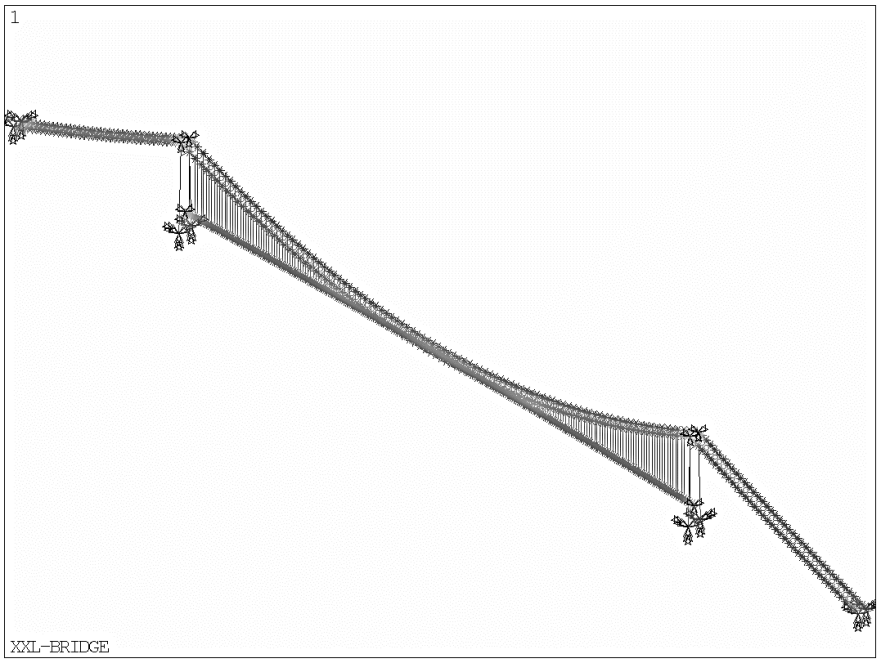

Figure 2-1-4: Main span FEM model

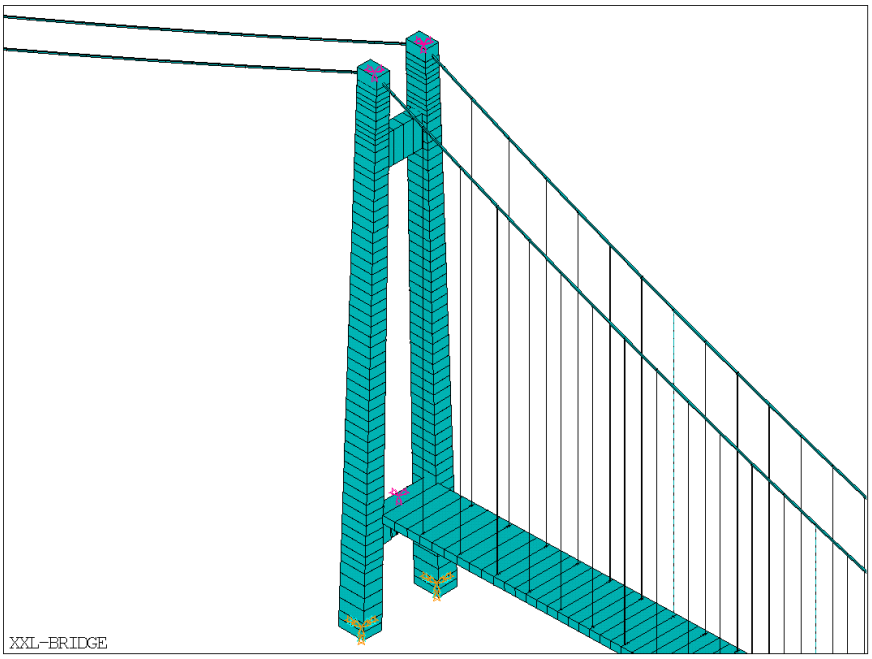

Figure 2-1-5: FEM model for main towers

The result of the structural dynamic characteristics analysis is shown in Table 2-1-1. The result from a parallel analysis is carried out to verify the result from ANSYS by a similar software called BANSYS is also shown in Table 2-1-1.

Table 2-1-1: Result of the dynamic characteristics analysis

Mode	ANSYS	BANSYS	Mode description	Equivalent mass/Equivalent mass moment of inertia
1	0.0409	0.0409	Sym. Horiz. bending	28.238 t
2	0.0773	0.0773	Asym. Vert. bending	35.438 t
3	0.0891	0.0891	Asym. Horiz. bending	23.766 t
4	0.1098	0.1098	Asym. Vert. bending	30.565 t
5	0.1494	0.1497	Sym. Vertical bending	32.216 t
6	0.1608	0.1608	Sym. Horiz. bending	24.742 t
7	0.1656	0.1655	Asym. Vert. bending	31.034 t

8	0.1820	0.1821	Cable swing	——
9	0.1864	0.1877	Cable swing	——
10	0.1883	0.1882	Cable swing	——
11	0.1902	0.1919	Cable swing	——
12	0.2100	0.2118	Cable swing	——
13	0.2114	0.2113	Sym. Vertical bending	31.915 t
14	0.2120	0.2131	Cable swing	——
15	0.2195	0.2196	Cable swing	——
16	0.2244	0.2240	Cable swing	——
17	0.2244	0.2240	Cable swing	——
18	0.2289	0.2213	Sym. Rotational mode	10484.657 t·m
19	0.2348	0.2331	Cable swing	——
20	0.2359	0.2356	Cable swing	——
21	0.2442	0.2475	Cable swing	——
22	0.2444	0.2492	Cable swing	——
23	0.2485	0.2433	Sym. Rotational mode	6757.680 t·m
24	0.2542	0.2540	Asym. Vert. bending	31.333 t
25	0.2795	0.2783	Asym. Rotational mode	15210.106 t·m
26	0.2834	0.2846	Longitudinal swing	34.504 t
27	0.2981	0.2953	Asym. Rotational mode	5219.147 t·m
28	0.3001	0.3005	Cable swing	——
29	0.3025	0.3022	Sym. Vertical bending	30.238 t
30	0.3233	0.3238	Cable swing	——

As seen in Table 2-1-1, the frequency results from ANSYS and BANSYS are in good agreement in lower modes but start to differ in higher modes, the error, however, is small, with the largest error being approximately 2% (mode 23, 0.2486 Hz and 0.2433 Hz). Mode shapes for mode 1 and mode 2 are shown in Figure 2-1-6 and Figure 2-1-7 as examples. Mode shapes for all modes are listed in the Appendix.

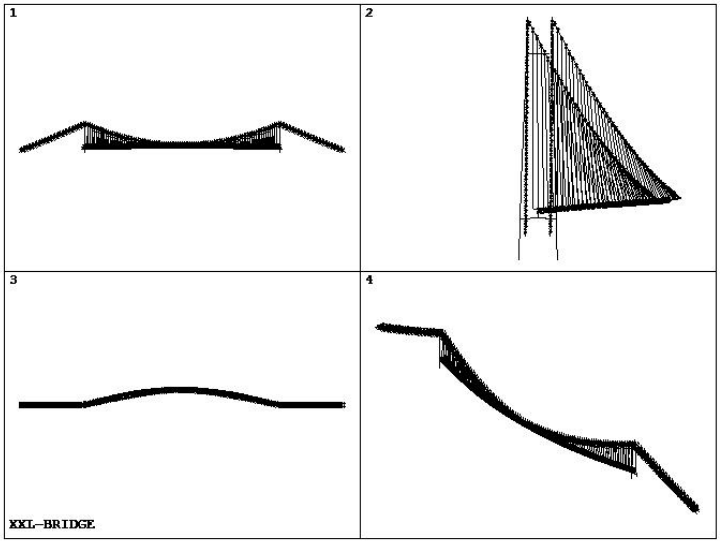

Figure2-1-6: Mode 1 shape

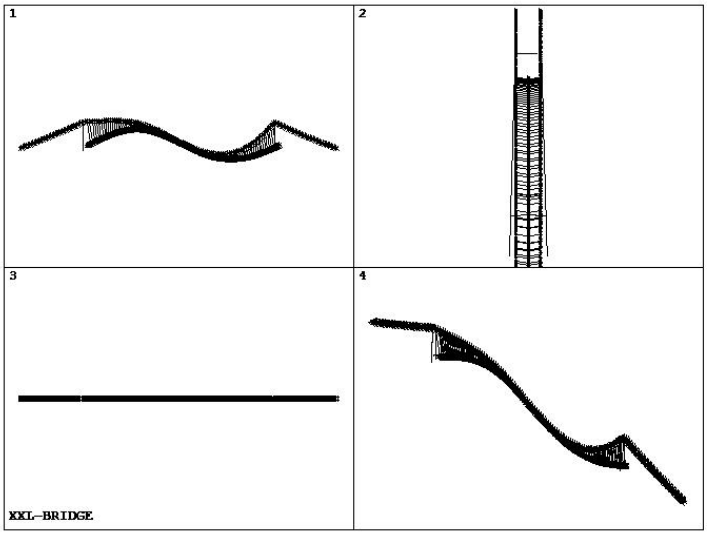

Figure2-1-7: Mode 2 shape

2.1.1.2 Wind tunnel experiment setup

The wind tunnel experiments are conducted in the 2nd testing section of the XNJD-1 wind tunnel in Emei, China. The scaled rectangular box girder sections with aspect ratios of 1:6 and 1:7.875 with additional wind noses are used. The effects of structural and non-structural components such as railings, wind barriers, and wind noses are also tested on the sections. The setup follows the Chinese Wind-resistant Design Specification for Highway Bridges [95]. Several requirements that need to be met are listed below:

1. The model satisfies geometrical similarity.
2. The model satisfies the consistency of elastic parameters $\frac{U}{f_h B}$, $\frac{U}{f_\alpha B}$, inertia parameters $\frac{m}{\rho B^2}$, $\frac{I_m}{\rho B^4}$, and damping parameters ξ_h, ξ_α.

where U is the wind speed, B is the girder width, f_h and f_α are the vertical vibration frequency and rotational frequency of the model, respectively, I_m is the mass moment of inertia per unit length of the model, ξ_h and ξ_α are the vertical and rotational damping ratios, respectively, and ρ is the air density.

3. The mass and mass moment of inertia of the bridge should be consistent with the equivalent mass and equivalent mass moment of inertia of the model.
4. Model width/height of the wind tunnel is smaller than 0.4.
5. Model length/model width is larger than 2.
6. The blocking rate of the wind tunnel is lower than 5%.

The model used in the experiment is scaled from its original size and shape by a scaling factor of 1:50. The lengths of the models are 2095 mm, the heights are 80.1 mm, and the wind tunnel height is 2 m. The girder section's mass and mass moment of inertia are scaled accordingly. Therefore, the setup of the experiment satisfies the requirements listed above.

The wind tunnel is equipped with a dedicated dynamic model testing system. Model sections are installed on the supporting frames using eight carefully calibrated springs, forming a two-degree-of-freedom system capable of moving vertically and rotating about the girders' longitudinal center lines. The setup of the model in the wind tunnel is shown in Figure 2-1-8.

Figure 2-1-8: Setup of model installation

The experiment used two LASER transducers to measure and record girder sections' vertical and rotational displacement. The setup of the transducers is shown in Figure 2-1-9.

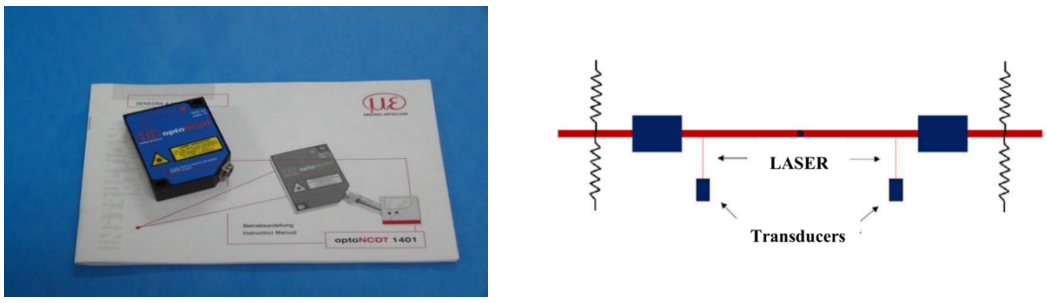

Figure 2-1-9: LASER transducer and setup

The frequency and damping ratio of structural vibration are achieved by calibrating the design stiffness of the springs and attaching oil dampers to the models. The free vibration attenuation method determined the specific modal frequency and damping ratio of each model. The fundamental frequencies of different modes of girder section models are summarized in Table 2-1-2.

Table 2-1-2: Fundamental frequencies of models in different modes

Girder section model	Modes	
	1st order vertical bending (Hz)	1st order rotation (Hz)
1:6 section model	1.94	4.78
1:7.875 section model	1.88	4.94

According to Eurocode 8 [116] and the Chinese Wind-resistant Design Specification [95], the recommended damping ratio for long-span bridges is 0.5%. However, according to several studies [1] [112] [117], the on-site measured damping ratios of long-span suspension bridges during actual VIV events can be as low as 0.3%. Therefore, the recommended value of the damping ratios in current codes is potentially over-estimated. For this experiment, the damping ratios are conservatively taken as values lower than 0.3%, ranging from 0.187% to 0.297%.

With the proper model setup completed, wind speed in the wind tunnel is incrementally increased from 0 m/s to 5 m/s to inspect the VIV response of the girder sections under different wind speeds. The TFI Cobra 3D pulse wind speed probe is used to monitor the wind speed in the tunnel. The device is a four-hole pressure head and monitors three-dimensional wind speed, static

pressure, and turbulence. The probe is attached to a support in front of the girder section model.

Each wind speed is sustained for 180 seconds or more before LASER transducers record the girder displacement to allow sufficient time to develop the flow field to avoid missing any potential girder VIV response. The displacement data recorded by the LASER transducers is 8 seconds long. It is worth mentioning that the displacement data recorded by the two LASER transducers could include displacement from both the 1st order vertical bending mode and the 1st order rotational mode. Therefore, explicit displacement data for each mode requires further calculation, as shown in Eq. 2-1-1 and Eq 2-1-2.

Vertical bending mode displacement, *V*:

$$\mathrm{V} = (\mathrm{H1} + \mathrm{H2})/2 \qquad \textbf{(Eq. 2-1-1)}$$

Rotational mode rotating angle, *R*:

$$\mathrm{R} = (\mathrm{H1} - \mathrm{H2})/\mathrm{L} \qquad \textbf{(Eq. 2-1-2)}$$

where *H1* and *H2* are the displacement recordings from the two LASER transducers, and *L* is the distance between the transducers.

2.1.1.3 Test of aerostatic coefficients

The test for the aerostatic coefficients is conducted for the same girder section models tested in the wind tunnel experiment. The test measures the drag, lift, and rotation moments the fixed model experiences under various wind speeds and attack angles. The test provides information on sectional aerodynamic characteristics for CFD simulation validation of the same girder section.

The static wind loads on bridge girders, such as the drag, lift, and rotational moments, are measured using the wind axis system and body axis system. They use the wind flow direction or the girder section orientation as the standard axis. Under the body axis system, the static wind load that acts on the unit-length girder section can be denoted with the following convention shown in Figure 2-1-10:

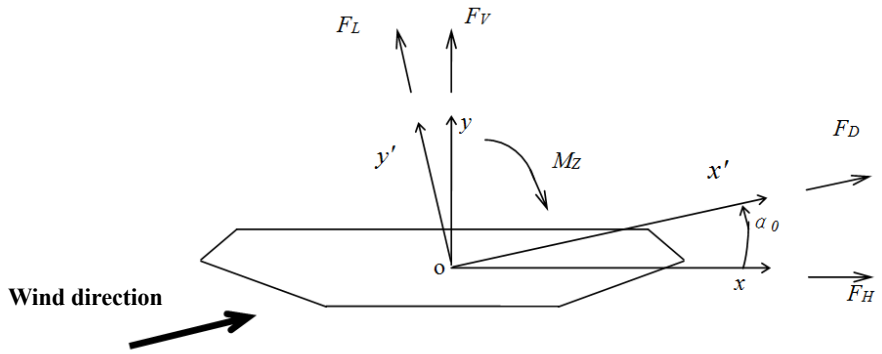

Figure2-1-10: Aerostatic coefficients coordinate system

The drag of the girder section is represented as:

$$F_H = \frac{1}{2}\rho U^2 C_H(\alpha_0) D \qquad \textbf{(Eq. 2-1-3)}$$

The lift of the girder section is represented as:

$$F_V = \frac{1}{2}\rho U^2 C_V(\alpha_0) B \qquad \textbf{(Eq. 2-1-4)}$$

The rotational moment of the girder section is represented as:

$$F_M = \frac{1}{2}\rho U^2 C_M(\alpha_0) B^2 \qquad \textbf{(Eq. 2-1-5)}$$

where ρ is the air density, U is the average incoming flow speed, $C_H(\alpha_0)$ $C_V(\alpha_0)$ $C_M(\alpha_0)$ are the aerostatic coefficients under attack angle α_0 when measured in the body axis system, and D and B are the height and width of the girder section, which are 4.0 m and 31.5 m, respectively.

The wind tunnel test for the aerostatic coefficients is conducted on a dedicated device to test the aerostatic coefficients in the 1st experimental section of the XNJD-1 wind tunnel laboratory. The model is connected to the wind tunnel supports with fixed connections, and force balances are installed on the supports to measure the aerostatic coefficients under different attack angles.

The aerostatic coefficients are determined with a static wind load experiment. The model is anchored with bolts to two built-in supports of the wind tunnel via end plates to guarantee the two-dimensional characteristics of the model. Model end plates and supports are anchored tightly together with small spaces in between to avoid contact friction so that the force balance could record properly. The supports are connected to a rotating device outside the tunnel to adjust attack angles. The setup of the aerostatic coefficients test is shown in Figure 2-1-11.

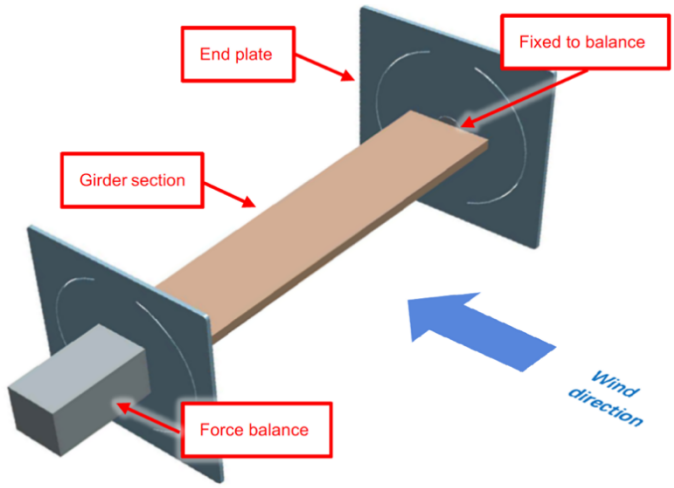

Figure 2-1-11: Girder section aerostatic coefficients testing setup

All girder section models used in the experiment are tested for their aerostatic coefficients. This test includes four wind speeds, 0 m/s, 10 m/s, 15 m/s, and 20 m/s. The attack angles are a

total of 25 angles ranging from -12 degrees to 12 degrees. Time histories of drag, lift, and rotational moment are measured for each working state under all attack angles and wind speeds. The time histories of 10 m/s, 15 m/s, and 20 m/s can be subtracted by that of 0 m/s to obtain the real-time histories without environmental disturbance and noises, representing the VIV forces the model experiences under different working states and conditions. By taking the average of the time histories under different working states, conditions, and attack angles, the spectrum of the aerostatic coefficient can be obtained.

The VIV force time histories can then be put through Fourier transformation to yield a frequency domain spectrum, which indicates the dominating vortex shedding frequencies under different working states and conditions. The Strouhal numbers, *St*, of the respective states can be calculated with the following equation.

$$St = \frac{f \times D}{U} \qquad \textbf{(Eq. 2-1-6)}$$

where *f* is the predominant vortex shedding frequency, *D* is the height of the girder section, and *U* is the wind speed.

The aerostatic coefficients and Strouhal numbers of the sections in the wind tunnel experiment can be compared with individual results from CFD analysis and additional experiments to verify the validation of CFD models and the consistency of repeated experiments.

2.1.2 Working states tested in the experiment

Several working states are selected for this experiment, including a 1:6 rectangular girder,

a 1:7.875 rectangular girder, a 1:6 rectangular girder with triangular wind noses, and a 1:7.875 rectangular girder with triangular wind noses. Each model is tested with different aerodynamic measurements under attack angles 0°. Selected working states are tested for their aerostatic coefficients performance for VIF characteristics under wind speeds of 5 m/s, 10 m/s, and 15 m/s, as well as dynamic VIV response performance of wind speed range of 0 m/s to approximately 20 m/s. The working states in the experiment are summarized below in Table 2-1-3.

Table2-1-3: Working states summary for rectangular girders

Working state number	Working state description
R1	1:6 No Aerodynamic measure
R2	1:7.875 No Aerodynamic measure
R3	1:7.875 With wind nose
RN2	1:6 With wind nose

2.1.3 Experiment results

The VIV response result of rectangular girder sections at 0° attack angle is summarized below in Table 2-1-4.

Table 2-1-4: Experimental results for rectangular girder sections at 0°

#	Measures (Damping ratio %)	1st order vertical (mm m/s Hz)	2nd order vertical (mm m/s Hz)	1st order rotational (° m/s Hz)	2nd order rotational (° m/s Hz)
R1	1:6 No measure (2.79 vertical) (2.60 rotational)	118 0.75-1.2 1.97	144 1.6-2.3 1.97	0.27 1.6-2.2 4.78	0.59 2.7-4.0 4.78
R2	1:7.875 No measure (2.98/2.88) (2.72/2.50)	35 0.7-1.1 1.84	176 1.45-2.5 1.84	0.06 1.7-2.2 4.56	0.47 3.0-4.25 4.56
R3	1:7.875 Wind nose (2.88) (2.49)	344 0.86-1.85 1.91	-	1.46 2.29-4.1- 5.00	-
RN2	1:6 Wind nose (2.74) (2.66)	465 0.87-1.85 2.00	-	1.60 2.26-4.09 4.68	-

As seen in Table 2-1-4, the 1:6 and 1:7.875 rectangular girder sections without aerodynamic measures experience two obvious VIV lock-in ranges for both vertical bending and rotational modes. There is only one obvious VIV lock-in range for both modes for the 1:6 and 1:7.875 rectangular girder sections with wind noses installed.

The VIV responses of the 1:7.875 section and the 1:6 sections at 0° attack angle in the wind tunnel experiment are shown in Figure 2-1-12 and Figure 2-1-13.

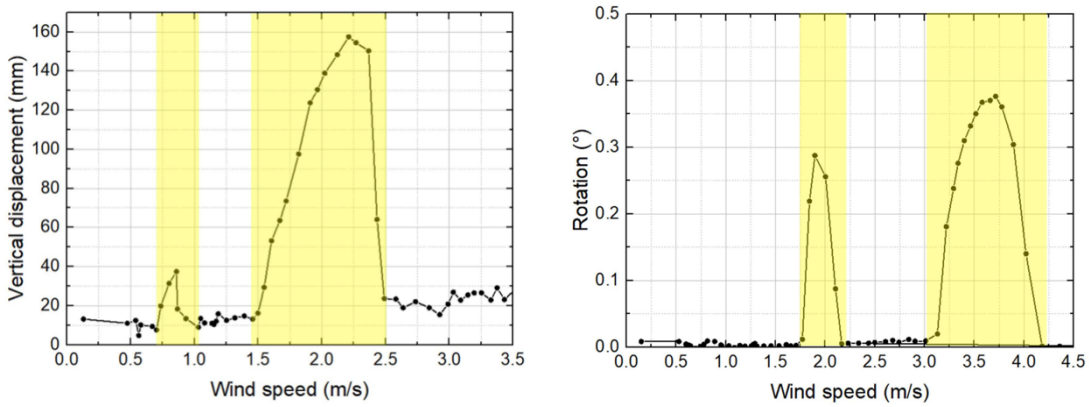

(a) 1st order vertical bending mode *(b) 1st order rotational mode*

Figure 2-1-12: Maximum responses of 1:7.875 section

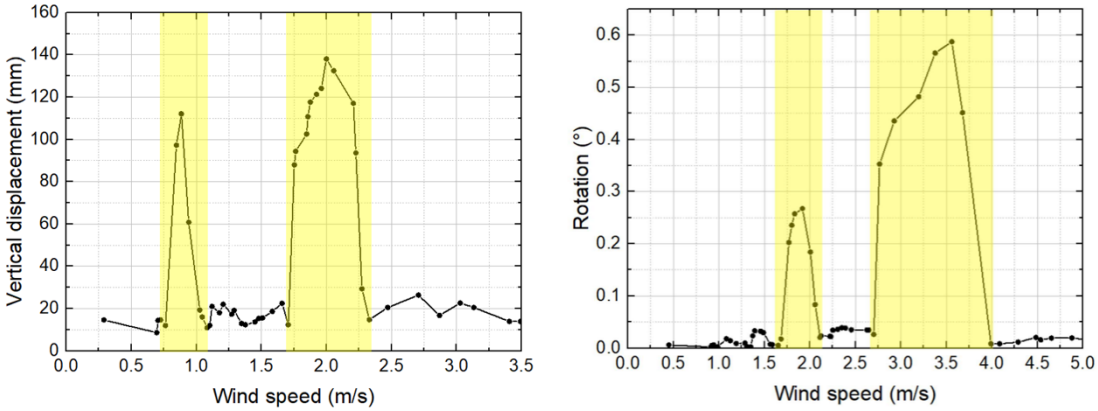

(a) 1st order vertical bending mode *(b) 1st order rotational mode*

Figure 2-1-13: Maximum responses of 1:6 section

Figure 2-1-12 shows two VIV lock-in ranges for the 1:7.875 section in the 1st order vertical bending mode and the 1st order rotational mode. Figure 2-1-13 shows two VIV lock-in ranges for the 1:6 section in the same two modes. All VIV ranges are highlighted. For both modes of each of the two sections, the first lock-in ranges are narrower and have a smaller amplitude than the second lock-in ranges. Figure 2-1-14 shows the VIV response for the 1:6 rectangular girder section with wind noses installed.

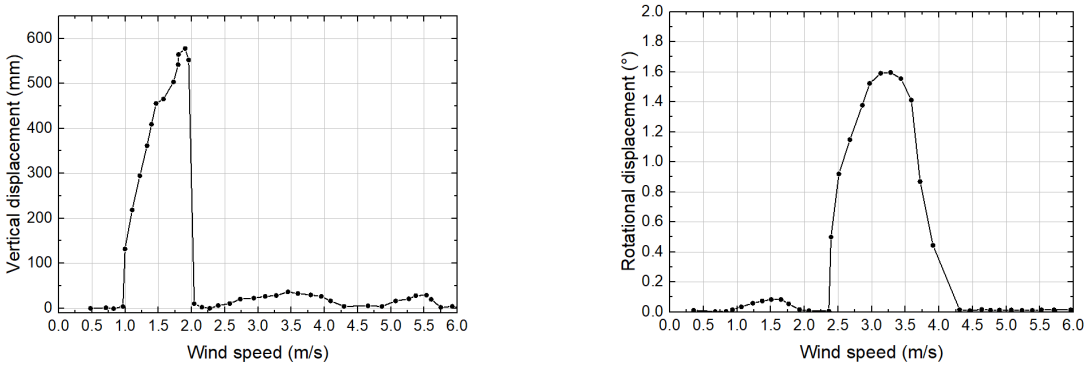

(a) Vertical bending mode (b) Rotational mode

Figure 2-1-14: VIV lock-in range of the 1:6 rectangular girder section with wind noses installed

As seen in Figure 2-1-14, it is clear that only one obvious VIV lock-in range is observed for both the vertical bending mode and the rotational mode for the 1:6 rectangular girder section with wind noses. Since the 1:6 rectangular girder section with wind noses can be viewed as either the 1:6 rectangular section with wind noses installed (same base shape) or the 1:7.875 rectangular girder section with its two ends shaped as wind noses (same aspect ratio), the VIV response of the 1:6 rectangular girder section with wind noses is comparable to that of the 1:6 and the 1:7.875 rectangular girder sections. When the responses are compared, it is reasonable to suspect that adding the wind noses to the rectangular girders altered the flow field in a certain way and caused the two lock-in ranges to become just one lock-in range. CFD analyses are conducted and discussed in the following sections to explore the mechanism of the two VIV lock-in ranges for the rectangular girders and the mechanism of the one VIV lock-in range for the rectangular girder with wind noses.

2.2 VIV response for rectangular box girder sections based on CFD analysis

This section involves the CFD numerical analysis of a rectangular girder section with an aspect ratio close to the prototypical bridge and seeks to analyze the mechanisms of VIV of a rectangular girder section with individual vortex tracking and girder surface pressure distribution analysis under two-dimensional space. The flow field around rectangular sections with an aspect ratio of 1:6 and 1:7.875 are monitored with monitoring faces consisting of monitoring points generated by a mass point setup process. A simplified two-dimensional vortex recognition method and a new vortex tracking method based on distributions of static pressure and velocity of the surrounding flow field are proposed to track the development of individual vortexes. Based on the vortex tracking result, a vortex merging pattern that reduces the number of vortexes on the upwind side to approximately half on the downwind side is observed, and the mechanism of such a pattern is analyzed. As a result of the vortex merging pattern, two different lift force frequencies on the upwind side and downwind side are revealed, and the contribution of lift forces from different locations of the girder to the total lift force is discussed.

2.2.1 Numerical model setup and validation

2.2.1.1 Meshing and modeling setup

This section of research focuses on the CFD simulation and analysis of a 1:7.875 rectangular cross-section with a sectional dimension of 80 mm-by-630 mm. The 1:7.875 aspect

ratio of the rectangular section used in the simulation is the same as the girder of the long-span suspension bridge currently under construction. The dimension of the rectangular section is scaled from the bridge girder using a scaling factor of 1:50. ANSYS Fluent is used as the analyzing software for the simulation, and MATLAB is used as the data processing platform. The research defines monitoring faces consisting of monitoring points that record flow field aerodynamic properties such as pressure, velocity, vorticity, etc., to understand the mechanisms and patterns of vortex-shedding around the girder.

The total number of mesh elements is approximately 540,000, the core layer locates around the girder section has approximately 400,000 elements, and the skew ratio for any elements is lower than 0.5%. Unstructured meshing is used in the core layer to accommodate the section's layout and improve the simulation accuracy of such layer, and structured meshing is used for the outer layer to increase simulation efficiency. The total meshing area has a height of 30 times the girder width and a width of 50 times the girder width. The setup follows the ANSYS Fluent theory guide [70]. The meshing layout is shown below in Figure 2-2-1.

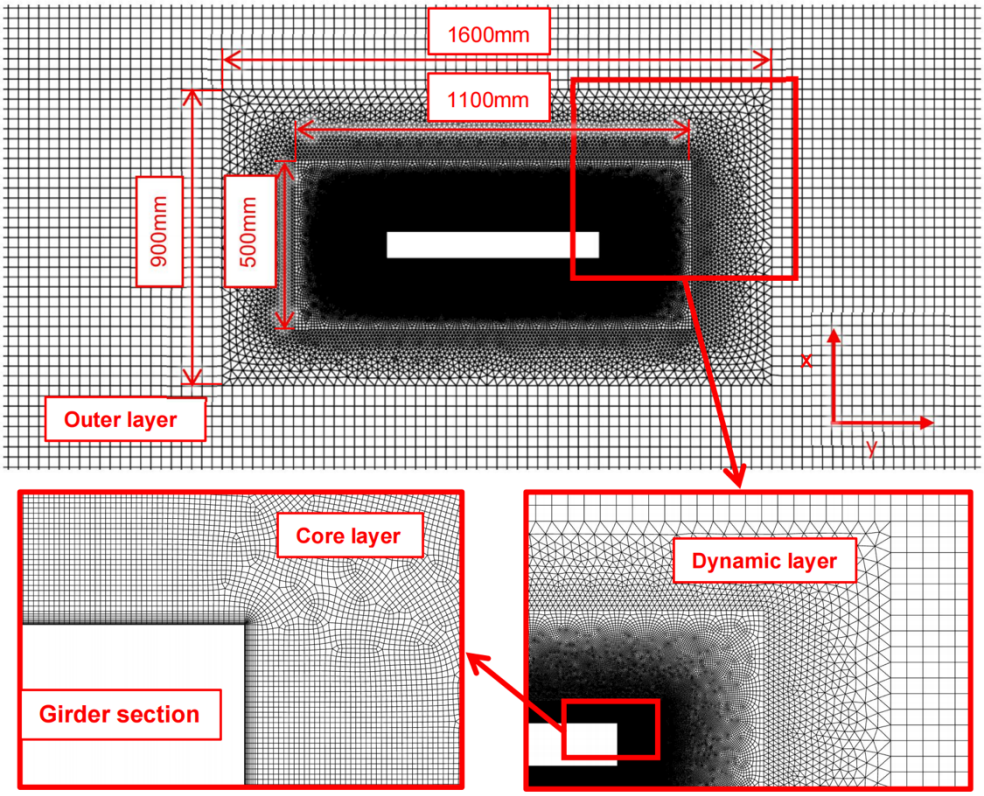

Figure 2-2-1: Meshing layout around the girder section

The server used for this simulation is equipped with a 64-core CPU. The turbulence model used in this simulation is the Detached-Eddy Simulation (DES), which is a combination of the Reynolds Average Navier-Stokes (RANS) model for near girder mesh elements and the Large Eddy Simulation (LES) model for elements away from the girder section. The RANS model used in this simulation is K-omega. The solution method is SIMPLEC, where turbulence and viscosity are taken as 0.5% and 2%, respectively.

In comparing the aerostatic coefficients (lift, drag, rotational moment) of the CFD model with different time step sizes, it is found that the values of coefficients start to converge when the simulation time step approaches 0.001 seconds. Therefore, the time step size of 0.001 seconds is

selected for better efficiency. The lift force coefficient comparison for different time step sizes at 0° attack angle is shown below in Figure 2-2-2.

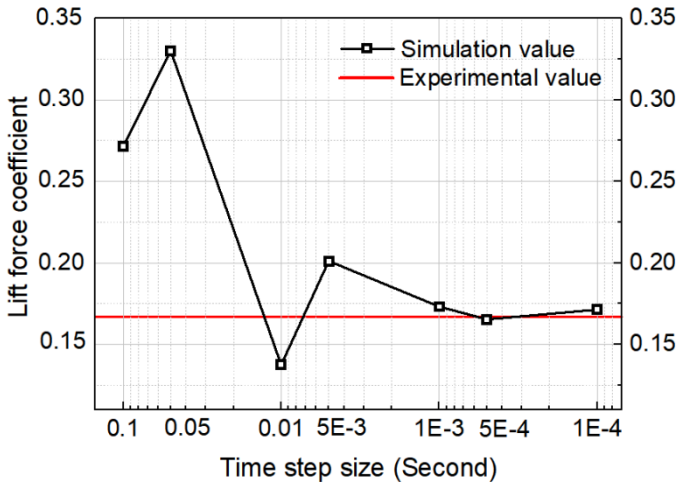

Figure 2-2-2: Lift force coefficient comparison of different simulation time step size

2.2.1.2 Monitoring points setup

2.2.1.2.1 Monitoring points and faces layout

To capture all potential vortexes traveling above and below the girder section and their respective pressure distribution details, the monitoring setup included 26 monitoring faces, each constituting 201 monitoring points with a length of 100 mm (0.5 mm between points, 50 mm between faces) set above and below the girder section. The monitoring faces are symmetrical with respect to the horizontal center line of the girder section to reveal the synchronicity of the vortexes above and below the girder. The layout and numbering of the monitoring faces are shown in Figure 2-2-3.

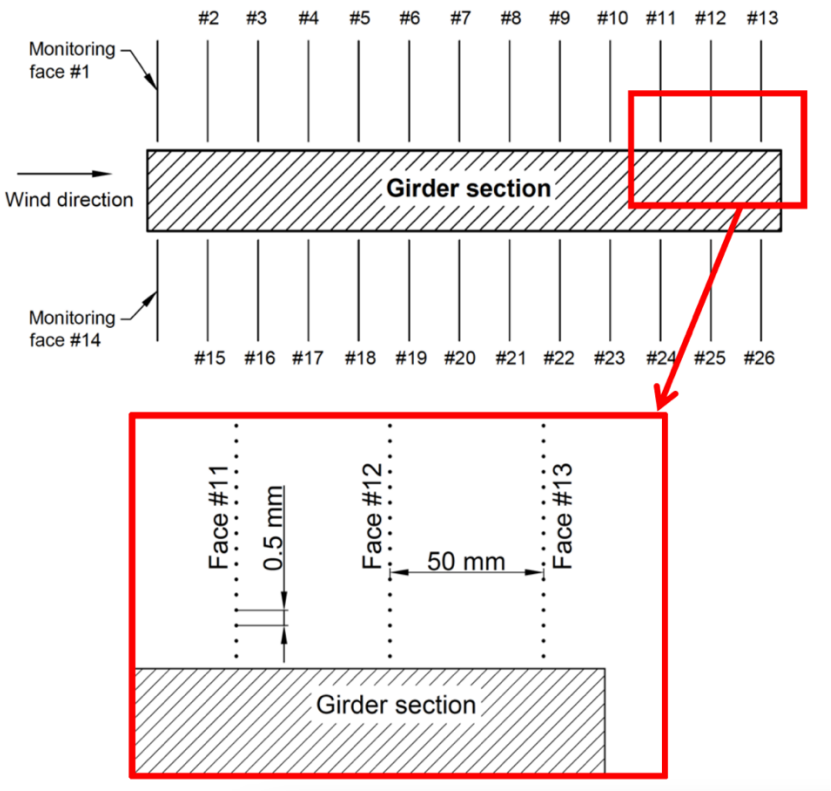

Figure 2-2-3: Monitoring face layout

2.2.1.2.2 Setup method and process

The easiest way to set up monitoring points is by clicking and typing in the GUI (Graphic User Interface). However, the GUI setup is only efficient for a small number of monitoring points. The setup process of this research involves thousands of points, and the traditional setup process utilizing GUI can be very time-consuming. To achieve an efficient setup process involving more than 8000 monitoring points around the girder section, this research performs a mass point setup process using MATLAB script, Fluent TUI input, and BAT command. Fluent TUI commands are generated using MATLAB scripts and entered into BAT command for background execution in

Fluent, automatically setting up the monitoring points around the girder. With all but one monitoring face located in the middle of the girder top surface being activated, the simulation for the flow field is run for 5 seconds before the pressure distribution time history of the monitoring face of 0.1 seconds duration is extracted for DMD growth/decay rate analysis conducted in MATLAB, if the growth/decay rate within the DMD analysis is higher than 100, then the flow field is considered to have not reached stable condition, then, the 5 seconds of data recording and DMD analysis process is repeated until the growth/decay rate is lowered than 100, in which case the flow field is considered stable. After the stable condition is achieved, all monitoring points are activated and used for data recording for 1 second, and the data recorded is exported for analysis. The setup process is shown in Figure 2-2-4.

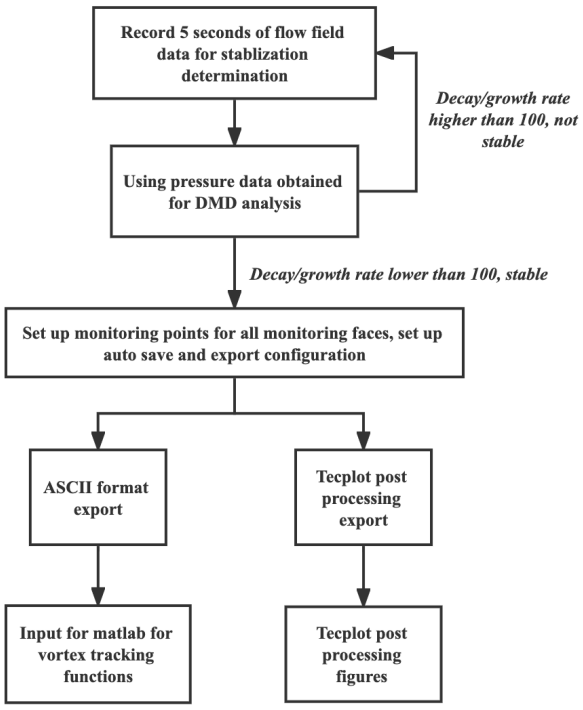

Figure 2-2-4: Monitoring points setup process

The setup process allows one-time setup and recording of desired data for all points around the girder section (velocity, static pressure, and vorticity) and exports the result in various data analysis formats.

2.2.1.2.3 Numerical model validation

Numerical model validation is performed by comparing the aerostatic coefficients of the CFD analysis with that of the wind tunnel experiment of the same girder section. The girder is tested for its aerostatic coefficients in three positive attack angles (0°, 3°, 5°) as the model is vertically symmetrical. The result is collected under the wind speed of 10 m/s and compared to the result of the wind tunnel aerostatic coefficients test for the same wind speed. The comparison of the result is shown in Figure 2-2-5.

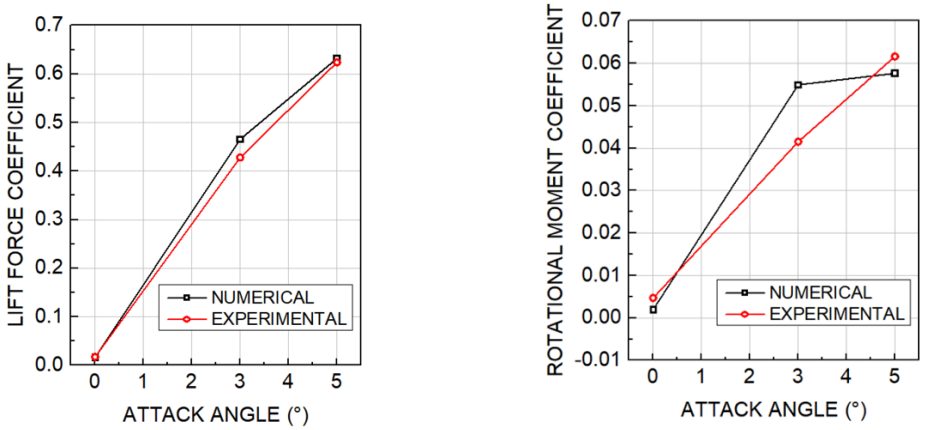

(a) Lift force coefficients *(b) Rotational moment coefficients*

Figure 2-2-5: Aerostatic coefficients comparison of lift and rotational moment

As seen in Figure 2-2-5, the aerostatic coefficients of lift force and rotational moment of the numerical simulation and the wind tunnel experiment match well.

The Strouhal number calculation of lift force in 0° attack angle under 10 m/s wind speed in the wind tunnel experiment yields a predominant frequency of 22.37 Hz, the characteristic length of the section (D) is 0.08m, and the wind speed (U) is 10 m/s. The resulting Strouhal number is 0.178. The frequency distribution of the girder section lift force under 10 m/s wind speed at 0° attack angle is shown below in Figure 2-2-6.

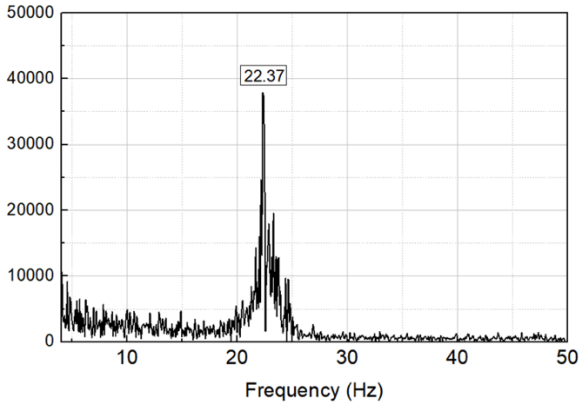

Figure 2-2-6: Experimental frequency distribution of girder section

For numerical simulation results of the same attack angle and wind speed, the corresponding predominant frequency is 20.11 Hz. The frequency yields a Strouhal number of 0.161, close to the experimental value of 0.178. The Strouhal number shows close results between wind tunnel experiments and numerical simulation for other attack angles under other wind speeds. The result of the numerical simulation fits well with the wind tunnel experiment.

By comparing the results of the aerostatic coefficients tests and the Strouhal number tests between wind tunnel experiments and numerical simulations, it is concluded that the numerical model used in this research is reliable and provides realistic flow field simulation around the rectangular box girder section.

2.2.2 Vortex recognition and path tracking

2.2.2.1 Method for vortex recognition

The flow field simulation in this research is in the two-dimensional space, and the vortexes mostly move in areas away from the girder section surface. Therefore, they are rarely affected by the near-surface shear layer disturbance. As a result, the second and third-generation vortex recognition methods categorized by Wang et al. [76] mentioned in the literature review section are unsuitable for the analysis. During post-processing of the simulation, upon close observation of both static pressure distribution and vorticity distribution, it is found that the centers of low-pressure zones in the static pressure distribution directly correspond to centers of high vorticity zones, which are defined as the centers of the vortexes according to first generation standard categorized by Wang et al. [76]. Since the lower pressure zone recognition requires less filtering than high vorticity zone recognition, this research chooses to utilize low-pressure zones as the centers for vortex recognition.

To verify the correlation between low-pressure zones and high vorticity zones in the flow field, 100 snapshots of 0.01 seconds intervals for pressure and vorticity distribution of the flow field around the girder are extracted from the simulation. For each of the snapshots, low-pressure zone centers and high-vorticity zone centers are identified, and these center locations of all 100 snapshots are compared for their respective location differences. Figure 2-2-7(a) shows the location extraction process of the center locations, and Figure 2-2-7(b) shows an example of center

location differences at one of the 100 flow field snapshots.

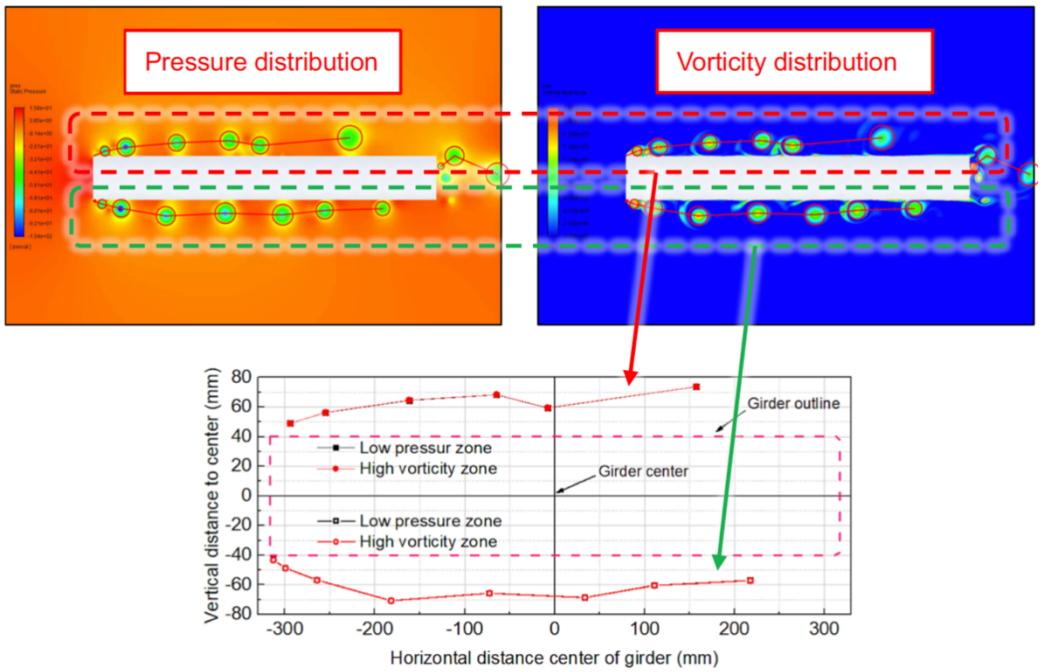

(a) Low-pressure zone and high vorticity zone comparison

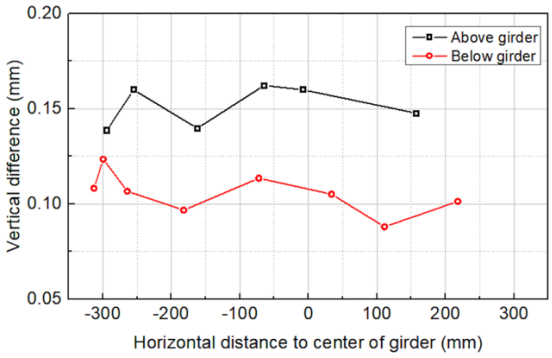

(b) Location difference between low-pressure zones and high-vorticity zones

Figure 2-2-7: Vorticity and pressure distribution of one snapshot

As shown in Figure 2-2-7(b), the differences between centers of low-pressure zones and high vorticity zones are all lower than 0.175 mm. Conducting similar analysis for all 100 snapshots extracted, the maximum difference is 0.189 mm, which is 0.23% of the total height of the girder

section (80 mm). It can be concluded that the centers of low-pressure zones are good indicators of centers of high vorticity zones and centers of vortexes.

2.2.2.2 Vortex tracking process

The flow field is first brought to a stable condition. All monitoring points around the girder are then activated and used to record vorticity, static pressure, and wind speed in the X and Y direction for a 1 second duration. The vortex tracking process is conducted as follows:

Step 1: Analyze the data of the initial face to determine the locations of the centers of all vortexes that flow past the initial face within a specific period of time. A monitoring point is considered the center of a vortex when it passes through the monitoring face if its pressure value is the local minimum on both spatial and time domains. Table 2-2-1 lists the distribution of vortex centers passing through monitoring face #3 between 40 seconds and 40.5 seconds of the numerical simulation. The point number in the table is marked in sequence, starting from the first monitoring point of the monitoring face #3 closest to the girder surface (point #1 of face #3) to the point furthest from the surface (point #201 of face #3). A schematic for step 1 is shown below in Figure 2-2-8.

Table 2-2-1: Vortex center distribution on face #3 from 40 to 40.5 s

time (s)	**40.018**	**40.06**	**40.105**	**40.144**	**40.185**	**40.246**	**40.301**	**40.351**	**40.399**	**40.441**	**40.478**
Point #	46	45	46	50	48	44	46	56	46	44	40

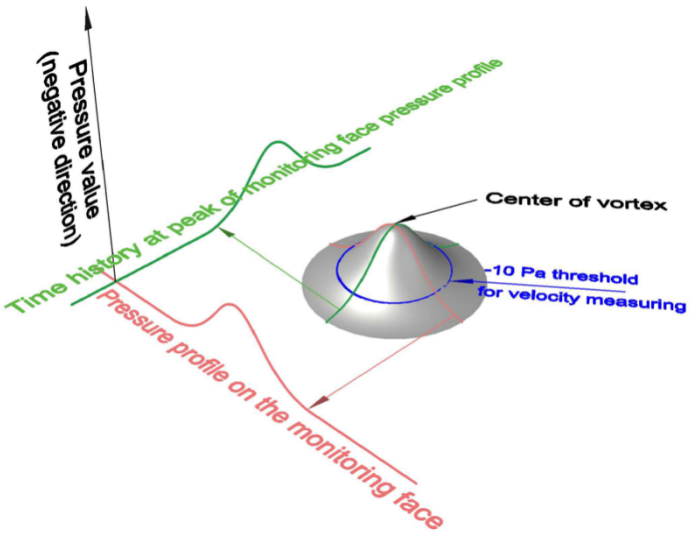

Figure 2-2-8: Schematic for vortex tracking step 1 (3D view)

Step 2: Predict the location and time of a vortex when it flows past the subsequent monitoring face. Take a vortex that flows from monitoring face #3 to monitoring face #4 as an example, the pressure distribution around its vortex center is scanned when it flows past monitoring face #3 and determines the perimeter of the vortex with a -10 Pa threshold value. Take the average of the velocity of the vortex perimeter in both X and Y directions for the velocity magnitude and moving direction of the vortex. The velocity magnitude and direction can be used to predict the vortex center location when it flows past monitoring face #4, as the distance between monitoring face #3 and monitoring face #4 is known (50 mm).

A schematic for step 2 is shown below in Figure 2-2-9.

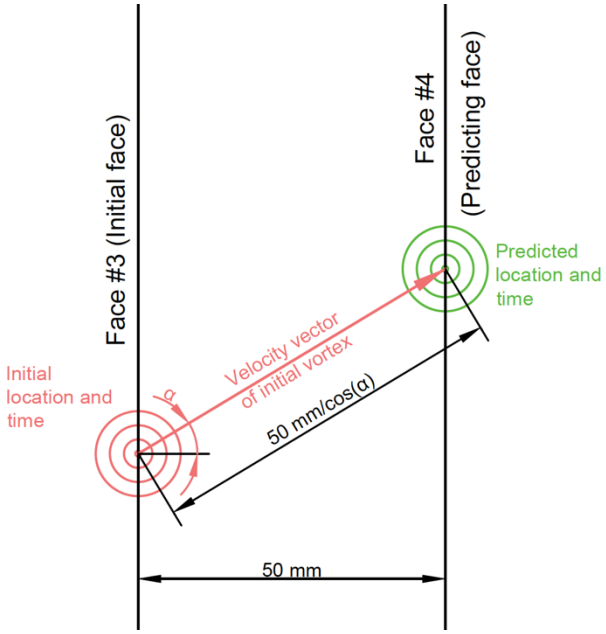

Figure 2-2-9: Schematic for vortex tracking step 2 (elevation view)

Step 3: At the predicted time and location of a vortex when it flows past monitoring face #4, scan the surroundings of the predicted values, then confirm and correct (if necessary) the location and time of the vortex center. Repeat process steps 1-3 to analyze the path of the vortex on all monitoring faces.

In the low-pressure zone vortex recognition method, it is found that vortex tracking is most accurate when the threshold of the low-pressure zone is set as -10 Pa, the time and spatial accuracies are 0.001 seconds and 0.5 mm, which are the smallest intervals of monitoring points and time steps, respectively.

The process is named the MPF-track method and is summarized in the flow chart in Figure 2-2-10.

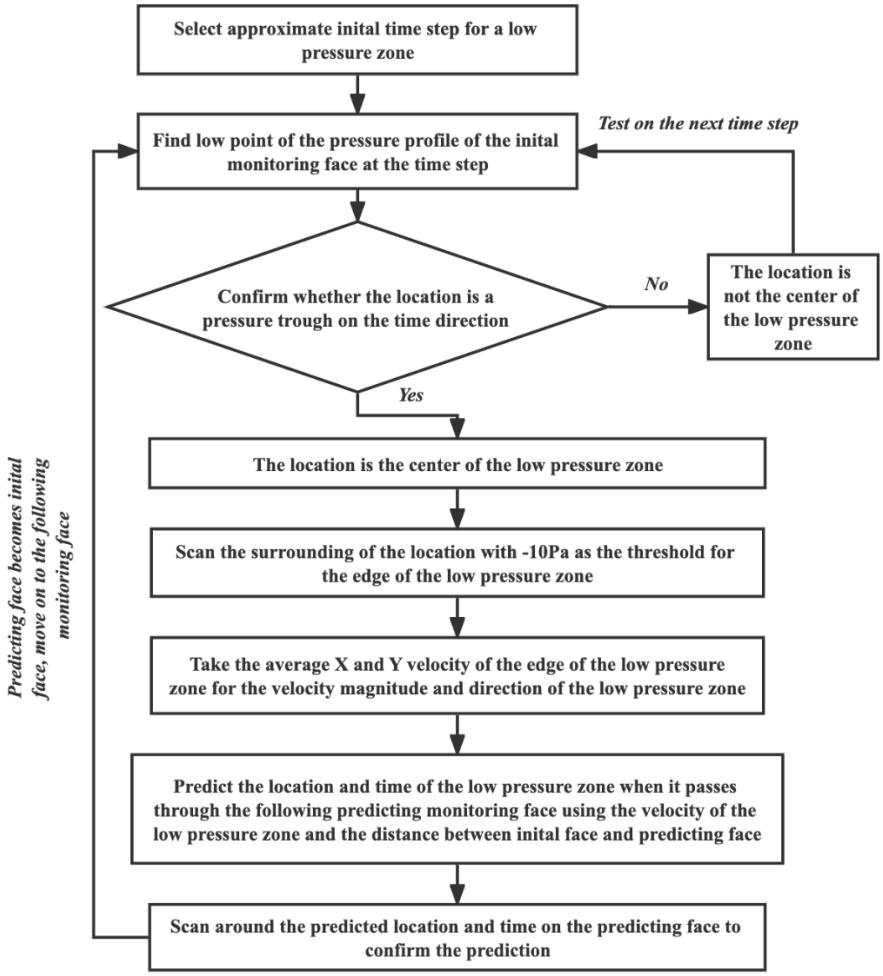

Figure 2-2-10: Vortex tracking flow chart

2.2.3 Vortex merging and its mechanism

2.2.3.1 Vortex merging

By monitoring the flow field above and below the girder section, a like-sign vortex merging pattern is observed and analyzed. When a vortex sheds from the upwind side leading edge, it tends to reattach to the girder surface and slow down. Matsumoto [46] verified the phenomenon of vortex

reattachment on rectangular sections and revealed that the reattachment would decrease the vortex speed to approximately 60% of its speed before reattachment. After the leading vortex is slowed down by the reattachment to the girder surface, the trailing vortex, which travels at its original speed and rotates like-sign with the leading vortex, would approach the leading vortex and start to interact with the leading vortex. The two vortexes would eventually merge to form a new vortex. Cerretelli et al. [118] investigated the physical mechanism of like-sign vortexes merging and revealed that there are two small co-rotating vortex pairs between the two merging vortexes when they approach and the pair induced velocity that pushes the two centroids together. Wang et al. [119] explored the interaction of two merging vortexes near a surface and revealed that the merging process of two like-sign vortexes would be accelerated due to the in-ground effect of the nearby surface.

A vortex merging process above the 1:7.875 section under 3 m/s wind speed is shown in Figure 2-2-11.

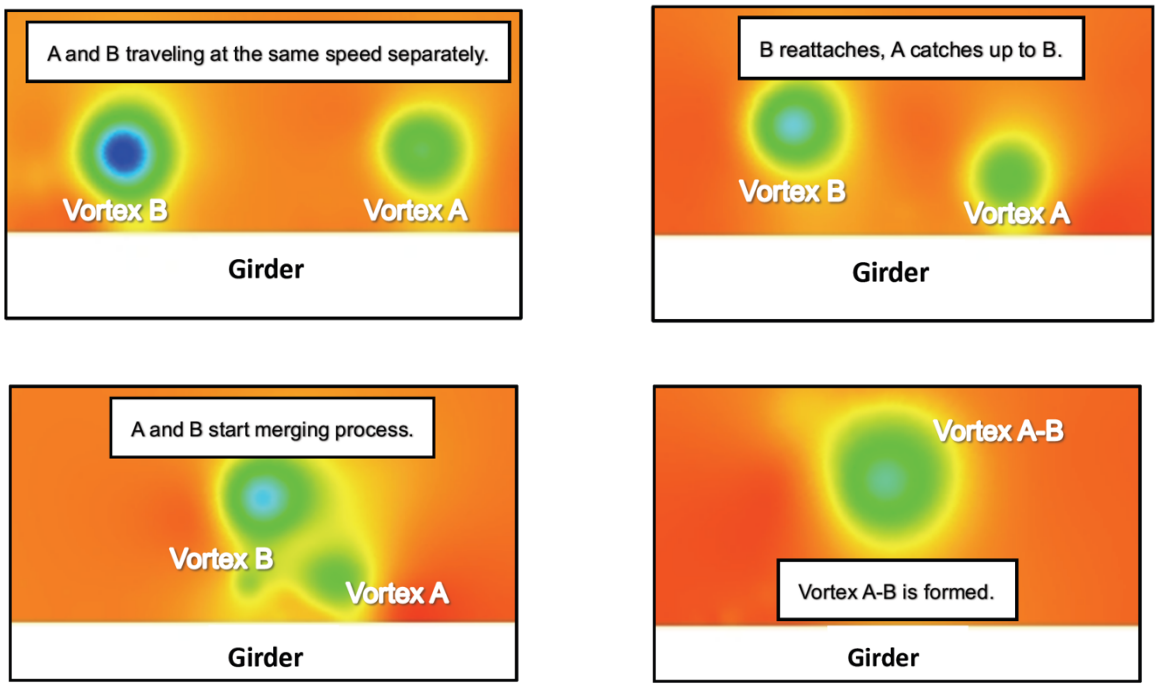

Figure 2-2-11: Merging process of two vortexes

As seen in Figure 2-2-11, two vortexes are formed and traveling with similar speeds from the upwind side to the downwind side of the girder. After the leading vortex (vortex A) is slowed down by its reattachment to the girder section, the trailing vortex (vortex B), which travels at the original speed, would catch up to vortex A. The two vortexes would start a merging interaction, in which vortex B would move away from the girder in a circular motion and merge with vortex A to form a new vortex (vortex A-B). After merging, the newly formed vortex A-B would experience acceleration and resume its travel toward the downwind side of the girder.

Utilizing the vortex tracking process introduced in the previous section (MPF-track), the paths of two vortexes during their merging process can be revealed. Take the two vortexes from the previous paragraph (vortex A and vortex B) as an example. The traveling paths for the two

vortexes until they merge are shown below in Figure 2-2-12.

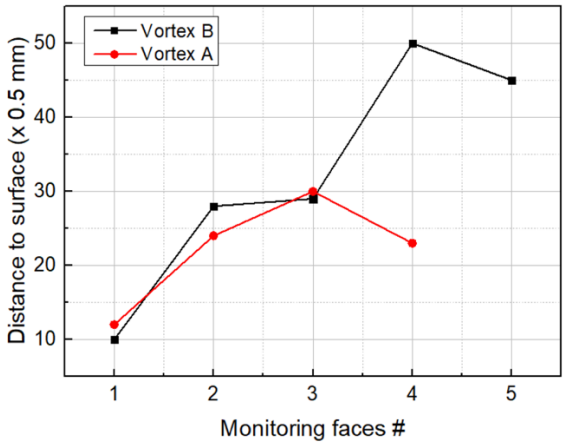

Figure 2-2-12: Paths of vortex A and vortex B until they merge

As seen in Figure 2-2-12, the two vortexes traveled separately before vortex A is not detected on face #5, indicating vortex A merged with vortex B between monitoring faces #4 and #5 to form the new vortex A-B. To monitor the detailed merging process of vortex A and B, 18 additional monitoring faces are added between faces #3 and #5, numbered as monitoring faces # 3-1 to #3-9 and #4-1 to #4-9, the distance between the newly added faces is 5 mm. The layout for monitoring faces is shown in Figure 2-2-13.

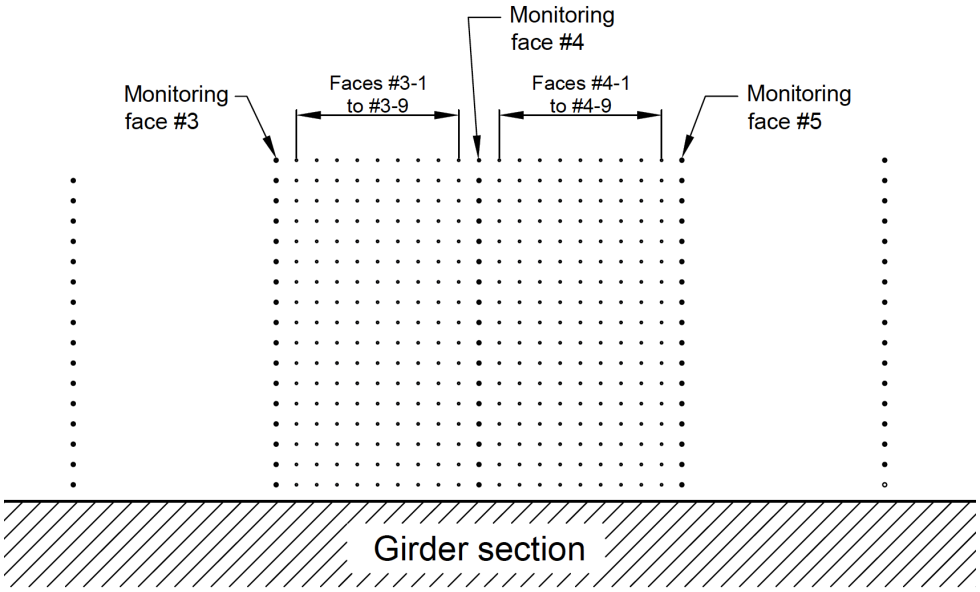

Figure 2-2-13: Newly added monitoring faces between face #4 and #5

With the newly added monitoring faces, the detailed location of vortexes A and B between monitoring faces #3 and #5 is revealed, as shown in Figure 2-2-14.

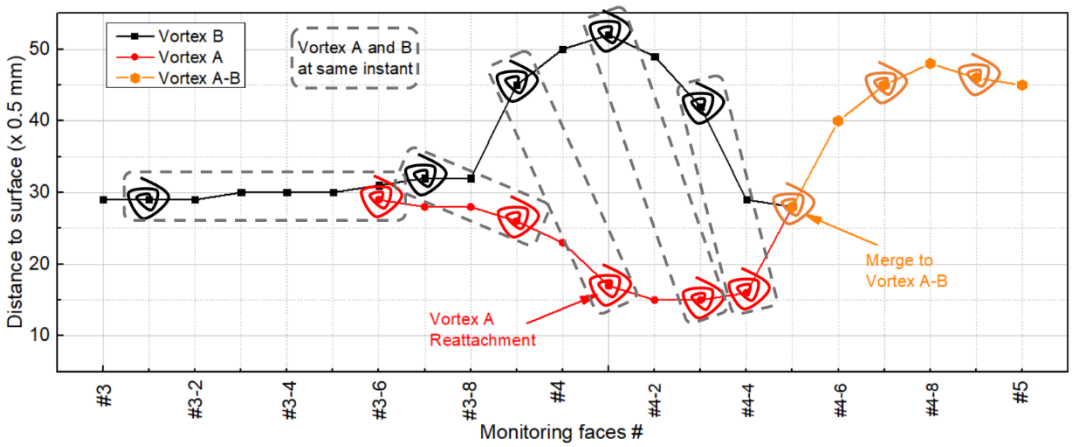

Figure 2-2-14: Location of vortex A and B between faces #4 and #5

Figure 2-2-14 shows the detailed paths for vortex A and vortex B during their merging process between monitoring faces #3 and #5. The red path is vortex A, the black path is vortex B, and the orange path is vortex A-B. Vortex A and B locations at the same instant are circled by one

gray box. It can be observed that vortex A starts to reattach to the girder surface at faces #3-9. After the reattachment and slowdown of vortex A, vortex B, traveling at its original speed trailing vortex A, catches up on vortex A, and the two vortexes start their merging process. The two vortexes eventually merged to form vortex A-B at faces #4-5.

As seen in Figure 2-2-14, after the merging, the newly formed vortex A-B tend to move away from the girder section, it is potentially because of a "dragging" effect due to the circular interaction of vortex A and vortex B during the merging process.

The velocity field during the merging process of two vortexes is shown in Figure 2-2-15.

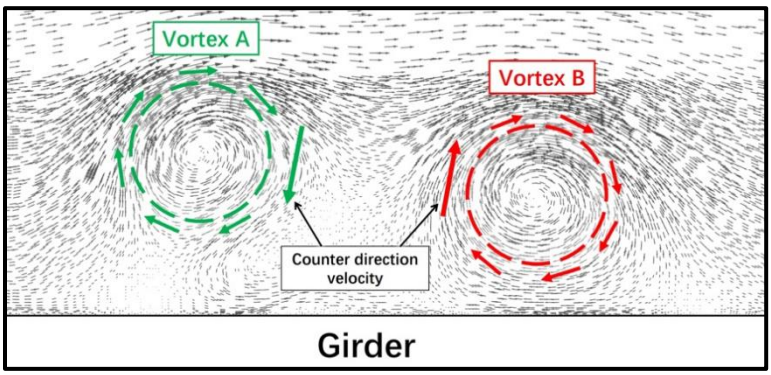

(a) Vortex A approaching Vortex B

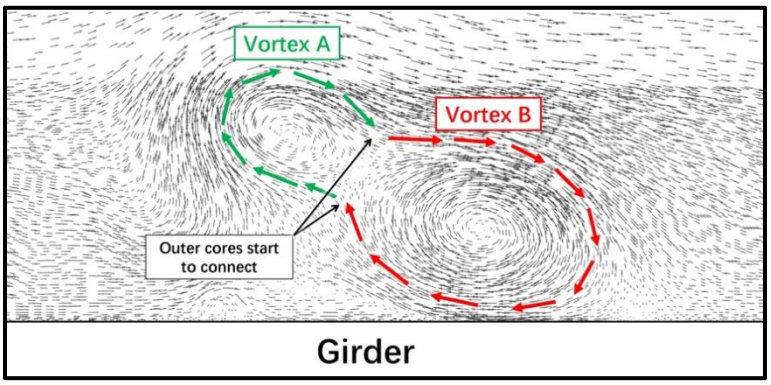

(b) Two vortex start merging

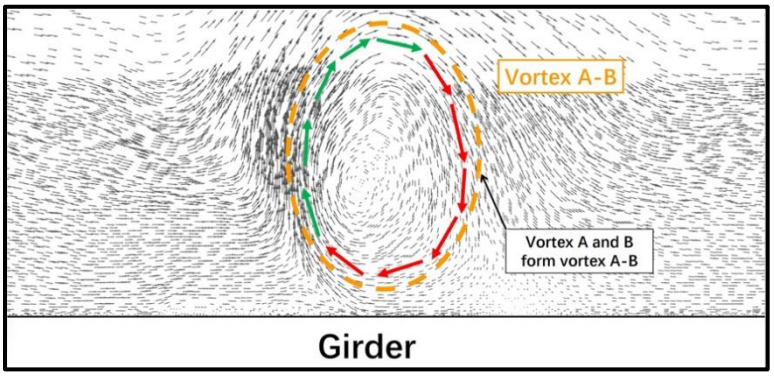

(c) Vortex A-B formed

Figure 2-2-15: Velocity field of vortex A and B during the merging process

As seen in 2-2-15(a), as the two vortexes approach each other, the interface between the two vortexes exhibits a counter direction of velocity. As they move closer, as seen in Figure 2-2-15(b), the outer layer of the two vortexes would connect. Figure 2-2-15(c) shows that the merging process continues, forming the new vortex A-B.

This merging process applies to all vortexes traveling above and below the girder. As a result, the number of vortexes traveling on the downwind side of the girder is lower than that on the upwind side. Monitoring the number of vortexes passing through different monitoring faces above and below the girder section, the decrease in the number of vortexes at different locations above and below the girder can be revealed. The result is shown in Figure 2-2-16.

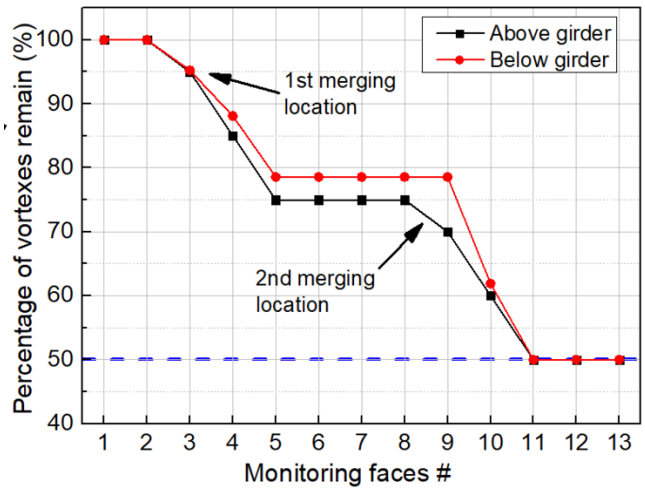

Figure 2-2-16: Number of vortexes at different monitoring faces below the girder

As seen in Figure 2-2-16, the number of vortexes on the downwind side is approximately half of that on the upwind side above and below the girder. Between face 2 and face 5 and between face 8 and face 11 are the largest drops in the number of vortexes passing through, indicating they are the locations where most of the vortexes merging occurs.

2.2.3.2 Diverging pattern after vortex merging

The paths of all vortexes detected on the downwind side of the girder are monitored, and their path from faces #3 to #10 above the girder and from face #16 to #23 below the girder is shown in Figure 2-2-17.

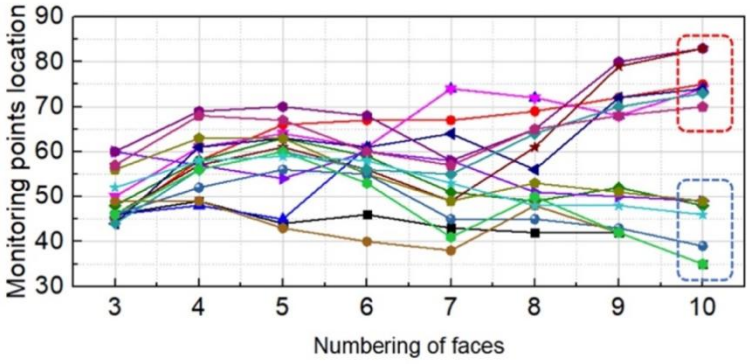

(a) Vortex paths above the girder

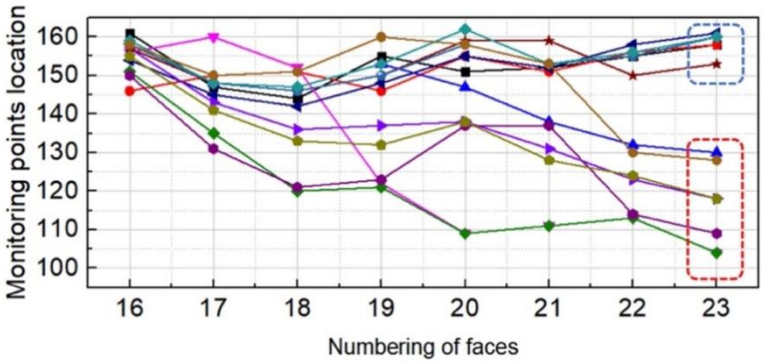

(b) Vortex paths below the girder

Figure 2-2-17: The path of vortexes traveled to the downwind side of the girder

It is clear that there is a diverging pattern of vortexes at the downwind side of the girder, where one branch of the vortexes would move away from the girder, and the other would stay close to the girder. Take the vortexes traveled above the girder in Figure 2-2-17(a) as an example, marking all vortexes passing through faces #9 and #10 in sequential order. The result is shown in Figure 2-2-18.

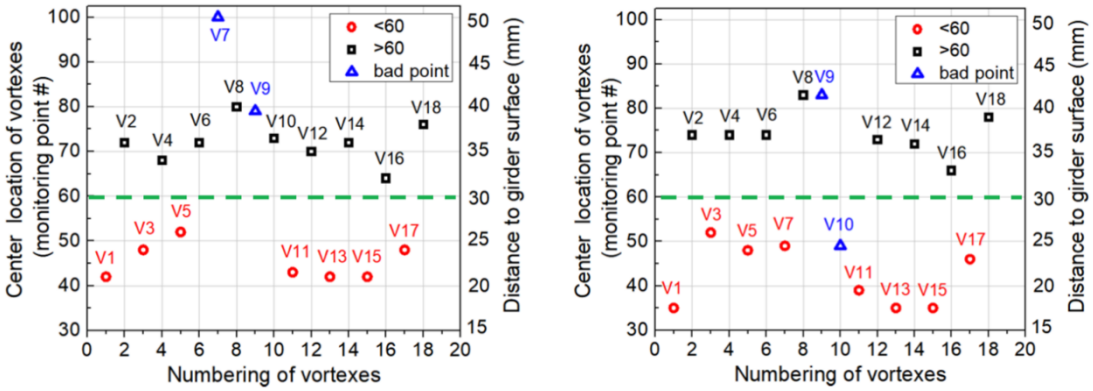

(a) Face 9 *(b) Face 10*

Figure 2-2-18 Vortex location on face 9 and face 10 above the girder

In Figure 2-2-18, all vortex locations are numbered based on their respective sequence when they flow past face #9 and face #10, e.g., the first vortex that passes face #9 is marked as V1, second is marked as V2 in Figure 2-2-18(a), etc. It is clear that most vortexes with values higher than average are even-numbered, and most vortexes with values lower than average are odd-numbered. Based on the observation, it can be seen that two different vortex development paths are formed, and the vortexes following the two paths demonstrate an alternating pattern. A similar sorting procedure for vortexes below the girder reveals the same alternating pattern. When one vortex flows through any path, the following vortex will flow through the other path.

The average path of the vortexes following the two branches of paths above the girder is shown in Figure 2-2-19.

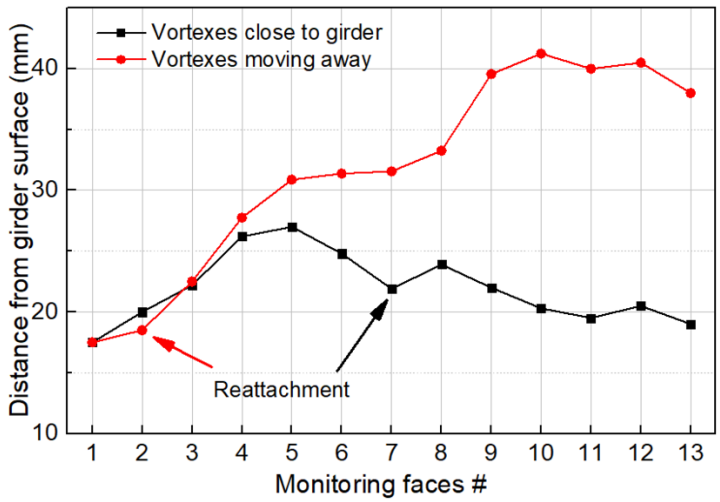

Figure 2-2-19: Average path of vortexes following the two paths

Figure 2-2-19 shows a clear trend of vortex reattachment for vortexes following the two paths at faces #2 and #7. In the previous section, it is found that there are two locations where most of the merging occurred, one initiates at face #2 and the other initiates at face #8. Therefore, the reattachment locations of the two branches coincide with the two merging locations. Further, by categorizing the vortexes following the two different branches of paths, it is confirmed that most of the vortexes following the path away from the girder merge in the first merging location, and all of the vortexes following the path close to the girder merge in the second merging location, the vortexes merge in the two locations follow an alternating pattern.

A possible cause for the diverging pattern is the “dragging” effect due to the circular interaction of the two merging vortexes during their merging process, as mentioned in the previous section. As shown in Figure 2-2-14, after the merging, the newly formed vortex tends to move away from the girder, and since the vortexes merged in the first merging location experienced such

tendency earlier in the process as compared to the other ones, they moved further away from the girder as compared to the vortexes merged in the second merging location, inducing the alternating diverging pattern.

2.2.3.3 Vortex merging pattern under different wind speeds

To investigate how the vortex merging patterns vary under different wind speeds, the vortexes travel below the 1:7.875 section under wind speeds of 0.7 m/s, 1 m/s, 1.45 m/s, 1.7 m/s, 3 m/s, 5 m/s, 7 m/s, and 10 m/s are monitored in the numerical simulation. The merging patterns of various wind speeds are shown in Figure 2-2-20.

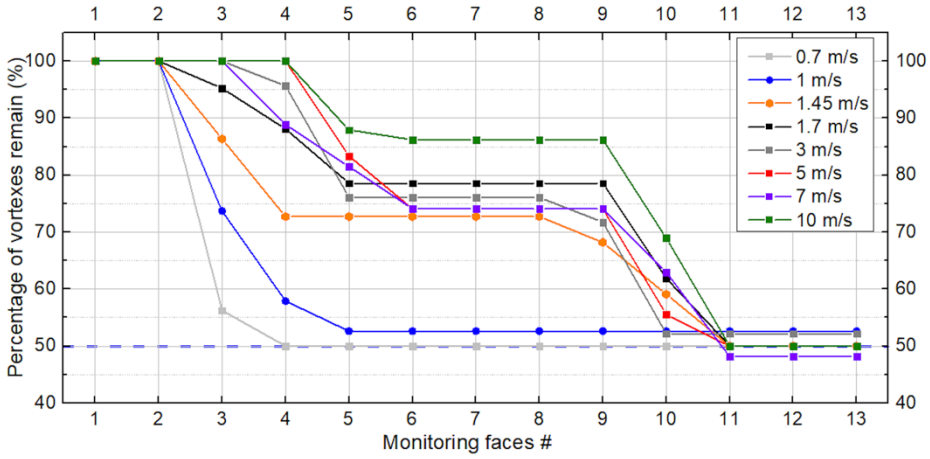

Figure 2-2-20: Merging pattern of different wind speeds

As seen in Figure 2-2-20, the trend of decreasing the number of vortexes varies under different wind speeds. For 0.7 m/s wind speed, the only drop in the number of vortexes occurs between faces #2 and #4. For 1 m/s wind speed, the only drop happens in faces #2 to #5. For 1.45 m/s wind speed, drops happen between faces #2 and #4 and between faces #8 and #11. For 1.7 m/s

wind speed, drops happen between faces #2 and #5 and between faces #9 and #11. For 3 m/s wind speed, drops happen between faces #3 and #5 and between faces #8 and #11. For 5 m/s, drops happen between faces #3 and #6 and between faces #9 and #11. For 7 m/s and 10 m/s wind speed, drops happen between faces #4 and #5 and between faces 9# and #11. It can be observed that as the wind speed increases, the initial merging locations tend to move toward the downwind direction. All mergings occur in the initial merging location for the lower wind speeds of 0.7 m/s and 1 m/s. There is a secondary merging location for all other wind speeds, approximately between faces #9 and #11.

Under all wind speeds, there are approximately half the number of vortexes passing through on the downwind side faces than the upwind side ones. Since the vortexes traveling close to the girder induce variance in the surface pressure of the girder, and the summation of the surface pressure produces total lift force on the girder, it can be concluded that this decrease in vortex number between upwind side and downwind side induced by the vortex merging pattern is the cause for the two different predominant frequencies of lift force on the two sides of the girder. The two different frequencies of lift force at the upwind and downwind sides of the girder lead to the two different total lift force and total rotational moment of the girder under each wind speed, which induce the two VIV lock-in range phenomenon observed in the wind tunnel experiments.

2.2.3.4 Vortex merging around girders with different aspect ratios

To investigate how the vortex merging patterns vary around rectangular sections with different aspect ratios, the vortexes travel below sections with aspect ratios of 1:6, 1:7.875, 1:10, and 1:12 are monitored in the numerical simulation. The merging patterns are shown in Figure 2-2-21.

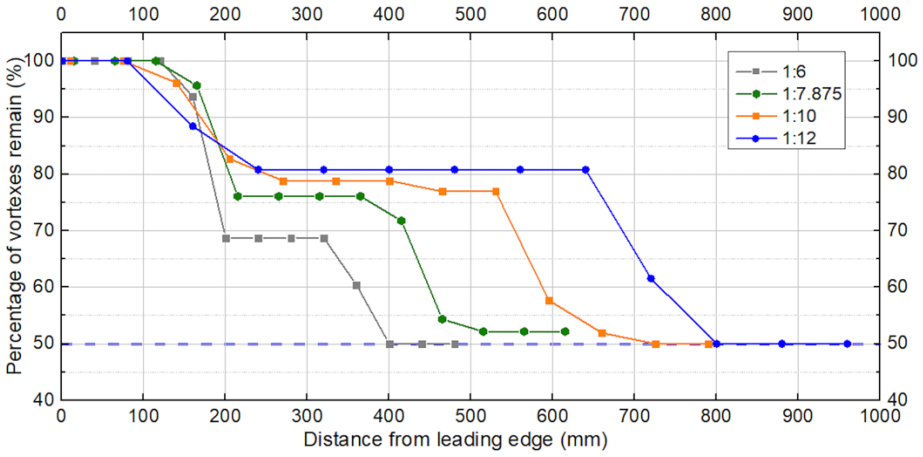

(a) Absolute coordinate

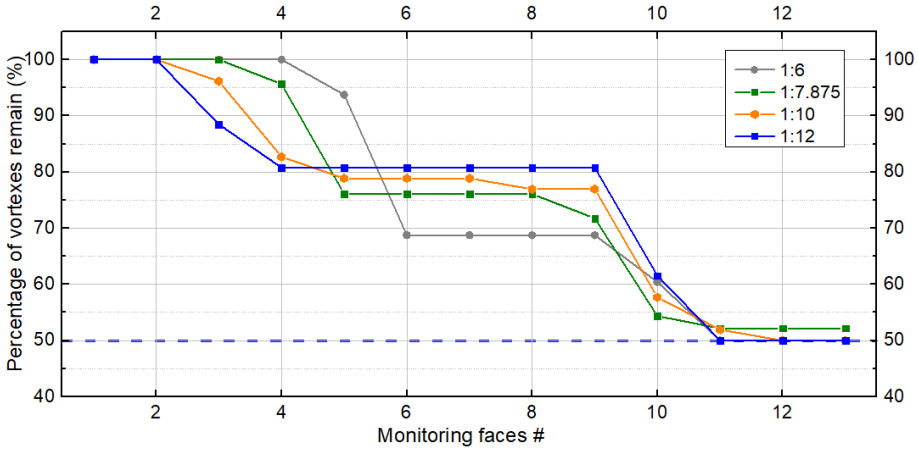

(b) Relative coordinate

Figure 2-2-21: Merging pattern of rectangular sections with different aspect ratios

As seen in Figure 2-2-21, the locations where the merging happens vary for rectangular girders with different aspect ratios. In Figure 2-2-21(a), the merging locations are measured by their horizontal distances from the leading edge of the girder or by absolute coordinates. It can be seen that the first merging locations for all girders are approximately at the same distance (100 – 200 mm) from the leading edge, while the second merging locations move further toward the downwind side as the girder aspect ratios increase. Putting the same comparison in a relative coordinate, as seen in Figure 2-2-21(b), where the locations are measured based on their proportional location to the total length of each girder, the first merging locations move further toward the downwind side of the girders as the girder aspect ratios increase, and the second merging locations remain the same (faces #9-#11). It can be concluded that the first merging locations of the girder are independent of the aspect ratio of the girder under the same wind speed. The second merging locations depend on the girder aspect ratio and would remain at approximately the same proportional location to the total length of each girder.

2.2.4 Characteristics of pressure distribution on girder surfaces

2.2.4.1 Surface pressure distribution

The pressure data of the girder surface can be obtained by setting up pressure monitoring points on the girder surface. To determine how the reduction in the number of vortexes due to the vortex merging pattern affects the girder, the pressure distribution on different locations of the

girder surface is monitored in the simulation.

1200 monitoring points 1 mm apart are placed on the girder section's top and bottom surfaces, and each is divided into 12 groups to record the pressure distribution of the girder's top and bottom surfaces. Each of the 12 groups includes 50 monitoring points, and these 12 groups are gathered into three bigger groups on both the top and bottom surfaces of the girder, namely the upwind side group (group #1 to #4), the middle group (group #5 to #8), and the downwind side group (group #9 to #12). The layout of the surface monitoring points and their respective grouping is shown in Figure 2-2-22.

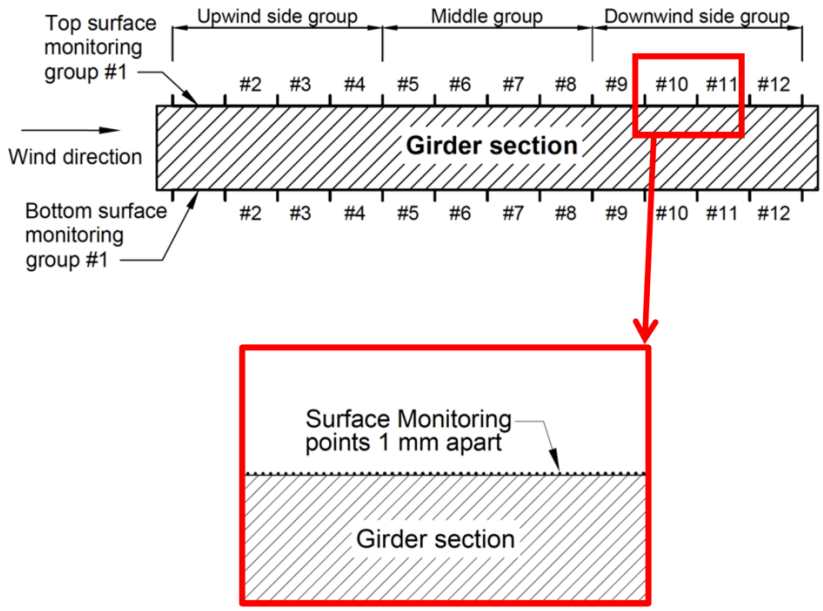

Figure 2-2-22: Girder surface monitoring point distribution and grouping

Adding the pressure of corresponding groups above and below the girder, then integrating the total pressure over the length of each group, the lift force of each group can be calculated. Typical lift force frequency distributions for different girder locations are shown in Figure 2-2-23.

The results for each group are shown in Table 2-2-2.

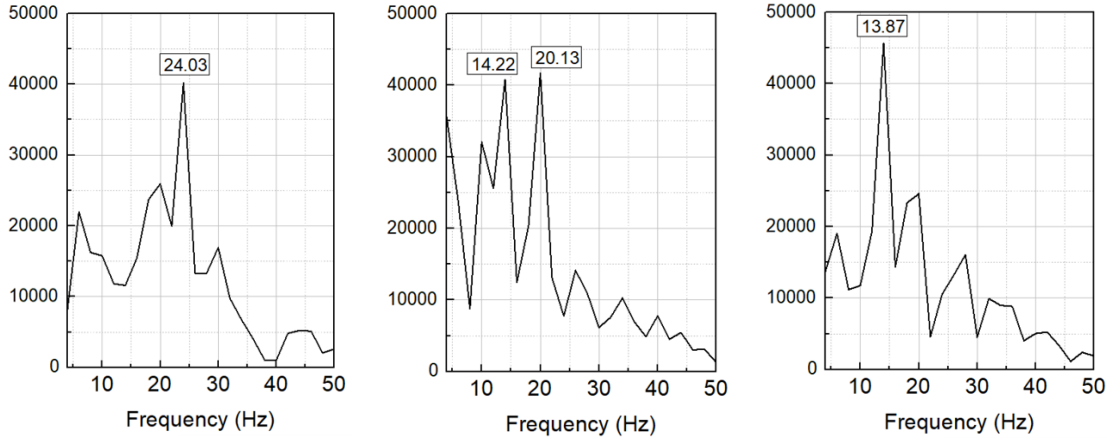

(a) Typical upwind side *(b) Typical middle side* *(c) Typical downwind side*

Figure 2-2-23: Typical frequency domain for upwind, middle, and downwind side

It can be observed from Figure 2-2-23 that there is only one predominant frequency for upwind groups (24 Hz) and two predominant frequencies that have similar contributions for middle groups (20 Hz and 14 Hz). In the downwind side groups, there is only one predominant frequency (14 Hz), the predominant frequency on the upwind side (24 Hz) becomes less dominant, and the less dominant frequency on the upwind side (14 Hz) becomes the predominant frequency.

Table 2-2-2 Pressure distribution of different groups

Group	1	2	3	4	5	6	7	8	9	10	11	12
	Upwind side				Middle side				Downwind side			
Pred. F. (Hz)	24	24	24	24	24/20	20/24	12/20	14/20	14	14	14	12

**Numbers are rounded for easier observation.*

It is clear from Table 2-2-2 that the predominant frequencies in the upwind groups are around 24 Hz, there are two predominant frequencies in the middle group, and in the downwind

groups, the predominant frequencies are around 14 Hz.

To verify the correlation between surface pressure variance and vortexes traveling in proximity, the surface pressure time history of monitoring group #3 on the top surface of the 1:7.875 section is plotted along with the time point where vortexes pass the monitoring face directly above the group. The result is shown in Figure 2-2-24.

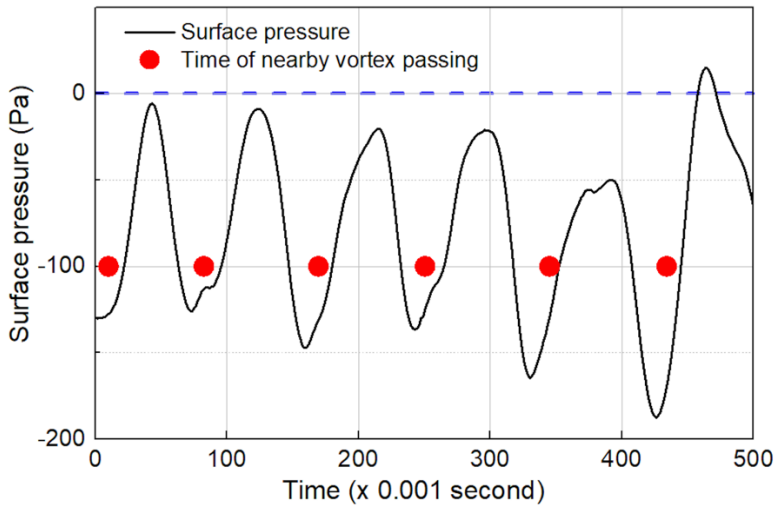

Figure 2-2-24: Time history of group #3 on the top surface with vortex passing by

As seen in Figure 2-2-24, the time points (marked as red circles) where the vortexes pass by the surface monitoring group coincide with the trough of the pressure time history of the group. It can be inferred that the variance of surface pressure on the girder is the direct result of the vortexes passing by. Since the lift force of the girder is a combination of the pressure on the top and bottom surface of the girder, it leads to the conclusion that the different numbers of vortexes on the upwind and downwind sides of the girder cause the two lift forces with different predominant frequencies on the two sides of the girder.

2.2.4.2 Synchronization of different surface locations with total lift force of girder

To analyze the contribution and the synchronicity of the lift force from different locations of the girder surface to the total lift force of the girder, lift forces from group #1-4, group #5-8, and group #9-12 of the girder are compared with the total lift force. Time history and frequency distribution comparisons are shown in Figure 2-2-25 and Figure 2-2-26.

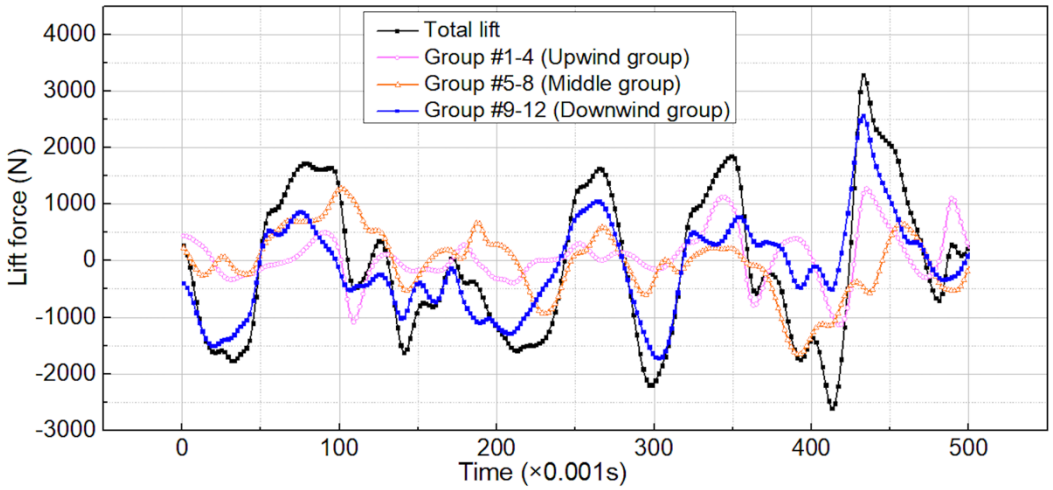

Figure 2-2-25: Lift time history of different groups

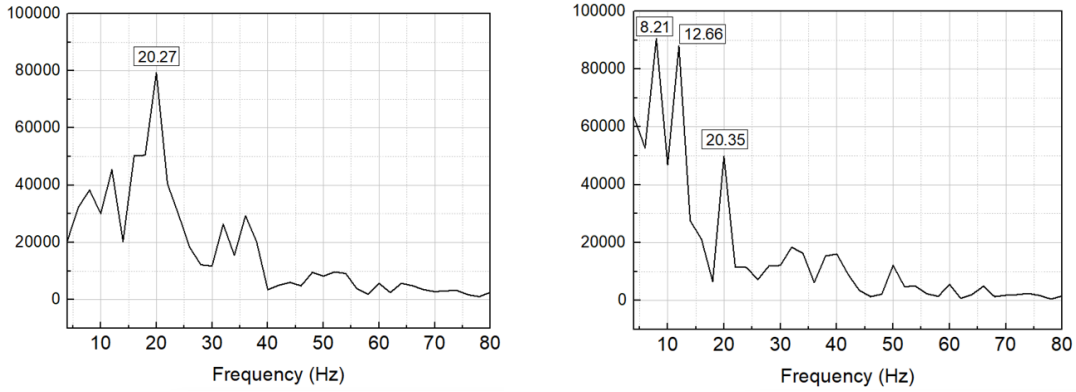

(a) Group #1-4 (b) Group #5-8

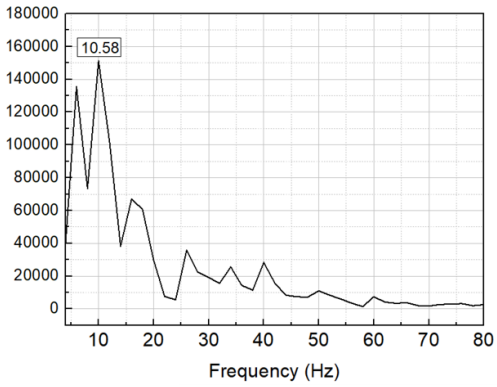

(c) Group #9-12

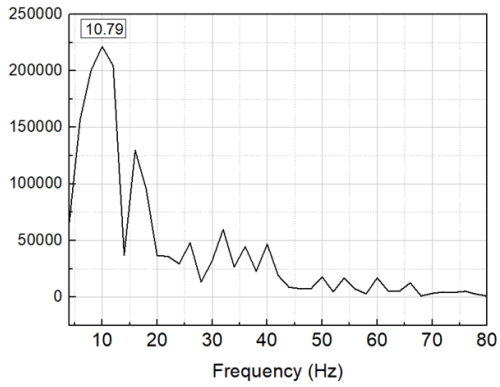

(d) Total lift

Figure 2-2-26: Frequency distribution of different groups

As seen in Figure 2-2-26, the lift force time history from group #9-12 most closely matches the total lift force time history. Its predominant frequency is 10.58 Hz, which matches the predominant frequency of total lift force (10.79 Hz) well. Conducting RMS analysis for time history curves of the total lift force, group #1-4 lift force, group #5-8 lift force, and group #9-12 lift force, the results are 1301.56 N, 451.52 N, 580.91 N, and 839.99 N, respectively, the RMS of group #9-12 is closest to that of total lift force. Performing RMS analysis for the difference of these lift force time history to the total lift force, the results are 1089.17 N for group #1-4, 1102.84 N for group #5-8, and 733.79 N for group #9-12. The RMS is lowest for the difference between group #9-12 lift force and total lift force. The RMS results are summarized in Table 2-2-3.

Table 2-2-3: Lift force RMS analysis result

Group name	RMS of time history (N)	RMS of difference to the total lift (N)
Group 1-4	451.52	1089.17
Group 5-8	580.91	1102.84

Group 9-12	839.99	733.79
Total lift force	1301.56	-

When performing the correlation coefficient analysis for the lift force time history of groups #9-12 with the total lift force time history, the correlation coefficient is calculated as shown in Eq. 2-2-1.

$$\rho_i = \frac{C(L_{overall}(t), L_i(t))}{D(L_{overall}(t)) * D(L_i(t))} \quad \textbf{(Eq. 2-2-1)}$$

where ρ is the correlation coefficient, $L_{overall}(t)$ is the time history for total lift force, $L_i(t)$ is the time history for a monitoring point, i is the numbering of the monitoring points, C is the covariance of the two signals within the parenthesis, D is the standard deviation of the signal in the parenthesis.

The distribution of the correlation coefficients of pressure data from all points in group #9-12 with the total lift force is shown in Figure 2-2-27. A positive coefficient represents a positive correlation, a negative coefficient represents a negative correlation, and the maximum coefficient is 1 (the correlation coefficient of two identical signals).

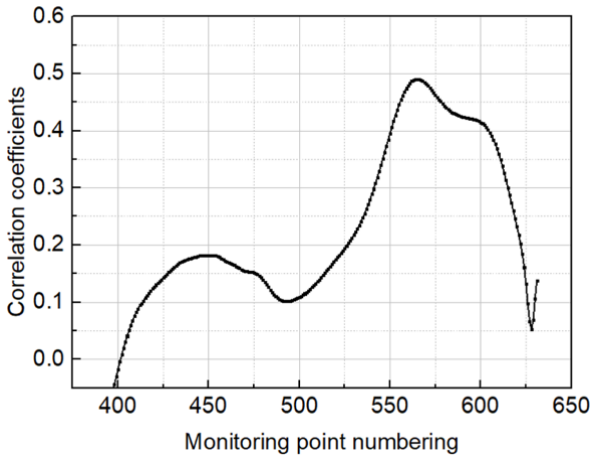

Figure 2-2-27: Distribution of correlation coefficients of group #9-12 with total lift force

As seen in Figure 2-2-27, correlation coefficients for all monitoring points in groups #9-12 with total lift force are positive. The coefficient rises from point #500 to point #570, reaching a maximum value of 0.5 at point #570, then decreases toward the rear of the girder surface.

To sum up, the lift force of group #9-12 has a similar predominant frequency compared to the total lift force of the girder, has the closest RMS with the total lift force, and has the lowest difference RMS with the total lift force compared to other groups. Therefore, it shows the best correlation to the total lift force in the correlation coefficient analysis.

In conclusion, when compared to other groups of the girder surface, group #9-12 provides the best synchronicity and contributes the most to the total lift force of the girder section.

2.2.5 Multi-order lock-in range initiation mechanism

This section compares results from the wind tunnel experiment and the numerical simulations of identical sections to provide a valid explanation for the multi-order VIV lock-in ranges. The VIV responses of the 1:7.875 section and the 1:6 sections in the wind tunnel experiment are shown in Figure 2-2-28 and Figure 2-2-29.

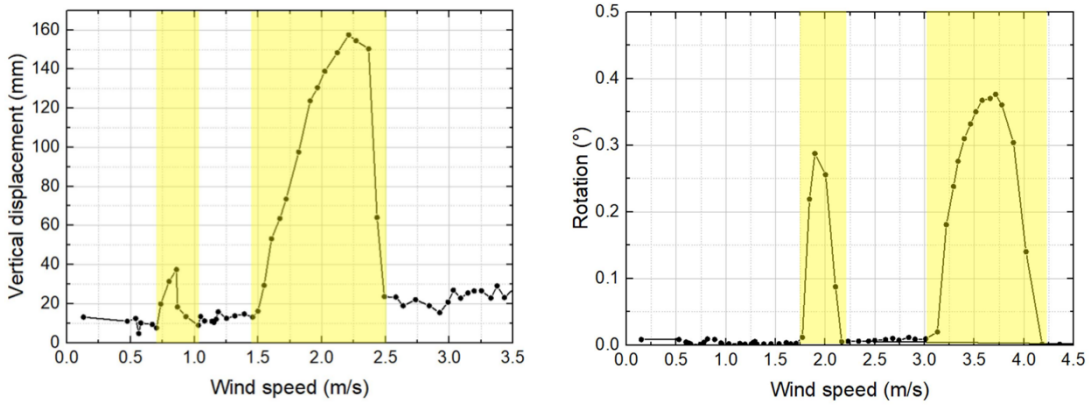

(a) 1st order vertical bending mode *(b) 1st order rotational mode*

Figure 2-2-28: Maximum responses of 1:7.875 section

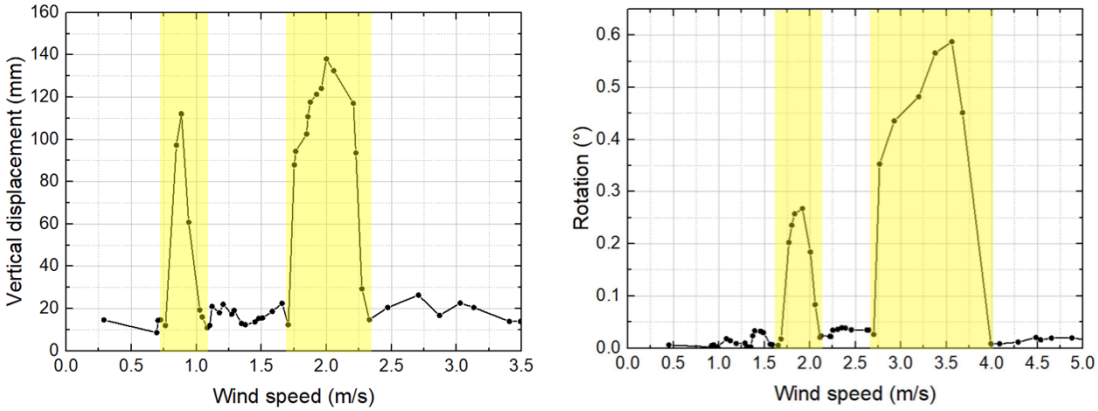

(a) 1st order vertical bending mode *(b) 1st order rotational mode*

Figure 2-2-29: Maximum responses of 1:6 section

Figure 2-2-28 shows two VIV lock-in ranges for the 1:7.875 section in the 1st order vertical bending mode and the 1st order rotational mode. Figure 2-2-29 shows two VIV lock-in ranges for the 1:6 section in the same two modes. All VIV ranges are highlighted. For both modes of the two sections, the first lock-in ranges are narrower and have a smaller amplitude than the second lock-in ranges.

2.2.5.1 Multi-order lock-in ranges initiation for 1:7.875 rectangular section

2.2.5.1.1 1st order rotational mode

To investigate the initiation mechanism of multi-order VIV lock-in ranges of the 1:7.875 girder section, the surface pressure distribution of the girder under initiation wind speeds of each lock-in range of the two modes is recorded and analyzed. The VIV response of the 1st order rotational mode is shown in Figure 2-2-30.

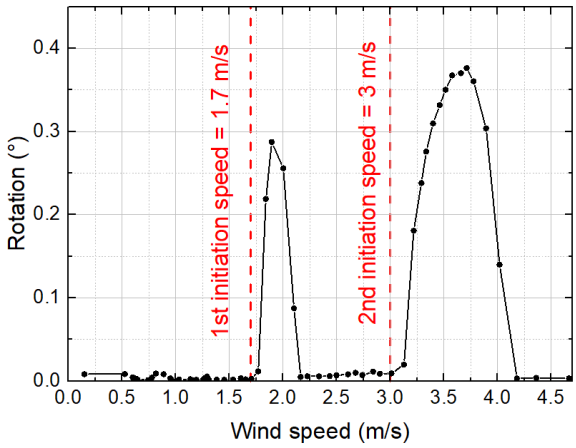

Figure 2-2-30: 1st order rotational mode VIV response

Figure 2-2-30 shows two different lock-in ranges in the 1st order rotational mode. The vibration frequencies of the two VIV lock-in ranges in the wind tunnel experiment are 4.938 Hz, which closely matches the fundamental modal frequency measured in the free vibration attenuation test, as listed in Table 2-1-2. The initiation speed of a lock-in range is defined as the wind speed immediately before the wind speed where an obvious VIV response is observed for the lock-in range. In Figure 2-2-30, the initiation wind speed of the first lock-in range is taken as 1.7 m/s. For the second VIV lock-in range, the initiation wind speed is 3 m/s. Both wind speeds are marked

with red dashed lines.

Under the first VIV lock-in range initiation wind speed of 1.7 m/s, the predominant frequencies of lift force on the up and downwind sides are shown in Figure 2-2-31.

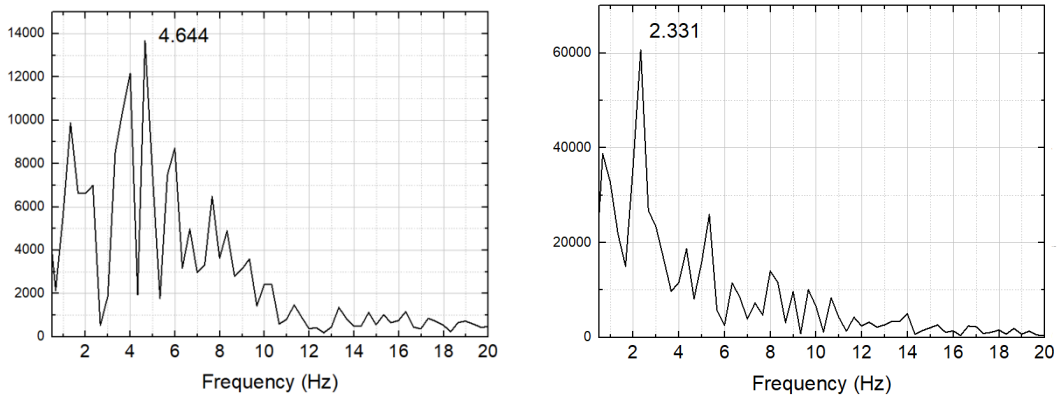

(a) Upwind side group *(b) Downwind side group*

Figure 2-2-31: Lift force predominant frequency under 1.7 m/s wind speed

Figure 2-2-31 shows that the predominant frequency of lift force on the upwind side is 4.644 Hz. On the downwind side, it is 2.331 Hz.

The total rotational moment caused by the lift force on the girder can be calculated by multiplying the lift force of each block with its distance to the center of gravity of the girder section. The predominant frequency of the total rotational moment of the 1:7.875 section under 1.7 m/s wind speed is shown in Figure 2-2-32.

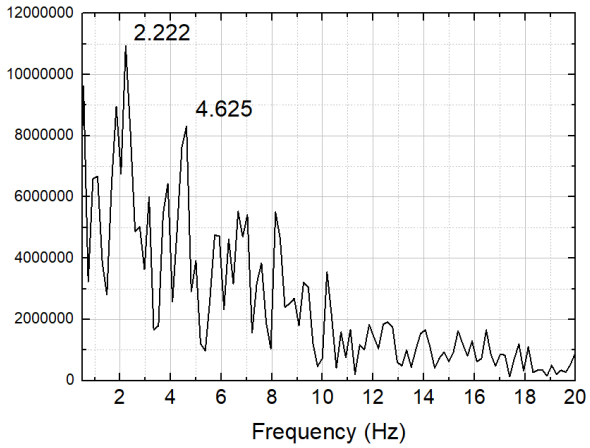

Figure 2-2-32: Predominant frequency of total rotational moment under 1.7 m/s

As seen in Figure 2-2-32, there are two predominant frequencies of the total rotational moment under 1.7 m/s wind speed, which are 2.222 Hz and 4.625 Hz. The frequencies correspond to the lift force frequencies on the downwind side and upwind side, respectively. The 4.625 Hz frequency is slightly lower than the girder's 1st order rotational mode frequency, 4.94 Hz.

For the second lock-in range, under 3 m/s wind speed, the predominant frequencies of lift force on the up and downwind sides are shown in Figure 2-2-33.

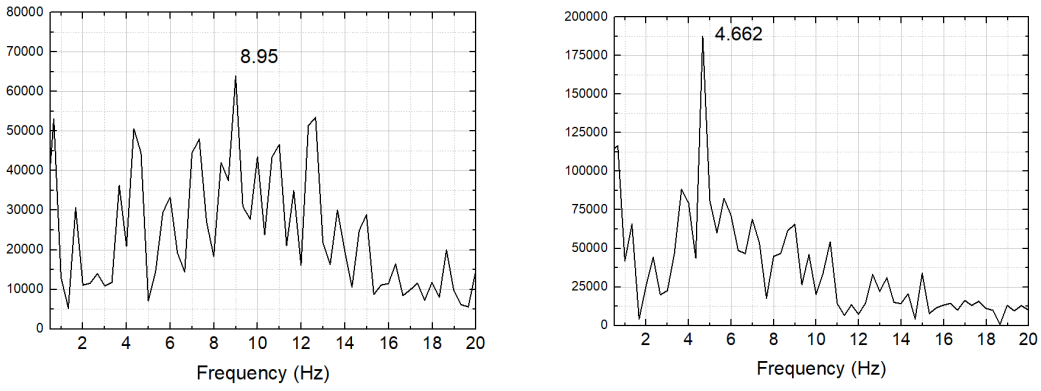

(a) Upwind side group *(b) Downwind side group*

Figure 2-2-33: Lift force predominant frequency under 3 m/s wind speed

Figure 2-2-33 shows that the predominant frequency of lift force on the upwind side is 8.95 Hz. On the downwind side, the predominant frequency is 4.662 Hz. The resulting predominant frequencies of the total rotational moment of the 1:7.875 section under 3 m/s wind speed are shown in Figure 2-2-34.

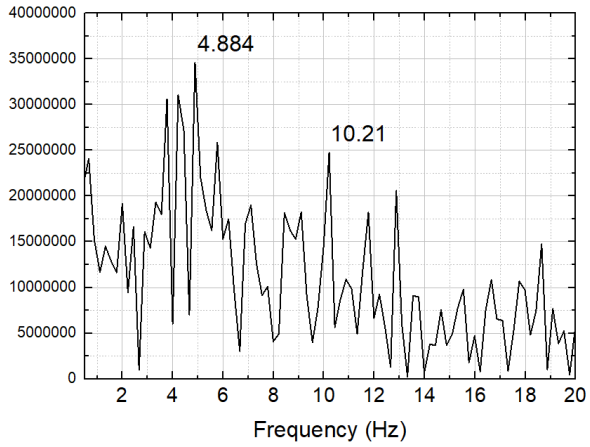

Figure 2-2-34: Predominant frequency of total rotational moment under 3 m/s

There are two predominant frequencies of the total rotational moment under 3 m/s, which are 4.884 Hz and 10.21 Hz. The frequencies correspond to the lift force frequencies on the downwind side and upwind side, respectively. The 4.884 Hz frequency is slightly lower than the girder's 1st order rotational mode frequency, 4.94 Hz.

It can be summarized that, for the 1st order rotational mode, under the initiation wind speeds of the two VIV lock-in ranges, there each exists a rotational moment predominant frequency slightly lower than the modal frequency of the girder section. The two rotational moment predominant frequencies correspond to the predominant frequencies from the upwind side lift force under 1.7 m/s and the downwind side lift force under 3 m/s.

2.2.5.1.2 1st order vertical bending mode

The VIV response of the 1st order vertical bending mode is shown in Figure 2-2-35.

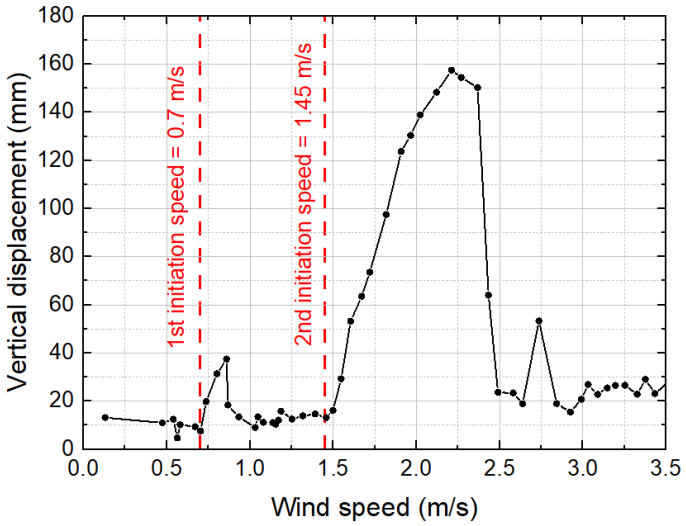

Figure 2-2-35: 1st order vertical bending mode VIV response

As seen from Figure 2-2-35, two different lock-in ranges exist in the 1st order vertical bending mode. The vibration frequencies of the two VIV lock-in ranges in the wind tunnel experiment are 1.88 Hz, which matches the fundamental modal frequency measured in the free vibration attenuation test, as listed in Table 2-1-2. For the first VIV lock-in range in Figure 2-2-35, the initiation wind speed is 0.7 m/s, and for the second VIV lock-in range, the initiation wind speed is 1.45 m/s.

Under the first VIV lock-in range initiation wind speed of 0.7 m/s, the predominant frequencies of lift force on the up and downwind sides are shown in Figure 2-2-36.

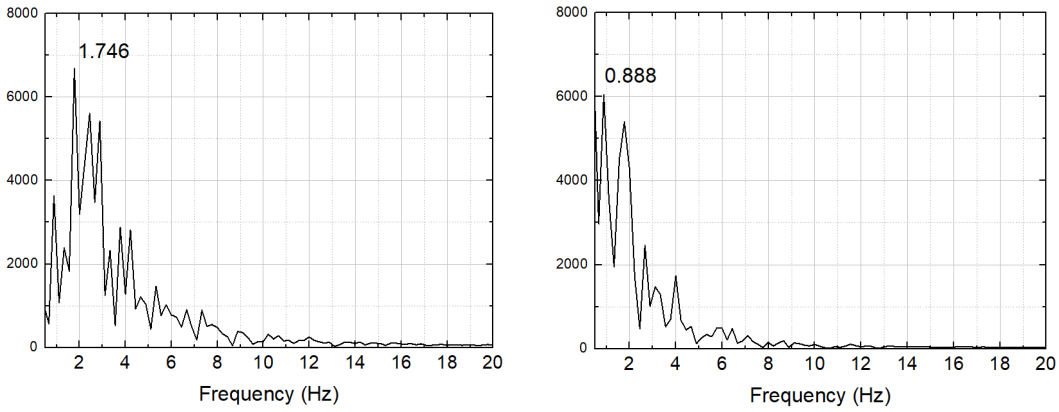

(a) Upwind side group *(b) Downwind side group*

Figure 2-2-36: Lift force predominant frequency under 0.7 m/s wind speed

Figure 2-2-36 shows that the predominant frequency of lift force on the upwind side is 1.746 Hz. On the downwind side, the predominant frequency is 0.888 Hz. By summing the total lift force on all blocks, the total lift force of the girder can be calculated. The predominant frequency distribution of the total lift force of the 1:7.875 section under 0.7 m/s wind speed is shown in Figure 2-2-37.

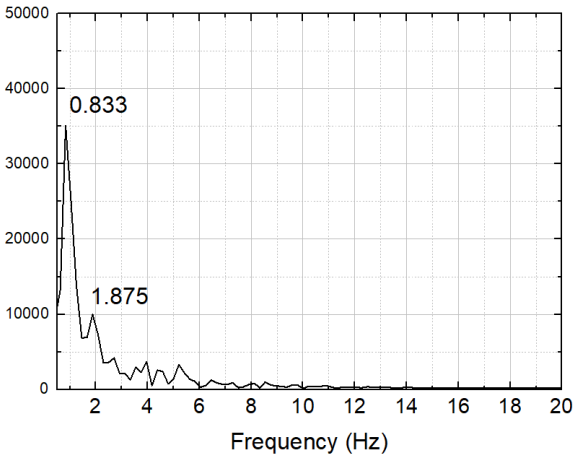

Figure 2-2-37: Predominant frequency of total lift force under 0.7 m/s

There are two predominant frequencies of total lift force under 0.7 m/s, which are 0.833 Hz

and 1.875 Hz. The 1.875 Hz frequency is slightly lower than the modal frequency of the girder, 1.88 Hz.

For the second lock-in range, under 1.45 m/s wind speed, the predominant frequencies of lift force on the up and downwind sides are shown in Figure 2-2-38.

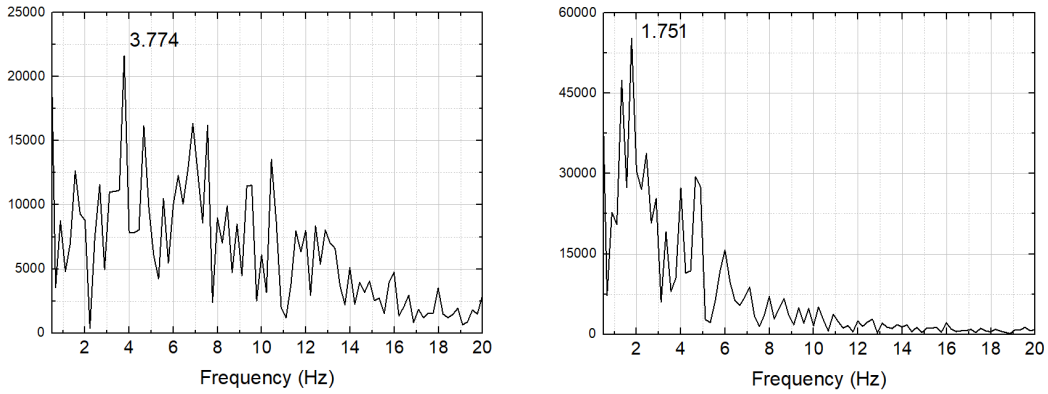

(a) Upwind side group *(b) Downwind side group*

Figure 2-2-38: Lift force predominant frequency under 1.45 m/s wind speed

Figure 2-2-38 shows that the predominant frequency of lift force on the upwind side is 3.774 Hz. On the downwind side, the predominant frequency is 1.776 Hz.

Calculating and analyzing the total lift force on the girder, the predominant frequency of total lift force of the 1:7.875 section under 1.45 m/s wind speed is shown in Figure 2-2-39.

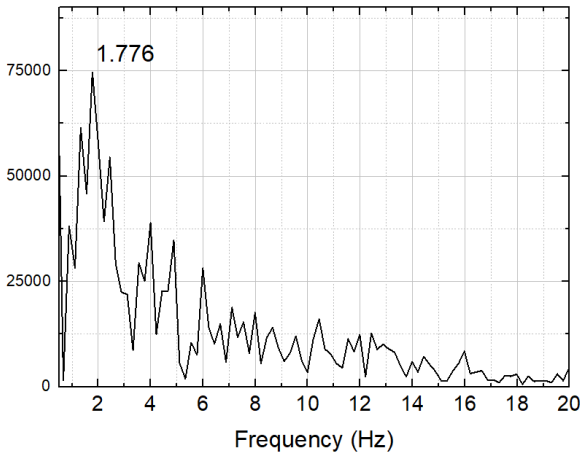

Figure 2-2-39: Predominant frequency of total lift force under 1.45 m/s

The predominant frequency of total lift force under 1.45 m/s is 1.776 Hz, slightly lower than the modal frequency of the girder.

For the 1st order vertical bending mode, under the initiation wind speeds of the two VIV lock-in ranges, the lift force predominant frequency of the upwind side (at 0.7 m/s) and downwind side (at 1.45 m/s) each is slightly lower than the modal frequency of the girder section. By calculating the total lift force of the girder, it can be seen there each exists a predominant frequency slightly lower than the modal frequency under both lock-in ranges' initiation wind speeds.

It can be summarized that, for the 1st order vertical bending mode, under the initiation wind speeds of the two VIV lock-in ranges, there each exists a total lift force predominant frequency slightly lower than the modal frequency of the girder section. The two lift force predominant frequencies correspond to the predominant frequencies from the upwind side lift force under 0.7 m/s and the downwind side lift force under 1.45 m/s.

Based on the observation of this section, it can be inferred that, for the 1:7.875 section,

under each wind speed point tested for both modes, there exist two lift force or rotational moment predominant frequencies. For a certain mode, when the wind speed is incrementally increased, the two predominant frequencies would each match with the modal frequency of the girder once and induce a different VIV vibration, thus causing the two VIV lock-in ranges to appear.

2.2.5.2 Multi-order lock-in ranges of the 1:6 rectangular section

To verify the generality of the inference made in the previous section, a wind tunnel experiment and numerical simulation with an identical setup are performed for a rectangular girder section with an aspect ratio of 1:6.

The 1st order vertical bending mode and 1st order rotational mode VIV response of the 1:6 section are shown in Figure 2-2-40.

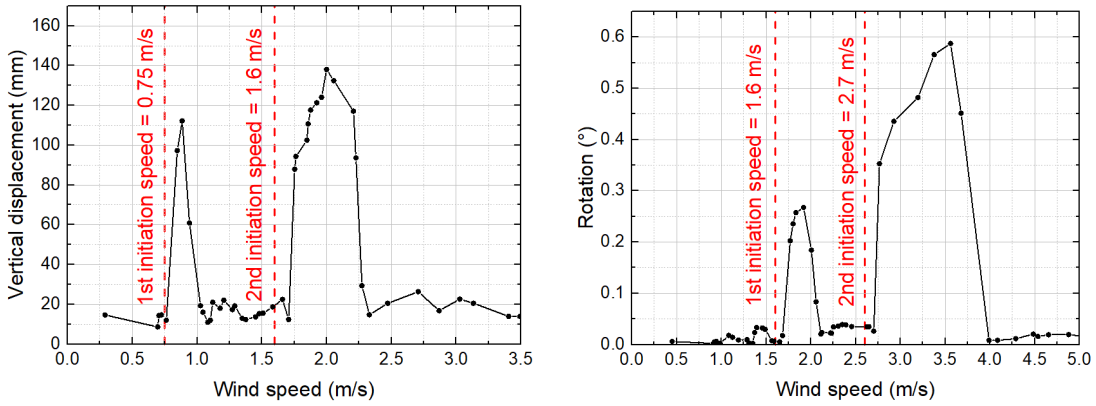

Figure 2-2-40: VIV response of two modes for the 1:6 girder section.

According to the wind tunnel experiment, the VIV initiation wind speeds for the 1st order vertical bending mode are 0.75 m/s and 1.6 m/s, and the wind speeds for the 1st order rotational mode are 1.6 m/s and 2.7 m/s. The initiation wind speeds are used for surface pressure monitoring.

In the wind tunnel experiments, the vibration frequencies for the 1st order vertical bending mode and 1st order rotational mode are 1.94 Hz and 4.78 Hz. Both values match the result obtained from the free vibration attenuation method listed in Table 2-1-2.

For the 1st order vertical bending mode and the 1st order rotational mode, the total lift force and total rotational moment predominant frequencies on the girder are shown in Figure 2-1-41. Values are summarized in Table 2-2-4.

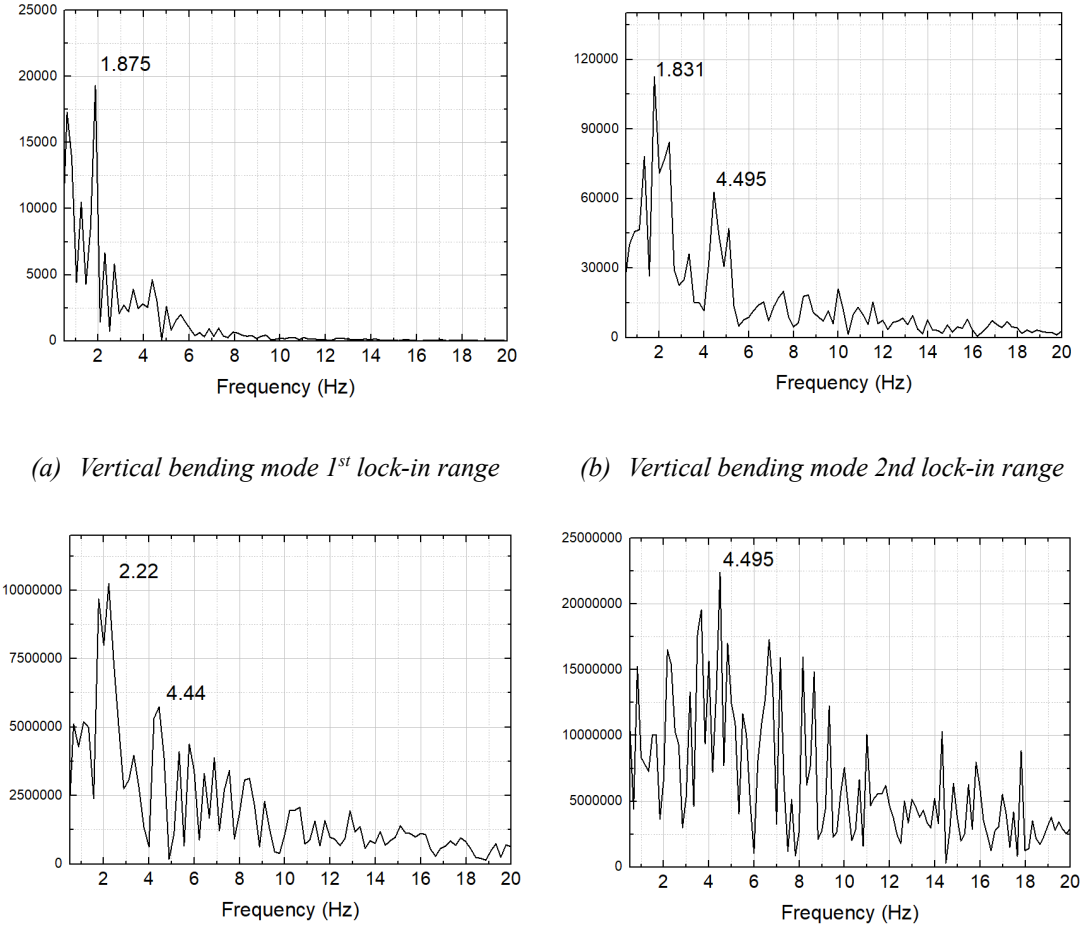

(a) Vertical bending mode 1st lock-in range

(b) Vertical bending mode 2nd lock-in range

c) Rotational mode 1st lock-in range

d) Rotational moment 2nd lock-in range

Figure 2-1-41: Frequency distribution for lock-in range initiation wind speed for both modes

Table 2-2-4: Predominant frequencies of total lift force and total rotational moment

Mode	1st lock-in range modal predominant frequency (Hz)	2nd lock-in range modal predominant frequency (Hz)	Fundamental frequency (Hz)
Vertical	1.875	1.831	1.94
Rotational	4.44	4.495	4.78

For the 1st order vertical bending mode, under the initiation wind speeds of the two VIV lock-in ranges, the total lift force predominant frequencies are slightly lower than the modal frequency of the girder section. For the 1st order rotational mode, under the initiation wind speeds of the two VIV lock-in ranges, the total rotational moment predominant frequency each is slightly lower than the modal frequency of the girder section.

Similar to the 1:7.875 section, for the 1:6 section, two lift force or rotational moment predominant frequencies exist under each wind speed point tested for both modes. For a certain mode, when the wind speed is incrementally increased, the two predominant frequencies would each match with the modal frequency of the girder once and induce a different VIV vibration, thus causing the two VIV lock-in ranges to appear.

2.2.6 Summary of findings in this section

This section of research utilizes monitoring faces consisting of monitoring points generated by a new mass point setup process to analyze the flow field around a rectangular girder section with an aspect ratio of 1:7.875. A simplified two-dimensional vortex recognition method and a new vortex tracking method based on distributions of static pressure and velocity of the

surrounding flow field (MPF-track) are proposed to track the development of individual vortexes. Based on the vortex tracking result, a vortex merging pattern that reduces the number of vortexes on the upwind side to approximately half on the downwind side is observed, and the mechanism of such a pattern is analyzed. As a result of the vortex merging pattern, two different lift force frequencies on the upwind side and downwind side are revealed, and the contribution of lift forces from different locations of the girder to the total lift force is discussed.

Further, this section investigates the VIV response of rectangular girder sections with different aspect ratios in wind tunnel experiments. The investigation then tracks the development of vortexes around the girders and monitors the surface pressure distribution as well as the resulting total lift force and total rotational moment of the girder in CFD numerical simulation, and finally proposes an explanation for the multi-order VIV lock-in ranges observed in wind tunnel experiments based on a vortex merging pattern discovered around rectangular girder sections.

The investigation in this section revealed that, under uniform flow field conditions, there exists a merging pattern for every two vortexes traveling close to the top and bottom surface of the girder, decreasing the number of vortexes from the upwind side to the downwind side. Due to such a pattern, the number of vortexes that influence the girder section on the downwind side is approximately half of that on the upwind side, thus leading to two different lift force predominant frequencies on the two sides. For the 1st order vertical bending mode, the two lift force frequencies on the upwind side and downwind side would induce two different total lift force frequencies under each wind speed. For the 1st order rotational mode, the two lift force frequencies on the upwind

and downwind side would induce two different total rotational moment frequencies under each wind speed. When wind speed is incrementally increased, these total lift force frequencies and rotational moment frequencies will match with the fundamental modal frequency of the girder section twice at different wind speeds, thus causing the multi-order VIV lock-in ranges phenomenon observed in the wind tunnel experiments to appear. The main conclusions are summarized as follows.

1. For a rectangular section with an aspect ratio of 1:7.875, it is revealed that there is a vortex merging pattern that reduces the number of vortexes traveling on the upwind side of the girder to approximately half on the downwind side of the girder.

2. There are two locations where the vortexes merged, and the paths of the vortexes merged in the two locations exhibit an alternating diverging pattern on the downwind side of the girder.

3. For rectangular girder sections with various aspect ratios, the first merging locations where the vortex merging patterns occur are approximately at similar distances from the leading edges of the girders, and the second merging location is dependent on the aspect ratio of the girder.

4. There exist two lift force frequencies on the upwind side and downwind side of the girder. The vortex merging pattern is the cause of the different lift force frequencies.

5. The downwind side 1/3 of the girder section contributes the most to and has the best synchronicity with the total lift force in amplitude, frequency, and synchronization.

6. The two different lift force predominant frequencies would cause two total lift force and two total rotational moment predominant frequencies on the girder under each wind speed. When

wind speed is incrementally increased, these total lift and total rotational moment frequencies would match with the fundamental modal frequencies of each mode of the girder twice and induce the multi-order VIV lock-in ranges.

2.3 Rectangular girder sections with wind noses installed

2.3.1 Wind tunnel experiment and numerical simulation

The setup of the numerical simulation for a rectangular girder section with wind noses is similar to that of the rectangular girder section. The section used in this simulation is the 1:6 rectangular girder section with two wind noses, each installed at the upwind side and downwind side of the girder section. The 1:6 rectangular girder section can be compared with the 1:6 rectangular girder section as it is the same section with the addition of the wind noses and with the 1:7.875 rectangular girder section as they have the same aspect ratio. The rectangular girder section has a height of 80 mm and a width of 480 mm. The added wind noses are symmetrical triangles with a base of 80 mm and a height of 75 mm.

ANSYS Fluent is used as the analyzing software for the simulation, and MATLAB is used as the data processing platform. The total number of mesh elements is approximately 600,000, the core layer locates around the girder section has approximately 420,000 elements, and the skew ratios for all elements are lower than 0.5%. The total meshing area has a height of 30 times the girder width and a width of 50 times the girder width. The setup follows the ANSYS Fluent theory

guide [70]. The meshing layout is shown below in Figure 2-3-1.

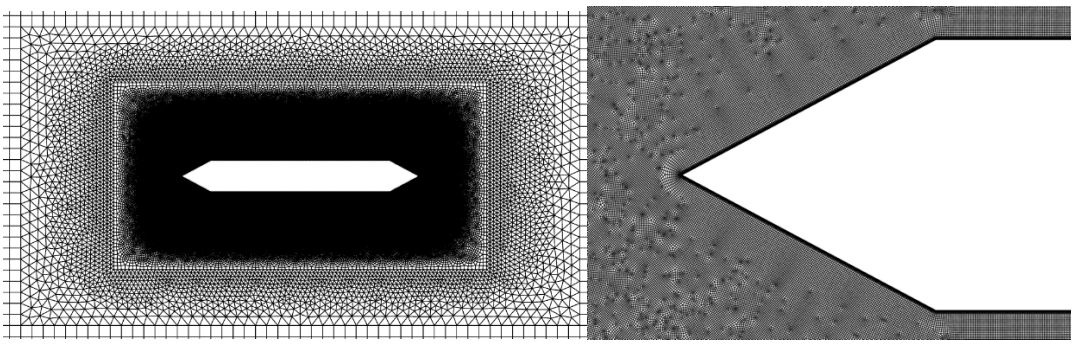

Figure 2-3-1: Meshing layout around the 1:6 girder section

The simulations are run on the same server of the rectangular girder section, equipped with a 64-core CPU with similar simulation settings. The turbulence model used in this simulation is the Detached-Eddy Simulation (DES), which is a combination of the Reynolds Average Navier-Stokes (RANS) model for near girder mesh elements and the Large Eddy Simulation (LES) model for elements away from the girder section. The RANS model used in this simulation is K-omega. The solution method is SIMPLEC, where turbulence and viscosity are taken as 0.5% and 2%, respectively. The time step size is 0.001 seconds.

Monitoring points are placed above, below, and on the surface of the girder sections to track the development of the vortexes around the girder sections with the MPF-track method and record the lift force time history of the girder sections with the similar procedure described in the simulation of rectangular girder sections in previous sections. A schematic of the CFD simulation of the 1:6 rectangular girder section with wind noses is shown in Figure 2-3-2.

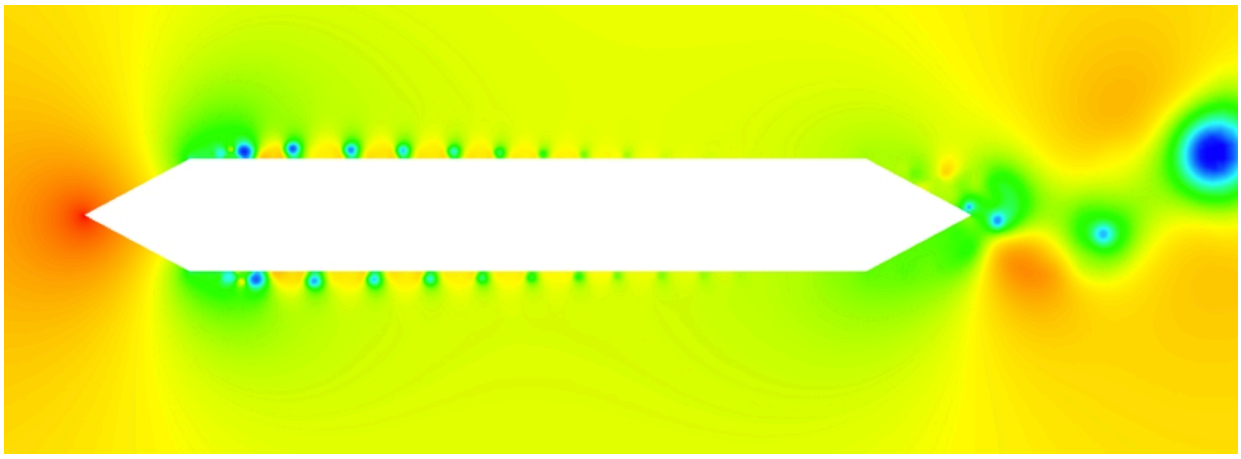

Figure 2-3-2: CFD simulation of the 1:6 girder section with wind noses

The two rectangular girder sections with wind noses installed are tested in the wind tunnel for their dynamic VIV responses. Two girder sections with the same geometry are tested in the 1st testing section of the XNJD-1 wind tunnel laboratory. The experiment follows the same setup as the experiments for rectangular girder sections. All experimental requirements are met, and dynamic characteristics such as model weight and spring stiffness are matched. The vertical bending modal frequency is 2.00 Hz, and the rotational modal frequency is 4.68 Hz. Wind speeds are incrementally increased, and the VIV response of the vertical bending mode and rotational mode of the girder sections are recorded using the LASER transducers.

The VIV responses of the 1:6 girder section with wind noses in the wind tunnel experiment are shown in Figure 2-3-3. The VIV responses of respective rectangular girder sections are shown for comparison purposes in Figure 2-3-4.

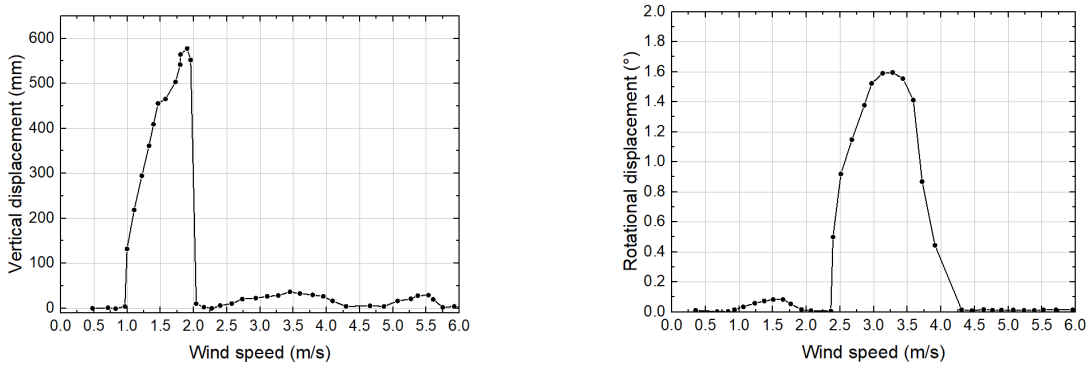

(c) Vertical bending mode

(d) Rotational mode

Figure 2-3-3: VIV lock-in range of the 1:6 rectangular girder section with wind noses installed

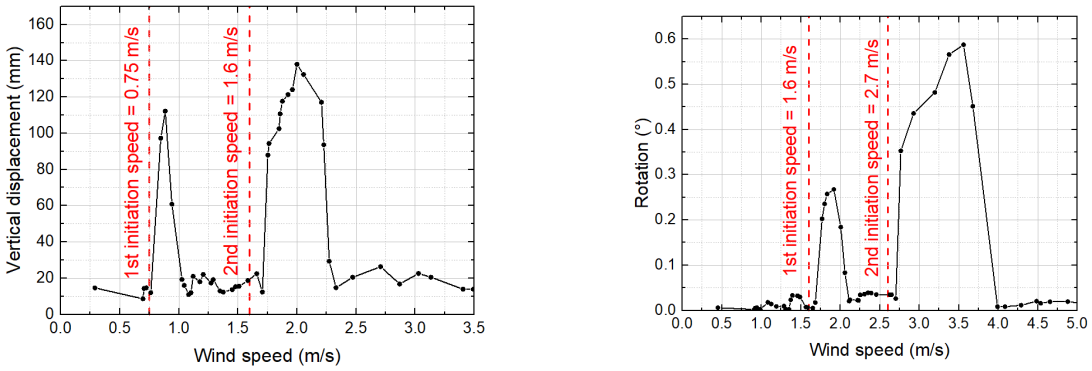

(a) VIV lock-in ranges of the 1:6 rectangular girder section

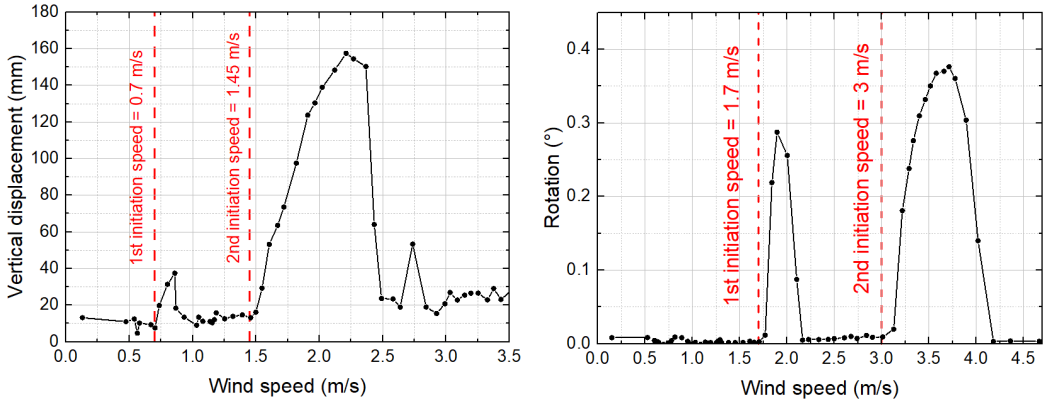

(b) VIV lock-in ranges of the 1:7.875 rectangular girder section

Figure 2-3-4: VIV lock-in ranges for rectangular girder sections

It is seen from Figure 2-3-3 and Figure 2-3-4, for both the vertical bending mode and rotational mode of the 1:6 rectangular girder section with wind noses, only one obvious VIV lock-in range is observed in the VIV wind speed range tested, as compared to the two obvious VIV lock-in ranges for the 1:6 and 1:7.875 rectangular girder sections without the installation of triangular wind noses. The one obvious VIV lock-in range for the girder sections with win noses is the first vertical bending mode lock-in range and 2nd rotational mode lock-in range. These two lock-in ranges are wider and slightly delayed compared to their respective lock-in ranges for the rectangular girder sections. For the vertical bending mode of the section with wind noses, there is a 2nd lock-in range smaller than that of the rectangular girder sections. For the rotational mode of the section with wind noses, there is a 1st lock-in range smaller than that of the rectangular girder section. According to the VIV responses, the installation of the wind noses decreased the magnitude of displacement of the 2nd lock-in range of the vertical bending mode and the 1st lock-in range of the rotational mode of the 1:6 and the 1:7.875 rectangular girder sections.

2.3.2 Total lift force and rotational moment at lock-in ranges' initiation wind speeds

To explore how the installation of wind noses affects the pattern of vortex shedding around the girder sections and to determine the reason that caused the decrease in the numbers of lock-in ranges, the numerical simulations of girder sections with wind noses at various wind speeds are performed. According to the wind tunnel experiments, shown in Figure 2-3-3, for the 1:6 rectangular girder section with wind noses, the two VIV lock-in ranges initiated at wind speeds of

0.85 m/s and 2.3 m/s for both the vertical bending mode and the rotational mode. To verify the initiation mechanism of the lock-in ranges for the 1:6 section with wind noses, the numerical simulation is performed at the identical 0.85 m/s and 2.3 m/s wind speeds.

The total lift force and rotational moment predominant frequency distributions of the 1:6 rectangular girder section with wind noses at 0.85 m/s and 2.3 m/s wind speeds are recorded and summarized in Table 2-3-1.

Table 2-3-1: Predominant frequency of lift force and rotational moment at various wind speeds

Wind speed	Total lift force frequency (Hz)		Total rotational moment frequency (Hz)	
0.85 m/s	1.11	**2.036**	2.035	**4.81**
2.3 m/s	**1.942**	4.718	**4.718**	9.435

At the 0.85 m/s wind speed, where the 1st lock-in range of vertical bending mode appears, two predominant frequencies exist for the total lift force (1.11 Hz and 2.035 Hz). The 2.035 Hz frequency is slightly higher than the modal frequencies of the vertical bending mode frequency (2.00 Hz). At the 2.3 m/s wind speed, where the 2nd lock-in range of vertical bending mode with smaller amplitude appears, there exists two predominant frequencies for the total lift force (1.942 Hz and 4.718 Hz), the 1.942 Hz frequency is slightly lower than the modal frequency of the vertical bending mode frequency.

As seen in Table 2-3-1, for both the 0.85 m/s and the 2.3 m/s wind speeds, there exists a predominant frequency of total lift force that is close to the vertical bending modal frequency (2.00

Hz). In addition, the energy magnitude of the total lift force predominant frequency at the 1st lock-in range is higher than that at the 2nd lock-in range. Therefore, for vertical bending mode, there exist two lock-in ranges, and the 1st lock-in range has a higher amplitude than the 2nd lock-in range, as seen in Figure 2-3-3.

For the rotational moment, the predominant frequencies at the 0.85 m/s and the 2.3 m/s wind speeds are 2.035 Hz/4.81 Hz and 4.718 Hz/9.435 Hz, respectively. For the 0.85 m/s wind speed, the 4.81 Hz frequency is slightly above the rotational modal frequency of the girder section (4.68 Hz). For the 2.3 m/s wind speed, the 4.718 Hz frequency is also slightly over the rotational modal frequency of the girder section.

As seen in Table 2-3-1, for both the 0.85 m/s and the 2.3 m/s wind speeds, there exists a predominant frequency of total rotational moment that is close to the rotational modal frequency (4.68 Hz). In addition, the energy magnitude of the total rotational moment predominant frequency at the 1st lock-in range is lower than that at the 2nd lock-in range. Therefore, for rotational mode, there exist two lock-in ranges, and the 1st lock-in range has a lower amplitude than the 2nd lock-in range, as seen in Figure 2-3-3.

2.3.3 Lift force and rotational moment from different locations on the girder section

To determine the contribution of each location of the girder section to the total lift force, the pressure monitoring points on the surface of the girder section are divided into four groups, namely the upwind wind nose group (#1), the upwind rectangular girder group (#2), the downwind

rectangular girder group (#3), and downwind wind nose group (#4), as shown in Figure 2-3-5.

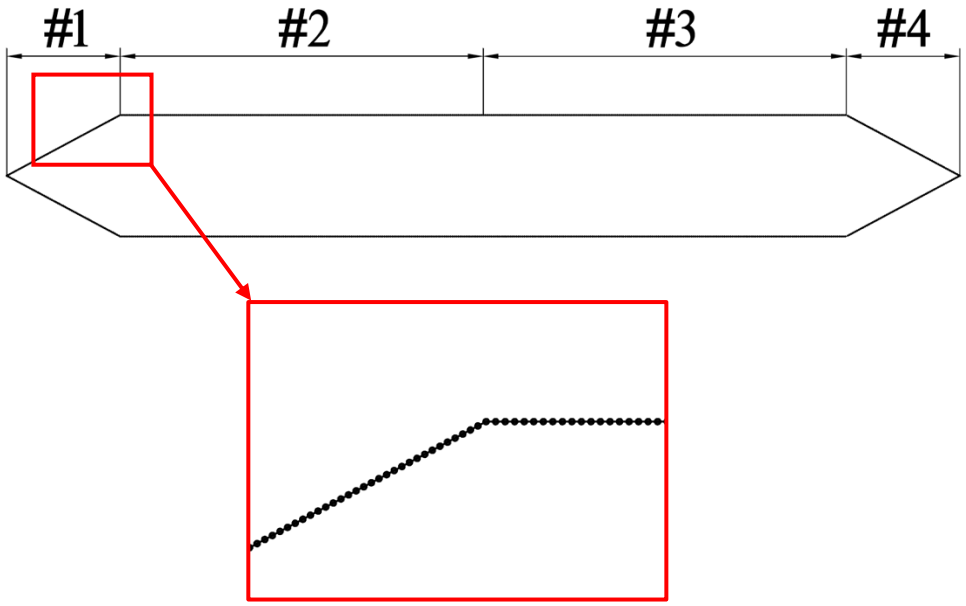

Figure 2-3-5 Grouping of monitoring points at different locations

The predominant frequencies of lift forces for different groups at the 0.85 m/s and the 2.3 m/s wind speeds are summarized in Table 2-3-2.

Table 2-3-2: Predominant frequencies of lift force at different locations

Wind speed (m/s)	Lift force frequencies at different locations (Hz)			
	Group #1	Group #2	Group #3	Group #4
0.85	1.11	4.81	4.81	2.035
2.3	1.942	9.435	9.435	4.718

As seen in Table 2-3-2, there are three different predominant frequencies, each at the upwind nose location (Group #1), rectangular girder section location (Group #2 and #3), and

downwind wind nose location (Group #4). The frequency of group #4 at the 0.85 m/s wind speed and the frequency of group #1 at the 2.3 m/s match with the vertical bending mode frequency of the girder section (2.00 Hz), the frequencies of groups #2 and #3 at the 0.85 m/s and frequency of group #4 at the 2.3 m/s wind speed match with the rotational mode frequency of the girder section (4.68 Hz).

For vertical bending mode, both the lift forces from Group #4 at the 0.85 m/s wind speed and Group #1 at the 2.3 m/s wind speed match with the modal frequency, these two locations are the only locations that have the matching modal frequency at their respective wind speed. It can be inferred that the lift forces from these two locations each are responsible for the two vertical bending lock-in ranges. However, the lift force from Group #1 at 2.3 m/s is significantly lower than that from Group #4 at 0.85 m/s. The amplitudes of lift force of the downwind wind nose group #4 at 0.85 m/s and the upwind wind nose group #1 at 2.3 m/s wind speeds are compared in Figure 2-3-6.

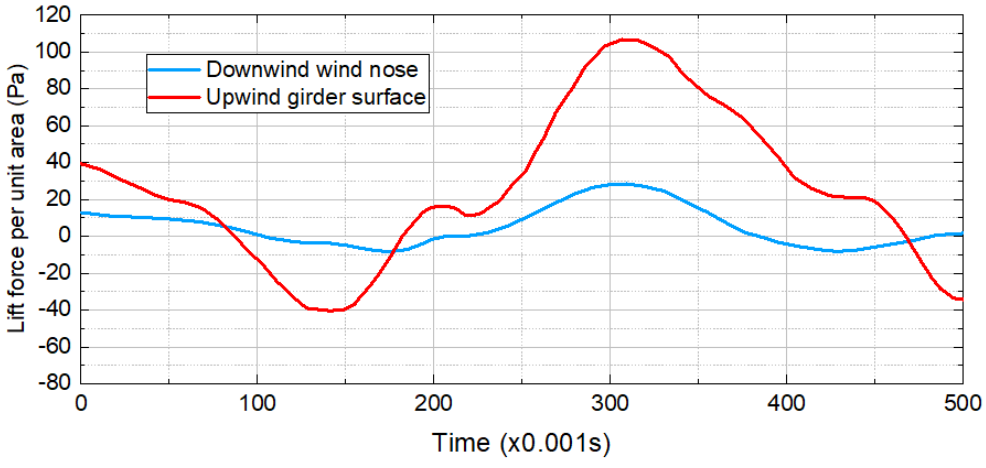

Figure 2-3-6: Amplitude comparison of lift force at different locations

It can be seen in Figure 2-3-6 that the lift force at group #1 at the 2.3 m/s wind speed is significantly lower than that at group #4 at 0.85 m/s. Therefore, this difference in lift force amplitude is inferred as the cause for the higher amplitude in the 1st vertical bending mode lock-in range and the smaller amplitude in the 2nd lock-in range.

Similarly, for rotational mode, the rotational moment calculated from the lift force of Group #2 at the 0.85 m/s wind speed and Group #4 at the 2.3 m/s wind speed each match with the modal frequency, these two locations are the only locations that have the matching modal frequency at their respective wind speed. It can be concluded that the rotational moment from these two locations each is responsible for the two rotational lock-in ranges. When calculating the rotational moment of the girder section, considering moment arms, the amplitude of the rotational moment at group #2 location at 0.85 m/s is smaller than the rotational moment at group #4 due to shorter moment arms. Therefore, this difference in rotational moment amplitude caused by different moment arms can be inferred as the cause for the higher amplitude in the 2nd rotational mode lock-in range and the smaller amplitude in the 1st lock-in range.

From the discussion above, it can be concluded that, similar to that of rectangular girder sections, there exist several vortex shedding mechanisms on the upwind side and downwind side of the girder, which would lead to different matching lift force and rotational moment frequencies with the modal frequency of the vertical bending mode and the rotational mode of the girder at different wind speeds, generating the multi-order lock-in range phenomenon.

For the vertical bending mode, the lift force responsible for the 2nd lock-in range is

significantly lower than that for the 1st lock-in range. Therefore, the 1st lock-in range has a higher amplitude and is more obvious in the girder response spectrum than the 2nd lock-in range.

For the rotational bending mode, the rotational moment caused by the lift force responsible for the 1st lock-in range is significantly lower than that for the 2nd lock-in range due to the shorter moment arm length. Therefore, the 2nd lock-in range has a higher amplitude and is more obvious in the girder response spectrum than the 1st lock-in range.

2.4 Chapter Summary

This chapter explores VIV's initiation mechanism for rectangular girder sections with and without wind noses. Girder sections of interest are first tested in wind tunnel experiments for their dynamic VIV responses and then simulated in CFD analyses to monitor the flow field characteristics around the girders.

From the wind tunnel experiments, it is observed that there exist two lock-in ranges for both the vertical bending mode and rotational mode of the 1:6 and 1:7.875 rectangular girder section. When wind noses are installed on the rectangular sections, only one obvious lock-in range exists for both modes of the 1:6 and 1:7.875 rectangular girder sections with wind noses.

A vortex recognition and path tracking method is proposed based on mass monitoring points setup (MPF-track). By tracking the path of vortexes around the rectangular girder sections, a vortex merging pattern that reduces the number of vortexes on the upwind side of the girder to

half on the downwind side of the girder is observed. It is concluded that this decrease in the number of vortexes on the upwind and downwind sides of the girder is the cause for the two VIV lock-in range phenomena.

For rectangular girder sections with wind noses installed, similar to that of rectangular girder sections, there also exist several vortex shedding mechanisms on the upwind side and downwind side of the girder, which would lead to the multi-order lock-in ranges phenomenon. However, for both the vertical bending mode and the rotational mode, there is one lock-in range with a significantly smaller lift force (rotational moment) when compared to the other one. Therefore, although there are still two lock-in ranges for each mode, one is significantly smaller than the other. By inspection, the installation of the wind noses reduce the magnitude of the vortexes on the upwind side as compared to those of the rectangular girder section, therefore reducing the magnitude of one of the VIV lock-in range, showing only one obvious VIV lock-in range for both modes.

Chapter 3 Initiation mechanisms of VIV for streamlined box girder sections

In the previous chapter, the initiation mechanism of VIV for the rectangular box girder section is discussed. To simulate the actual VIV response of the streamlined box girder of the prototypical bridge, two wind tunnel experiments of the streamlined box girder section of the original design with scaling factors of 1:50 and 1:20 are conducted in this chapter. Aerodynamic measures are installed on the girder sections in the experiment to test their effectiveness on the VIV of the streamlined girder sections, and the influence of the Reynolds number effect is discussed. The 1:50 streamlined girder section is tested in CFD numerical analysis to explore the flow field characteristics and VIV mechanisms. This chapter uses a computer vision vortex recognition and tracking method based on Convolutional Neural Network machine learning that is suitable for more complex flow fields to track the development of vortexes around the streamlined girder section.

3.1 VIV response for streamlined box girder sections based on 1:50 model wind tunnel experiments

3.1.1 Experimental setup

The 1:50 streamlined box girder section wind tunnel experiments are conducted in the XNJD-1 wind tunnel in Emei, China. A streamlined box girder section scaled from the original

design of the box girder of the prototypical bridge with a scaling factor of 1:50 is used. The setup is identical to the previous section's rectangular box girder section wind tunnel experiments and follows the Chinese Wind-resistant Design Specification for Highway Bridges [95].

The main girder section is made of timber boards with five longitudinal chords and nine struts. End boards are installed on both ends of the girder section for anchoring purposes. The inner structure and the external appearance of the girder section are shown in Figure 3-1-1 and Figure 3-1-2, respectively:

Figure3-1-1: Inner structure of the girder section

Figure 3-1-2: External appearance of the girder section

The pavements and railings on top of the model are ABS plastic. The pavement is 1.2 mm thick and is attached to the timber girder section with acrylate adhesive. The railings are laser-printed to ensure geometric precision and to provide a proper ventilation rate. Details of the railings and pavements are shown in Figure 3-1-3.

Figure 3-1-3: Close-up view of the pavements and railings of the model

Tracks for maintenance vehicles are made of plastic and attached to the girder section with acrylate adhesive, as shown in Figure 3-1-4.

Figure 3-1-4: Track for maintenance vehicles at the bottom of the model

The model is attached to external supports with eight calibrated steel springs to enable vertical and rotational degrees of freedom. The installed model is shown in Figure 3-1-5:

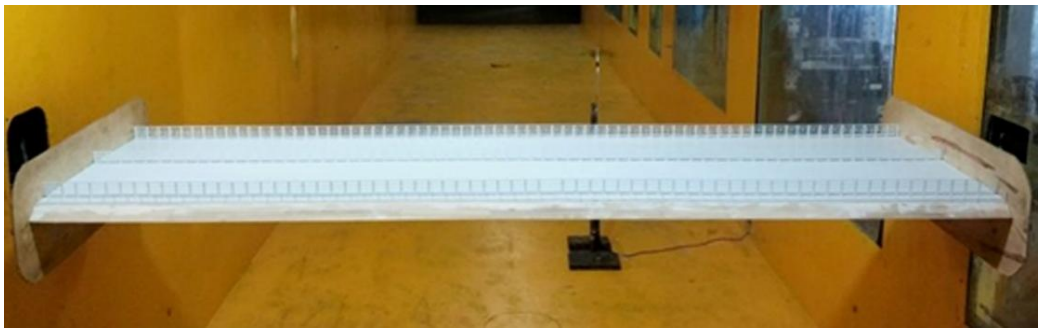

Figure 3-1-5: Dynamic model of original working state

The vertical and rotational displacements of the model are directly measured using the LASER displacement measure device in a manner similar to the setup of the rectangular girder section wind tunnel experiment.

The geometric similarities of the girder and the railings are strictly satisfied. Mass and mass moment of inertia are determined with proper scaling factors to the equivalent mass and the equivalent mass moment of inertia to ensure similarity to accurately simulate possible coupling effects on displacements on all degrees of freedom. Table 3-1-1 compares the required values and the actual measured values.

Table 3-1-1: Similarity requirements

Parameter	Sign	Unit	Scale	Bridge	Model required	Model measured
Girder height	H	m	50	4.005	0.0801	0.0801
Girder width	B	m	50	31.50	0.630	0.630
Unit length mass	m	kg/m	50^2	30565	12.23	12.23
Mass moment of inertia	Im	kg·m^2/m	50^4	6757680	1.081	1.081
Rotation radius	r	m	50	14.869	0.297	0.297

According to the vortex shedding frequencies under possible wind speed that induces VIV phenomenon obtained from the static wind load test in the wind tunnel laboratory and the data obtained from the modal analysis by ANSYS, the 1st order symmetrical vertical bending mode and 1st order symmetrical rotational mode are chosen as the target mode for the experiment. The modal frequencies of the vertical bending and rotational modes are 1.88 Hz and 4.94 Hz, respectively.

The range of the damping ratio requirement by the Chinese Wind-resistant Design Specification for Highway Bridges [95] is 0.3-0.5%. This experiment uses four damping ratios to explore the impact of low, standard, and high damping ratios on the model vibration. The ratios selected are 0.18% and 0.25% (low), 0.3% (standard), and 0.56% (high).

3.1.2 Wind tunnel test for the aerostatic coefficients

The wind tunnel test for the aerostatic coefficients of the streamlined box girder section is conducted in the XNJD-1 industrial wind tunnel laboratory in the identical setup as that of the rectangular girder sections discussed in the previous chapter. The model is connected to the wind tunnel supports with fixed connections, and force balances are installed on the supports to measure the aerostatic coefficients under different attack angles. The setup for the test is shown below in Figure 3-1-6.

Figure 3-1-6: Set-up of the aerostatic coefficients test

TFI Cobra 3D pulse wind speed probe is used to monitor the wind speed in the tunnel. All working states of the experiment's streamlined box girder section model are tested for its aerostatic coefficients. This test included four wind speeds, 0 m/s, 10 m/s, 15 m/s, and 20 m/s. The attack angles are a total of 25 angles ranging from -12 degrees to 12 degrees. A sample aerostatic coefficients spectrum is shown in Figure 3-1-7.

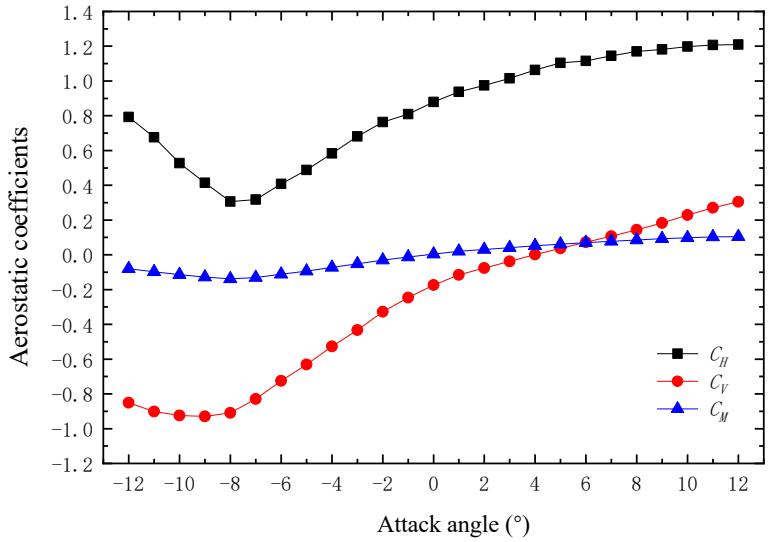

Figure 3-1-7: The aerostatic coefficients spectrum for the original condition at 15 m/s wind

The VIV force time histories can then be put through Fourier transformation to yield the frequency domain spectrum of the respective working states. The aerostatic coefficients and predominant frequencies of lift force and rotational moment experienced by the models in different working states can be used to validate the accuracy and reliability of the CFD analyses performed later in this chapter.

3.1.3 Working states tested in the experiments

Wind tunnel experiments are conducted for the streamlined box girder section with different attack angles and damping ratios with various aerodynamic VIV mitigation measures installed. The working states of the experiment are listed below in Table 3-1-2.

Table 3-1-2: Working states tested

Working state	Aerodynamic measures		Damping ratio (Vertical/Rotational)	Attack angle (121°)
	Central stabilizing board	Horizontal stabilizing board		
B1	——	——	Low damping (0.2%/0.05%)	+3, +5
B2	0.67 m	——	Low damping (0.2%/0.05%)	+3
B3	0.67/1.02 m (6 m interval)	——	Low damping (0.2%/0.05%)	+3
B4	0.67/1.02 m (6 m interval)	0.58 m	Low damping (0.2%/0.05%)	+3
B5	0.67/1.02 m (6 m interval)	1.0 m	Low damping (0.2%/0.05%)	+3,+5
B6	0.67/1.02 m (6 m interval)	1.0/0.5/0.25 m (6m interval)	Low damping (0.2%/0.05%)	+3

B7	0.67/1.02 m (6 m interval)	1.0/0.0 m (12 m interval)	Low damping (0.2%/0.05%)	+3
B8	0.67/1.02 m (6 m interval)	0.0/1.0 m (12 m interval)	Low damping (0.2%/0.05%)	+3
B9	0.0/1.02 m (6 m interval)	0.0/1.0 m (12 m interval)	Low damping (0.2%/0.05%)	+3
B10	0.67 m	1.0/0.0 m (12 m interval)	Low damping (0.2%/0.05%)	+3
B11	0.67 m	1.0/0.0 m (12 m interval) (Offset by 12 m on both sides)	Low damping (0.2%/0.05%)	+3
B12	0.67 m	1.0/0.0 m (12 m interval) (Offset by 24 m on both sides)	Low damping (0.2%/0.05%)	+3
B13	——	1.0 m	Low damping (0.2%/0.05%)	+3
B14	——	1.35 m	Low damping (0.2%/0.05%)	+3
B15	——	1.35/0.0 m (12 m interval)	Low damping (0.2%/0.05%)	+3
B16	0.67 m	1.35 m	Low damping (0.2%/0.05%)	+3
B17	0.67 m	1.0 m	Low damping (0.2%/0.05%)	0~±5
BZ1	——	——	Standard damping (0.3%/0.2%)	+3
BZ17	0.67 m	1.0 m	Standard damping (0.22%/0.2%)	+5

It is notable that the dimensions of aerodynamic measures listed in Table 3-1-2 are unscaled, e.g., the 0.67 m central stabilizing board is 1.34 cm in the experiment, the 12 m interval for the horizontal stabilizing board is 24 cm wide, etc. Each working state uses Different damping ratios for vertical bending and rotational modes. The attack angles tested are specified in the table. Photos

of tested working states can be found in the Appendix.

3.1.4 Experimental results

The VIV responses of the streamlined box girder section under different attack angles, damping ratios, and various aerodynamic VIV mitigation measures are recorded. Different working states are carried out in the experiment, and the result is summarized in Table 3-1-3.

Table 3-1-3: Experimental results

Working state	Aerodynamic measures		Damping ratio	Attack angle (°)	1st vertical bending (mm)	2nd vertical bending (mm)	Rotational displacement (°)
	Central stabilizing board	Horizontal stabilizing board					
B1	——	——	Low damping (0.2/0.05%)	+3	276	348	1.00
				+5	328	250	0.80
B2	0.67 m	——	Low damping (0.2/0.05%)	+3	281	30	0.71
B3	0.67/1.02 m (6 m interval)	——	Low damping (0.2/0.05%)	+3	231	251	0.80
B4	0.67/1.02 m (6m interval)	0.58 m	Low damping (0.2/0.05%)	+3	219	207	0.56
B5	0.67/1.02 m (6m interval)	1.0 m	Low damping (0.2/0.05%)	+3	196	26	0.60
				+5	10	——	——
B6	0.67/1.02 m (6m interval)	1.0/0.5/0.25 m (6 m interval)	Low damping (0.2/0.05%)	+3	215	74	0.63
B7	0.67/1.02 m (6m interval)	1.0/0.0 m (12 m interval)	Low damping (0.2/0.05%)	+3	173	——	——
B8	0.67/1.02 m (6m interval)	0.0/1.0 m (12 m interval)	Low damping (0.2/0.05%)	+3	210	——	——

B9	0.0/1.02 m (6m interval)	0.0/1.0 m (12 m interval)	Low damping (0.2/0.05%)	+3	244	——	——
B10	0.67 m	1.0/0.0 m (12 m interval)	Low damping (0.2/0.05%)	+3	252	——	——
B11	0.67 m	1.0/0.0m (12 m interval) (Offset by12 m on two sides)	Low damping (0.2/0.05%)	+3	247	——	——
B12	0.67 m	1.0/0.0m (12 m interval) (Offset by 24 m on two sides)	Low damping (0.2/0.05%)	+3	224	——	——
B13	——	1.0 m	Low damping (0.2/0.05%)	+3	181	——	——
B14	——	1.35 m	Low damping (0.2/0.05%)	+3	117	——	——
B15	——	1.35/0.0 m (12 m interval)	Low damping (0.2/0.05%)	+3	257	——	——
B16	0.67 m	1.35 m	Low damping (0.2/0.05%)	+3	11.3	9.6	0.51
B17	0.67 m	1.0 m	Low damping (0.2/0.05%)	+5	8.5	10.1	0.84
				+3	15	9.8	0.58
				0	7.8	10.3	0.26
				-3	4.3	5.2	0.011
				-5	7.7	×	0.013
BZ17	0.67 m	1.0 m	Standard damping (0.22/0.2)	+5	5.8	6.0	0.012

The VIV response spectrum of the streamlined box girder section without any additional aerodynamic VIV mitigation measures (B1) serves as the benchmark for comparison of the effectiveness of various aerodynamic measures. The VIV response of working state B1 at +3° and

+5° attack angles are shown in Figure 3-1-8 and Figure 3-1-9.

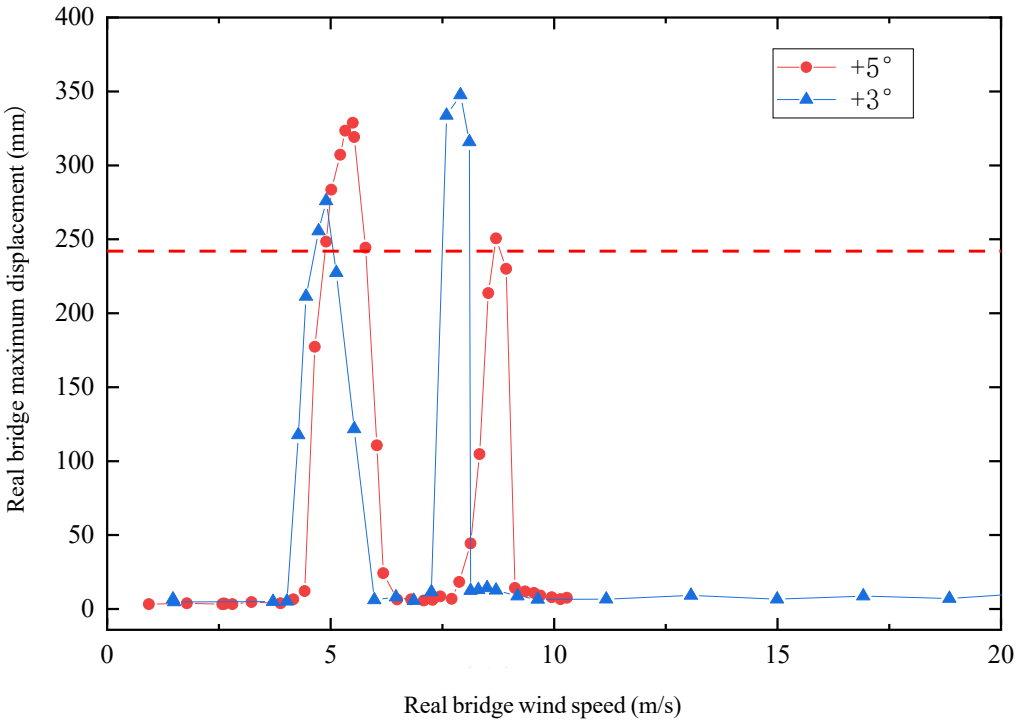

Figure 3-1-8: Vertical bending VIV response of working state B1 with 0.2% damping ratio

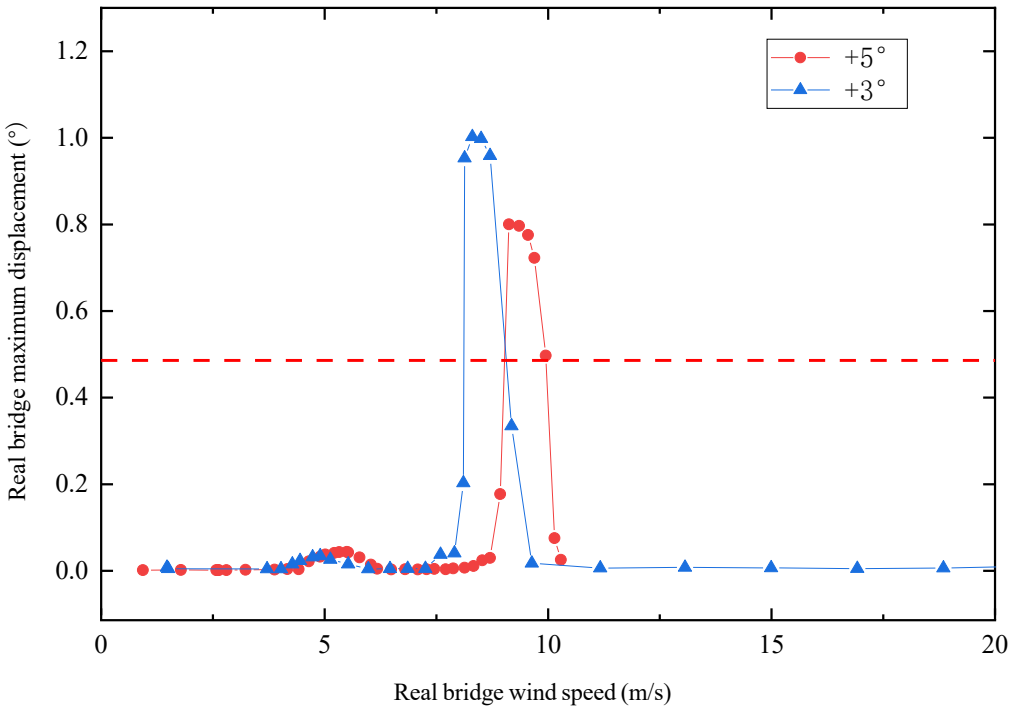

Figure 3-1-9: Rotational VIV response of working state B1 with 0.05% damping ratio

As seen in Figure 3-1-8 and Figure 3-1-9, for the vertical bending mode of the B1 working state, there exist two lock-in ranges for both the +3° and +5° attack angle, for rotational mode, there also exist two lock-in ranges for both attack angles, but displacement magnitude of the first lock-in ranges of the two attack angles are significantly smaller than that of the second lock-in ranges.

3.1.5 Effect of aerodynamic measures

VIV responses of girder sections with different aerodynamic measures installed are discussed in this section. To illustrate the effect of aerodynamic measures, results in critical mode, critical attack angles, and under critical damping ratios are compared.

3.1.5.1 VIV performance of the original girder section

Figure 3-1-8 and Figure 3-1-9 exhibit the VIV performance of the original girder section at 3° and 5° attack angles under low damping ratio conditions (0.20% for vertical bending mode and 0.05% for rotational bending mode). The results are summarized below.

Working state S1 (original girder section, 3°/5° attack angle, 0.20/0.05% damping ratio): at 3° attack angle, between 4.0-6.0 m/s and 7.3-8.1 m/s real bridge wind speed ranges, vertical bending mode VIV appeared with maximum vertical displacements of 276 mm and 348 mm, between 7.9-9.6 m/s real bridge wind speed range, rotational mode VIV appeared with a maximum rotational displacement of 1.00°. At 5° attack angle, between 4.4-6.2 m/s and 7.9-9.1 m/s real

bridge wind speed ranges, vertical bending mode VIV appeared with maximum vertical displacements of 328 mm and 250 mm, between 8.7-10.3 m/s real bridge wind speed range, rotational mode VIV appeared with a maximum rotational displacement of 0.80°.

3.1.5.2 Effect of the central stabilizing board

Figure 3-1-10 and Figure 3-1-11 show the performance of the original girder section with different central stabilizing boards installed at 3° attack angle under low damping ratio condition (0.20% for vertical bending mode and 0.05% for rotational bending mode), the results are summarized below.

Working state B2 (0.67 m central stabilizing board, 3° attack angle, 0.20/0.05% damping ratio): at 3° attack angle, between 4.9-6.5 m/s and 8.3-9.0 m/s real bridge wind speed ranges, vertical bending mode VIV appeared with maximum vertical displacements of 281 mm and 30 mm, between 7.2-8.4 m/s real bridge wind speed range, rotational mode VIV appeared with a maximum rotational displacement of 0.71°.

Working state B3 (0.67/1.02 m central stabilizing board, 3° attack angle, 0.20/0.05% damping ratio): at 3° attack angle, between 4.0-6.7 m/s and 8.1-9.7 m/s real bridge wind speed ranges, vertical bending mode VIV appeared with maximum vertical displacements of 231 mm and 257 mm, between 7.9-9.3 m/s real bridge wind speed range, rotational mode VIV appeared with a maximum rotational displacement of 0.80°.

It can be seen that when only the central stabilizing boards are installed, the 0.67 m central

stabilizing board is most effective in mitigating the displacement of the 2nd VIV lock-in range in the vertical bending mode, and the 0.67/1.02 m central stabilizing board could lower the 1st VIV lock-in range of the vertical bending mode but not as effective as the 0.67 m central stabilizing board.

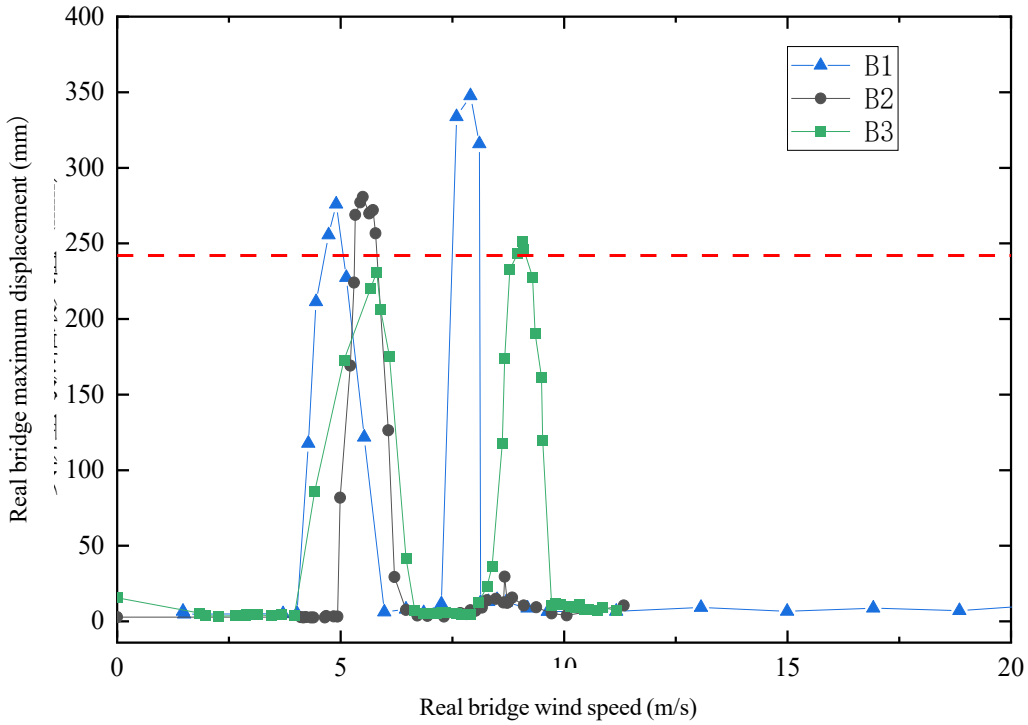

Figure 3-1-10: Vertical bending VIV response of working states B1, B2, B3

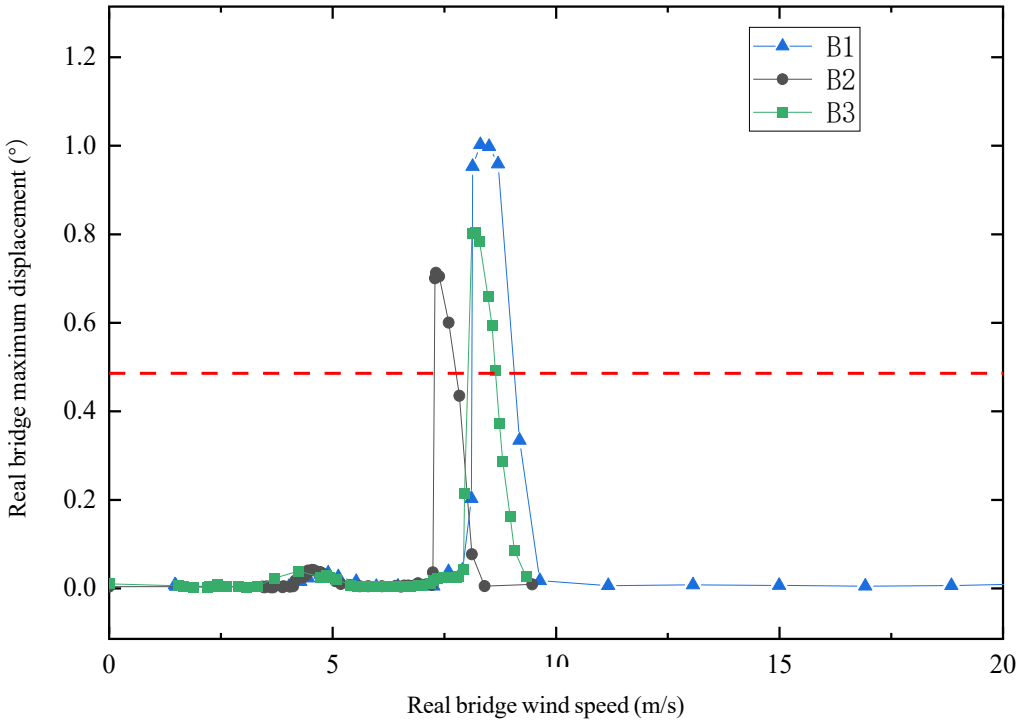

Figure 3-1-11: Rotational VIV response of working states B1, B2, B3

3.1.5.3 Effect of the horizontal stabilizing board

Figure 3-1-12 shows the performance of the original girder section with different horizontal stabilizing boards installed at 3° attack angle under low damping ratio conditions (0.20% for vertical bending mode). For a clear illustration of the result, only the response of the 1st lock-in range of the vertical bending mode is summarized below.

Working state B13 (1.0 m horizontal stabilizing board, 3° attack angle, 0.20/0.05% damping ratio): at 3° attack angle, between 5.2-6.4 m/s real bridge wind speed range, vertical bending mode VIV appeared with maximum vertical displacements of 181 mm.

Working state B14 (1.35 m horizontal stabilizing board, 3° attack angle, 0.20/0.05% damping ratio): at 3° attack angle, between 4.4-5.5 m/s real bridge wind speed range, vertical bending mode VIV appeared with maximum vertical displacements of 117 mm.

Working state B15 (1.35 m horizontal stabilizing board with an interval of 12 m, 3° attack angle, 0.20/0.05% damping ratio): at 3° attack angle, between 4.6-5.6 m/s real bridge wind speed range, vertical bending mode VIV appeared with maximum vertical displacements of 257 mm.

The 1.0 m and 1.35 m horizontal stabilizing boards could reduce the 1st lock-in range displacement from 276 mm on the original girder section to 181 mm and 117 mm, respectively. The 1.35 m horizontal stabilizing board with 12 m intervals is ineffective in reducing the displacement of the 1st lock-in range of the vertical bending mode.

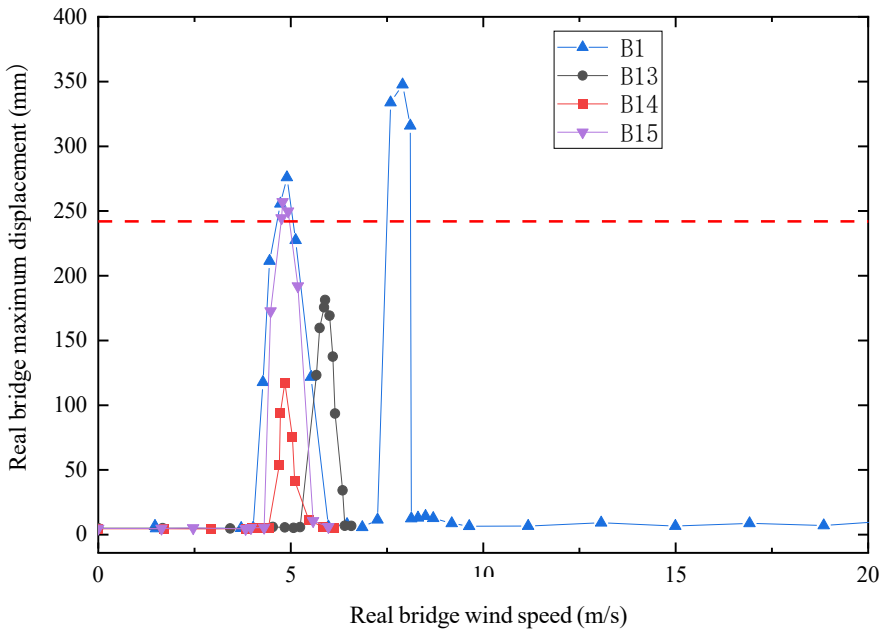

Figure 3-1-12: Vertical bending VIV response of working states B1, B13, B14, B15

3.1.5.4 Effect of the combination of the central and horizontal stabilizing boards

Figure 3-1-13 shows the performance of the original girder section with different central/horizontal stabilizing boards combination installed at 3° attack angle under low damping ratio conditions (0.20% for vertical bending mode and 0.05% for rotational bending mode). For a clear illustration of the result, only the response of the 1st lock-in range of the vertical bending mode is summarized below.

For working states of B1, B4-B12, B16, and B17, the maximum displacements of the 1st lock-in range of the vertical bending mode are 276 mm, 219 mm, 196 mm, 215 mm, 173 mm, 210 mm, 244 mm, 252 mm, 247 mm, 224 mm, 11.3 mm, and 15 mm, respectively. In **working state B16** (0.67 m central stabilizing board and 1.35 m horizontal stabilizing board) and **working state B17** (0.67 m central stabilizing board and 1m horizontal stabilizing board), there is no visible vertical bending VIV response in both the 1st and the 2nd lock-in ranges.

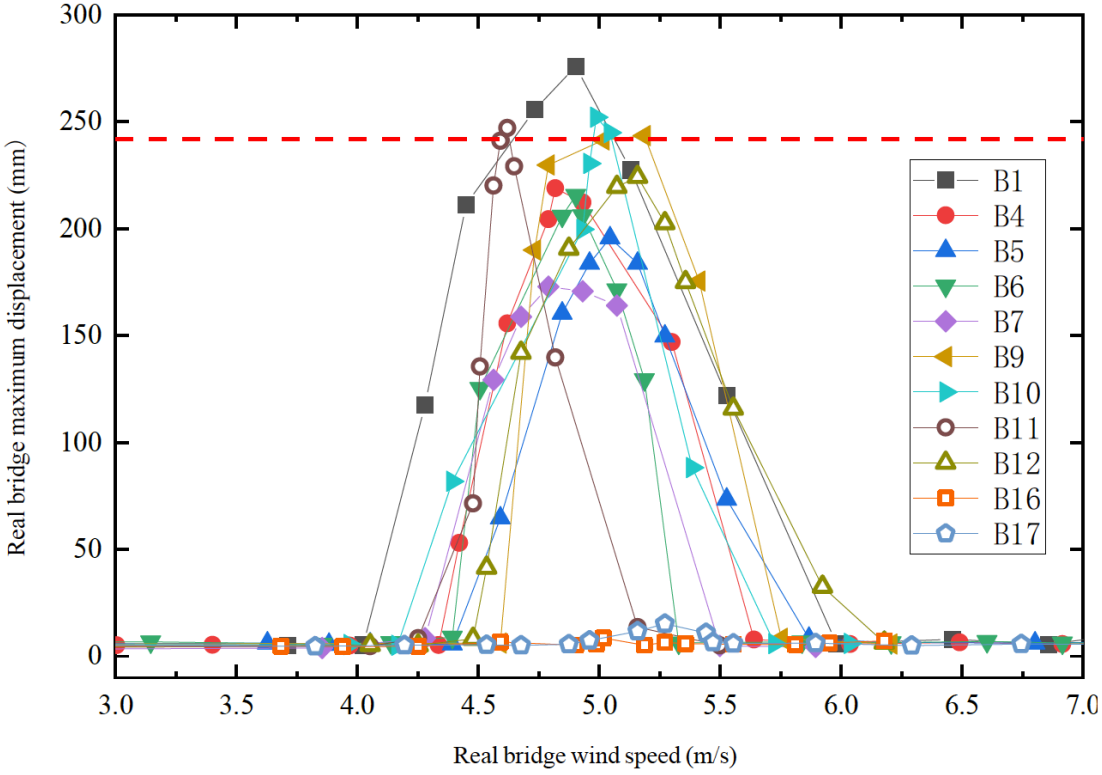

Figure 3-1-13: Vertical bending VIV response of working states B4-B12, B16-B17

3.1.5.5 Effect of damping ratio

(1) Comparing the response of the original girder section at 3° attack angle under the low damping ratio (B1, 0.20/0.05%) and under the standard damping ratio (BN1, 0.30/0.20%), the displacement of the 1st and 2nd lock-in ranges of the vertical bending mode from 276 mm and 348 mm to 88 mm and 7 mm, rotational mode displacement is reduced from 1.00° to 0.015°, as shown in Figure 3-1-14 Figure 3-1-15.

(2) Comparing the response of the original girder section with 0.67 m central stabilizing board and 1m horizontal board at 5° attack angle under the low damping ratio (B17, 0.20/0.05%) and

under standard damping ratio (BN17, 0.30/0.20%), the displacement of the 1st and 2nd lock-in ranges of the vertical bending mode from 8.5 mm and 5.8 mm to 10.1 mm and 6.0 mm, rotational mode displacement is reduced from 0.84° to 0.012°, under rotational damping ratio higher than 00.20%, the rotational displacement is completely mitigated, as shown in Figure 3-1-16 and Figure 3-1-17.

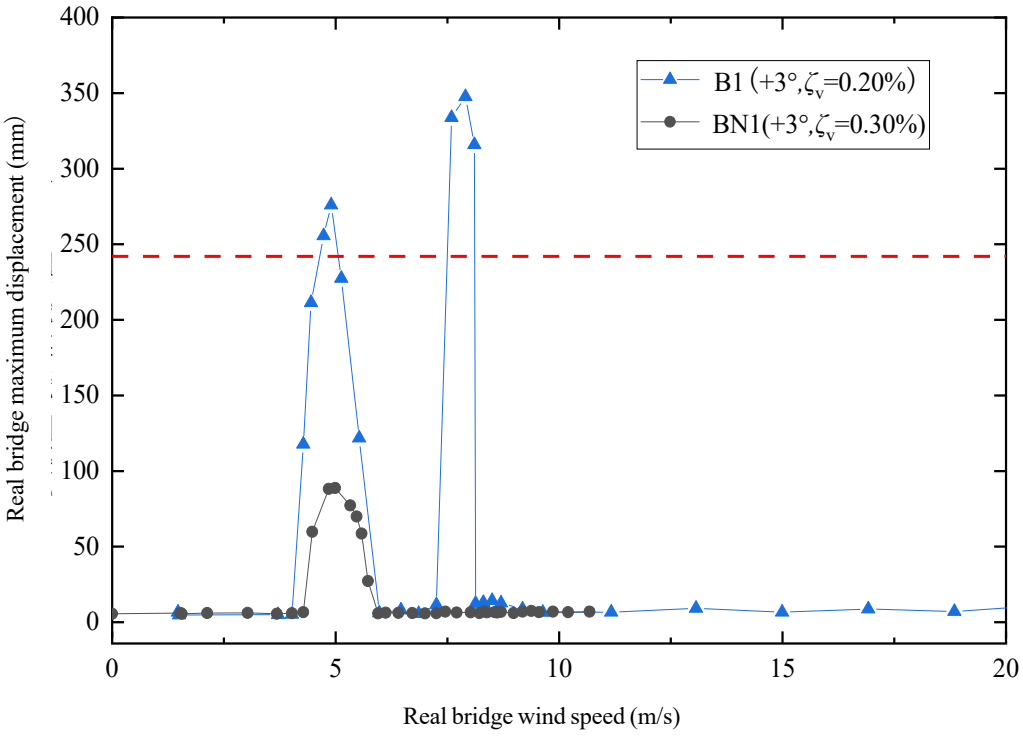

Figure 3-1-14: Vertical bending VIV response of working states B1, BN1

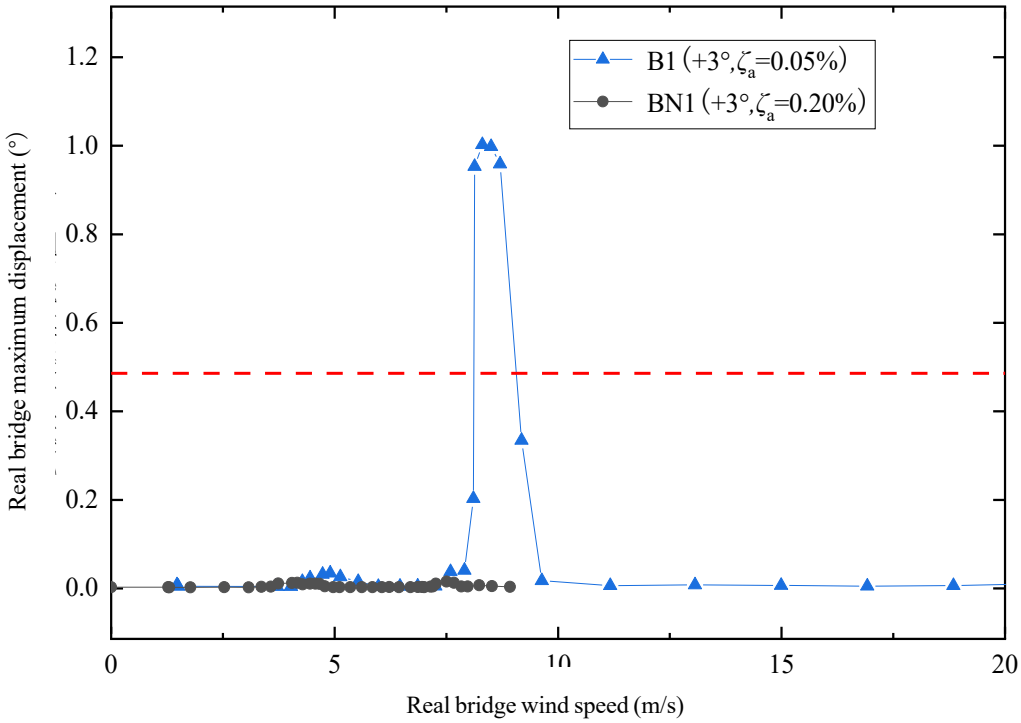

Figure 3-1-15: Rotational VIV response of working states B1, BN1

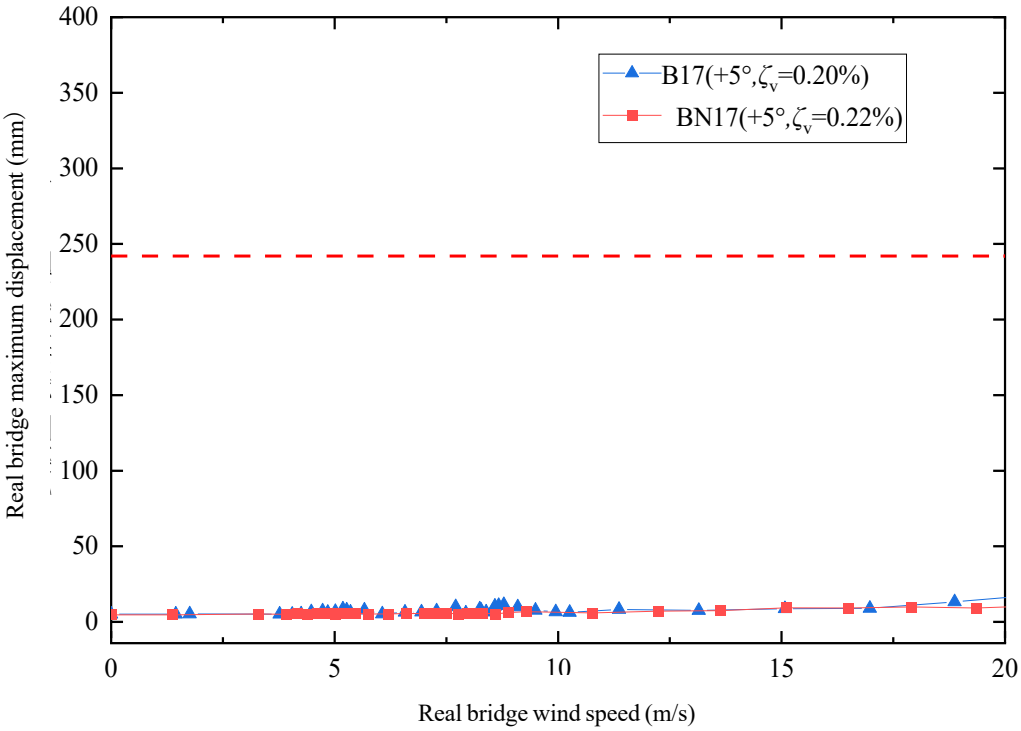

Figure 3-1-16: Vertical bending VIV response of working states B17, BN17

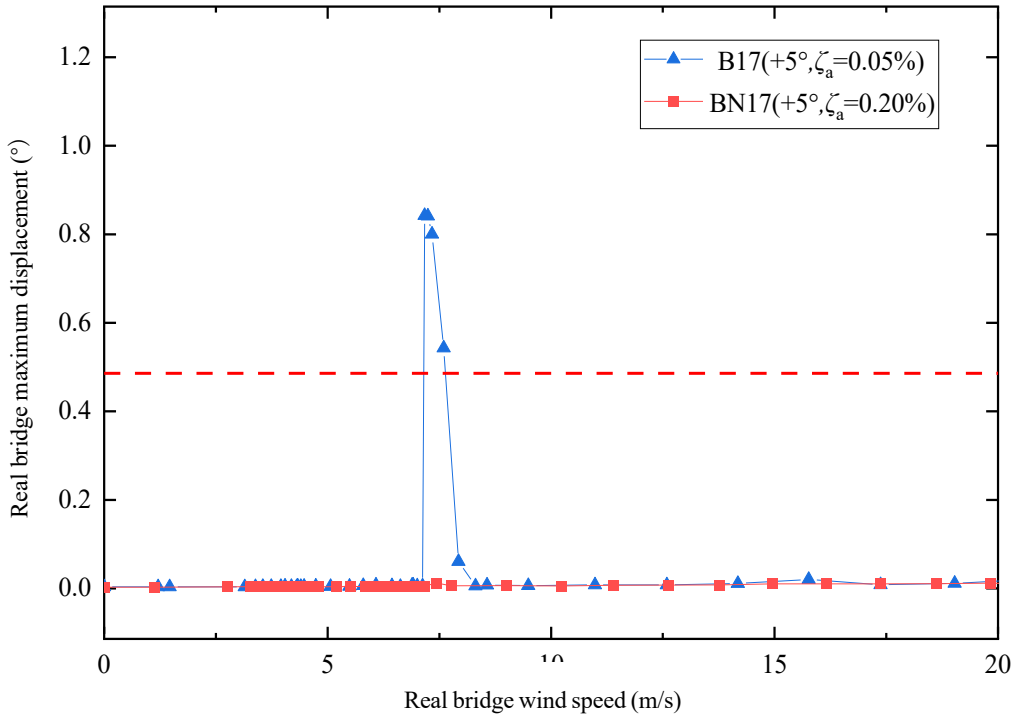

Figure 3-1-17: Rotational VIV response of working states B17, BN17

3.1.5.6 Summary of effects of aerodynamic measures

This section tests central and horizontal stabilizing boards separately for their effectiveness in mitigating vertical bending and rotational VIV response for the streamlined girder.

Compared to the original girder at the critical attack angle (+3°), the 0.67 m central stabilizing board (**working state B2**) is effective in mitigating the magnitude of the 2nd lock-in range of the vertical bending mode and the 1st lock-in range of the rotational mode, reducing the maximum displacement by 91.3% (2nd vertical bending lock-in range, 348 mm to 30 mm) and 29% (1st rotational lock-in range, 1.00° to 0.71°).

Compared to the original girder at the critical attack angle (+3°), the 1.35 m horizontal

stabilizing board (**working state B14**) is effective in mitigating the magnitude of displacement of the 1st vertical bending lock-in range, reducing the displacement by 57.6% (276 mm to 117 mm).

When the central stabilizing boards and the horizontal stabilizing boards are combined, the **working state B16** (0.67 m central stabilizing board and 1.35 m horizontal stabilizing board) is the most effective. Under low damping conditions, vertical bending VIV response is effectively mitigated. When the rotational mode damping ratio increases to 0.20% or higher, the rotational mode VIV response is also effectively mitigated.

The addition of central stabilizing boards and horizontal stabilizing boards (**working states B2, B14, and B16**) are proven effective in mitigating both the vertical bending mode and rotational mode VIV response of the streamlined box girder section. The mechanisms of such mitigations are analyzed and discussed later in this chapter with the result from the CFD analysis of the streamlined box girder section.

3.2 VIV initiation mechanism of the streamlined box girder section based on CFD analysis

3.2.1 Numerical model setup

To explore the flow field characteristics and the VIV mechanism around the streamlined girder section, a CFD numerical analysis is performed for the 1:50 streamlined girder section. The analysis includes two working states, namely the streamlined girder section with accessory

components and the streamlined girder section without accessory components, to differentiate the effect of non-structural components such as railings and maintenance tracks.

The overall mesh dimension and layout for the simulation are shown in Figure 3-2-1. The mesh's left side and right side are set as velocity inlet and pressure outlet, respectively, and the mesh's upper side and lower side are set as symmetry face to avoid shear effect on the boundaries.

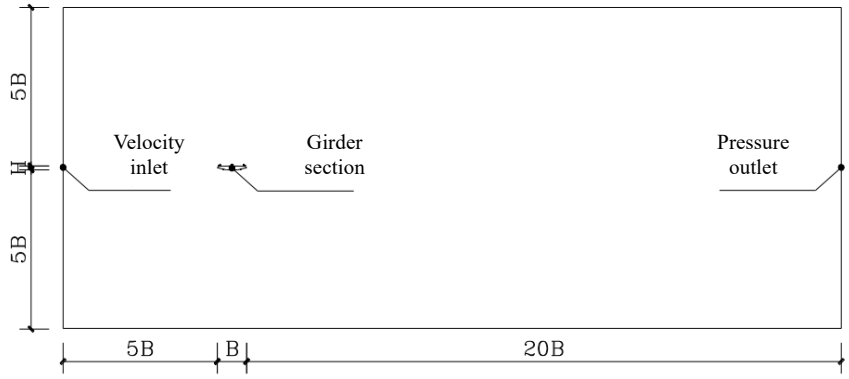

(a) Boundary condition of the mesh area

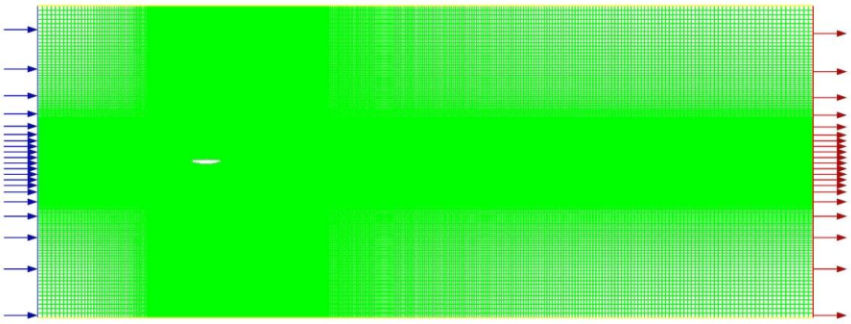

(b) Mesh layout of the mesh area

Figure 3-2-1: Overall mesh dimension for the streamlined girder section

For sections with and without accessory components, the total number of mesh elements is approximately 480,000 and 380,000, respectively. In the core layers near the girder section, the

number of mesh elements is approximately 330,000 and 230,000, respectively. The maximum skew ratio for all mesh elements for sections with and without accessory components are 0.462 and 0.456, respectively, indicating that the mesh elements of the two working states are well configured. Close-up pictures of the mesh layout around the two sections are shown in Figure 3-2-2.

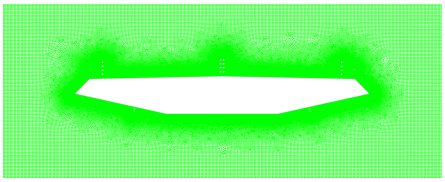

(a) Mesh of section with non-structural components

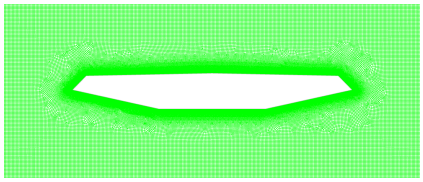

(b) Mesh of section without non-structural components

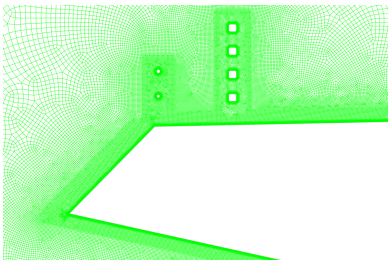

(c) Close-up on section with non-structural components

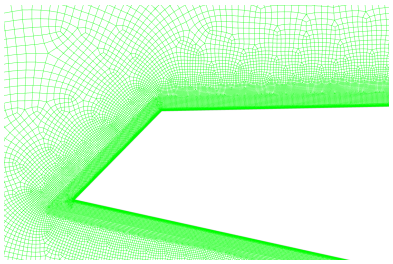

(d) Close-up on section without non-structural components

Figure 3-2-2: Close-up of the mesh layouts

The simulations are performed on the same 64-core server used for CFD simulation of the rectangular girder sections. The simulations are transient with double-precision, conducted using the SST k-omega turbulence model, and solved with SIMPLEC solver.

A time step size sensitivity test is performed to determine the most efficient time step size while maintaining simulation accuracy. For both working states, 0.0001 seconds time step size and

0.001 seconds time step size are tested. Their respective aerostatic coefficients, such as drag, lift, and moment coefficients, are summarized in Table 3-2-1.

Table 3-2-1: Aerostatic coefficients **comparison for different time step size**

Time step	With accessory components			Without accessory components		
	C_H	C_V	C_M	C_H	C_V	C_M
0.001s	0.7962	-0.1984	-0.000451	0.2659	-0.2975	0.000625
0.0001s	0.8159	-0.1967	-0.003036	0.2660	-0.2979	0.000580
Difference (%)	-2.4%	0.8%	-85.1%	-0.1%	-0.1%	7.8%

As seen in Table 3-2-1, the difference between drag coefficients and lift coefficients of 0.0001 seconds and 0.001 seconds time step size is small. For the moment coefficient, although the percentages of differences are relatively big, the absolute differences of values are very small. Therefore, it can be concluded that the 0.001 seconds and 0.0001 second time step sizes post little difference, and the simulation calculation is converged at 0.001 seconds time step size. Since 0.001 seconds time step size is more time-efficient than other converged time step sizes, it is selected as the time step size for simulations.

To verify the validity and reliability of the numerical model in the simulation, the aerostatic coefficients of the sections from the CFD simulation and the wind tunnel experiment are compared. Three attack angles from the CFD simulation (+3°, 0°, -3°) are tested for the girder sections with and without the accessory components. The comparison result is shown in Figure 3-2-3.

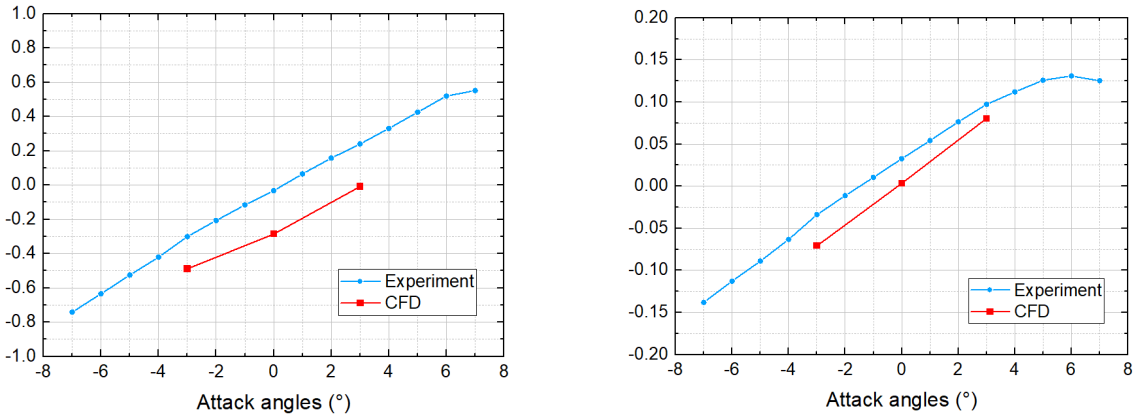

(a) Lift force coefficient *(b) Rotational moment coefficient*

Figure 3-2-3: Aerostatic coefficients comparison of CFD simulation and wind tunnel experiment

From Figure 3-2-3, the simulation aerostatic coefficients of the three attack angles exhibit similar values and trends. Therefore, it is concluded that the simulation is valid and reliable for further analysis.

3.2.2 Vortex recognition and tracking based on Deep learning utilizing Convolutional Neural Network (CNN)

The previous chapter presents a two-dimensional flow field vortex recognition and tracking method based on static pressure monitoring points utilizing MATLAB (MPF-track). This vortex recognition and tracking method is suitable for simple girder shapes such as rectangular sections and rectangular sections with vertically symmetrical wind noses. Around these sections, the number of vortex-shedding mechanisms is small, the areas where the vortexes travel are obvious, and the setup of monitoring points is, therefore, straightforward. For example, in rectangular girder sections and rectangular sections with symmetrical wind noses, there each are two vortex shedding

mechanisms that travel close to the girder surface above and below the girder. For streamlined girder sections with or without accessory components and for other girder section shapes that are more complicated, the recognition and tracking method based on manual monitoring points setup would become more and more time-consuming, the recognition and tracking process, as well as the post-simulation process such as data analysis, would become increasingly difficult. Therefore, to efficiently recognize and track the vortexes around more complicated girder section shapes, a computer vision vortex recognition and tracking method based on deep learning utilizing Convolutional Neural Network is proposed.

This visual vortex recognition and tracking method uses source code from open-source deep learning projects named You Only Look Once 5th version (YOLOv5) [120] and Simple Online and Realtime Tracking with a Deep Association Metric (DeepSORT) [121] [122], respectively. The recognition and tracking source code is run in the virtual Python environment software Anaconda [123]. The functions used are from open-source machine-learning libraries of Pytorch [124] and PaddlePaddle [125].

3.2.2.1 The machine learning process for vortex recognition

Snapshots of the flow field around the 1:6 rectangular girder section with wind noses are used as the data source for the training process. All the visible vortexes (low-pressure zones) in these snapshots of the flow field are manually labeled and categorized into a training set and a validation set. Figure 3-2-4 shows a schematic for the labeling of vortexes in the flow field around

the 1:6 rectangular girder section with wind noses at 1.6 m/s wind speed.

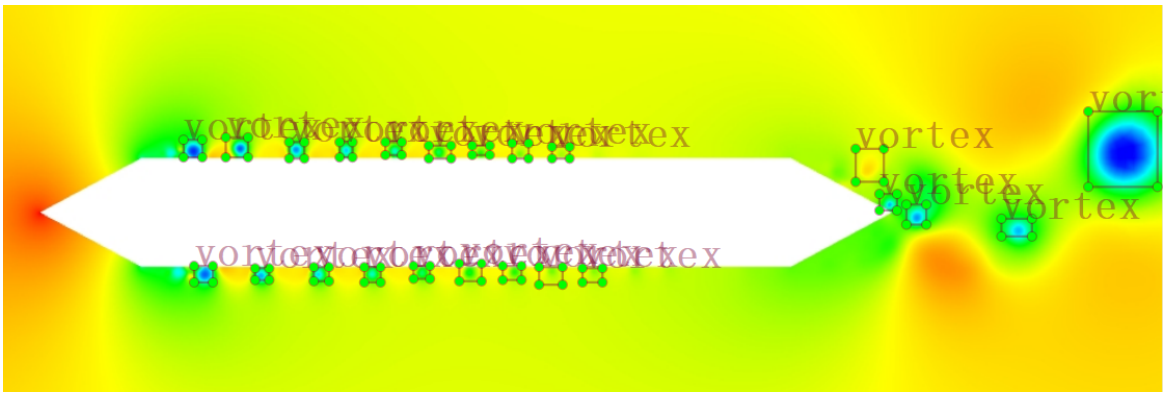

Figure 3-2-4: Vortexes labeled in the flow field

All snapshots in the training set are then fed into the Convolutional Neural Network learning model for the 1st round of machine learning. In the 1st round of learning, the labeled vortexes in the snapshots are processed to form an "average portrait" of how the learning model understands a vortex looks like, then the "portrait" is weighted by a pre-determined weight and compared to each of the labeled vortexes in the snapshots of the validation set to generate a matching probability that describes how well the model's understanding of the vortex after this round of learning match with the vortexes in the snapshots of the validation set. After the 1st round of learning, the pre-determined weight of the 1st round is optimized based on the validation result and is used as the pre-determined weight for the 2nd round. By repeating the process mentioned above, the matching probability after each round starts to increase. To optimize the converging rate of the matching probability for the learning process, the default YOLOv5 weight (YOLOv5s.pt) is modified in accordance with the visual characteristics (spatial feature) of the vortexes and the number of labeled flow field snapshots is increased to 50. Figure 3-2-5 compares the growth rate

of the matching probabilities when different weights and numbers of snapshots are used.

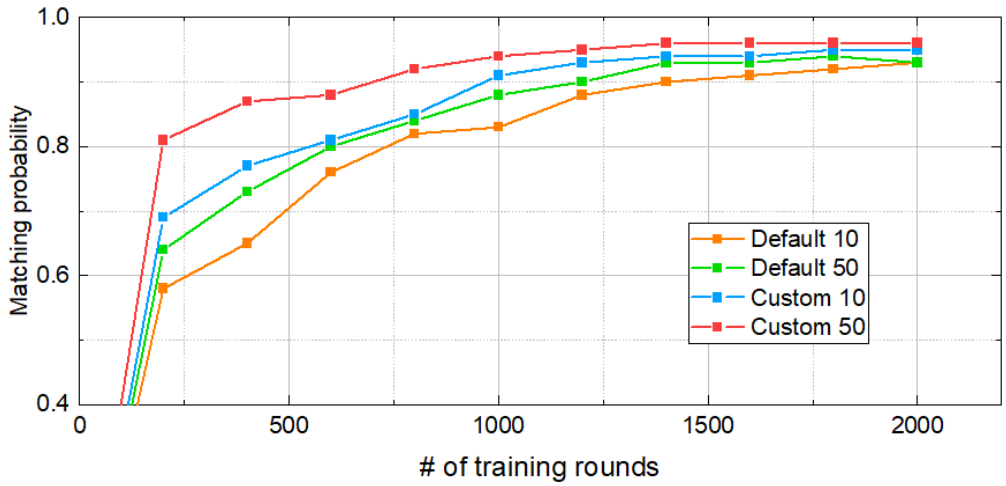

Figure 3-2-5: Matching probability growth curves for different weights and numbers of snapshots

As seen in Figure 3-2-5, the growth rate of the matching probability increases when the calibrated weight is used. The matching probability exceeds 80% after 200 rounds of training. The calibrated weight gives the model a better initial understanding of the visual characteristics (spatial feature) of the vortexes from the early rounds compared to the default YOLO weight and is more suitable for this research. The increase in the number of snapshots also increased the growth rate of the matching probability. However, more snapshots require more pre-training manual labeling and processing time for the model during each round of the training process. Therefore, the calibrated weight for vortexes and 50 snapshots of the flow field around the 1:6 rectangular girder section with wind noses are used for this part of the research for efficiency.

The recognition process utilizes all 50 snapshots and the best weight file produced during the training process as its “perception” of the spatial feature of the vortexes to recognize the vortexes in the input files (pictures or videos). The YOLO model first scans all possible objects in

the input pictures (frames of videos), treats them as labeled vortexes in the learning process's validation set, and generates a matching probability for each object in the input pictures (frames of videos). Objects with lower matching probabilities are filtered in a process called Non-Max Suppression, and the remaining objects with higher probabilities are the recognized vortexes in the input files. Figure 3-2-6 shows a flow chart that describes the learning and recognition process for vortexes using a YOLOv5 model modified for this research.

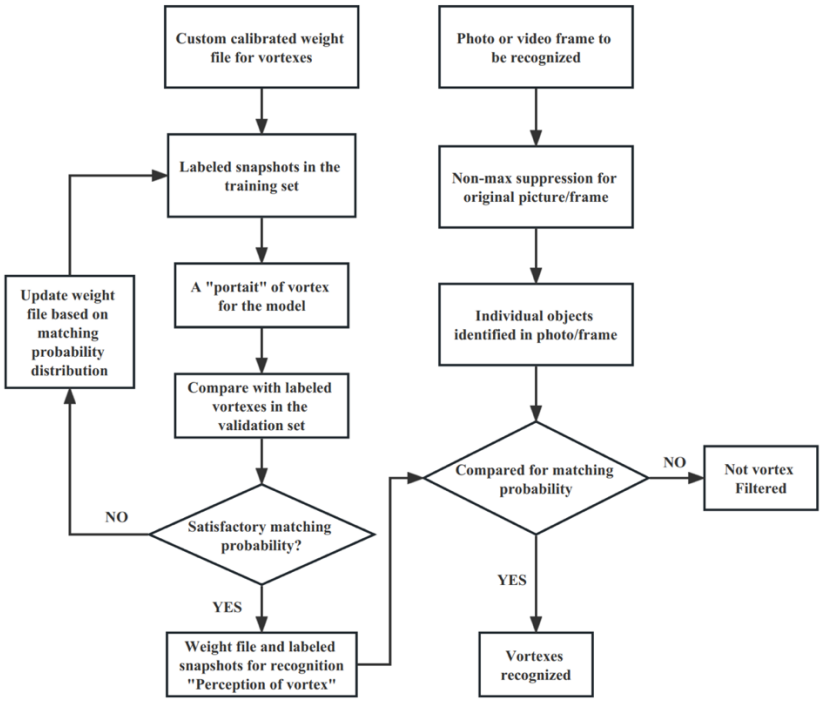

Figure 3-2-6: Flow chart for the modified YOLOv5 machine learning and recognition process

The recognition result based on 50 snapshots of the flow field around the 1:6 rectangular girder section with wind noses is shown in Figure 3-2-7. Note that the girder section is also included in the training process as a different category and, therefore, recognized.

Figure 3-2-7: Recognition results for the 1:6 rectangular section with wind noses

As seen in Figure 3-2-7, all visible vortexes are successfully recognized along with the girder section. Figure 3-2-8 shows the recognition result for the streamlined girder section with the same training result as the 1:6 girder section with wind noses.

Figure 3-2-8: Recognition results for the streamlined girder section

As seen in Figure 3-2-8, the vortexes around the streamlined girder section are successfully recognized using the learning result from the 1:6 rectangular girder section with wind noses. Notably, the streamlined girder section is also successfully recognized, which indicates that the training result applies to box girder sections with different shapes.

3.2.2.2 Vortex tracking based on DeepSORT

Based on the recognition result of vortexes around girder sections with YOLOv5 discussed

in the previous section, the vortex path tracking functionality is implemented with DeepSORT. DeepSORT is an add-on algorithm to the YOLOv5 algorithm for Multi-Object Tracking (MOT) tasks. It is a Tracking-By-Detection (TBD) solution that utilizes the recognition functionality provided by detection algorithms (e.g., YOLOv5) and performs its tracking functionality.

The DeepSORT algorithm utilizes the same set of pictures used to train the YOLOv5 vortex recognition model for its machine learning process and extract the dynamic characteristics (temporal feature) of vortexes traveling around the girder sections to generate a tracking weight file. The vortexes are first recognized by the YOLOv5 algorithm using the previously trained recognition weight file, and the tracking weight file from the training of the DeepSORT model is then used to track individual vortexes with the Kalman filter [126] and the Hungarian algorithm [127], which associates the vortexes with the same IDs from different frames of the input video and tracks their paths around girder sections using a predict-verification logic.

The tracking process is introduced as follows. All vortexes are first recognized and assigned a unique ID using the YOLOv5 functionality in the n^{th} frame of a video file. With the tracking weight file, which describes the dynamic characteristics (temporal feature) of vortexes, the Kalman filter would predict the locations of the vortexes in the $n+1^{th}$ frame of the video. Then, the Hungarian algorithm would associate the predicted vortex in the $n+1^{th}$ frame with all the recognized vortexes by calculating their cost matrices. With the Kalman filter and the Hungarian algorithm, the paths of the same vortexes from the n^{th} and $n+1^{th}$ frames of the video are tracked. Repeating the process for all the video frames, the full paths of vortexes traveling around the girder

can be obtained. Figure 3-2-9 shows a flow chart that describes the recognition and tracking process for vortexes using the YOLOv5 and DeepSORT model modified for this research.

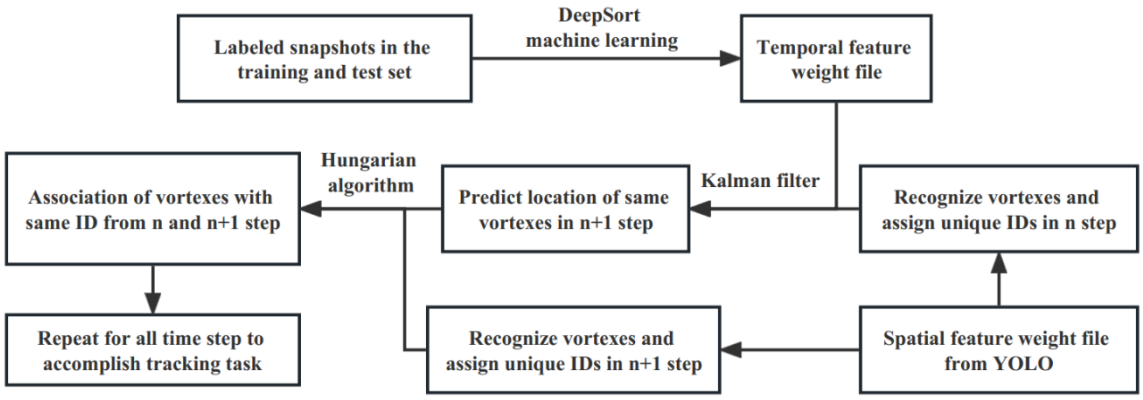

Figure 3-2-9: Flow chart for the modified DeepSORT machine learning and tracking process

The tracking result of the vortexes around the streamlined girder section using a spatial feature weight file trained from pictures of the flow field around the 1:6 rectangular girder section wind noses are shown in Figure 3-2-10.

Figure 3-2-10: Tracking result for the streamlined girder section

In Figure 3-2-10, all vortexes are assigned with a unique ID and tracked continuously. The information on their paths and the number of vortexes at each time step are saved in text files and used for post-processing.

3.2.2.3 Comparison with the recognition and tracking method based on monitoring point setup (MPF-track)

The recognition and tracking method based on monitoring point setup (MPF-track) is introduced in detail in Chapter 2. The MPF-track method is a Single-Object Tracking (SOT) method that utilizes monitoring faces constructed by an automatic monitoring points setup process before simulations by Fluent. The static pressure values of the monitoring points at each time step are recorded during the Fluent simulation, and the vortex recognition and tracking are performed using MATLAB scripts in the post-processing of the data.

The vortex recognition and tracking method based on YOLOv5 and DeepSORT is a python-based Multi-Object Tracking (MOT) method that is performed in real-time in videos of the flow field around girder sections with spatial and temporal features of vortexes trained from a pre-determined machine learning process of manually labeled flow filed images. The spatial and temporal features are used for recognizing the vortexes in each frame and tracking the paths of vortexes in continuous frames.

In both the MPF-track method and the YOLOv5/DeepSORT method, the vortexes are recognized according to their spatial features. The spatial feature of vortexes in the MPF-track method is manually integrated into the recognition scripts. It identifies the bulges in the static pressure time history of a certain monitoring face as vortexes and locates the centers and perimeters of the vortexes by scanning for zero derivative points and points surrounding the centers with a threshold value. Figure 3-2-11 shows a schematic of vortex recognition by the MPF-track method.

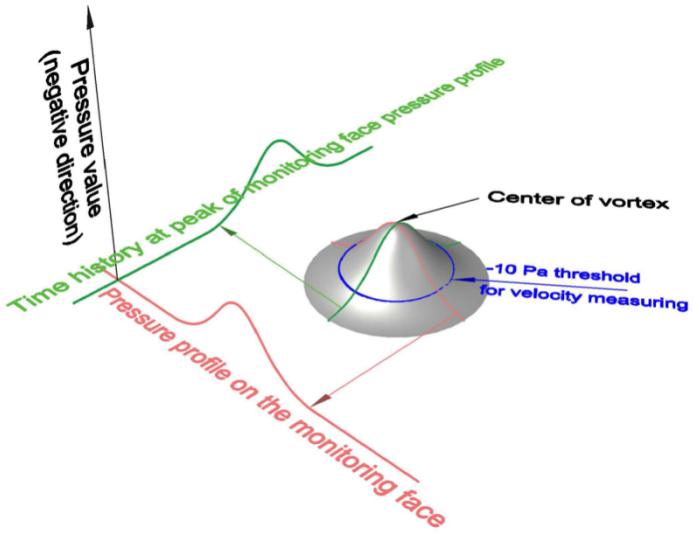

Figure 3-2-11: Schematic of vortex recognition in MPF-track method

In the YOLOv5/DeepSORT method, the spatial feature of vortexes is obtained by a pre-determined machine learning process based on manually labeled vortexes in flow field images. The YOLOv5 algorithm compares a weighted average of the labeled vortexes from the training set and the labeled vortexes from the validation set after each round of training and updates the weight file that describes the spatial feature of the vortexes. The training process is repeated until a weight file with satisfactory matching probability is achieved.

For the tracking process, both the MPF-track and YOLOv5/DeepSORT methods are based on a predict-and-verify logic. In the MPF-track method, the traveling direction and velocity of a vortex being tracked when it passes through a certain monitoring face are extracted, and its predicted time and location when it passes the following monitoring face are calculated based on the distance between monitoring faces. The recognition process is repeated at the predicted time and location at the following monitoring face and corrected if necessary to verify the actual time

and location when the same vortex passes through the following monitoring face. The process is repeated for all the vortexes at each monitoring face to reveal the paths of vortexes in the monitored range.

The YOLOv5/DeepSORT method uses machine learning to generate a weight file containing the temporal feature that describes how vortexes travel in the flow field of interest, then utilizes the Kalman filter and the Hungarian algorithm to predict and verify the locations of vortexes in continuous frames of a video. It is capable of tracking multiple objects at the same time as well as temporarily blocking objects in real-time.

With the predict-verification logic of the Kalman filter and the Hungarian algorithm, the DeepSORT algorithm can identify objects that are blocked without switching or losing the assigned IDs with a good quality training process. Therefore, the DeepSORT algorithm is applicable for monitoring the merging process of vortexes and is a more suitable and effective tracking method for this research than other tracking algorithms. Figure 3-2-12 shows the vortex tracking results around the 1:6 rectangular girder section where the vortex merging phenomenon is prevalent using YOLOv5/DeepSORT algorithm.

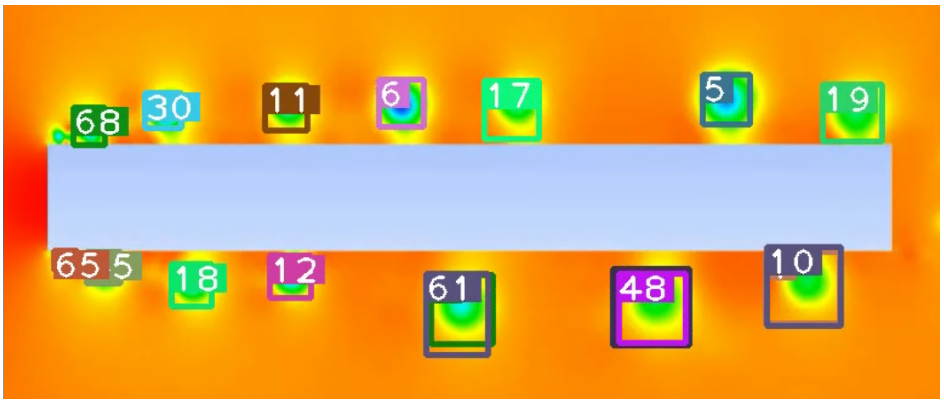

Figure 3-2-12: Vortex tracking around rectangular girder section with YOLOv5/DeepSORT algorithm

As seen in Figure 3-2-12, several ID boxes overlapped with each other toward the downwind side of the girder. This overlap of ID boxes indicates that two vortexes with different IDs have merged and formed a new vortex prior to the moment (e.g., ID boxes 61, 48, and 10). The two ID boxes of the vortexes before their merging will continue to follow the merged vortex without creating a new ID. The location and time where the two ID boxes overlapped can be easily extracted by post-processing their respective path information to reveal the time and location of the merging. The MPF-track method can track the location of vortex merging by counting and comparing the number of vortexes passing through each monitoring face.

A vortex traveling above the 1:6 rectangular girder section is recognized and tracked with both methods. The result is shown in Figure 3-2-13.

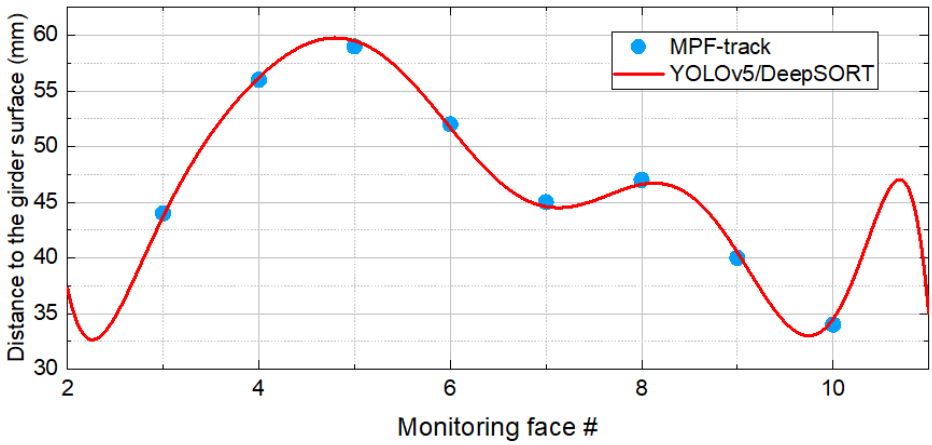

Figure 3-2-13: Path comparison of a vortex by MPF-track method and YOLOv5/DeepSort method

As seen in Figure 3-2-13, the path tracked by the MPF-track method is a polygonal line, and the path tracked by the YOLOv5/DeepSORT method is a continuous curve line. By comparing the two path lines, the results match well. The largest error between the two lines is 0.5 mm, which is caused by the gap between the monitoring points in the MPF-track method.

Although the MPF-track method automates the monitoring setup and data recording process, and optimizes the post-processing process of the vortex recognition and tracking process, it can only track one vortex at a time in a pre-defined range of the flow field. It is efficient when the number of vortex shedding mechanisms is small (two for rectangular girder section), and the range for the vortex development is obvious since the MPF-track method only requires computers capable of running MATLAB and Fluent. In contrast, the YOLOv5/DeepSORT method requires sufficient hardware capabilities, virtual environment configuration, image labeling, machine learning for spatial and temporal features of vortexes, etc. When the number of vortex shedding mechanisms increases (e.g., streamlined girder section with non-structural components and

aerodynamic measures installed), the YOLOv5/DeepSORT method is a better choice because it only requires the CFD flow field video as the input, which is significantly less time-consuming for Fluent to produce compared to the long pressure data read/write process for all the monitoring points at each time step in the MPF-track method, among other reasons.

For vortex recognition and tracking in Chapter 3, the YOLOv5/DeepSORT method is used.

3.2.3 Surface pressure characteristics at initiation wind speeds

The VIV responses of the streamlined girder section for both vertical bending and rotational mode at +3° attack angle in the wind tunnel experiment are shown in Figure 3-2-14.

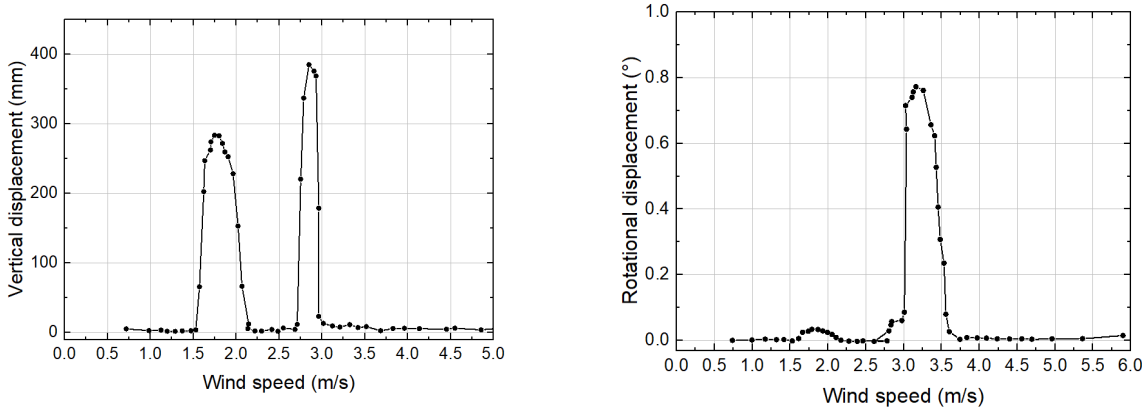

(a) Vertical bending mode **(b) Rotational mode**

Figure 3-2-14: VIV lock-in range of the streamlined girder section at +3° attack angle

It is seen from Figure 3-2-14 that for the vertical bending mode of the streamlined girder section, there exist two VIV lock-in ranges. For the rotational mode of the streamlined girder section, there exists only one VIV lock-in range.

To explore the initiation mechanism of VIV lock-in ranges of streamlined girder sections, the pattern of vortex shedding around the girder section and its resulting girder surface pressure distribution characteristics at VIV initiation wind speeds needs to be understood. According to the VIV response measured in the wind tunnel experiment, shown in Figure 3-1-14, for the streamlined girder section, the two vertical bending VIV lock-in ranges initiated at wind speeds of 1.47 m/s and 2.62 m/s and the one rotational mode VIV lock-in range initiated at wind speed of 2.88 m/s. To verify the initiation mechanism of the lock-in ranges for the streamlined girder section, numerical simulations are performed at the 1.47 m/s, 2.62 m/s, and 2.88 m/s wind speeds.

The predominant lift force frequencies of the streamlined girder section at 1.47 m/s and 2.62 m/s wind speeds and the predominant rotational moment frequency of 2.88 m/s wind speed are summarized in Table 3-2-2.

Table 3-2-2: Predominant frequencies of lift force at different locations

Wind speed (m/s)	Predominant total force frequencies at the wind speed (Hz)	
	Lift force	**Rotational moment**
1.47	0.745/**1.935**	-
2.62	**1.866**/4.587	-
2.88	-	2.052/**5.012**

For vertical bending mode, at the 1.47 m/s wind speed, where the 1st lock-in range of vertical bending mode appears, two predominant frequencies exist for the total lift force (0.745 Hz and 1.935 Hz). The 1.935 Hz frequency is slightly higher than the modal frequencies of the vertical

bending mode frequency (1.88 Hz). At the 2.62 m/s wind speed, where the 2nd lock-in range of vertical bending mode with smaller amplitude appears, there exists two predominant frequencies for the total lift force (1.866 Hz and 4.587 Hz), the 1.866 Hz frequency is slightly lower than the modal frequency of the vertical bending mode frequency. For both the 1.47 m/s and the 2.62 m/s wind speeds, there exists a predominant frequency of total lift force that is close to the vertical bending modal frequency (1.88 Hz). For the rotational moment, the predominant frequencies at 2.88 m/s wind speeds are 2.052 Hz and 5.042 Hz. The 5.012 Hz frequency is slightly above the rotational modal frequency of the girder section (4.94 Hz).

To determine the contribution of vortexes from different locations of the streamlined girder section to the total lift force, the vortexes are tracked using the AI-based vortex tracking method. A detection box is placed for each vortex-shedding mechanism around the streamlined girder section, and the ID boxes of vortexes crossing the edge of the box are counted to reveal the vortex-shedding frequencies, as shown in Figure 3-2-15.

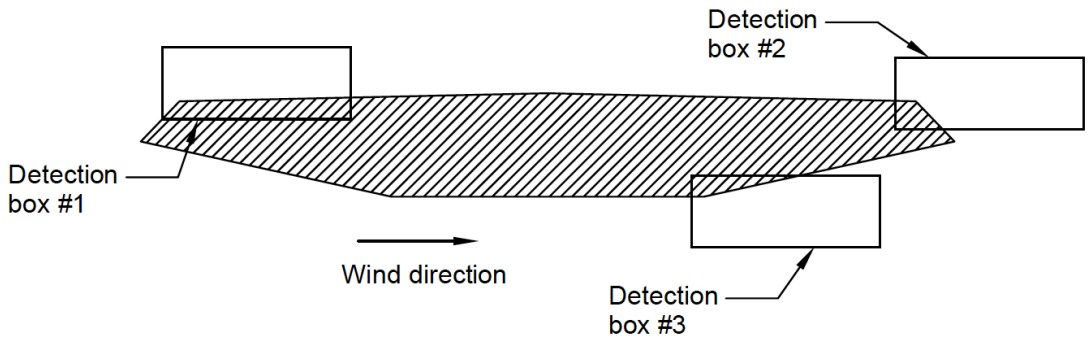

Figure 3-2-15: Detection boxes at different locations around streamlined girder section

The number of vortexes exiting the detection boxes in 10 seconds of elapsed time is summarized in Table 3-2-3.

Table 3-2-3: Number of vortexes exiting the detection boxes in 1 second of time

Wind speed (m/s)	Lift force frequencies at different locations (Hz)		
	Box #1	Box #2	Box #3
1.47	20	7	8
2.62	42	20	19

As seen in Table 3-2-3, the vortex shedding frequency on the upwind side is approximately two times that on the downwind side of the streamlined girder section. The vortexes exited in box #2 and box #3 have similar numbers. When comparing the vortex shedding frequencies with the lift force frequencies summarized in Table 3-2-2, it can be inferred that the vortex shedding mechanism on the upwind side is responsible for the higher predominant frequency, and the vortex shedding mechanism on the downwind side is responsible for the lower predominant frequency.

3.2.4 Comparison of the three box girder sections

In this part of the research, three different box girder sections are tested and studied with similar procedures to reveal the similarities and differences in their respective VIV initiation mechanisms. Wind tunnel experiments are conducted to test their dynamic responses in vertical bending and rotational modes. At the same time, CFD analyses are performed to monitor the flow field characteristics around the girder sections at the initiation wind speeds of their respective VIV

lock-in ranges. Additional explorations, such as girder surface pressure distribution monitoring and vortex tracking, are carried out to reveal the details of the initiation mechanisms.

For the rectangular girder section, two VIV lock-in ranges exist for both the vertical bending and rotational modes. By monitoring the surface pressure distribution at different locations of the girder, it is found that there are two sets of lift force with different frequencies on the upwind and downwind sides of the girder. The upwind side frequency is the double of the downwind side frequency. The vortexes are tracked using the MPF-track method in the previous chapter, and it is revealed that there exists a vortex merging pattern caused by the reattachment of the vortexes to the section surface that would decrease the number of vortexes on the upwind side to approximately half the number on the downwind side. The decrease in the number of vortexes caused by the merging pattern is the reason for the two frequencies on both ends of the girder, which proved to be the cause for the two VIV lock-in ranges in both modes.

Similarly, wind tunnel experiments are conducted for rectangular girder sections with wind noses. The dynamic responses of the girder section showed only one obvious VIV lock-in range for both the vertical bending and rotational modes. According to the CFD analysis, several vortex-shedding mechanisms exist on the upwind side and downwind side of the girder. However, for both the vertical bending mode and the rotational mode, there is one vortex shedding mechanism with a significantly smaller lift force or rotational moment when compared to the other one. By inspection, the installation of the wind nose reduces the magnitude and influencing range of the vortexes on the upwind side as compared to those of the rectangular girder section, therefore

decreasing the magnitude and moment arm of one of the VIV lock-in ranges, showing only one obvious VIV lock-in range for both modes.

For the streamlined girder section, the wind tunnel experiments show two VIV lock-in ranges for the vertical bending mode and one for the rotational mode. Utilizing the AI-based vortex tracking method, it is revealed that the vortex shedding frequency on the upwind side is approximately twice that on the downwind side. By inspection, when compared to the rectangular box girder section with wind noses, the upper half of the wind noses on the streamlined girder section has a steeper inclination, which led to vortexes with higher magnitude, thus causing the two VIV lock-in range to appear in the vertical bending mode. The wind noses reduce the influencing range of the vortexes and decreased the moment arm of the vortex mechanisms on the upwind side, showing only one obvious VIV lock-in range for the rotational mode.

3.3 Influence of the Reynolds number effect based on 1:20 model wind tunnel experiments

The 1:50 model wind tunnel experiments performed in the previous sections of this chapter provide a good indicator of the VIV performance for the streamlined girder section and some effective aerodynamic VIV mitigation measures. However, according to several studies [26] [128] [129], the Reynolds number effect that came along with scaled models and scaled experimental wind speeds in wind tunnel experiments cannot be overlooked. To explore the influence of the

Reynolds number effect, a 1:20 scaled model for the same streamlined box girder section is tested in wind tunnel experiments. The effectiveness of several aerodynamic measures is tested and discussed in this section as well.

3.3.1 1:20 Model design

The setup follows the Chinese Wind-resistant Design Specification for Highway Bridges. Several requirements that need to be met are listed below:

1. The model satisfies geometrical similarity (for scaled streamlined girder section models).
2. The model satisfies the consistency of elastic parameters $\frac{U}{f_h B}$, $\frac{U}{f_\alpha B}$, inertia parameters $\frac{m}{\rho B^2}$, $\frac{I_m}{\rho B^4}$, and damping parameters ξ_h, ξ_α.

where U is the wind speed, B is the girder width, f_h and f_α are the vertical vibration frequency and rotational frequency of the model, respectively, I_m is the mass moment of inertia per unit length of the model, ξ_h and ξ_α are the vertical and rotational damping ratios, respectively, and ρ is the air density.

3. The mass and mass moment of inertia of the bridge should be consistent with the equivalent mass and equivalent mass moment of inertia of the model.
4. Model width/height of the wind tunnel is smaller than 0.4.
5. Model length/model width is larger than 2.
6. The blocking rate of the wind tunnel is lower than 5%.

The model has a scaling factor of 1:20, and the mass and mass moment of inertia

requirements are met. The length of the model is 3900 mm, the width is 1576.6 mm, the height is 300.3 mm, wind tunnel height is 4 m. Therefore, the setup of the experiment satisfies the local code requirement. The design of the streamlined box girder section model can be seen in Figure 3-3-1:

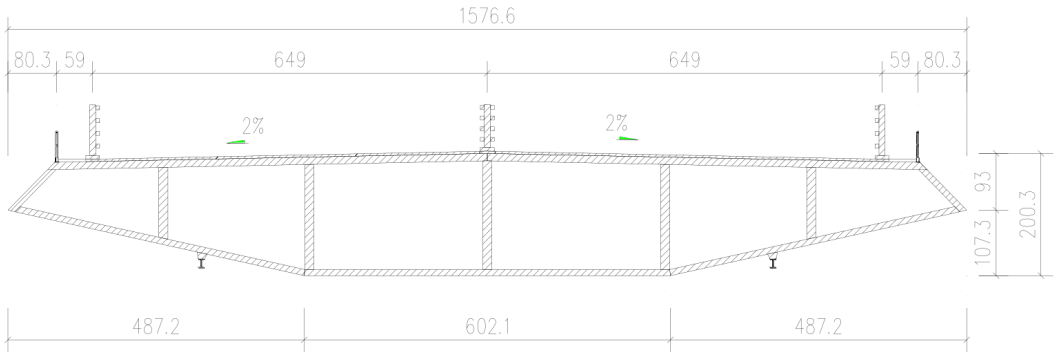

Figure 3-3-1: Girder section model design

The stiffness of the girder section model is provided by eight sets of springs carefully designed and installed in accordance with the dynamic characteristics analysis result. The manufacturing of the model includes the girder section, railings, pavements, and maintenance tracks.

The main girder section is made of timber boards with five longitudinal chords and nine struts. End boards are installed on both ends of the girder section for anchoring purposes. The inner structure and the external appearance of the girder section are shown in Figure 3-3-2 and Figure 3-3-3, respectively:

Figure 3-3-2: Internal structure of the girder section

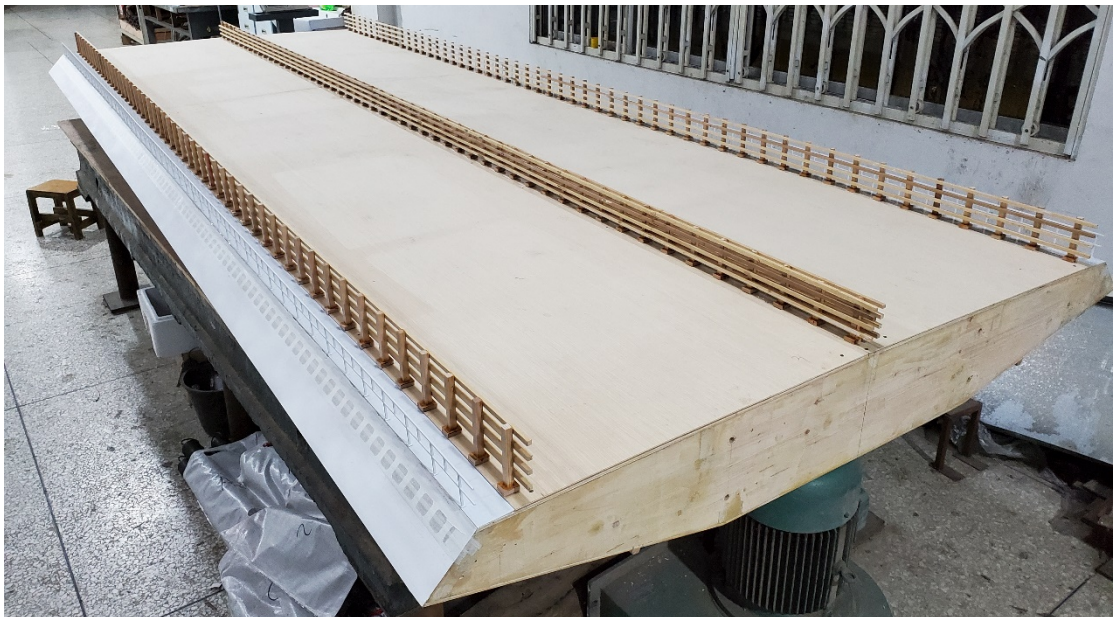

Figure 3-3-3: Exterior view of the girder section

The railings and pavements are made of timber and anchored to the girder section with nails and glue, and the maintenance tracks are made of ABS plastics, as shown in Figure 3-3-4 and Figure 3-3-5.

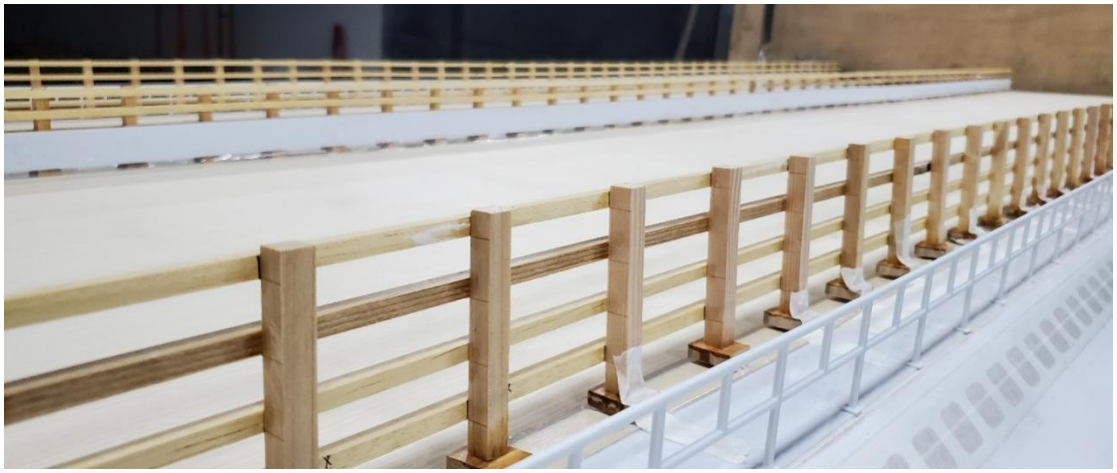

Figure 3-3-4: Close-up of railings and pavements

Figure 3-3-5: Maintenance tracks below the girder section

3.3.2 Experimental setup

3.3.2.1 Model installation and determination of frequency and damping ratio

The 1:20 girder section model wind tunnel experiment is conducted in the XNJD-3 industrial wind tunnel laboratory in Chengdu, China. The wind tunnel is equipped with a dedicated device for bridge girder section model aerodynamic experiments. The girder section is installed on

the device with eight carefully calibrated springs, forming a two-degree-of-freedom vibration system capable of moving vertically and rotating about its center line. The setup of the experiment is shown in Figure 3-3-6 and Figure 3-3-7.

Figure 3-3-6: 1:20 girder section experiment setup

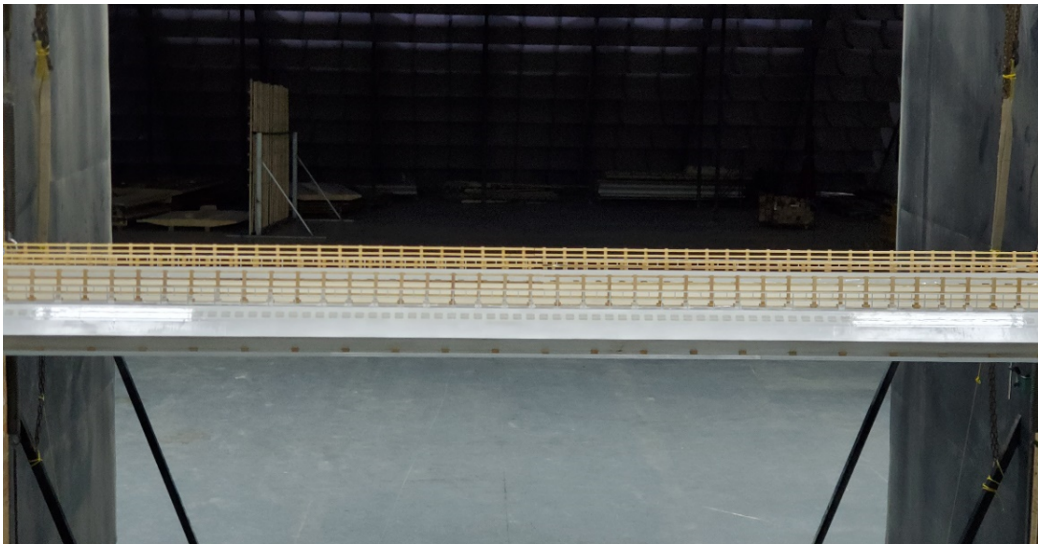

Figure 3-3-7: Close-up on the installed 1:20 girder section model

The movement of the girder section is recorded by two LASER transducers installed on the

upwind side and downwind side below the girder section, as shown in Figure 3-3-8 and Figure 3-3-9.

Figure 3-3-8: LASER transducer used in the experiment

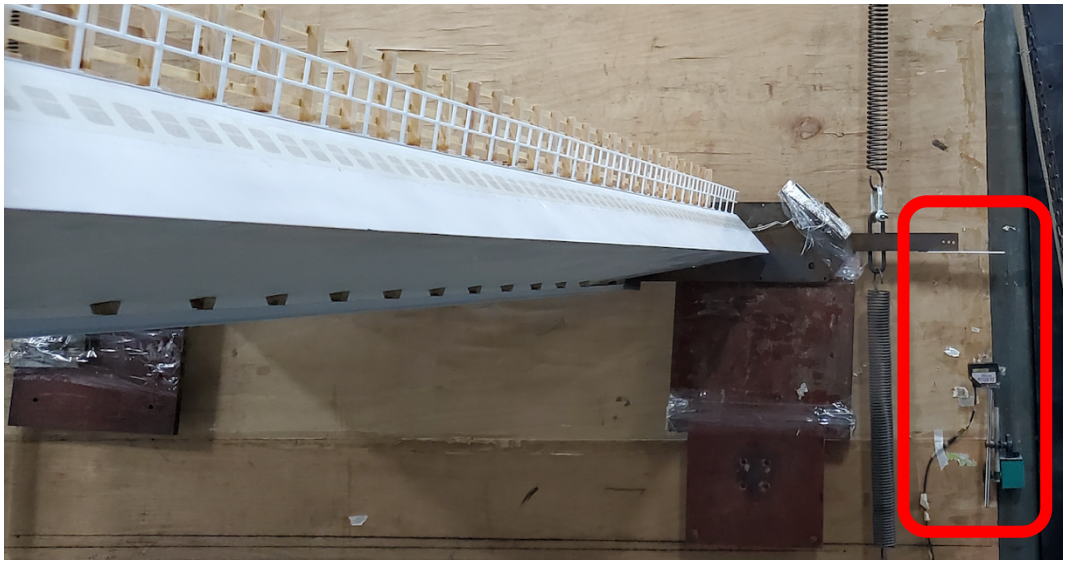

Figure 3-3-9: Location of LASER transducers

The vertical displacement of the model, V, is therefore calculated as follows:

$$V = (H1 + H2)/2 \quad \textbf{(Eq. 3-3-1)}$$

The rotational angle of the model, *R*, is calculated as follows:

$$R = (H1 - H2)/L \quad \textbf{(Eq. 3-3-2)}$$

where *H1* and *H2* are the displacement recordings from the two LASER transducers, and *L* is the distance between the transducers.

Structural vibration's frequency and damping ratio are achieved by calibrating the design stiffness of the springs and attaching friction rubber bands to the springs. The free vibration attenuation method determines each model's modal frequency and damping ratio, similar to the 1:50 girder section model experiment.

3.3.2.2 Model parameters used in the experiment

Several similarity requirements are met besides the geometric similarity according to the Chinese Wind-resistant Design Specification for Highway Bridges. They are:

a) Elastic parameters $\frac{U}{f_h B}$, $\frac{U}{f_\alpha B}$

b) inertia parameters $\frac{m}{\rho B^2}$, $\frac{I_m}{\rho B^4}$,

c) damping parameters ξ_h, ξ_α.

where *U* is the wind speed, *B* is the girder width, f_h and f_α are the vertical vibration frequency and rotational frequency of the model, respectively, I_m is the mass moment of inertia per unit length of the model, ξ_h and ξ_α are the vertical and rotational damping ratios, respectively, and ρ is the air density.

The geometric similarities of the girder and the railings are strictly satisfied. Mass and mass moment of inertia are determined with a proper scaling factor to the equivalent mass and the equivalent mass moment of inertia to ensure similarity to accurately simulate possible coupling effects on displacements on all degrees of freedom.

Table 3-3-1 compares the required values and the actual measured values of the model. Table 3-3-2 shows the frequency, damping ratio, and wind speed ratio of each mode of the model tested. The similarities are fully satisfied.

Table 3-3-1: Similarity comparison

Parameters	Sign	Unit	Scaling factor	Real bridge value	Model required value	Model value
Girder height	H	m	20	4.005	0.200	0.200
Girder width	B	m	20	31.50	1.575	1.575
Unit mass	m	kg/m	20^2	30565	76.413	76.413
Vertical bending mode f	f_v	Hz	—	0.1098	1.4531	1.4531
Rotational mode f	f_a	Hz	—	0.2485	2.2545	2.2813

Table 3-3-2: Modal parameters of the model tested

Mode	Frequency（Hz）	Damping ratio（%）	Wind speed ratio
1st order vertical bending	1.4531	0.07	1.511
1st order rotational	2.2813	0.03	2.179

3.3.2.3 Working states in the experiment

Working states tested in the 1:20 girder section experiment are listed in Table 3-3-3.

Table 3-3-3: Working states tested

Working states	Aerodynamic measures			Damping condition	Attack angle (°)
	Central board	Horizontal board	Side board		
CS1	——	——	——	Low damping	+3/+5
CS2	0.67 m	——	——	Low damping	+3
CS3	0.67/1.02 m	——	——	Low damping	+3
CS4	0.67 m	Step shaped	——	Low damping	+3
CS5	0.67 m	Triangle shaped	——	Low damping	+3
CS6	0.67/1.02 m	——	Gapped	Low damping	+3
CS7	0.67/1.02 m	——	Full length	Low damping	+3
CS8	0.67/1.02 m	——	Gapped	Low damping	+3
CS9	0.67/1.02 m	——	Full length	Low damping	+3
CS10	0.67/1.02 m	Step shaped	Gapped	Low damping	-3/0/+3/+5
CS11	——	——	——	Standard damping	+3

The specifications of the center/side stabilizing board and the horizontal stabilizing boards are listed below. It is notable that the dimensions of aerodynamic measures listed in Table 3-3-3 and in the rest of this section are unscaled, real-bridge dimensions.

Center stabilizing board: full-length 0.67 m stabilizing board and alternating height stabilizing board (0.67 m and 1.02 m with sectional length of 6 m) are used on the center barrier.

Side stabilizing board: full-length 1.02 m stabilizing board is used on side barriers.

Horizontal stabilizing board: Step-shaped and zigzagging boards are used, the width of the step-sized board has a width of 0 m, 0.25 m, 0.5 m, 0.75 m, and 1 m, and the zigzagging boards constitutes triangles with a base of 6 m and height of 1 m.

The boards installed are shown in Figure 3-3-10, Figure 3-3-11, and Figure 3-3-12.

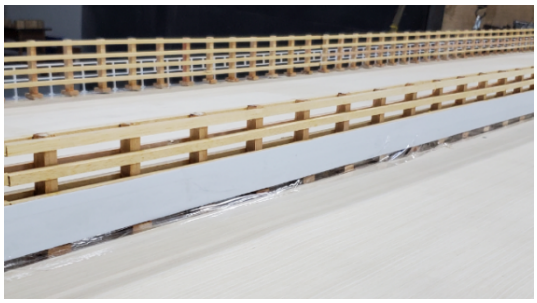

(a) 0.67m central board

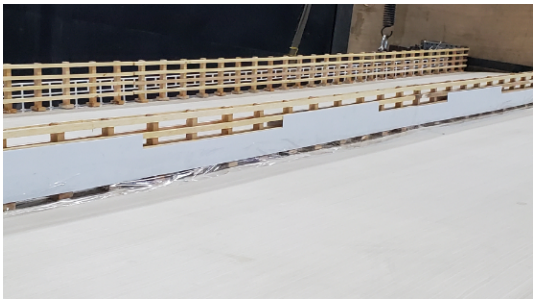

(b) 0.67/1.02m central board

Figure 3-3-10: Central stabilizing boards tested

(a) Step-shaped horizontal board

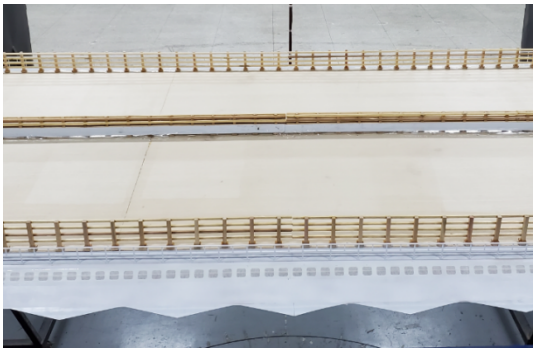

(b) Triangle-shaped horizontal board

Figure 3-3-11: Horizontal stabilizing board tested

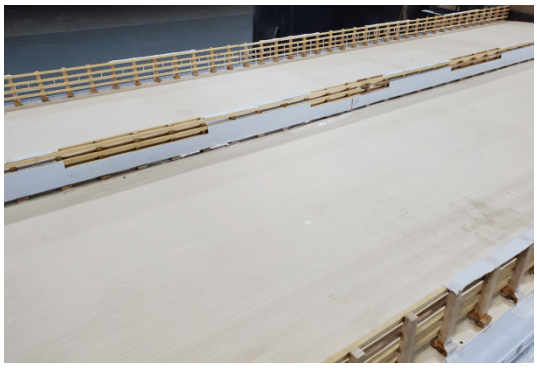

(a) Gapped sideboard (bottom right)

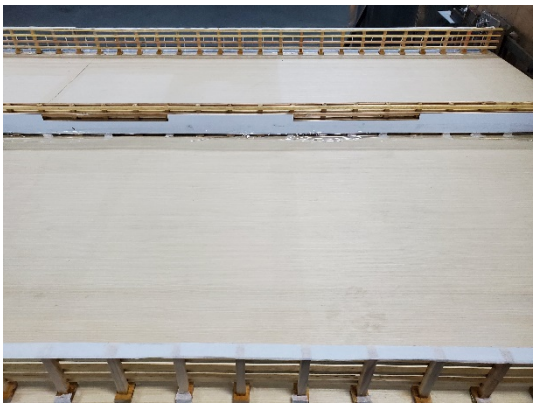

(b) Full-length sideboard (bottom)

Figure 3-3-12: Side board tested

3.3.3 Experimental results

The experiment is conducted in a uniform wind environment. The wind speed ranges from 0-10.2 m/s (corresponding wind speed is 0-15.4 m/s for vertical bending mode and 0-22.2 m/s for rotational mode). The wind speed step size is 0.01-0.5 m/s (corresponding step size is 0.02-1 m/s for vertical bending mode and 0.02-1.5 m/s for rotational bending mode). The maximum vertical bending displacement and rotational mode rotation of working states CS1-CS11 are summarized in Table 3-3-4.

a) For working state CS1, at 3° and 5° attack angle and under low damping conditions, in the wind speed range of 0-15 m/s, there is no obvious vertical bending displacement. In the 6.84-8.17 m/s wind speed range, obvious rotation is observed. The maximum rotation for 3° attack angle is 0.168°.

b) For working states CS2-CS7, at 3° attack angle and under low damping conditions, no obvious vertical bending displacement is observed. In the wind speed range of 6.84-8.17 m/s, rotational displacement is observed in all working states.

c) For working states CS8-CS10, at 3° attack angle and under low damping conditions, no visible vertical bending and rotational displacement is observed. In working state CS10, no visible vertical bending and rotational displacement are observed for all attack angles tested.

d) For working state CS11, at 3° attack angle and under standard damping conditions, no obvious vertical bending and rotational displacement is observed.

Table 3-3-4: Maximum VIV response of each working state

Working state	Aerodynamic measures			Vertical bending (mm)	Rotation (°)
	Central board	Horizontal board	Side board		
CS1	——	——	——	4.17	0.168
CS2	0.67 m	——	——	3.19	0.114
CS3	0.67/1.02 m	——	——	3.78	0.029
CS4	0.67 m	Step shaped	——	2.95	0.060
CS5	0.67 m	Triangle shaped	——	3.30	0.076
CS6	0.67/1.02 m	——	Gapped	3.08	0.018
CS7	0.67/1.02 m	——	Full length	11.78	0.011
CS8	0.67/1.02 m	——	Gapped	3.04	0.009
CS9	0.67/1.02 m	——	Full length	4.00	0.007
CS10	0.67/1.02 m	Step shaped	Gapped	3.35	0.008
CS11	——	——	——	3.14	0.006

3.3.4 Aerodynamic measures on 1:20 girder section model wind tunnel experiment

The dynamic responses of the 1:20 girder section model wind experiment of various aerodynamic measures are shown in Table 3-3-4. Comparing the response of the center stabilizing board, the horizontal stabilizing board, and the side stabilizing boards, the effectiveness of the aerodynamic measures and damping conditions are discussed in the following section.

3.3.4.1 VIV response of the original girder section

The girder section experiences small vertical bending and rotational mode displacement. The maximum vertical bending mode displacement is 4.17 mm, and the maximum rotational mode displacement is 0.168°.

3.3.4.2 Effect of center stabilizing board

Based on the VIV dynamic response of working states CS1-CS3, it is seen that the center stabilizing boards tested (0.67 m full length, 0.67/1.02 m varying height) have little effect on the vertical bending VIV displacements but can be effective for rotational VIV displacement. In working state CS3, the 0.67/1.02 m varying height center stabilizing board is the most effective, reducing the VIV response of the original girder section from 0.168° to 0.029°.

3.3.4.3 Effect of horizontal stabilizing board

Based on the VIV dynamic response of working states CS2, CS4, and CS5, it is seen that the horizontal stabilizing boards tested (step-shaped, zigzagging) have little effect on the vertical bending VIV displacements but are effective for rotational VIV displacement. In the working state CS4, the addition of step-shaped horizontal stabilizing board lowered the rotational response of CS2 from 0.114° to 0.060°.

3.3.4.4 Effect of side stabilizing board

Based on the VIV dynamic response of working states CS3 and CS6-C9, it can be seen that the side stabilizing board casts a negative impact on the mitigation of VIV on the girder section. In CS7, the vertical bending displacement is increased from 11.78 mm to 3.78 mm in the original girder section working state, and rotational displacement is not increased. The full-height sideboard has little effect on vertical bending VIV displacement but effectively reduces rotational VIV displacement. In CS9, the rotation is reduced to 0.007° from 0.029° in the original girder section working state.

3.3.4.5 Summary of effect of aerodynamic measures

This section tests central stabilizing boards, horizontal stabilizing boards, and side stabilizing boards for their effectiveness in mitigating vertical bending and rotational VIV response for the streamlined girder.

For the central stabilizing board, **working state CS3 (**0.67/1.02m varying height center stabilizing board) is the most effective, reducing the VIV response of the original girder section from 0.168° to 0.029°. For the horizontal stabilizing board, **working state CS4** (0.67 m central stabilizing board with the addition of step-shaped horizontal stabilizing board) lowers the rotational response of CS2 from 0.114° to 0.060°. For the side stabilizing board, **working state CS9** (0.67/1.02 m central board with the addition of full height sideboard) reduces the rotational to 0.007° from 0.029° in CS3 working state.

3.3.5 The Reynolds number effect

The result of VIV responses tested for the 1:20 girder section model varies significantly from the VIV responses tested for the 1:50 girder section model in the previous sections in terms of displacement magnitude for both the vertical bending mode and rotational mode. In the 1:50 model, the original girder sections experience two vertical bending mode lock-in ranges and one rotational mode lock-in range with amplitudes of 276 mm, 348 mm, and 1.00°, respectively. In the 1:20 model, the original girder sections experience small amplitude for both vertical bending and rotational modes, with amplitudes of 4.17 mm and 0.168°. This difference can be potentially attributed to the Reynolds number effect.

3.3.5.1 Definition and the research status quo of the Reynold number effect

The Reynolds number is a dimensionless quantity used in fluid mechanics to describe the flow of a fluid and is defined as the ratio of inertial forces to viscous forces within a fluid, calculated as shown in Eq. 3-3-3.

$$Re = \frac{\rho \cdot u \cdot D}{v} \quad \textbf{(Eq. 3-3-3)}$$

where ρ is the density of the fluid, u is the velocity of the fluid relative to the surface, D is the height of the girder, and v is the fluid's dynamic viscosity.

The Reynolds number is used to determine the type of flow of a fluid, which can be laminar or turbulent. The flow is laminar when the Reynolds number is below a critical value, and the fluid moves in smooth layers. However, when the Reynolds number exceeds the critical value, the flow

becomes turbulent, characterized by chaotic and random motion of fluid particles.

When conducting wind tunnel experiments for girder sections in this research, several similarities are considered, including geometric, kinematic, and dynamic similarities. Not all parameters in these similarities can be fully satisfied simultaneously. One notable conflict is between the Reynolds number (Re) and the Froude number (Fr).

The Froude number is defined as the ratio of the inertial forces to the gravitational forces acting on a fluid and is used to classify the type of flow, such as whether it is subcritical or supercritical, as shown in Eq. 3-3-4.

$$Fr = \frac{u^2}{g \cdot B} \quad \textbf{(Eq. 3-3-4)}$$

where u is the velocity of the fluid, g is the gravity acceleration, and B is the width of the girder section.

When the girder sections of different scaling factors are tested in wind tunnel experiments, their respective wind speed ranges must also be scaled properly. To satisfy the Froude number, the wind speed range should increase as the dimension of the section increases. However, to satisfy the Reynolds number, the wind speed range should decrease as the dimension of the section increases. As some other similarities requirements (such as the kinematic similarity) also require wind speed range to increase as the dimension of the section increases, combined with the limitation of wind speed capabilities of wind tunnel laboratories, the Reynolds number is chosen to be unsatisfied to yield for the satisfaction of other similarity requirements.

During the construction phase of the Storebelt Suspension Bridge, which was opened to traffic in Denmark in 1998, VIVs were observed with frequencies and amplitudes that were inconsistent with predictions based on wind tunnel experiment results [130]. On this incident, Larsen et al. [131] concluded that the Reynolds number effect on the Strouhal number of the girder caused the inconsistency, and Schewe et al. [36] stated that the different rear-end vortex structures caused by the Reynolds number effect is the cause.

Scholars have since done extensive research on the Reynolds number effect on other bridges. In some research, the same aerodynamic components exert different effects for girder sections tested under different Reynolds numbers. Larose et al. [129] compared the effect of the spoiler effect on the girder section model of the Stonecutters Bridge in Hongkong with different scaling factors and found that the spoiler would decrease VIV amplitude in high Reynolds number conditions but increase VIV amplitude in low Reynolds number condition. Zhang et al. [128] found that spoilers have the same effect on the Xihoumen Bridge under certain attack angles.

The scaled VIV amplitudes under different Reynolds number conditions differ significantly in other research. Li et al. [132] observed from a wind tunnel experiment on the Xihoumen Bridge that the higher the Reynolds number, the lower the VIV lock-in range wind speed the lower the VIV amplitude. Cui et al. [133] found that for a streamlined box girder section, the VIV lock-in range wind speed and the amplitude for the high Reynold number condition are lower than that of the low Reynolds number condition. In comparison, Li et al. [134] discovered that for a specific streamlined girder section, the VIV amplitude is higher for the high Reynolds number condition

than the low Reynolds number condition.

As seen above, the Reynolds number effect is a complicated problem and can differ significantly for different girder sections. The conclusions of related research show little consistency for VIV lock-in range wind speeds and VIV amplitudes, among others. For the two geometrically similar streamlined girder section models with 1:50 and 1:20 scaling factors tested in this research, the influence of the Reynolds number effect is discussed in the following section.

3.3.5.2 VIV responses under different Reynolds number conditions

The detailed scaling parameters of the 1:50 and the 1:20 streamlined girder sections are summarized in Table 3-3-5.

Table 3-3-5: Scaling parameters of the two sections

Parameters	1:50 streamlined girder section	1:20 streamlined girder section
Scaling factor	50	20
Width/Height (m)	0.63/0.0801	1.575/0.20
Unit mass (kg/m)	12.23	76.413
Unit mass moment of inertia (kg·m2/m)	1.081	31.002
Vertical bending mode/Rotational mode frequencies (Hz)	1.88/4.94	1.453/2.281
Damping ratio Vertical/Rotation (%)	0.2/0.05	0.07/0.03

The wind tunnel experiment wind speed range for the original 1:50 streamlined girder section is 0.7-5.59 m/s. Based on the girder height, the Reynolds number range is 3.996×10^3–3.191×10^4 (Low Reynolds number condition). The wind speed range for the original 1:20 section

is 2.0-10.02 m/s, and the respective Reynolds number based on the girder height is 2.851×10^4-1.428×10^5 (High Reynolds number condition). The VIV response of vertical bending and rotational mode for both the low and high Reynolds number condition at the most critical +3° attack angle is shown in Figure 3-3-13.

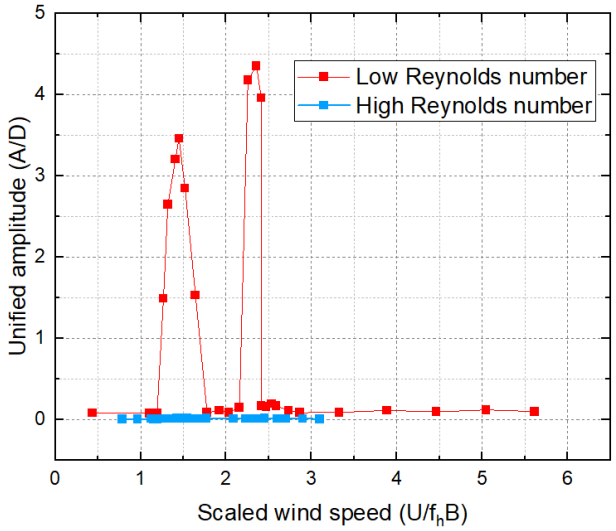

(a) Vertical bending mode

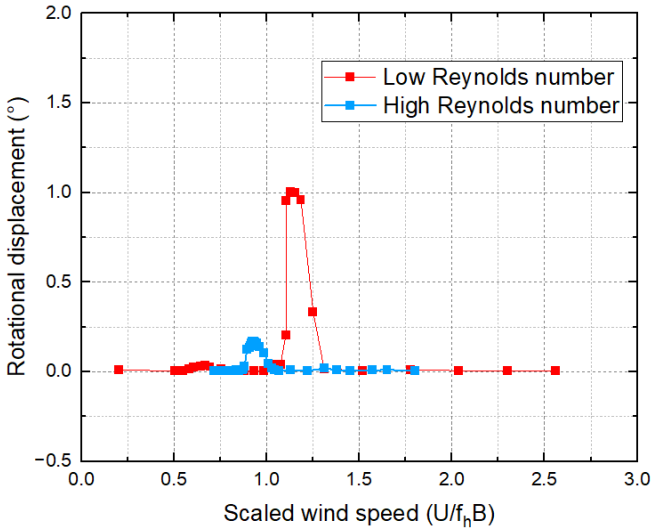

(b) Rotational mode

Figure 3-3-13: Comparison of VIV responses at different Reynolds number conditions

In Figure 3-13, the horizontal axis is the scaled wind speed, calculated as follows to compare the VIV lock-in wind speed range and VIV amplitude.

$$Scaled\ wind\ speed = \frac{U}{f_h \cdot B} \quad \textbf{(Eq. 3-3-5)}$$

where U is the wind speed, f_h is the vertical frequency, and B is the width of the girder. The vertical axis for Figure 3-3-13 (a) is the unified amplitude, calculated as follows.

$$Unified\ amplitude = \frac{A}{D} \quad \textbf{(Eq. 3-3-6)}$$

where A is the amplitude, and D is the height of the girder.

As seen in Figure 3-3-13, the result of VIV responses for both the low Reynolds number condition and the high Reynolds number condition differ significantly in terms of numbers of VIV lock-in ranges, unified vertical bending amplitude, and rotational amplitude under the most critical +3° attack angle. For the girder section under the high Reynolds number condition, there each exists one VIV lock-in range for vertical bending and rotational mode, while for the girder section under the low Reynolds number condition, there exist two vertical bending lock-in ranges and one rotational lock-in range. Under high Reynolds number condition, the girder section experiences a small vertical unified amplitude of 0.02, and the maximum rotational mode displacement is 0.168°. Under low Reynolds number condition, the girder section experiences maximum vertical unified amplitude of 3.44 and 4.34 and a maximum rotational displacement of 1.00°.

The results from the above comparisons indicate that, when compared to that under the high Reynolds number condition, the girder section under the low Reynolds number condition is

more critical as it experiences more VIV lock-in ranges and higher unified amplitude in both modes considered. This conclusion aligns with the conclusions drawn in the research by Li et al. [132] and Cui et al. [133].

3.4 Chapter Summary

This chapter focuses on exploring the initiation mechanism of VIV for a streamlined girder section and its VIV performance with various aerodynamic VIV mitigation measures installed. A 1:50 streamlined girder section model with aerodynamic measures installed is first tested in wind tunnel experiments for their dynamic VIV responses and effectiveness of aerodynamic measures and then simulated in CFD analyses to monitor the flow filed characteristics around the girders to explore the VIV mechanisms of the girder section. To evaluate the influence of the Reynolds number effect for wind tunnel experiments with different scaling factors, a 1:20 streamlined girder section model is tested in wind tunnel experiments.

The original section is tested in the 1:50 streamlined girder section wind tunnel experiments, and two vertical bending VIV lock-in ranges and one rotational mode VIV lock-in range are observed. The streamlined girder section is then tested with various aerodynamic VIV mitigation measures installed, among which the 0.67 m central stabilizing board and the 1.35 m horizontal stabilizing board are the most effective. When the two measures are installed as a combination on the streamlined girder section, the VIV response of vertical bending and rotational modes are

effectively reduced.

Since the flow field is more complex for streamlined girder sections when compared to the flow fields around the rectangular girder sections with or without wind noses discussed in the previous chapter, especially when aerodynamic measures and accessory non-structural components are installed, a visual vortex recognition and tracking method based on Convolutional Neural Network (CNN) and machine learning (YOLOv5/DeepSORT) is utilized in this chapter. The method uses weight files obtained from two separate machine learning processes that contain the spatial and temporal features of vortexes to recognize and track the development of vortexes. The initial spatial feature weight file is optimized in accordance with the visual characteristics of the vortexes to increase recognition machine learning efficiency. The tracking process is capable of tracking the merging processes of vortexes as it utilizes the Kalman filter and the Hungarian Algorithm.

CFD analyses revealed different frequencies of total lift force and rotational moment on the girder. Utilizing the AI-based vortex tracking method, it is revealed that the vortex shedding frequency on the upwind side is approximately twice that on the downwind side. By inspection, when compared to the rectangular box girder section with wind noses, the upper half of the wind noses on the streamlined girder section has a steeper inclination, which led to vortexes with higher magnitude, thus causing the two VIV lock-in range to appear in the vertical bending mode. The wind noses appear to have reduced the influencing range of the vortexes and decreased the moment arm of the vortex mechanisms on the upwind side, showing only one obvious VIV lock-in range

for the rotational mode.

The influence of different Reynolds number conditions in wind tunnel experiments is discussed by comparing the results from the 1:50 and the 1:20 streamlined girder section wind tunnel experiments. It is found that when compared to that under the high Reynolds number condition, the girder section under the low Reynolds number condition is more critical as it experiences more VIV lock-in ranges and higher unified amplitude in both modes considered.

Chapter 4 Comfort level on bridges with VIV

This chapter focuses on exploring the comfort level of drivers and passengers in a vehicle traveling on long-span suspension bridges under VIV. A methodology for determining the allowable magnitude of VIV of suspension bridges based on vibration serviceability of the human body via wind-traffic-bridge (WTB) analysis is proposed. The proposed methodology first establishes a numerical model for WTB coupled vibration analysis when the VIV event of long-span bridges occurs, then evaluates the human comfort of vehicle drivers and workers via two indices, i.e., the overall vibration total value (OVTV) and motion sickness incidence (MSI) as recommended by ISO 2631. The proposed methodology is applied to the 1760 m prototypical long-span suspension bridge for validation, and the comfort level of drivers and passengers traveling on the bridge under VIV based on MSI is presented and discussed.

4.1 Wind-traffic-bridge coupled analysis

4.1.1 Modeling of vortex-induced vibration

4.1.1.1 Equation of motion under VIV

The equation of motion for the wind-traffic-bridge system under the VIV condition is expressed as follows.

$$\mathrm{M}_b\ddot{\mathrm{u}}_b + \mathrm{C}_b\dot{\mathrm{u}}_b + \mathrm{K}_b\mathrm{u}_b = \mathrm{F}_{wb} + \mathrm{F}_{vb} \quad \textbf{(Eq. 4-1-1)}$$

$$\mathrm{M}_v\ddot{\mathrm{u}}_v + \mathrm{C}_v\dot{\mathrm{u}}_v + \mathrm{K}_v\mathrm{u}_v = \mathrm{F}_{wv} + \mathrm{F}_{bv} \quad \textbf{(Eq. 4-1-2)}$$

where M, C, and K represent the mass matrix, the damping matrix, and the stiffness matrix of the system, $\ddot{u}_0$ $\dot{u}_0$, and u_0 denote vectors of acceleration, velocity, and displacement, F_{vb} and F_{bv} represent the force between the vehicle and bridge, F_{wv} is the wind load on vehicles, and F_{wb} is a function of VIF from the bridge girder. Subscripts b, v, and w denote bridge, vehicle, and wind load, respectively.

The equation of motion shown in Eq. 4-1-1 and Eq. 4-1-2 are calculated separately in each time step and iterated based on the equilibrium of the two equations.

The body, axles, and wheels of a vehicle are treated as components of a rigid body system connected by springs and dampers to form a mass-spring-damper model. The FEM model of the bridge in the system models the towers, the girder, and the bridge's pier as beam elements and the main cables and hangers as spatial bar elements.

4.1.1.2 VIF model

The VIF model adopted in this chapter is the simple harmonic oscillator model (SHM), which denotes the wind load on the bridge under nth order VIV, $\boldsymbol{F}_{wb}$, as follows:

$$\mathbf{F}_{wb} = \int_0^L \varphi_n(x) \cdot P(t) \cdot dx \qquad \textbf{(Eq. 4-1-3)}$$

where $\varphi_n(x)$ is the mode shape for the nth order vibration; L is the bridge span; $P(t)$ is the SHM VIF input, which can be calculated as follows.

$$P(t) = \frac{1}{2} \cdot \rho \cdot U^2 \cdot D \cdot \tilde{C}_L \cdot \sin\left(\omega_n \cdot t + \theta\right) = a \cdot \sin\left(\omega_n \cdot t + \theta\right) \qquad \textbf{(Eq. 4-1-4)}$$

where ρ is the air density, U is the incoming wind speed, D is the characteristic width of the girder,

$\tilde{C}_L$ is the lift force coefficient, ω_n is the modal frequency, θ is the phase angle. The coefficient a can be calculated using the following equation.

$$a = \frac{A_1}{A_0} \quad \textbf{(Eq. 4-1-5)}$$

where A_1 is the measured vertical displacement of the girder, and A_0 is the numerically calculated vertical displacement under unit VIF input.

A_0 is calculated as follows: input A_1 and ω_n into Eq. 4-1-4 by assuming $a=1$ *and* $\theta=0$ for a new unit VIF input, $P(t)$, then input the newly calculated $P(t)$ into Eq. 4-1-3 and Eq. 4-1-1 to calculate the bridge dynamic response under unit VIF input, which yields the value of A_0. The value of A_0 is then used to calculate coefficient a in Eq. 4-1-5.

4.1.2 Wind-traffic-bridge coupled modeling

4.1.2.1 Conditions considered in the analysis

To analyze the wind-traffic-bridge coupled effects under VIV, three different vehicle travel conditions are considered: single vehicle travels on the stable road surface, single vehicle travels on stable bridge, and single vehicle travels on bridge with VIV (2nd order anti-symmetric vertical bending mode, with amplitude of 0.5 m and frequency of 0.166 Hz). All vehicles are traveling at a speed of 40 km/h. For each of the three vehicle travel conditions, three road surface conditions are compared: R0 condition (perfect smooth surface), R1 (ideal roughness), and R2 (sub-grade roughness).

4.1.2.2 Coupled vibration analysis in windless environment

The coupled effects of wind-traffic-bridge under a windless environment are analyzed with the vehicle travel and road surface conditions mentioned in the previous section.

For a vehicle that travels on three different road surface conditions (R0, R1, and R2) under three different travel conditions (stable road, stable bridge, bridge under VIV), the vehicle's dynamic response, such as its vertical acceleration, vertical velocity, and vertical displacement at different locations of the bridge are measured. The measured dynamic response data can be used for analyzing the comfort level of the driver and passengers in the vehicle by monitoring the magnitude and RMS of acceleration data, predominant frequencies of acceleration and displacement data, etc.

4.1.2.3 Coupled vibration analysis in wind environment

In this section, horizontal wind flowing around the bridge girder with various velocities is added to the research to achieve a more realistic modeling in the WTB analysis.

To discuss the effect of wind under the research framework established in this chapter, the RMS of accelerations at the center of gravity of a vehicle traveling at a speed of 40 km/h on the different axes is analyzed with different road surface conditions (R0, R1, R2) and travel conditions (stable road, stable bridge, bridge under VIV) under wind with velocities of 5 m/s, 10 m/s, and 15 m/s. With the addition of the wind flowing in the horizontal direction, transverse acceleration of the vehicle becomes more predominant, and its effect on comfort level is discussed with different

wind speeds, road surfaces, and vehicle travel conditions as well.

4.1.3 Dynamic response of vehicles on a prototypical long-span suspension bridge

4.1.3.1 Case setup of the prototypical bridge

This part of the research lays its background on the same prototypical long-span suspension bridge with a main span of 1760 m, which is currently under construction, as introduced in Chapter 2. The FEM model used is the one used for dynamic characteristics analysis of the prototypical bridge, it models the girder, tower, and piers as spatial beam elements, and the main cables and hangers as spatial bar elements.

As mentioned in the previous section, the comfort level analysis is performed under several road surfaces and vehicle travel conditions. The road surface conditions describe the road surface roughness level on which the vehicle travels. The R0 condition provides a perfectly smooth road surface with zero road surface roughness, the R1 condition represents ideal road roughness, and the R2 condition gives less-than-ideal (sub-grade) road roughness. The three different roughness condition of the road surface yields different vertical accelerations, velocities, and displacements to the vehicle traveling on the road.

The travel conditions describe how stable the vehicle travels on the road. It includes three different conditions. The first condition is a stable road, where no movement occurs when the vehicle travels on top of it. The second condition is a stable bridge road where no externally induced movement is present, but the bridge road is free to vibrate due to vehicle weight and

movements. The third condition is a bridge road where a VIV vibration of 2nd order anti-symmetric mode with a frequency of 0.166 Hz and an amplitude of 0.5 m is present.

The vehicle is a passenger car traveling at 40 km/h for all road surfaces and travel conditions. The analysis is first performed in a windless condition, then under wind speeds of 5 m/s, 10 m/s, and 15 m/s for comparison purposes.

4.1.3.2 Time history

4.1.3.2.1 R0 road surface condition

When the vehicle travels on the R0 road surface condition, i.e., perfectly smooth road surface, its vertical acceleration under three different travel conditions (stable road, stable bridge road, and bridge road with VIV) is monitored and shown in Figure 4-1-1.

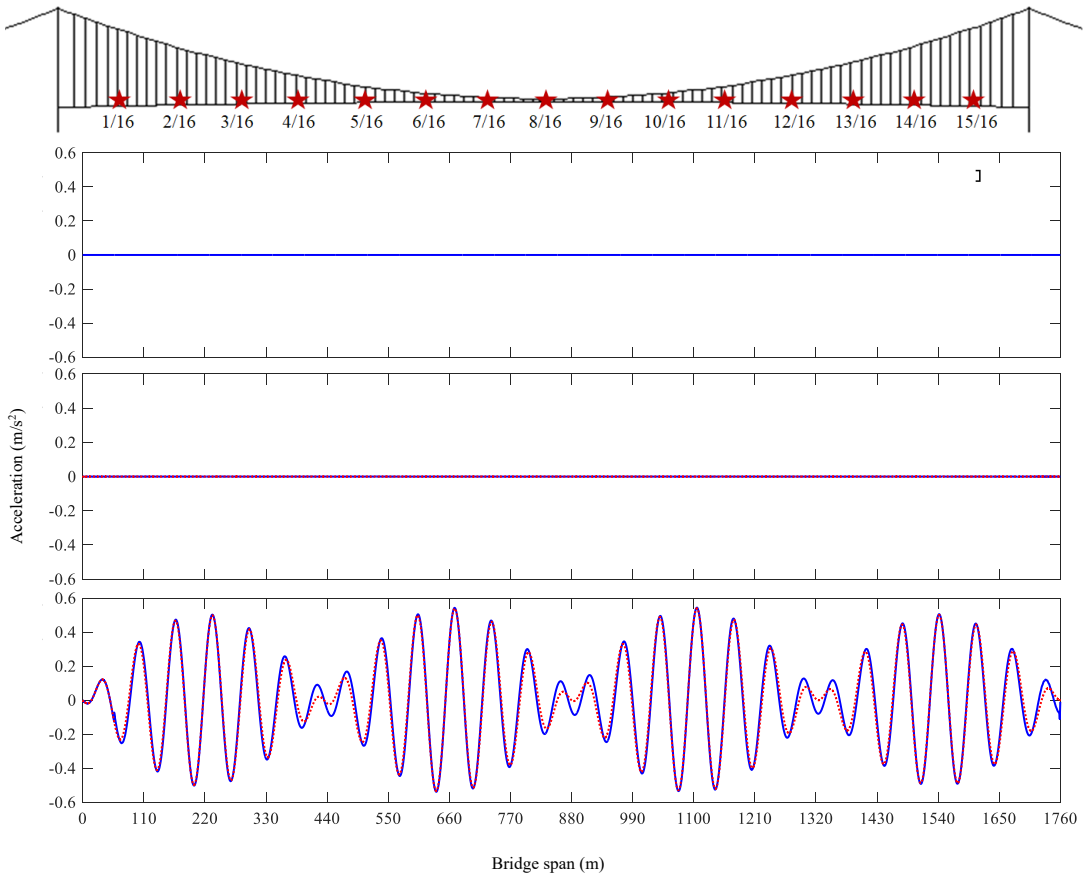

Figure 4-1-1: R0 road surface condition acceleration under different travel conditions

In Figure 4-1-1, the acceleration experienced by the vehicle is marked in blue and the acceleration of the bridge at the vehicle contact point is marked in red. As seen in Figure 4-1-1, when traveling on R0 road surface conditions, the vehicle experienced no vibration on a stable road. Its vibration on a stable bridge road is also small (magnitude is 0.0019 m/s^2). For a bridge road with VIV, the vertical acceleration can be as high as 0.5443 m/s^2, and the acceleration time history is very similar to the acceleration time history of the bridge girder at the same locations. The result indicates that when the vehicle is traveling on the R0 road surface condition, the vertical movement of the bridge girder is the sole source of vehicle vibration, and the vertical acceleration

of the girder at the location where it makes contact with the vehicle is a good indicator of the acceleration experienced by the vehicle.

4.1.3.2.2 R1 road surface condition

When the vehicle travels on the R1 road surface, i.e., the ideal road surface, its vertical acceleration under three different travel conditions (stable road, stable bridge road, and bridge road with VIV) is monitored and shown in Figure 4-1-2.

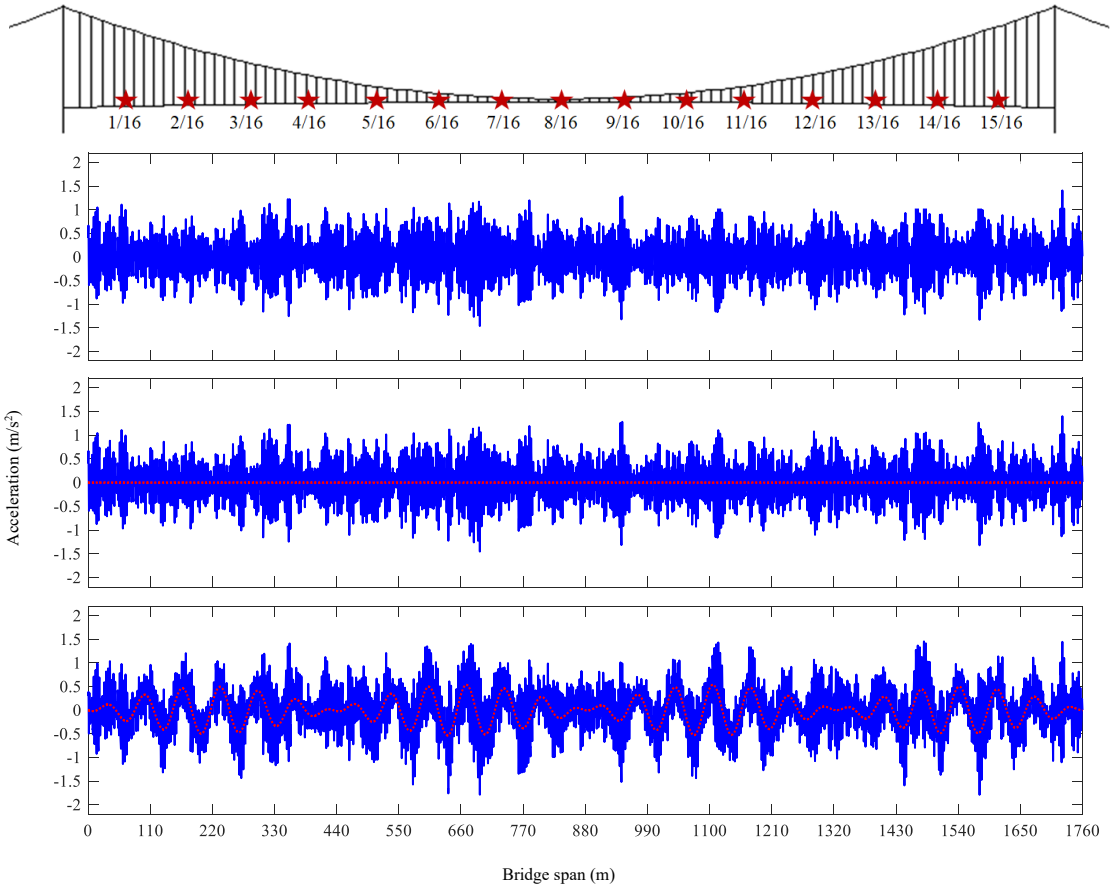

Figure 4-1-2: R1 road surface condition acceleration under different travel conditions

As calculated and shown in Figure 4-1-2, the maximum vertical accelerations (RMS value) of three different travel conditions are 1.3093 m/s^2 (0.3901), 1.3986 m/s^2 (0.3990), and 1.4568 m/s^2

(0.4793). The road surface roughness caused an increase in vertical acceleration experienced by the vehicle. By comparing the acceleration time histories of stable road and stable bridge road cases, it is found that the vertical acceleration (RMS value) of the stable bridge is higher than that of the stable road by 6.8% (2.3%), which is caused by the coupling effect of bridge girder and vehicle. When comparing the acceleration time histories of the stable bridge road and bridge road with VIV, it is seen that the vertical acceleration (RMS value) of the bridge road with VIV is higher than that of the stable bridge road by 4.2% (20.1%).

The result indicates that the road surface roughness, the bridge-vehicle coupling effect, and the VIV of the bridge girder would increase the vertical acceleration experienced by the vehicle.

4.1.3.2.3 R2 road surface condition

When the vehicle travels on the R2 road surface condition, i.e., less than ideal road surface, its vertical acceleration under three different travel conditions (stable road, stable bridge road, and bridge road with VIV) is monitored and shown in Figure 4-1-3.

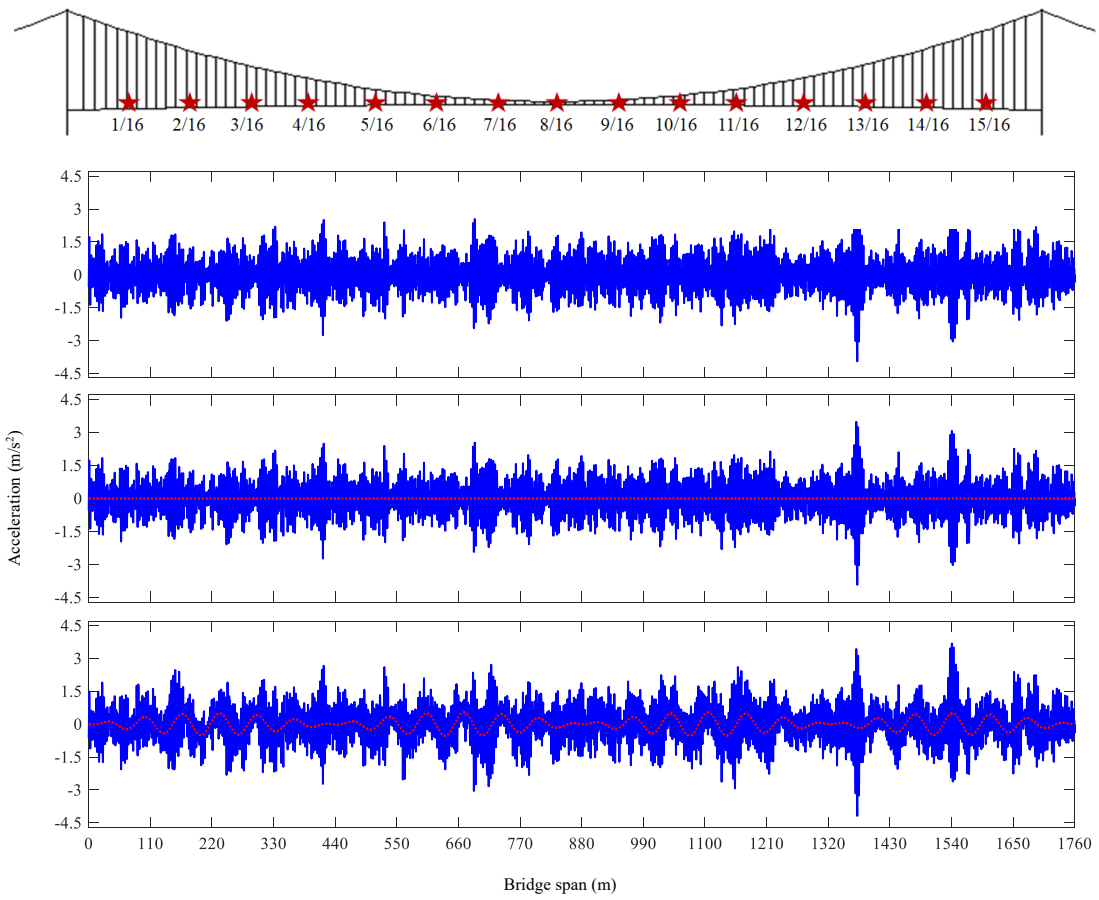

Figure 4-1-3: R2 road surface condition acceleration under different travel conditions

As seen in Figure 4-1-3, where the R2 road surface condition is applied, the maximum vertical accelerations (RMS value) of three different travel conditions are 3.2683 m/s^2 (0.7710), 3.4800 m/s^2 (0.7731), and 3.6812 m/s^2 (0.8439). The worst road surface condition (R2) further increased the vertical acceleration experienced by the vehicle. By comparing the acceleration time histories of stable road and stable bridge road cases, it is found that the vertical acceleration (RMS value) of the stable bridge is higher than that of the stable road by 6.5% (0.3%), which is caused by the coupling effect of bridge girder and vehicle. When comparing the acceleration time histories of the stable bridge road and bridge road with VIV, it is seen that the vertical acceleration (RMS

value) of the bridge road with VIV is higher than that of the stable bridge road by 5.8% (9.2%).

The result further verified the observation made in the previous section where the road surface roughness, the bridge-vehicle coupling effect, and the VIV of the girder would increase the vertical acceleration experienced by the vehicle. The maximum accelerations and their RMS values of different conditions are summarized in Table 4-1-1 and Table 4-1-2.

Table 4-1-1: Peak value of acceleration

Road condition	Vehicle acceleration (m/s^2)			Bridge-vehicle contact point acceleration (m/s^2)			Bridge peak acceleration (m/s^2)		
	R0	R1	R2	R0	R1	R2	R0	R1	R2
Stable road	0.0000	1.3093	3.2683	\	\	\	\	\	\
Stable bridge	0.0019	1.3986	3.4800	0.0029	0.0039	0.0083	\	\	\
VIV bridge	0.5443	1.4568	3.6812	0.5399	0.5404	0.5403	0.5399	0.5404	0.5403

Table 4-1-2: RMS of acceleration

Road condition	Vehicle acceleration (m/s^2)			Bridge-vehicle contact point acceleration (m/s^2)			Bridge peak acceleration (m/s^2)		
	R0	R1	R2	R0	R1	R2	R0	R1	R2
Stable road	0.0000	0.3901	0.7710	\	\	\	\	\	\
Stable bridge	0.0003	0.3990	0.7731	0.0001	0.0009	0.0017	\	\	\
VIV bridge	0.2676	0.4793	0.8439	0.2623	0.2623	0.2624	0.2623	0.2623	0.2624

4.1.3.3 Frequency analysis

The frequencies of acceleration experienced by the vehicle when it travels on different road

surface conditions and travel conditions are analyzed. For R0 condition with stable road condition, there is no vibration. For a stable bridge and bridge with VIV conditions of the same road surface (R0 condition), the frequency distribution of power spectrum density (PSD) for acceleration and displacement experienced by the vehicle and girder at its contact locations with the vehicle are shown in Figure 4-1-4 and Figure 4-1-5.

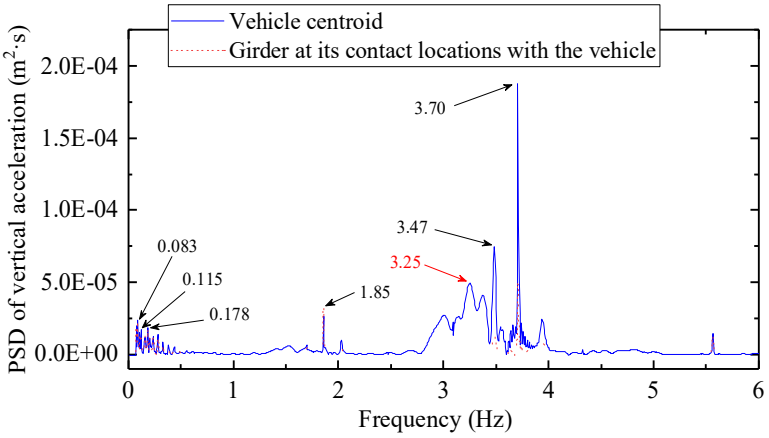

(a) Acceleration

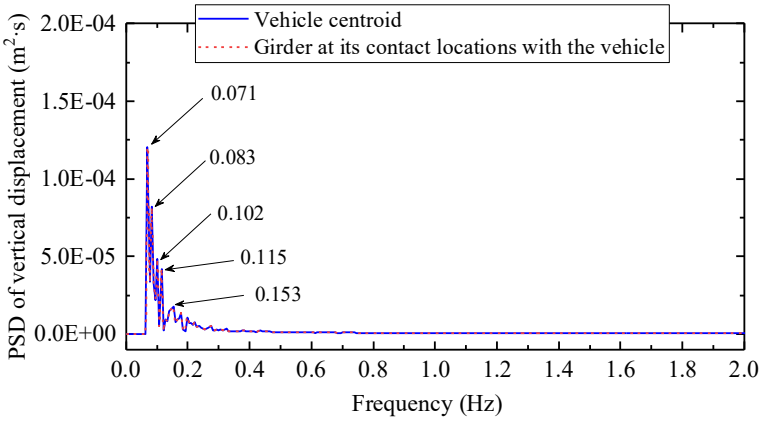

(b) Displacement

Figure 4-1-4: R0 road surface condition on stable bridge road

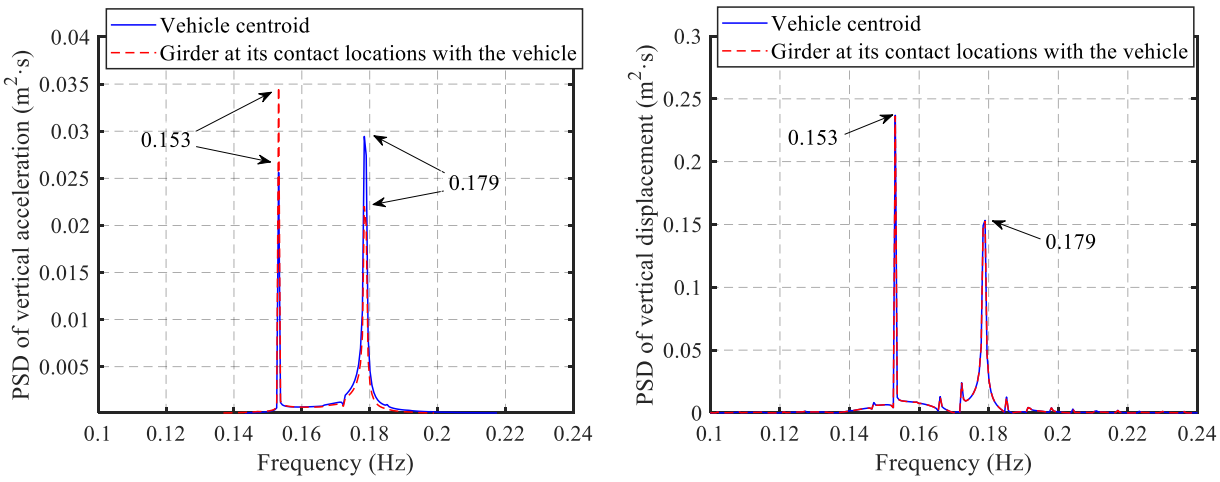

(a) Acceleration *(b) Displacement*

Figure 4-1-5: R0 road surface condition on bridge road with VIV

As seen in Figure 4-1-4 and Figure 4-1-5, the frequency distribution of acceleration and displacement experienced by the vehicle (blue data lines) are in close agreement with that experienced by the bridge girder at contact locations with the vehicle. It indicates, for perfectly smooth road surface conditions (R0), the acceleration and displacement of the girder at contact locations with the vehicle is a good indicator of that experienced by the vehicle and that the coupling effect and the VIV of the girder do not increase the dynamic response of the vehicle.

For the R1 road surface condition, the frequency distribution of PSD for acceleration and displacement experienced by the vehicle on a stable road are shown in Figure 4-1-6.

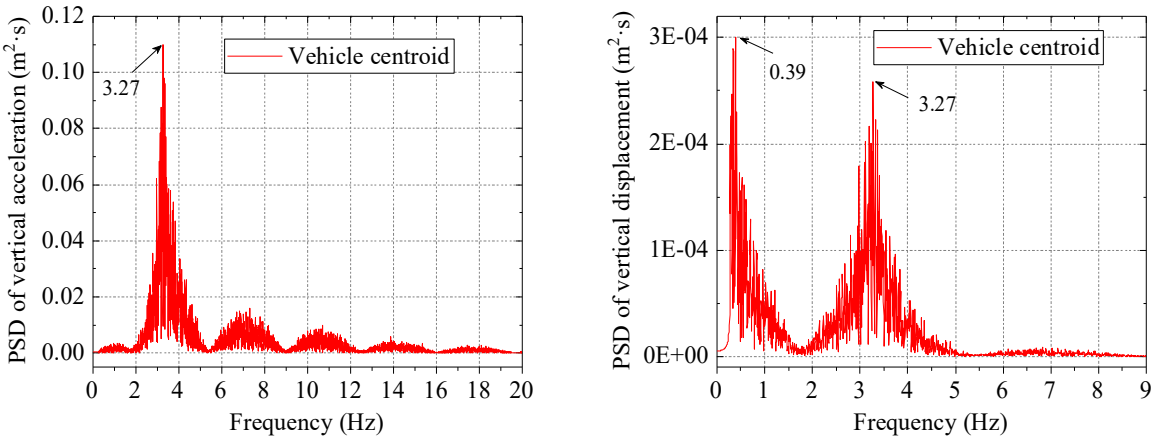

(a) Acceleration *(b) Displacement*

Figure 4-1-6: Frequency distribution of vehicles on R1 stable road

From Figure 4-1-6, for stable road conditions, it is seen that the predominant frequency imposed by road surface roughness, 3.27 Hz, is recognized in both the acceleration and displacement of the vehicle. In vehicle displacement, an additional predominant frequency of 0.37 Hz is recognized.

For the R1 road surface condition, the frequencies distribution of PSD for acceleration and displacement experienced by the vehicle and bridge girder at its contact locations with the vehicle on a stable bridge road and bridge road with VIV are shown in Figure 4-1-7 and Figure 4-1-8.

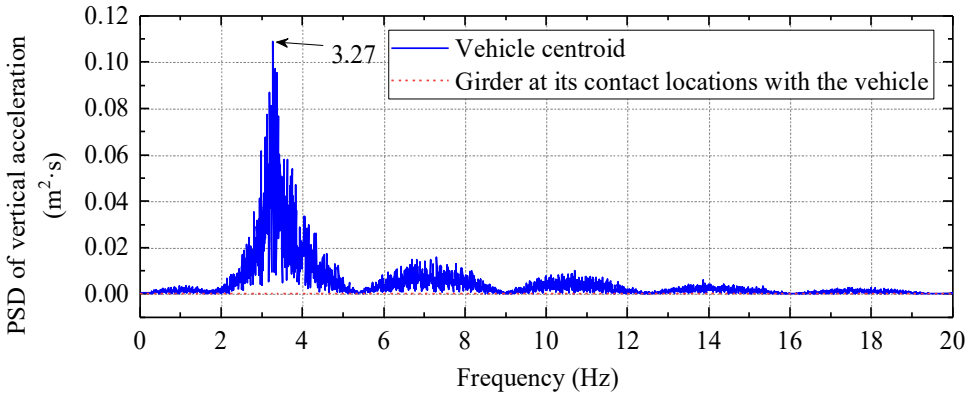

(a) Acceleration

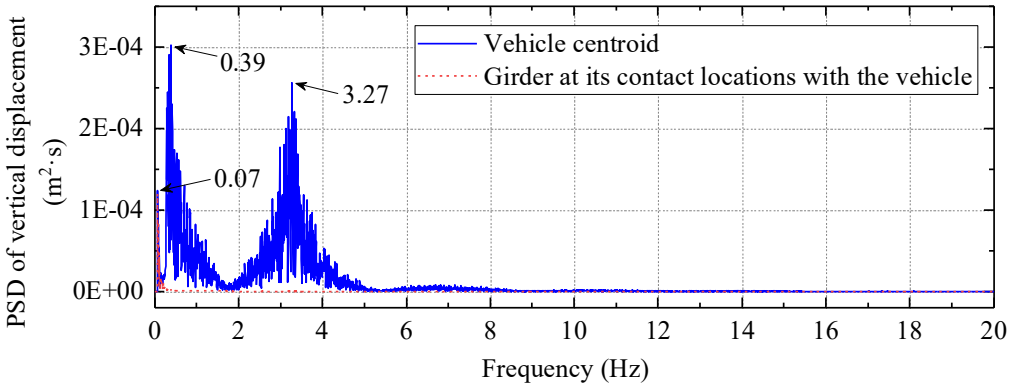

(b) Displacement

Figure 4-1-7: Frequency distribution of vehicle on R1 stable bridge

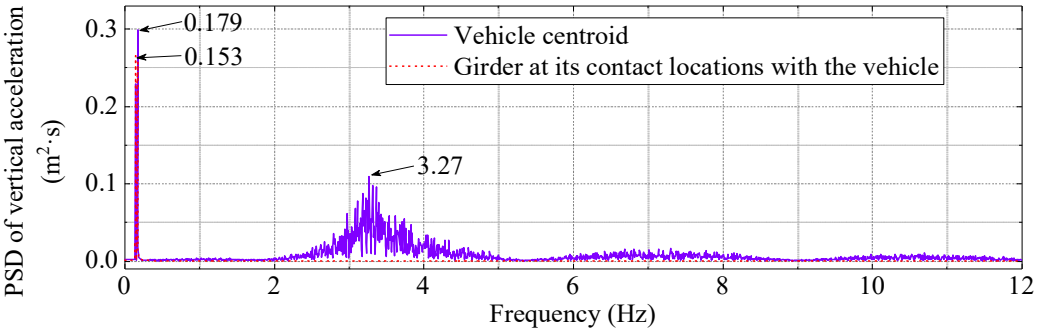

(a) Acceleration

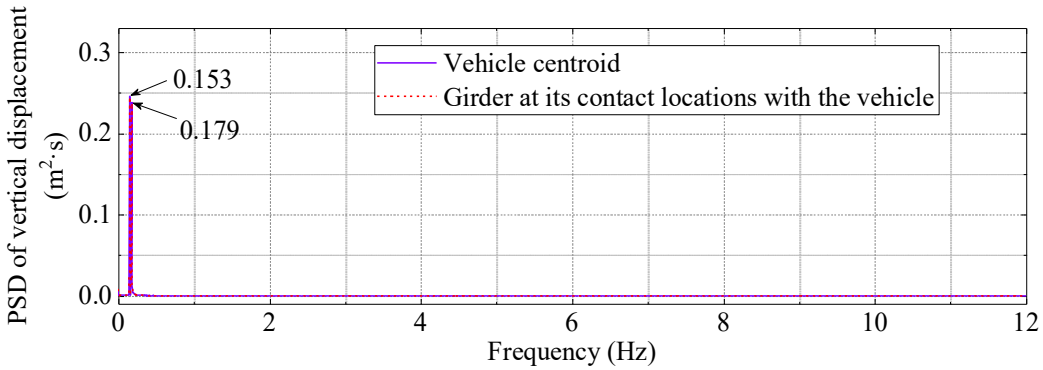

(b) Displacement

Figure 4-1-8: Frequency distribution of vehicle on R1 VIV bridge

As seen in Figure 4-1-7, for stable bridge road conditions, similar predominant frequencies of 3.27 Hz and 0.39 Hz are recognized in acceleration and displacement experienced by the vehicle, respectively. An additional predominant frequency of 0.07 Hz is recognized for girder vibration, which coincides with the girder's fundamental modal frequency of 0.0773 Hz. The result indicates that road surface roughness is the main source of vehicle vibration, and the vehicle's vibration does not significantly influence the vibration of the bridge girder.

Figure 4-1-8 shows the predominant frequencies of acceleration and displacement experienced by the vehicle and the bridge girder at its contact location with the vehicle. For vehicle and girder acceleration, aside from the predominant frequency caused by the road surface roughness (3.27 Hz), there are additional predominant frequencies of 0.153 Hz and 0.179 Hz for the girder and the vehicle, respectively, which are close to the VIV modal frequency (0.166 Hz). By comparing the predominant acceleration frequencies in Figure 4-1-6 (a), Figure 4-1-7 (a), and Figure 4-1-8 (a), it is found that the acceleration experienced by the vehicle on the R1 road surface

condition in bridge with VIV is roughly the linear addition of the acceleration caused by road roughness and the VIV, which indicates that the road roughness and girder VIV are both significant contributors to the acceleration experienced by the vehicle. For the R2 road surface condition, a similar result to that of the R1 road surface condition is observed.

4.2 Vibration serviceability of the human body

4.2.1 Vibration serviceability indices

4.2.1.1 OVTV index

During vibration events, the drivers and passengers of vehicles traveling on the bridge experience accelerations of various frequency ranges and along different directions (axes). To conveniently describe the overall comfort level during vibration events, for events with a frequency between 0.5 to 8 Hz, the Overall Vibration Total Value (OVTV) index is usually utilized. The OVTV index adds different frequency weighting functions for accelerations from corresponding frequency ranges and multiplying factors for accelerations along different directions (axes). It calculates an overall value that evaluates the comfort level experienced by the drivers and passengers in vehicles during VIV.

Table 4-2-1 and Figure 4-2-1 exhibit the frequency weighting function of different axes, ranging from 0.1 to 400 Hz on the x, y, and z direction of the backrest, seat, and feet of a sitting person in the vehicle based on the ISO-2631 standard. W_k represents the function in the z-direction

at the seat location and the x, y, and z direction at the feet location. W_d represents the function in the x and y direction on the seat location and the y and z direction of the backrest. W_c represents the function of the x direction on the backrest location. W_e represents the function for rotation on the x, y, and z-axis of the seat location.

Table 4-2-1: Frequency weighting functions of various frequencies

Frequency f (Hz)	W_k (×1000)	W_d (×1000)	W_c (×1000)	W_e (×1000)
0.1	31.2	62.4	62.4	62.5
0.125	48.6	97.3	97.2	97.5
0.16	79.0	158.0	158.0	159.0
0.2	121.0	243.0	243.0	245.0
0.25	182.0	365.0	364.0	368.0
0.315	263.0	530.0	527.0	536.0
0.4	352.0	713.0	708.0	723.0
0.5	418.0	853.0	843.0	862.0
0.63	459.0	944.0	929.0	939.0
0.8	477.0	992.0	972.0	941.0
1	482.0	1011.0	991.0	880.0
1.25	484.0	1008.0	1000.0	772.0
1.6	494.0	968.0	1007.0	632.0
2	531.0	890.0	1012.0	512.0
2.5	631.0	776.0	1017.0	409.0

3.15	804.0	642.0	1022.0	323.0
4	967.0	512.0	1024.0	253.0
5	1039.0	409.0	1013.0	202.0
6.3	1054.0	323.0	974.0	160.0
8	1036.0	253.0	891.0	125.0
10	988.0	212.0	776.0	100.0
12.5	902.0	161.0	647.0	80.1
16	768.0	125.0	512.0	62.5
20	636.0	100.0	409.0	50.0
25	513.0	80.0	325.0	39.9
31.5	405.0	63.2	256.0	31.6
40	314.0	49.4	199.0	24.7
50	246.0	38.8	156.0	19.4
63	186.0	29.5	118.0	14.8
80	132.0	21.1	84.4	10.5
100	88.7	14.1	56.7	7.1
125	54.0	8.6	34.5	4.3
160	28.5	4.6	18.2	2.3
200	15.2	2.4	9.7	1.2
250	7.9	1.3	5.1	0.6
315	4.0	0.6	2.6	0.3
400	2.0	0.3	1.3	0.2

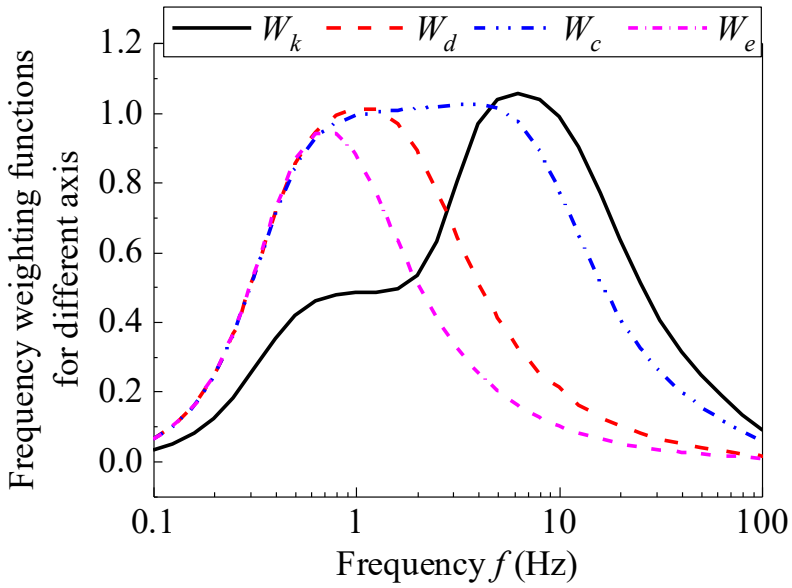

Figure 4-2-1: Frequency weighting functions of various frequencies

A Fast Fourier Transformation Convolution method is proposed to apply the frequency weighting functions to different axes' accelerations. The process converts the acceleration time histories of the vehicle (*x(k)*) into the frequency domain (*X(r)*) and applies the frequency weighting functions (*W(r)*) to obtain the weighted acceleration time history (*X'(r)*).

$$X(r) = \sum_{k=0}^{N-1} x(k)\omega_N^{rk} \qquad \textbf{(Eq. 4-2-1)}$$

where $\omega_N = e^{-2\pi r/N}$, r=0, 1, …N-1.

$$X'(r) = X(r) \cdot W(r) \qquad \textbf{(Eq. 4-2-2)}$$

Then, the weighted time history *X'(r)* is converted back into the time domain using reverse Fast Fourier Transformation and produces acceleration time histories with weights for acceleration (*x'(j)*) of different frequency ranges.

$$x'(j) = \frac{1}{N}\sum_{r=0}^{N-1} X(r)\omega_N^{-jr} \quad \textbf{(Eq. 4-2-3)}$$

The weighted acceleration time histories (*x'(j)*) are then calculated for their Crest Factors (CF). If the CF value is smaller than 9, then the 2nd order RMS of the weighted acceleration time history is used for comfort level evaluation, and if the CF value is larger than 9, then the 4th order RMS of the weighted acceleration is used for comfort level evaluation. The 2nd order and 4th order RMS are calculated as follows.

$$a_{wi-RMS} = \{\frac{1}{T}\int_0^T [a_{wi}(t)]^2 \ dt\}^{1/2} = \{\frac{\sum_{j=1}^{N} a_{wi}(j)^2}{N}\}^{1/2} \quad (\text{CF} < 9) \quad \textbf{(Eq. 4-2-4)}$$

$$a_{wi-VDV} = \{\frac{1}{T}\int_0^T [a_{wi}(t)]^4 \ dt\}^{1/4} = \{\frac{\sum_{j=1}^{N} a_{wi}(j)^4}{N}\}^{1/4} \quad (\text{CF} \geq 9) \quad \textbf{(Eq. 4-2-5)}$$

where *T* is the total time of the acceleration time histories, and $a_{wi\text{-}VDV}$ is the Vibration Dose Value (VDV).

The acceleration VDVs from the different axes are then multiplied with corresponding multiplying factors to calculate an Overall Vibration Dose Value (OVDV) used to evaluate the comfort level. The multiplying factors for each axis are listed in Table 4-2-2.

Table 4-2-2: Multiplying factors for each axis

Location of input	Axis	Weighting function	Multiplying factor(*k*)
Seat	x_s	W_d	1.00
	y_s	W_d	1.00
	z_s	W_k	1.00
	r_x	W_e	0.63
	r_y	W_e	0.40
	r_z	W_e	0.20

Backrest	x_b	W_c	0.80
	y_b	W_d	0.50
	z_b	W_d	0.40
Feet	x_f	W_k	0.25
	y_f	W_k	0.25
	z_f	W_k	0.40

The OVDV value is compared to Table 4-2-3 to determine comfort level.

Table 4-2-3: Comfort level based on OVDV acceleration

a_{OVTV}(m/s^2)	Comfort level
<0.315	No discomfort felt
0.315~0.630	Slightly uncomfortable
0.500~1.000	Relatively uncomfortable
0.800~1.600	Uncomfortable
1.250~2.500	Very uncomfortable
>2.000	Extremely uncomfortable

4.2.1.2 MSI index

For VIV events with lower frequencies (<0.5 Hz), the Motion Sickness Incidence (MSI) Index is used for comfort level evaluation. The MSI Index mainly considers accelerations in the vertical direction (a_{zs}, a_{zf}, a_{zb}), the pitching direction (a_{rx}), and the rolling direction (a_{ry}) for drivers and passengers in vehicles. These acceleration time histories are weighted using a similar process as seen in the calculation of the OVDV in the previous section with the Fast Fourier Transformation Convolution, which converts acceleration time histories to the frequency domain and multiplies

them by respective frequency weighting functions W_f, then convert them back to the time domain with a reverse FFT process. The frequency weighting functions for MSI index accelerations are shown in Table 4-2-4 and Figure 4-2-2.

Table 4-2-4: MSI index frequency weighting functions.

f (Hz)	W_k (×1000)	W_d (×1000)	W_c (×1000)	W_e (×1000)	W_f (×1000)
0.02	--	--	--	--	24.2
0.025	--	--	--	--	37.7
0.0315	--	--	--	--	59.7
0.04	--	--	--	--	97.1
0.05	--	--	--	--	157
0.063	--	--	--	--	267
0.08	--	--	--	--	461
0.1	31.2	62.4	62.4	62.5	695
0.125	48.6	97.3	97.2	97.5	895
0.16	79.0	158.0	158.0	159.0	1006
0.2	121.0	243.0	243.0	245.0	992
0.25	182.0	365.0	364.0	368.0	854
0.315	263.0	530.0	527.0	536.0	619
0.4	352.0	713.0	708.0	723.0	384
0.5	418.0	853.0	843.0	862.0	224
0.63	459.0	944.0	929.0	939.0	116
0.8	477.0	992.0	972.0	941.0	53

1	482.0	1011.0	991.0	880.0	23.5
1.25	484.0	1008.0	1000.0	772.0	9.98
1.6	494.0	968.0	1007.0	632.0	3.77
2	531.0	890.0	1012.0	512.0	1.55
2.5	631.0	776.0	1017.0	409.0	0.64
3.15	804.0	642.0	1022.0	323.0	0.25
4	967.0	512.0	1024.0	253.0	0.097
5	1039.0	409.0	1013.0	202.0	--
6.3	1054.0	323.0	974.0	160.0	--
8	1036.0	253.0	891.0	125.0	--
10	988.0	212.0	776.0	100.0	--
12.5	902.0	161.0	647.0	80.1	--
16	768.0	125.0	512.0	62.5	--
20	636.0	100.0	409.0	50.0	--
25	513.0	80.0	325.0	39.9	--
31.5	405.0	63.2	256.0	31.6	--
40	314.0	49.4	199.0	24.7	--
50	246.0	38.8	156.0	19.4	--
63	186.0	29.5	118.0	14.8	--
80	132.0	21.1	84.4	10.5	--
100	88.7	14.1	56.7	7.1	--
125	54.0	8.6	34.5	4.3	--

160	28.5	4.6	18.2	2.3	--
200	15.2	2.4	9.7	1.2	--
250	7.9	1.3	5.1	0.6	--
315	4.0	0.6	2.6	0.3	--
400	2.0	0.3	1.3	0.2	--

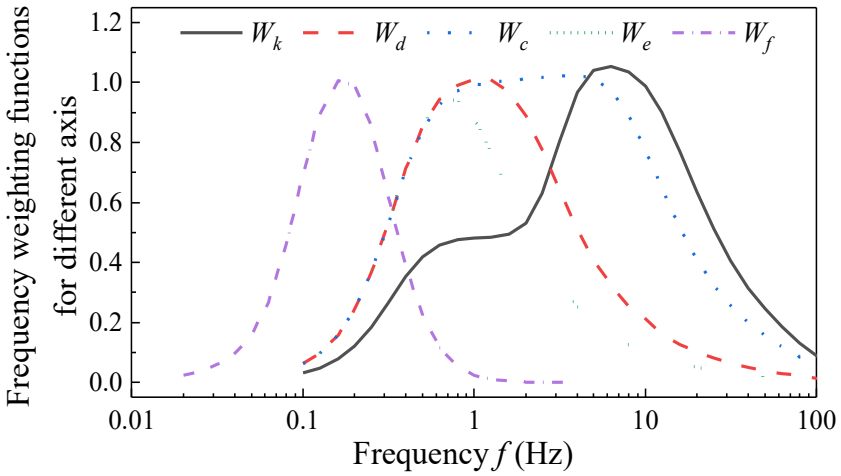

Figure 4-2-2: Weighting functions

With the weighed accelerations calculated in the previous step, the Motion Sickness Dose Value (MSDV) is calculated using the following equation.

$$\text{MSDV}_i = \{\int_0^T [a_{wi}(t)]^2 \ dt\}^{1/2} \qquad \textbf{(Eq. 4-2-6)}$$

where a_{wi} is the weighted acceleration calculated in the previous step and T is the total time of the acceleration time histories.

Multiplying the MSDV of each axis with the multiplying factor, k, the total MSDV can be calculated.

$$\mathrm{MSDV}_T = \{\sum_{i=1}(k_i \mathrm{MSDV}_i)^2\}^{1/2} \quad \textbf{(Eq. 4-2-7)}$$

Based on the people group of passengers in the vehicle, the MSI (%) can be further calculated.

$$\mathrm{MSI}\ (\%) = K_m\ \mathrm{MSDV}_T \quad \textbf{(Eq. 4-2-8)}$$

where K_m is a constant based on the people group, and K_m is usually taken as 1/3 for male and female adults.

Comparing the MSI (%) obtained from the previous step to Table 4-2-5, the level of motion sickness can be defined.

Table 4-2-5: Level of MSI comfort

MSI	Comfort level
0.00	Very comfortable
0.25	Comfortable
0.50	Neither comfortable nor uncomfortable
0.75	Uncomfortable
1.00	Very uncomfortable

4.2.2 Serviceability indices under VIV

4.2.2.1 Overall Vibration Total Value (OVTV) index

Applying the comfort level calculation process introduced in 3.1.1 to the FEM model result of the prototypical bridge, the value of Overall Vibration Total Values (OVTV) index of drivers,

passengers, and standing pedestrians on the bridge under different road surface conditions and travel conditions are calculated and summarized in Table 4-2-6.

Table 4-2-6: OVTV on the prototypical bridge

Road condition	Driver/Passenger			Pedestrian		
	R0	**R1**	**R2**	**R0**	**R1**	**R2**
Stable road	0	0.3863	0.7526	0	0	0
Stable bridge	2.82E-04	0.3842	0.7489	4.68E-05	1.47E-04	2.84E-04
VIV bridge	0.0313	0.3853	0.7766	0.0314	0.0314	0.0314

It is seen from Table 4-2-6 that the OVTVs are all relatively small for different travel conditions on R0 road surfaces. Under the most critical condition (VIV bridge road), the value is 0.0313, significantly lower than the discomfort threshold listed in Table 4-2-5. For R1 and R2 conditions, the increase in OVTVs is mostly provided by road roughness. The contribution of VIV is also very small. The reason for such observation is that the OVTV mostly takes vibrations with frequencies ranging from 0.5-8 Hz into consideration, and the vibration of VIV is usually lower than that range (frequency is 0.166 Hz in this case). Therefore, the contribution of VIV to the OVTV is small. For pedestrians, since the road surface roughness does not influence the acceleration experienced by pedestrians, the OVTVs are also very small and do not reach the threshold of discomfort listed in Table 4-2-5. Therefore, it can be concluded that existing methods that categorize comfort level are insufficient to consider the discomfort caused by bridge VIV due to the mismatch in the application range of acceleration frequencies.

4.2.2.2 Motion Sickness Incidence (MSI) index

Applying the Motion Sickness Incidence (MSI) index calculation process to the FEM model result of the prototypical bridge obtained in this section, the value of the MSI index of drivers, passengers, and standing pedestrians on the bridge under different road surface conditions and travel conditions are calculated and summarized in Table 4-2-7.

Table 4-2-7: MSI index on prototypical Bridge

Road condition	Driver/Passenger			Pedestrian		
	R0	R1	R2	R0	R1	R2
Stable road	0	0.02%	0.02%	0	0	0
Stable bridge	0	0.04%	0.06%	0	0	0
VIV bridge	1.93%	1.93%	1.93%	1.61%	1.61%	1.61%

As seen in Table 4-2-7, the influence of road surface roughness conditions is negligible in all cases because the MSI index mostly considers vibrations with frequencies ranging from 0 Hz to 0.5 Hz, and the vibration caused by road surface roughness is outside of the applicable range (3.7 Hz). Therefore, the road surface roughness does not contribute to the evaluation of motion sickness in this case. However, the VIV predominant frequency (0.166 Hz) falls into the 0-0.5 Hz range. As a result, for vehicles, in the case where bridge VIV is present for all road surface roughness conditions, the MSI index is 1.93%. For pedestrians, the MSI index is 1.61%, slightly lower than that for the case with vehicles, which is because only the vertical acceleration on the feet of pedestrians is considered, whereas for drivers and passengers in vehicles, vertical

accelerations acting on the feet, seat, and backrest, among other accelerations, are all taken into considerations.

To conclude, since the accelerations acting on drivers and passengers of vehicles and pedestrians on the bridge caused by VIV fall within the applicable range of MSI index evaluation (0-0.5 Hz), the VIV of long-span bridges is a potential cause for motion sickness and can be categorized by the MSI index. The higher the MSI index, the more discomfort drivers and passengers perceive in vehicles traveling and pedestrians standing on the bridge. It is also concluded that the road surface roughness is not a significant influencing factor for the MSI index, as its typical range of frequency is outside of the applicable frequency range of the MSI index (0-0.5 Hz).

4.2.2.3 Influencing factor of MSI index

To analyze the sensitivity of the MSI index from influencing factors such as vehicle speed, VIV frequency, VIV amplitude, wind speed, etc., each potential influencing factor is singled out in the MSI index calculation.

For analysis with variable vehicle speed, the VIV of the bridge is set to vibrate on 2nd order anti-symmetric mode shape with a frequency of 0.1656 Hz, the amplitude of VIV varies from 0.1 m to 0.9 m. The road surface condition is set as R0 (smooth road surface). The result is shown in Figure 4-2-3 and Table 4-2-8.

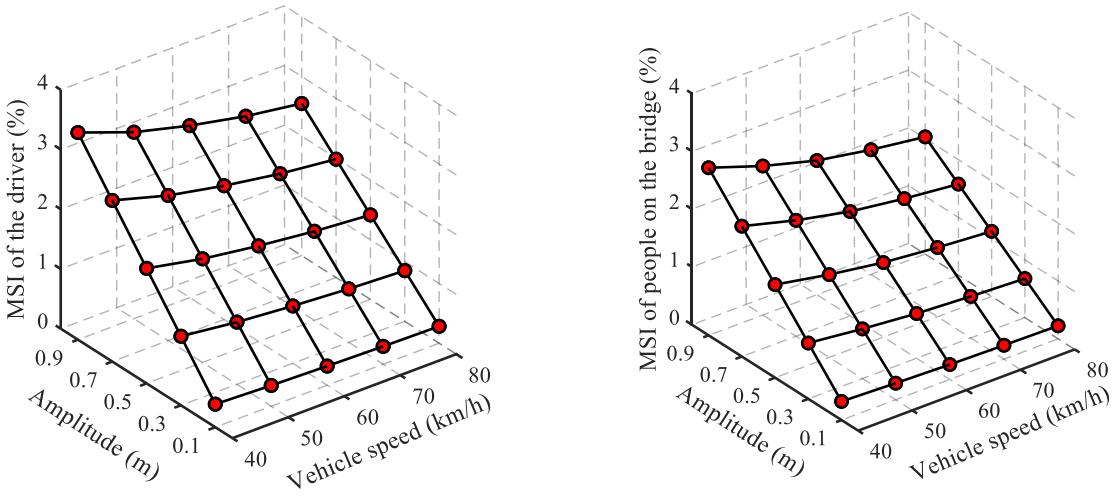

(a) Driver *(b) Pedestrian*

Figure 4-2-3: MSI index with various vehicle speeds and VIV amplitude

Table 4-2-8: MSI index with various vehicle speeds and VIV amplitude

	Speed (km/h)	0.1	0.3	0.5	0.7	0.9
Driver	40	0.385%	1.156%	1.926%	2.697%	3.467%
	50	0.347%	1.041%	1.734%	2.428%	3.121%
	60	0.320%	0.960%	1.600%	2.240%	2.880%
	70	0.298%	0.895%	1.492%	2.089%	2.686%
	80	0.283%	0.849%	1.415%	1.982%	2.548%
Pedestrian at peak of mode shape	40	0.322%	0.966%	1.611%	2.255%	2.899%
	50	0.287%	0.859%	1.432%	2.005%	2.578%
	60	0.258%	0.774%	1.289%	1.805%	2.321%
	70	0.240%	0.719%	1.198%	1.677%	2.156%
	80	0.225%	0.676%	1.126%	1.577%	2.028%

For analysis of VIV modes of the bridge with different frequencies, the vehicle is set to travel at a speed of 40 km/h with R0 road surface condition, the amplitude of VIV varies from 0.1 m to 0.9 m. The result is shown in Figure 4-2-4 and Table 4-2-9.

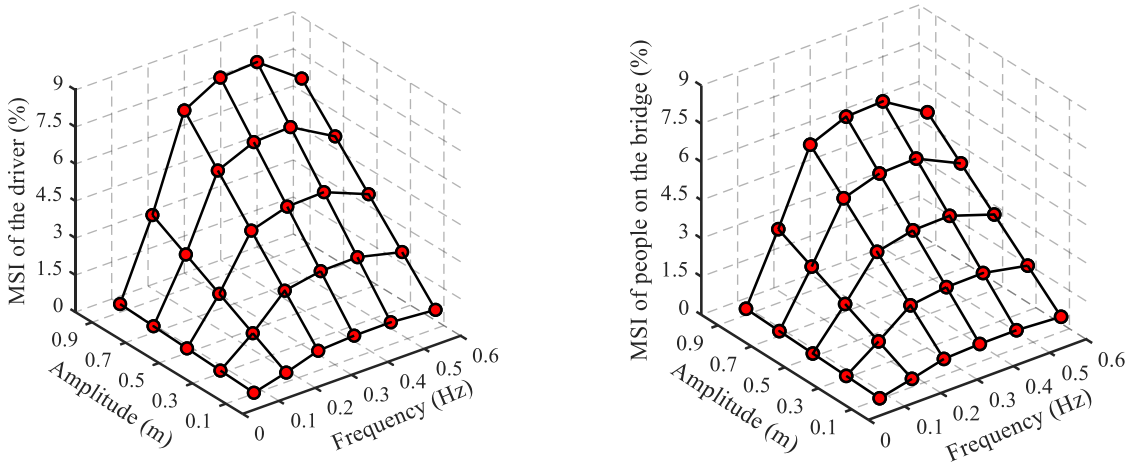

(a) Driver *(b) Pedestrian*

Figure 4-2-4: MSI index for VIV modes with different frequencies

Table 4-2-9: MSI index for VIV modes with different frequencies

	Frequency (Hz)	**0.1**	**0.3**	**0.5**	**0.7**	**0.9**
Driver	VAS1(0.077)	0.0369	0.1109	0.1849	0.2589	0.3329
	VAS2(0.166)	0.3852	1.1557	1.9262	2.6967	3.4672
	VAS3(0.254)	0.8048	2.4143	4.0237	5.6332	7.2426
	VAS4(0.353)	0.8946	2.6837	4.4728	6.2618	8.0509
	VAS5(0.454)	0.9053	2.7160	4.5266	6.3371	8.1476
	VAS6(0.577)	0.7589	2.2767	3.7940	5.3125	6.8322
Pedestrian at peak of modal shape	VAS1(0.077)	0.0271	0.0814	0.1356	0.1899	0.2442
	VAS2(0.166)	0.3221	0.9663	1.6105	2.2548	2.8990
	VAS3(0.254)	0.6392	1.9175	3.1957	4.4740	5.7523
	VAS4(0.353)	0.7034	2.1104	3.5173	4.9242	6.3313
	VAS5(0.454)	0.7109	2.1326	3.5543	4.9761	6.3981
	VAS6(0.577)	0.5914	1.7742	2.9571	4.1402	5.3233

4.2.2.4 MSI index under various conditions

The results from previous sections indicate that parameters such as vehicle speed, road surface roughness, and wind speed are not significant contributors to the MSI index compared to VIV frequency, amplitude, and time length. By controlling VIV frequency and VIV time length values, allowable VIV amplitude can be analyzed based on consideration of the MSI index.

The travel time for vehicles traveling on long-span bridges is usually relatively short. Therefore, VIV time length for vehicles considered in this section is taken as 5 minutes, 10 minutes, 20 minutes, and 30 minutes. For pedestrians and workers, the time length is taken as 1 hour, 2 hours, 4 hours, and 8 hours.

The six lowest vertical bending modes are selected for analysis. Three levels of MSI percentage are considered, which are the 10%, 20%, and the 30% MSI level. The percentage represents the portions of the general public that would perceive motion sickness, e.g., 30% of people would experience motion sickness after exposure to the 30% MSI level vibration.

Considering the above-mentioned variables, the allowable amplitude of VIV based on the MSI index is shown below in Table 4-2-10.

Table 4-2-10: Allowable VIV amplitude (unit: m)

	Time length	**f（Hz） MSI（%）**	**VAS1 （0.077）**	**VAS2 （0.166）**	**VAS3 （0.254）**	**VAS4 （0.353）**	**VAS5 （0.454）**	**VAS6 （0.577）**
Driver	5 min	10	19.6302	1.8862	0.9030	0.8123	0.8027	0.9571
		20	39.1778	3.7723	1.8063	1.6240	1.6054	1.9129
		30	58.5579	5.6583	2.7107	2.4332	2.4081	2.8723

	10 min	10	13.8854	1.3337	0.6385	0.5744	0.5676	0.6770
		20	27.7420	2.6675	1.2770	1.1487	1.1351	1.3529
		30	41.5396	4.0011	1.9159	1.7224	1.7027	2.0290
	20 min	10	9.8202	0.9431	0.4515	0.4061	0.4013	0.4788
		20	19.6302	1.8862	0.9030	0.8123	0.8027	0.9571
		30	29.4196	2.8293	1.3545	1.2184	1.2040	1.4349
	30 min	10	8.0186	0.7700	0.3686	0.3316	0.3277	0.3909
		20	16.0317	1.5401	0.7372	0.6632	0.6554	0.7817
		30	24.0336	2.3101	1.1059	0.9948	0.9831	1.1719
Pedestrian/ worker	1 h	10	7.7305	0.6512	0.3282	0.2982	0.2951	0.3547
		20	15.4586	1.3024	0.6564	0.5964	0.5902	0.7093
		30	23.1817	1.9537	0.9846	0.8945	0.8852	1.0639
	2 h	10	5.4665	0.4605	0.2321	0.2109	0.2087	0.2508
		20	10.9320	0.9210	0.4641	0.4217	0.4173	0.5016
		30	16.3959	1.3814	0.6962	0.6325	0.6260	0.7523
	4 h	10	3.8655	0.3256	0.1641	0.1491	0.1475	0.1773
		20	7.7305	0.6512	0.3282	0.2982	0.2951	0.3547
		30	11.5950	0.9768	0.4923	0.4473	0.4426	0.5320
	8 h	10	2.7334	0.2302	0.1160	0.1054	0.1043	0.1254
		20	5.4665	0.4605	0.2321	0.2109	0.2087	0.2508
		30	8.1994	0.6907	0.3481	0.3163	0.3130	0.3762

As seen in Table 4-2-10, the allowable amplitude is relatively high in mode VAS1 (0.077 Hz). For example, the amplitude for 30% MSI at 30 minutes time length is 24.0336 m, which exceeds the normal amplitude range of VIV for long-span bridges, indicating this mode of VIV does not usually cause MSI. For modes with higher orders, the allowable amplitude follows a decreasing trend due to the increasing acceleration for higher-order modes. With longer exposing time, the allowable amplitude decreases as well.

4.2.3 Comparison of VIV amplitude limits

Comparing the MSI index-based VIV allowable amplitude discussed in the previous section with other widely adopted VIV allowable amplitude, such as the Chinese limit, the Japanese limit, the UK limit, and RWDI standards, etc. of the prototypical bridge, the result is shown in Table 4-2-11.

Table 4-2-11: Allowable VIV amplitude of various codes

F(Hz) Codes		VAS1 (0.077)	VAS2 (0.166)	VAS3 (0.254)	VAS4 (0.353)	VAS5 (0.454)	VAS6 (0.577)
Chinese/Japanese codes		0.5195	0.2410	0.1575	0.1133	0.0881	0.0693
British rule		5.0036	1.0766	0.4598	0.2381	0.1439	0.0891
RWDI-British		2.1383	0.4601	0.1965	0.1017	0.0615	0.0381
RWDI-North America		1.7106	0.3681	0.1572	0.0814	0.0492	0.0305
Dickman index		16.8663	3.6290	1.5500	0.8025	0.4852	0.3004
The MSI-based limit for driver	5 min	58.5579	5.6583	2.7107	2.4332	2.4081	2.8723
	30 min	24.0336	2.3101	1.1059	0.9948	0.9831	1.1719
The MSI-based limit for pedestrian	1 h	23.1817	1.9537	0.9846	0.8945	0.8852	1.0639
	8 h	8.1994	0.6907	0.3481	0.3163	0.3130	0.3762
Limit based on diver vision		/	0.3500	0.3500	0.3500	0.3500	0.3500

As seen in Table 4-2-11, for the allowable VIV amplitude of the prototypical bridge based on VAS1 mode shape, the Chinese code and the Japanese code give the strictest limit at 0.5195 m, and the MSI index based allowable amplitude based on 30% MSI at 5 minutes to 30 minutes produce the most relaxed limit, at 58.5579 m when the time length is 5 minutes.

4.3 Chapter Summary

In this chapter, a wind-traffic-bridge coupling vibration model is established. Based on the coupling vibration model, the displacement, velocity, and acceleration that vehicles and pedestrians experience on the bridge during different modes of VIV can be calculated. With the dynamic responses of vehicles and pedestrians on a bridge under VIV, the OVTV and MSI indices can be calculated using a Fast Fourier Transform Convolution method to evaluate the comfort level experienced by the drivers, passengers, and pedestrians. The calculation is performed on the 1760 m prototypical long-span suspension bridge currently under construction for verification. The main conclusion of this chapter is summarized as follows:

1. In cases where no road surface roughness is present on a bridge, the dynamic response of the bridge girder is a good indicator of the dynamic response experienced by the vehicle.

2. The comfort level represented by OVTV is not significantly influenced by VIV events because the frequency ranges of VIVs (0-0.5 Hz) do not fall within the applicable frequency range of OVTV (0.5-80 Hz).

3. VIV mainly influences comfort level represented by the MSI index. Vibration amplitude, length of vibration, and frequency of vibration are the main influencing factors, while wind speed and surface roughness do not contribute much to the MSI index. Hence, compared to OVTV, the MSI index is a preferred indicator of VIV-induced driving discomfort.

Chapter 5 Mechanical mitigation measures and AI-based detection method for VIV on long-span suspension bridges

In previous chapters, the VIV mechanisms of the rectangular girder sections with or without wind noses and the streamlined box girder section are explored and discussed, and several aerodynamic VIV mitigation measures installed on the streamlined girder section are proposed and tested for their effectiveness. Although the central stabilizing board, the horizontal stabilizing board, and the combination of the two boards effectively reduce the magnitude of VIV displacement for the streamlined girder section, the VIV response is not entirely mitigated, and their applicability to girder sections of other shapes is not verified. This first part of this chapter focuses on developing mechanical VIV mitigation measures that supplement the aerodynamic mitigation measures and are effective for wider application on long-span suspension bridges regardless of the aerodynamic shapes of their box girder sections. The FEM model created in the previous chapters for dynamic characteristic analysis is used to validate the effectiveness of the mechanical mitigation measures proposed in this chapter. In the second part of this chapter, an AI-based VIV detection method utilizing the machine learning and object-tracking algorithms is introduced. The method tracks the coordinates of target objects on the main span of bridges in a video of a bridge VIV event and converts the two-dimensional coordinates of the lamps on the video to a three-dimensional space to reveal the amplitude, frequency, and mode shape of the bridge VIV.

5.1 Mechanical mitigation measures of VIV

5.1.1 Potential mechanical VIV counter-measures

Six counter-measures are added to the FEM model of the prototypical bridge to examine their respective effectiveness in mitigating bridge VIV responses of 1st order symmetrical vertical bending mode, the maximum mid-span displacement of the girder is taken as 0.4311 m.

i) Counter-measure 1: Damping cable on the main cable

Based on ANSYS dynamic analysis results, the 1st order vibration modal shape is shown in Figure 5-1-1.

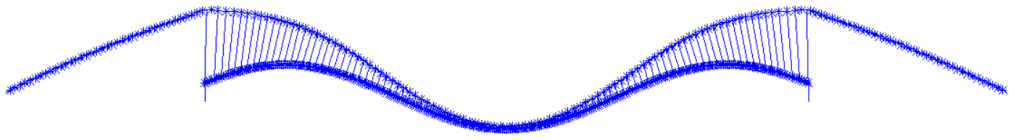

Figure 5-1-1: 1st order bending mode shape

As seen in Figure 5-1-1, the displacement of the main bridge girder is closely associated with the movement of the main bridge cable. Therefore, installing damping cables on the main girder is worth exploring. Two schemes are proposed to install damping cables: Longitudinal damping cable connecting the main cable on the bridge's main span and side span and vertical damping cable connecting the main cable and girder on the side span, shown in Figure 5-1-2.

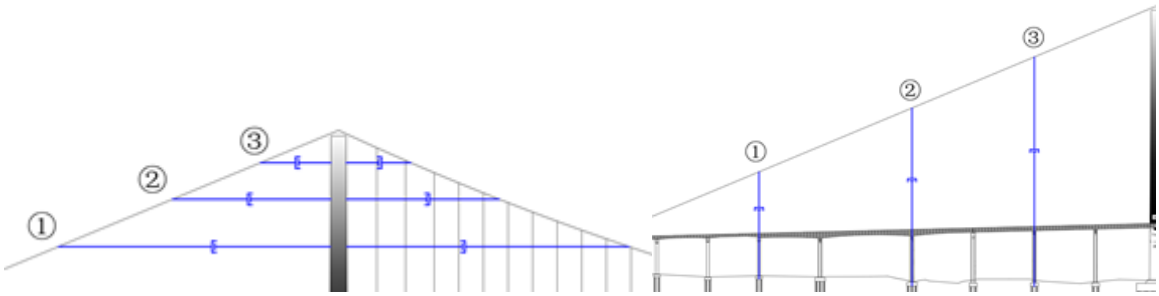

(a) Longitudinal damping cables *(b) Vertical damping cables*

Figure 5-1-2: Installation scheme for damping cables on the main cable

The damping cables are added to the model as Combine14 elements in ANSYS Workbench. The Combine14 element is a connection element capable of providing stiffness and damping in all three directions (x, y, and z). In this part of the research, the element's stiffness in all three directions is set as 0 to avoid altering the original structural stiffness of the bridge. The damping capabilities of the elements, c_v, are expressed as follows:

$$c_v = (c_v)_1 + (c_v)_2 v \qquad \textbf{(Eq. 5-1-1)}$$

where c_v is the damping coefficient, c_{v1} is the linear damping coefficient, and c_{v2} is the nonlinear damping coefficient, v is the velocity of the damper.

The respective damping force, Fx and T_θ, are expressed as:

$$F_x = -\frac{c_v du_x}{dt} \quad \text{or} \quad T_\theta = -\frac{c_v d\theta}{dt} \qquad \textbf{(Eq. 5-1-2)}$$

where u and θ are displacement and rotational angle of the damper, respectively.

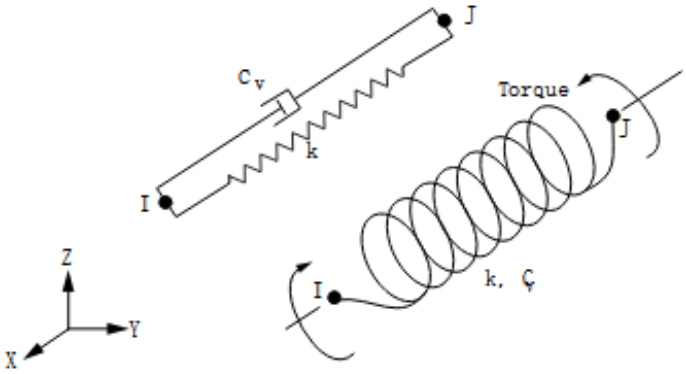

Figure 5-1-3: Combine14 element

The schematic of the Combine14 element is shown in Figure 5-1-3. Only longitudinal damping capability is considered in this scheme. The VIV response of the bridge with damping cables of various damping capabilities installed is summarized in Table 5-1-1. The effect of cables installed at three locations for the longitudinal and vertical damping cables with various damping coefficients is compared.

Table 5-1-1: VIV response with damping cables installed

Scheme	Location	Damping coefficient (KN·s/m)	Midspan displacement before installation (m)	Midspan displacement after installation(m)	Change of displacement (%)
Longitudinal damping cable connecting main cable on the main span and side span of the bridge	①	0	0.4311	0.43113	-0.00
		100		0.3408	-20.95
	②	0		0.4070	-5.59
		100		0.3733	-13.42
		500		0.2397	-44.40
	③	0		0.43113	-0.00
		100		0.4184	-2.94

Vertical damping cable connecting main cable and girder on the side span	①	0	0.43113	-0.00
		100	0.4013	-6.93
	②	0	0.4306	-0.12
		100	0.3868	-10.28
		500	0.2763	-35.91
	③	0	0.43113	-0.00
		100	0.4027	-6.60

ii) Counter-measure 2: Viscous damping devices at the midspan of the main span

For the 1st order symmetrical vertical bending mode of VIV, maximum VIV displacement appears in the midspan of the bridge's main span. Therefore, hard rubber damping rods are installed in the longitudinal direction along the girder section at mid-span to explore their effectiveness in mitigating VIV response. The rods are installed on the main girder's upper surface and lower surface at mid-span and deform longitudinally when the girder bends and deforms during VIV. The cables are modeled as Combine14 elements and are shown in Figure 5-1-4.

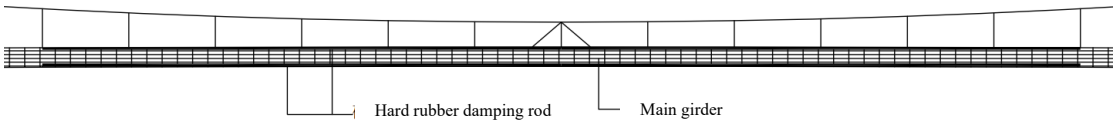

Figure 5-1-4: Longitudinal damping cables between main cable and main girder

The effectiveness of the damping rods with various damping capabilities is summarized in Table 5-1-2.

Table 5-1-2: VIV response with damping rods installed

Damping coefficient (KN·s/m)	Midspan displacement before installation (m)	Midspan displacement after installation(m)	Change of displacement (%)
0	0.4311	0.4311	-0.00
4000		0.4248	-1.47
8000		0.4186	-2.90

ii) Counter-measure 3: Bearing support damping device

Counter-measure 3 dissipates the energy of VIV with the longitudinal displacement of the main girder. Bridge-bearing supports at the tower/girder connection experience longitudinal displacement when the girder moves during VIV. Therefore, four damping devices are installed on all four support bearings of the main span in the longitudinal direction to test their effectiveness in mitigating VIV. The support-bearing damping device is shown below in Figure 5-1-5. The effectiveness of the device with various damping capabilities is summarized in Table 5-1-3.

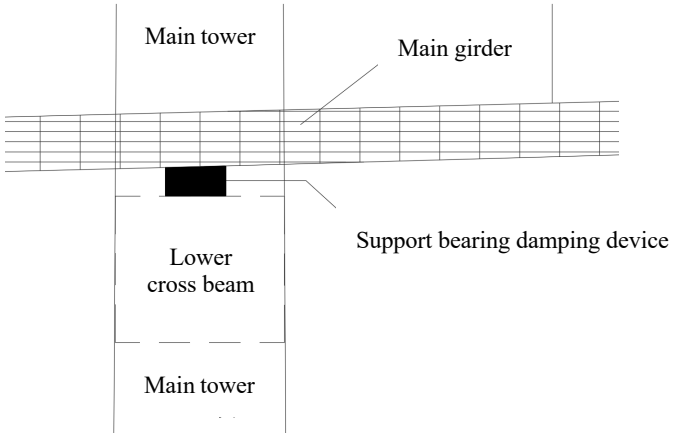

Figure 5-1-5: Support damping devices

Table 5-1-3: Effectiveness of the damping devices

Damping coefficient (KN·s/m)	Midspan displacement before installation (m)	Midspan displacement after installation(m)	Change of displacement (%)
0	0.4311	0.4311	-0.00
6000		0.4191	-2.78
12000		0.4080	-5.36
24000		0.3882	-9.96
96000		0.3178	-26.30
230000		0.2868	-33.47
270000		0.2862	-33.61

iii) Counter-measure 4: Hanger longitudinal damping device

During VIV, the main cables move as well under the influence of the main girder. Therefore, rubber and viscous damping devices can be installed on the hangers that connect the main girder and the main cables to dissipate the energy. The installed devices are shown in Figure 5-1-6.

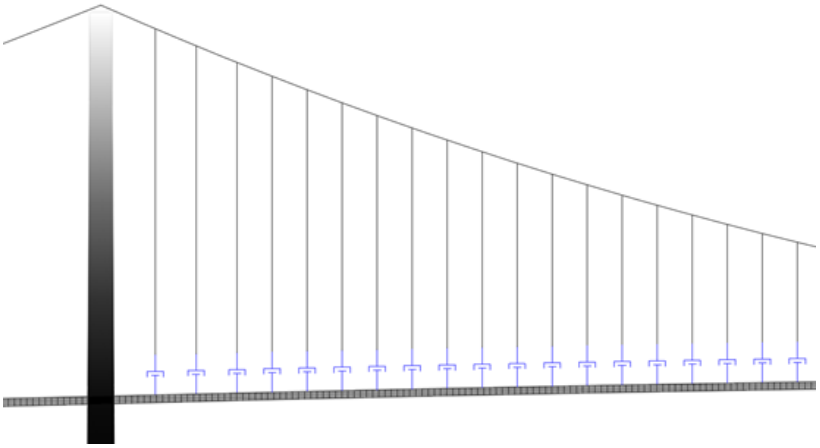

Figure 5-1-6: Damping devices on hangers

The effectiveness of the device with various damping capabilities is summarized in Table 5-1-4.

Table 5-1-4: Effectiveness of damping devices

Damping coefficient (KN·s/m)	Midspan displacement before installation (m)	Midspan displacement after installation(m)	Change of displacement (%)
0	0.4311	0.4311	-0.00
2000		0.4199	-2.61
4000		0.4123	-4.38
6000		0.4080	-5.36

iv) Counter-measure 5: Hanger rotational damping device

During VIV, there is relative rotation between the main girder and hangers. Therefore, rotational damping devices can be installed at the connections of hangers and the main girder to dissipate VIV energy. The damping devices are Combine14 elements with rotational damping capabilities, as shown in Figure 5-1-7

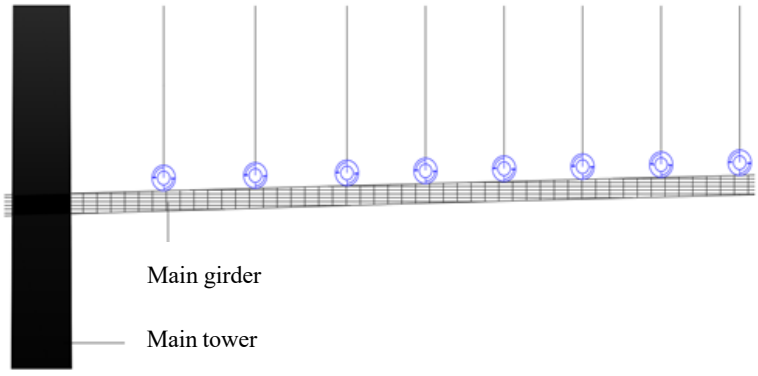

Figure 5-1-7: Rotational damping devices on hangers

The effectiveness of the device with various damping capabilities is summarized in Table 5-1-5.

Table 5-1-5: Effectiveness of damping devices

Damping coefficient (KN·s/m)	Midspan displacement before installation (m)	Midspan displacement after installation(m)	Change of displacement (%)
0	0.4311	0.4311	-0.00
100		0.4311	> -0.50
500		0.4311	> -0.50
1000		0.4311	> -0.50

v) Counter-measure 6: Rubber damper installed at the lower end of hangers

As seen in Figure 5-1-8, rubber dampers with a length of 0.5 m are installed at the lower end of the hangers to dissipate VIV energy via rotational deformation from the damper. The effectiveness of the device with various damping capabilities is summarized in Table 5-1-6.

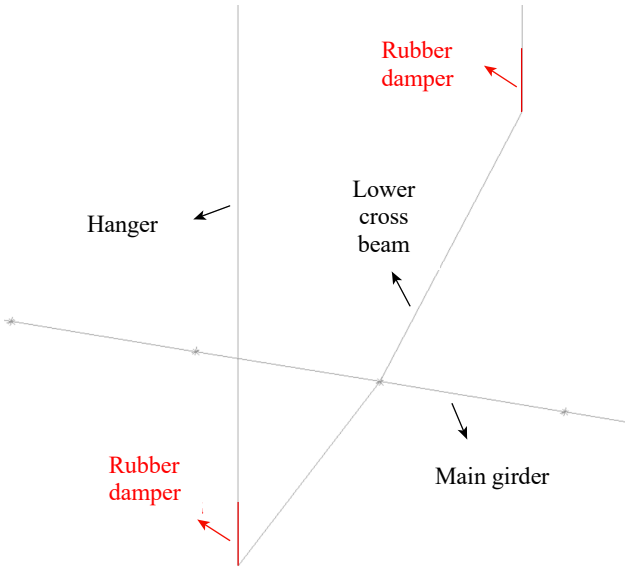

Figure 5-1-8: Rubber dampers installed at the lower end of hangers

Table 5-1-6: Effectiveness of damping devices

Damping coefficient (KN·s/m)	Midspan displacement before installation (m)	Midspan displacement after installation(m)	Change of displacement (%)
0	0.4311	0.4311	-0.00
1000		0.4309	-0.04
3000		0.4123	-1.38

vi) Summary of tested counter-measures

Based on the above analysis, damping devices installed on the main and side span main cables are the most effective. The longitudinal damping cable connecting main cable on the main span and side span decreased the VIV displacement by 20.95% with 100 KN·s/m damping coefficient, and the vertical damping cable connecting main cable and girder on the side span reduced the VIV displacement by 10.28% with 100 KN·s/m coefficient.

The results above indicate that the relative displacement between main cables on the main span and side span is most efficient in mitigating VIV displacement when installed damping devices are used. Therefore, it is reasonable to focus on optimizing the design of the damping device connected to the main cables in the following section.

5.1.2 Effective counter-measures on main cables and parameter analysis

In the previous section, VIV counter-measures installed on main cables have proven the most effective. This section discusses several VIV counter-measures installed on main cables in detail.

i) Counter-measure 1: rotation restriction dampers at the top of hangers

Dampers utilizing lower-end rotation of hangers between hangers and the main girder are discussed in the previous section. However, the rotation between hangers and main cables on the top of the hangers is more significant. To utilize the hanger top rotation to dissipate VIV energy, damping cables that connect hangers and main cables at the top of hangers are installed, forming triangular shapes that restrict rotation between hangers and main cables. The damping cables are shown in Figure 5-1-9. The effectiveness of the device with various damping capabilities is summarized in Table 5-1-7.

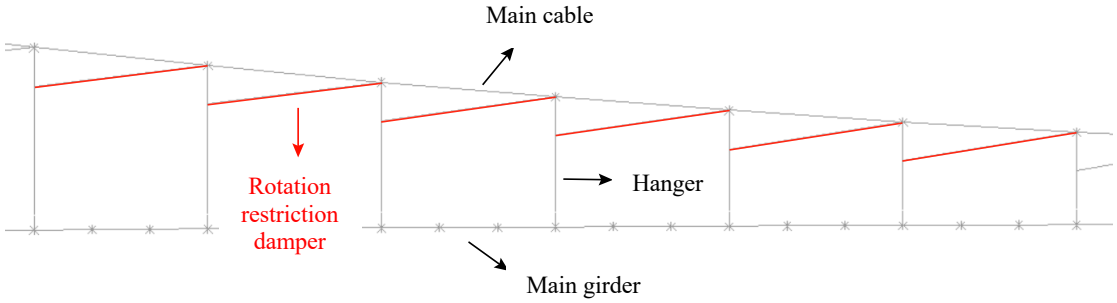

Figure 5-1-9: Rotation restriction dampers of hangers

Table 5-1-7: Effectiveness of damping devices

Damping coefficient (KN·s/m)	Midspan displacement before installation (m)	Midspan displacement after installation(m)	Change of displacement (%)
0	0.4311	0.4311	-0.00
100		0.4221	-2.09
500		0.4040	-6.30

ii) Counter-measure 2: TMD on side span main cables

Tuned Mass Damper (TMD) is a widely utilized structural vibration mitigation measure in engineering practice. Since significant movement from VIV of the main girder is observed on the side span main cables, TMD installed on side span main cables could be potentially effective in mitigating VIV on bridges. As seen in Figure 5-1-10 and Figure 5-1-11, TMDs are installed on quarter points of side-span main cables. The modeling of the TMD uses Combine14 and Mass21 elements to represent the damping and mass characteristics of the TMDs. The damping ratio of TMDs is taken as 2.5%.

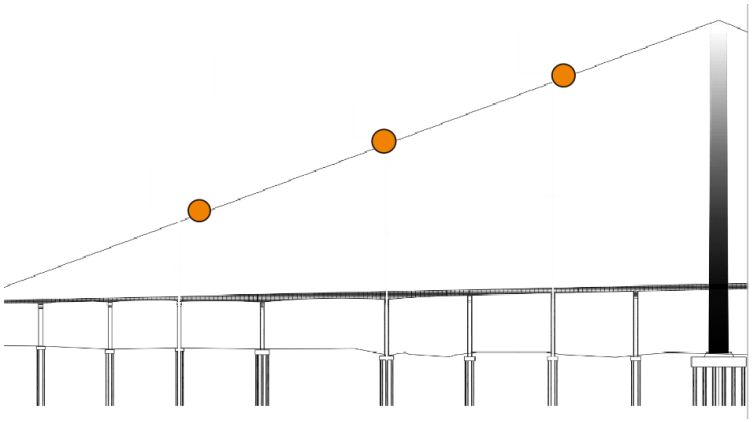

Figure 5-1-10: TMD on side span main cables

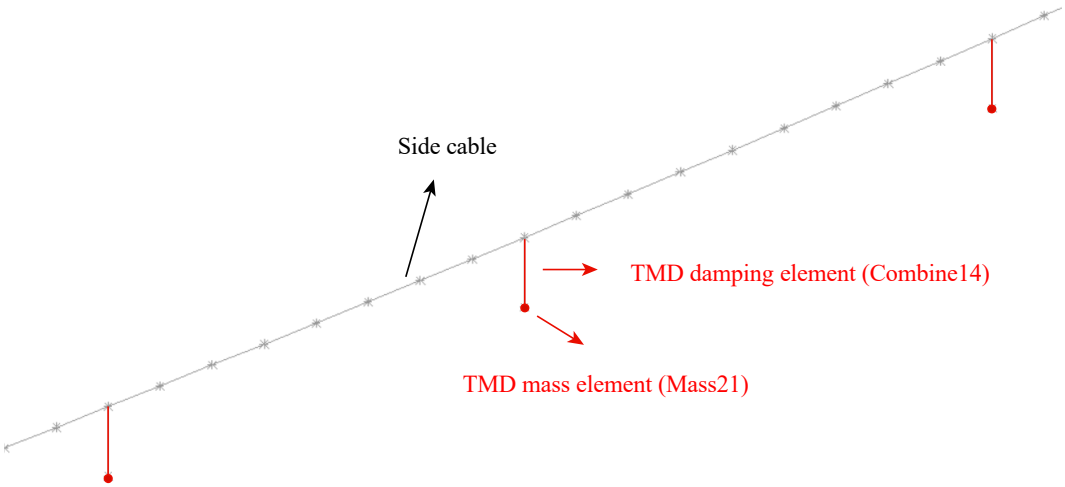

Figure 5-1-11: Cable TMDs simulation details

The effectiveness of the TMD damping device installed at three different locations with various damping capabilities is summarized and compared in Table 5-1-8.

Table 5-1-8: Effectiveness of damping devices

Location	Damping coefficient (KN·s/m)	Stiffness (N/m)	Mass (kg)	Damping ratio (%)	Midspan displacement before installation (m)	Midspan displacement after installation (m)	Change of displacement (%)
Quarter point near side span	17.239	237.7	500	2.50	0.4311	0.429	0.49
	34.477	475.5	1000			0.427	0.98
	68.954	950.9	2000			0.423	1.95
	137.909	1901.9	4000			0.415	3.82
	275.818	3803.8	8000			0.399	7.34
Center point	17.239	237.7	500			0.428	0.75
	34.477	475.5	1000			0.425	1.50
	68.954	950.9	2000			0.418	2.95
	137.909	1901.9	4000			0.406	5.72
	275.818	3803.8	8000			0.385	10.81

Quarter point near the main tower	17.239	237.7	500		0.429	0.47
	34.477	475.5	1000		0.427	0.94
	68.954	950.9	2000		0.423	1.85
	137.909	1901.9	4000		0.415	3.63
	275.818	3803.8	8000		0.401	7.00
All 3 locations	17.239	237.7	500		0.424	1.70
	34.477	475.5	1000		0.417	3.34
	68.954	950.9	2000		0.403	6.46
	137.909	1901.9	4000		0.379	12.13
	275.818	3803.8	8000		0.338	21.56

The damping coefficient of TMDs, c, is calculated as follows:

$$c = 4m\pi f\xi \quad \textbf{(Eq. 5-1-3)}$$

where ξ is the damping ratio, taken as 2.5%, m is the additional mass by TMD, and f is the frequency of TMD, set as 1st order vertical bending mode frequency of 0.1098 Hz.

The stiffness of the TMD, k, is calculated as follows:

$$k = 4\pi^2 f^2 m \quad \textbf{(Eq. 5-1-4)}$$

As seen in Table 5-1-8, the heavier the TMD is, the better the mitigation effect of VIV.

iii) Counter-measure 3: V-shaped cable

Since the main cables on the side span and main span have significant movement due to the main girder VIV, a V-shaped damping cable is proposed to restrict the movement of the main cables and dissipate the VIV energy of the main girder. As seen in Figure 5-1-12 and Figure 5-1-13, the

V-shape cables connect the mid-point of the side span main cables and the corresponding location of the main span cables to a rotational damper at the tower-girder intersection. The cable is modeled as Combine14 damping elements, allowing movements in the longitudinal direction of the bridge. The effectiveness of the device with various damping capabilities is summarized in Table 5-1-9.

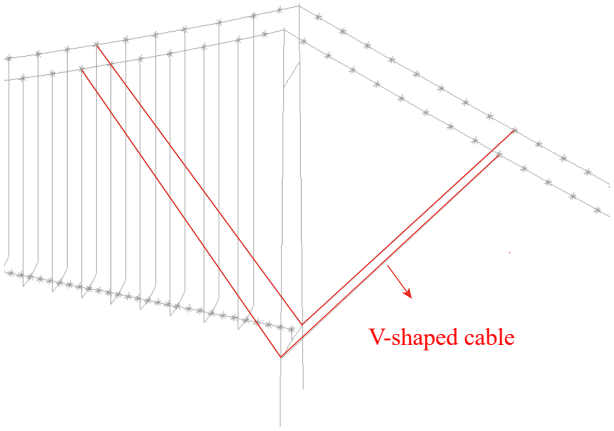

Figure 5-1-12: V-shaped damping cable

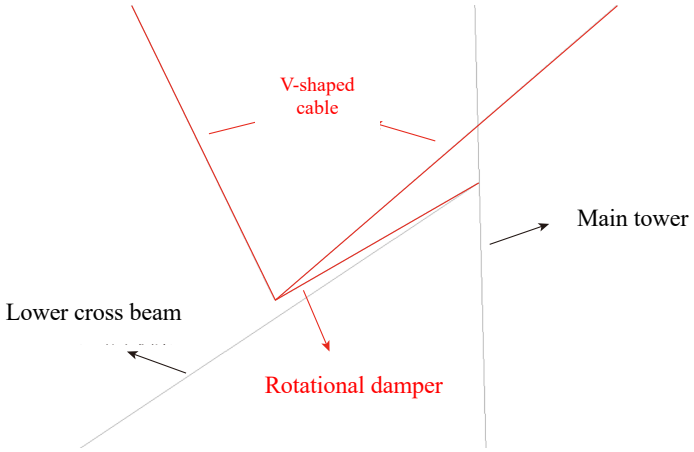

Figure 5-1-13: Damping device detail of the V-shaped damping cable

Table 5-1-9: Effectiveness of the devices

Damping coefficient (KN·s/m)	Midspan displacement before installation (m)	Midspan displacement after installation (m)	Change of displacement (%)	Change of displacement compared to 0 damping coefficient (%)
0	0.4311	0.4172	-3.23	N/A
50		0.3633	-15.74	-12.93
100		0.3216	-25.40	-22.91
200		0.2620	-39.22	-37.19
500		0.1723	-60.05	-58.71

It is notable that the V-shape damping cables increase the structural stiffness and, therefore, increase the structural model frequency slightly. According to the result in Table 5-1-9, this counter-measure effectively mitigates VIV on the main girder.

The V-shape damping cable is proven to be effective for the 1st order symmetrical vertical bending mode. In this part of the section, the device is tested on additional modes (1st order anti-symmetrical vertical bending mode, 2nd order symmetrical vertical bending mode), and the maximum mid-span displacements of the girder are consistently taken as 0.4311 m. The result is summarized in Table 5-1-10.

Table 5-1-10: Parameter analysis for V-shaped damping cable on higher order modes of the bridge

1st order symmetrical vertical bending mode					
Damping coefficient (KN·s/m)	**Midspan displacement before installation (m)**	**Midspan displacement after installation (m)**	**Change of displacement (%)**	**Change of displacement compared to 0 damping coefficient (%)**	**Equivalent damping ratio (%)**
0	0.4311	0.4172	-3.23	N/A	0.19
50		0.3633	-15.74	-12.93	0.21

100		0.3216	-25.40	-22.91	0.24
200		0.2620	-39.22	-37.19	0.30
500		0.1723	-60.05	-58.71	0.45
2nd order symmetrical vertical bending mode					
Damping coefficient (KN·s/m)	**Midspan displacement before installation (m)**	**Midspan displacement after installation (m)**	**Change of displacement (%)**	**Change of displacement compared to 0 damping coefficient (%)**	**Equivalent damping ratio (%)**
0	0.4311	0.4075	-5.49	N/A	0.19
100		0.2998	-30.46	-26.43	0.26
500		0.1362	-68.40	-66.57	0.57
1st order anti-symmetrical bending mode					
Damping coefficient (KN·s/m)	**Midspan displacement before installation (m)**	**Midspan displacement after installation(m)**	**Change of displacement (%)**	**Change of displacement compared to 0 damping coefficient (%)**	**Equivalent damping ratio (%)**
0	0.4311	0.4255	-1.30	N/A	0.18
100		0.2260	-47.59	-46.90	0.34

As seen in Table 5-1-10, the V-shaped damping cable is effective for 2nd order symmetrical vertical bending mode and the 1st order anti-symmetrical vertical bending mode. With 100 KN·s/m damping coefficients applied to the damping device for all three modes, the percentages of change in displacement are -25.4%, -30.46%, and -47.59%, respectively. Not only does the V-shaped damping cable remain effective for higher-order modes, its effectiveness also increases as the order of the mode increases.

5.2 Bearing support friction

5.2.1 Girder end displacement

For suspension bridges, the longitudinal stiffness of the girder is significantly higher than the bending stiffness of the girder. When the girder experiences bending deformation, the change in the total length of the girder is relatively negligible. Therefore, during VIV vibrations of the vertical bending mode, relative displacements between the girder ends and the bearing supports are induced due to structural nonlinearity. The concept is introduced on a simply supported beam in Figure 5-2-1.

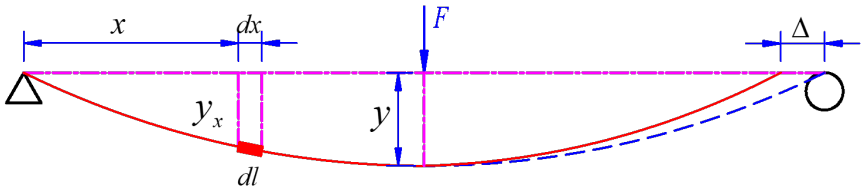

(a) Full span of the girder

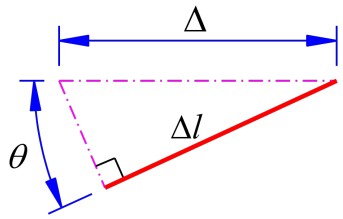

(b) Right support displacement

Figure 5-2-1: Girder end displacement of a simply supported girder

In Figure 5-2-1, a mid-span displacement of y is imposed by a point load F on the girder. The longitudinal displacement of the girder end is Δ, and it can be calculated by Eq. 5-2-1.

$$\Delta = \frac{\Delta l}{cos\theta} \qquad \textbf{(Eq. 5-2-1)}$$

where θ is the rotational angle at the right support, Δl is the difference between the girder length

and fix-support deflection curve length, as depicted in red and dashed line in Figure 5-2-1(a), respectively.

For any interval on the girder, the vertical deflection, *dy,* and rotation, θ_x, as shown in Figure 5-2-2, can be represented by Eq. 5-2-2.

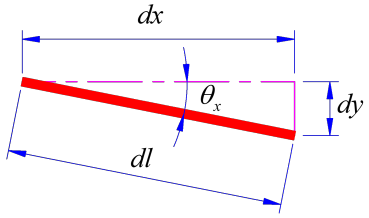

Figure 5-2-2: Deflection and rotation of the girder

$$\begin{cases} dy = \dfrac{F}{12EI} x\left(\dfrac{3}{4}l^2 - x^2\right) \\ \theta_x = \dfrac{F}{12EI}\left(\dfrac{3}{4}l^2 - 3x^2\right) \end{cases} \quad \textbf{(Eq. 5-2-2)}$$

where *x* is the x-coordinate of the interval, *l* is the girder's total length, *E* is the elastic modulus of the girder, and *I* is the moment of inertia of the girder section.

Assuming small angle approximation, the higher order of the equation can be neglected. The interval length, *dl*, can be described by Eq. 5-2-3.

$$dl = dx\left(1 + \frac{1}{2}\theta_x^2\right) \quad \textbf{(Eq. 5-2-3)}$$

The deflection curve length can be calculated by integrating the interval length over the girder length. Subtracting the girder length from the deflection curve length, Δl can be calculated, as shown in Eq. 5-2-4.

$$\Delta l = 2\int_0^{l/2} \sqrt{1+\theta_x^2}\, dx - l \qquad \textbf{(Eq. 5-2-4)}$$

Assuming small angle approximation and combining Eq. 5-2-1 and Eq. 5-2-4, the relationship between the maximum midspan displacement, *y,* and the longitudinal displacement of the girder end, Δ, for a simply supported beam with a point load in the center span is shown in Eq. 5-2-5.

$$\Delta = \frac{12y^2}{5l\cos\theta} \approx \frac{12y^2}{5l} \qquad \textbf{(Eq. 5-2-5)}$$

Similarly, the same relationship for a simply supported beam with distributed load is shown in Eq. 5-2-6.

$$\Delta = \frac{2176y^2}{875l} \qquad \textbf{(Eq. 5-2-6)}$$

To conclude, the girder end displacement of a girder can be expressed with the form shown in Eq. 5-2-7.

$$\Delta = \alpha y^2/l \qquad \textbf{(Eq. 5-2-7)}$$

where α is the coefficient for girder end displacement, *y* is the maximum vertical displacement of the girder, and *l* is the length of the girder.

5.2.2 Equation of motion for girder end displacement

For convenience in constructing the equation of motion for the girder end displacement, the girder is represented as a multi-degrees-of-freedom system, as shown in Figure 5-2-3.

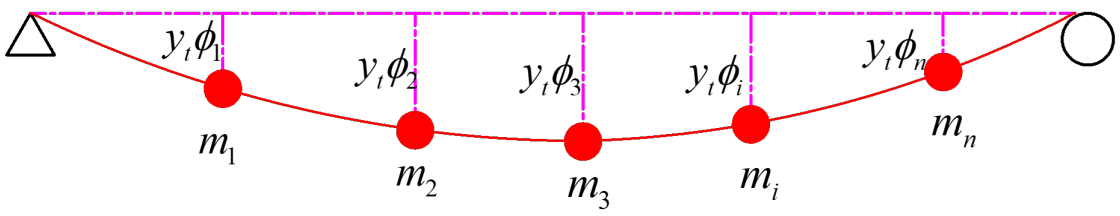

Figure 5-2-3: Multi-degrees-of-freedom representation of the girder

In Figure 5-2-3, m is the mass of each point, y is the vertical deflection of each point, and ϕ is the modal shape coefficient of each point. For this system with n degrees-of-freedom, M is the mass matrix, K is the stiffness matrix, y is the vertical displacement vector, and α is the coefficient matrix of girder end displacement. To clearly distinguish the effect of bearing support friction, no additional structural/non-structural damping capability is considered. The girder end displacement can be calculated as shown in Eq. 5-2-8.

$$\Delta = y^T \alpha y \qquad \textbf{(Eq. 5-2-8)}$$

Based on the principle of energy conservation, during an arbitrary time interval dt, the energy lost in the system is equal to the energy dissipated from girder end bearing friction, as described in Eq. 5-2-9.

$$\frac{1}{2}\dot{y}_t{}^T M \dot{y}_t - \frac{1}{2}\dot{y}_{t+dt}{}^T M \dot{y}_{t+dt} = (dy_t)^T K y_t + f_t d\Delta_t \qquad \textbf{(Eq. 5-2-9)}$$

where f is the bearing support friction force.

Combining Eq. 5-2-8 and Eq. 5-2-9, the equation of motion for girder vertical bending displacement with friction on the bearing support can be derived, as shown in Eq. 5-2-10 and Eq. 5-2-11.

$$\phi^T M\phi\ddot{y} + \phi^T K\phi y + 2f_t\phi^T\alpha\phi y = 0 \quad \textbf{(Eq. 5-2-10)}$$

$$M\ddot{y} + Ky + 2f_t\alpha y = 0 \quad \textbf{(Eq. 5-2-11)}$$

With the equation of motion of the girder vertical bending displacement, the equivalent damping effect of the friction on the bearing supports can be calculated with numerical integration.

5.2.3 Equivalent damping effect of bearing support friction

A sample calculation of the equivalent damping effect of the bearing support friction is carried out on a simply supported girder with a 100 m main span. The girder has a dead load of 300 kN/m, the stiffness (EI) is 3.91×108 kN·m, and 20 mass points are assumed on the girder section with a 5 m interval. Dynamic characteristics of the girder of vertical bending modes, such as modal frequencies and modal shapes, are extracted from the FEM model. The friction coefficients for the bearing support, *u*, are taken as 0.06 and 0.10.

Initial displacements based on 1st order vertical bending mode shape are imposed on the girder. The girder is then released to vibrate freely. The decay rate of the vertical bending displacement of the girder is monitored to calculate the equivalent damping effect of the friction on the girder. The result of the sample calculation is summarized in Table 5-2-1.

Table 5-2-1: Sample calculation result

Mode	Frequency (rad/s)	Generalized mass (kg)	Generalized stiffness (kN/m)	α	Equiv. damping effect($\cdot 10^5$)	
					u=0.06	u=0.10
1st order symm. Vertical bending	3.529	1529676	19050	2.40	7.30	12.16
1st order asymm. Vertical bending	14.116	1529676	304798	9.60	4.55	5.95
2nd order symm. Vertical bending	31.760	1529676	1542949	21.60	3.74	4.23
2nd order asymm. Vertical bending	56.457	1691168	5390412	38.40	3.29	3.58

As seen from Table 5-2-1, bearing support friction provides the effective equivalent damping capability for girder vibrating in vertical bending modes. The damping effect increases as the friction coefficient increases. It can be inferred that adding friction on bridge bearing supports can provide meaningful damping capability.

5.3 An AI-based detection method of VIV

This section explores a potential method that monitors the VIV dynamic characteristics of real bridge VIV events utilizing machine learning and computer vision techniques. In Chapter 3, a visual recognition and tracking method based on the open-source deep learning projects YOLOv5

and DeepSORT is discussed and applied to vortex tracking around CFD flow fields of various box girder sections. In this chapter, a similar recognition and tracking method is applied to monitor the amplitude, frequency, and mode shape of the VIV of the bridge by tracking the movements of target objects on bridges, such as roadside lamps and drainage outlets.

In recent years, the implementation of computer vision methods in the field of structural health monitoring (SHM) has reshaped the landscape of structural assessment and maintenance [135] [136]. In the field of bridge monitoring, scholars have explored the application of computer vision as well [137]. Pan et al. [138] developed a video deflectometer using the off-axis Digital Image Correlation (DIC) technique for real-time, non-contact, and targetless measurement of vertical deflection of bridges. Dong et al. [139] presented a vision-based structural dynamic displacement measurement method based on multi-point pattern matching and verified the result with on-site measured data from accelerometers. Li et al. [140] carried out on-site bridge VIV detection based on video inputs with DIC techniques and obtained sub-pixel level deformation information of the bridge girder. Zhao et al. [141] performed bridge VIV monitoring with the Channel and Spatial Reliability Tracker (CSRT) technique at five different locations on the bridge girder and estimated the bridge VIV dynamic characteristics based on a hand-held camera recorded video. Lin et al. [142] proposed a vision-based modal analysis framework based on frequency domain decomposition capable of directly performing modal decomposition on vision data of bridges without needing to recover the velocity and displacement. Wang et al. [143] established a contactless vision-based modal testing framework based on gradient-based matching via voting

(GMV) technique for identifying modal parameters of bridges in uncontrolled field conditions. The aforementioned methods provide sufficiently reliable results. However, these methods either require that the target objects remain in consistent environments, rendering them vulnerable to external environmental interference, or depend on multiple-device setups, making the result prone to cross-device systematic errors. Therefore, these methods are less than ideal for sustained, cost-effective, real-time bridge VIV monitoring over extended durations. Based on the above insufficiencies, Shao et al. [144]proposed a monocular vision-based three-dimensional displacement measurement approach for structures that utilizes machine learning algorithms and conducted experiments on cantilever beams, which yielded good results. The method is promising in the field of structural health monitoring. However, the experiments are conducted in close camera-to-object distances under laboratory condition and requires accurate camera calibration, thus is unproven for on-site structural monitoring from a distance and for bridge monitoring videos without prior camera calibrations.

To address the abovementioned technical challenges, this research introduces an innovative framework for bridge VIV dynamic characteristic monitoring, driven by computer vision and AI-based machine-learning target object detection and tracking techniques with keypoint detection. Due to its machine-learning nature, this framework exhibits robustness and flexibility in the presence of external interferences, such as temporary blockage and bridge environmental variations affecting target objects. The framework only requires a single-camera and an on-site or remote processing device setup, thus suitable for sustained and cost-effective real-time bridge

monitoring. It also offers versatile applicability, adaptive to scenarios with or without camera setup information through the utilization of camera calibration with homography matrix conversion and distance-based conversion methods. To improve the accuracy of VIV dynamic analysis recognition for videos with short duration, a peak/trough-based statistical method for calculating VIV frequency and amplitude is proposed. Through validation, the method's effectiveness in both real-bridge video recordings and simulated bridge VIV animations is validated using a single camera setup and a Python-supported data processing device, affirming its usability and robustness, as well as the potential for real-time bridge VIV monitoring and other applications such as wind tunnel experiment monitoring.

5.3.1 Preliminary tracking of roadside lamps

As a preliminary exploration for the VIV determination based on an AI-based detection method, the section tracks the coordinates of road-side lamps on the main span of bridges in a surveillance monitor video on the longitudinal direction of the bridge and converts the two-dimensional coordinates of the lamps on the video to a three-dimensional space to reveal the amplitude, frequency, and mode shape of the VIV.

In May 2020, a significant VIV phenomenon was observed on the Humen Bridge, a suspension bridge located in Guangdong, China, with a span of 888 m and was opened to traffic in 1997. The VIV phenomenon on the Humen Bridge underwent extensive media coverage and

attracted substantial public attention, and as a result, videos of VIVs on the Humen Bridge were widely circulated on the internet. Figure 5-3-1 shows a snapshot of a surveillance video found online that faced toward the longitudinal direction of the bridge when the VIV occurred.

Figure 5-3-1: Humen bridge VIV surveillance video
(https://youtu.be/TBmpGuzdvZ4)

By inspection of the video, it can be inferred that it is a recording of the surveillance monitor footage on a hand-held personal mobile device by the reporter of the news of VIV. Therefore, the video quality is subpar and visible camera movements are present. The traffic sign at the bottom right of the video is tracked to remove any rigid body vibration in the vertical and horizontal directions. The traffic sign appears to be mounted to the bridge tower on the girder level and can be considered a stationary point during the VIV of the bridge. The coordinates of the traffic sign are then tracked, and the change of its coordinates over time serves as a correction factor for the rigid vibrations of the video. The correction factor can be subtracted by the coordinates of other tracked objects to reduce the influence of the rigid body vibration of the vertical and horizontal

directions. The correction of vertical and horizontal rigid body vibration is shown in Eq. 5-3-1.

$$p(t)_{object-stable} = p(t)_{object-vibrate} - p(t)_{sign}$$

$$p(t)_i = (x(t), y(t))_i \quad \textbf{(Eq. 5-3-1)}$$

where *p(t)* is the coordinate of the objects in the video.

The movements of roadside lamps are tracked to monitor the VIV amplitude, frequency, and mode shape. Due to the limitation of the video resolution, the nearest six roadside lamps of the bridge main span on the left-hand side of the video are selected for recognition and tracking as they are relatively more recognizable than other lamps during the entirety of the video.

Twenty snapshots are marked manually for each of the six lamps selected and are used as the training set and the verification set during the training process in the YOLOv5 algorithm modified for this specific task. The training process lasted approximately 8,000 rounds, and the peak precision occurred around 7,000 rounds (96.5%), and the precision rate started to remain stable after around 4,500 rounds. The best weight file during the training process is used for recognition and tracking. Figure 5-3-2 shows a snapshot of the surveillance video in which the six nearest lamps of the main span on the left-hand side of the video are tracked.

Figure 5-3-2: Lamps tracked

The coordinates of the center of each tracking box for the lamps tracked are exported as text files and saved for post-processing. Since the distance between each lamp is known and equal, the relative scaling factors of the nearest lamp and the other lamps can be calculated by the following equation.

$$S = \frac{w_n}{w_1} = \frac{D - d * n}{D} \qquad \textbf{(Eq. 5-3-2)}$$

where S is the relative scaling factor, w_n and w_1 are the measured width of the n^{th} and 1^{st} lamp from left to right on the screen, d is the distance between lamps, which is 12 m according to Google map measurement, and D is the distance between the center of the first lamp and the infinite point of the bridge on the frame of the video and can be calculated with Eq. 5-3-2 with several measurements of the width of adjacent lamps.

It is noticeable that as the video is found online, the installation and technical specification of the surveillance camera is unknown. Therefore, it is difficult to calculate the exact vertical displacement of the lamps accurately. However, the relative displacement of the lamps, the modal

frequency, and the mode shape are obtainable. Figure 5-3-3 shows a snapshot of the vertical displacement of the lamps tracked in the three-dimensional space.

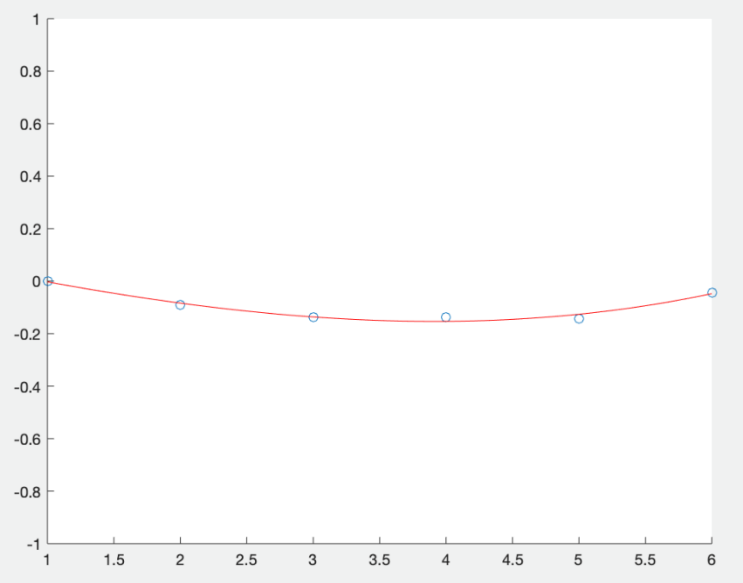

Figure 5-3-3: Lamps tracked (Amplitude (m) vs. Roadside lamps #)

As seen in Figure 5-3-3, a polynomial fitting curve is overlaid on the graph to demonstrate the mode shape of the girder within the tracked length of the bridge. The detection result based on the tracking of the nearest six roadside lamps of the bridge main span on the left-hand side of the surveillance video is summarized in Table 5-3-1.

Table 5-3-1: Parameter analysis for V-shaped damping cable on higher order modes of the bridge

	Estimated	**Onsite measurement** [145]
Mode shape	3rd order vertical bending	3rd order vertical bending
Frequency (Hz)	0.355	0.386

As seen in Table 5-3-1, the mode shape matched the information by Zhao et al. [145], and the vibration frequency does not match exactly with the frequency recorded by onsite investigation.

The accuracy needs to be further improved by changing the target object and utilizing more accurate detection, tracking, and post-processing methods.

5.3.2 AI-based VIV detection with drainage outlets

In the previous section, a preliminary exploration of the VIV monitoring based on machine learning and object detection for a recorded video is carried out with six roadside lamps as the target object. The initial functionalities were developed and a VIV frequency is estimated. This section further promotes the preliminary exploration and proposes a VIV dynamic characteristics monitoring framework utilizing AI-based machine-learning target object detection and tracking with keypoints. The framework uses drainage outlets on the side of the main girder as the target object and provides accurate frequency, amplitude, and mode shape monitoring results for a video of a bridge VIV event as well as a simulation animation of a bridge with VIV.

5.3.2.1 Detection and tracking based on machine learning

This framework utilizes open-source algorithms YOLOv8 [146] and ByteTrack [147] to perform target-object-based keypoint detection and subsequent keypoint tracking to achieve VIV dynamic characteristics determination in a video of a real bridge VIV phenomenon captured by a hand-held camera.

The target object detection and tracking tasks are performed in another video of a VIV event on Humen Bridge in Guangdong, China, on May 5th, 2020. For the detection task, the target

objects used are the drainage outlets of the box girder on the side of the girder section, as shown in Figure 5-3-4 and Figure 5-3-5.

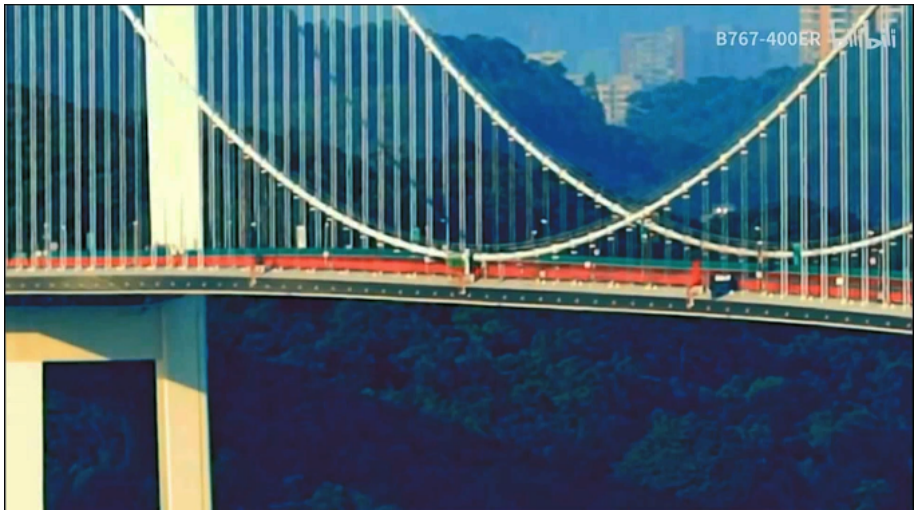

Figure 5-3-4: Drainage outlets on the side of the girder section

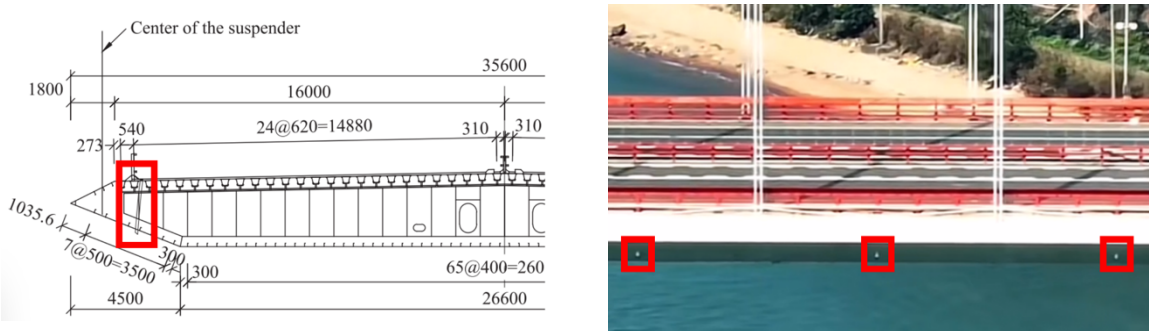

(a) Location of the outlets on cross-section **(b) Location of the outlets from the side**

Figure 5-3-5: Drainage outlets position on the cross-section of the girder

According to the design of the Humen bridge, the spacing between the drainage outlets along the girder is 12 m, and there are 73 outlets on each side of the main span girder. In the video where the detection and tracking task is performed [148], 48 outlets are visible throughout the 33.8-second video length, the movements of the drainage outlets in the video are sufficient to reveal the VIV dynamic characteristics of the bridge.

5.3.2.1.1 Object detection with detection boxes

The detection task is performed with the open-source algorithm YOLOv8, a computer vision model developed by Ultralytics that supports object detection tasks written on the Python framework.

YOLOv8 first uses a group of Convolutional-Neural-Network-based (CNN) machine learning models to develop a spatial feature of the target object from user-specified training and validation sets of labeled data. The model would then plot different sizes of grids to detect all objects in a picture or a frame in a video and utilizes the Non-Maximum Suppression (NMS) technique to filter out untargeted detection boxes by assessing their Intersection-Over-Union (IOU) value with the spatial feature of the target object generated from the machine learning model, thus accomplishing the object detection task. The YOLOv8 scans the picture or frame only once, hence the name YOLOv8 (You Only Look Once, 8th version). Figure 5-3-6 shows the flow chart describing the training and detection process above.

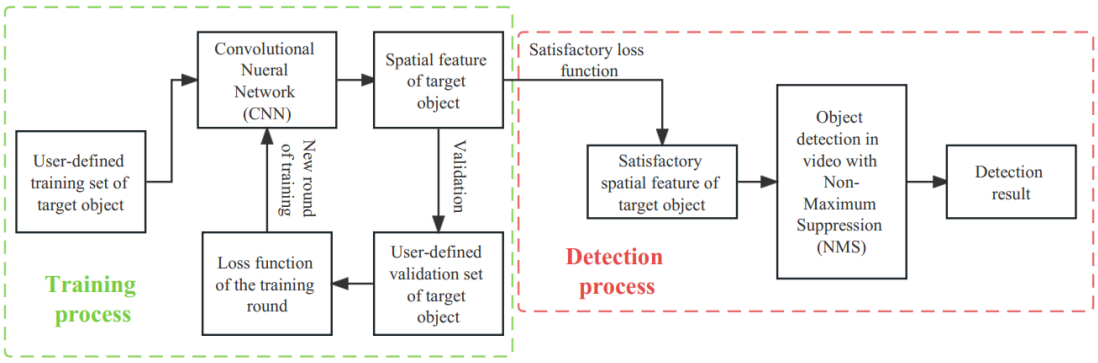

Figure 5-3-6: Flow chart for object detection based on YOLOv8

To achieve computer-vision-based VIV dynamic characteristic recognition, this framework first creates detection boxes for clearly visible drainage outlets in the video.

For the training of the machine learning models, twenty snapshots of the video are taken, and the drainage outlets in each of the snapshots are manually labeled with rectangular boxes using the labeling software LabelMe [149], which records the center point coordinates, width, and height of each labeled box. The twenty snapshots and their labeled boxes' information are randomly assigned to training sets (twelve snapshots) and validation sets (eight snapshots). The CNN-based machine learning model would then develop an initial spatial feature of the drainage outlets based on the labeled outlets in the training sets and compare it with the labeled outlets in the validation sets to generate a loss function that reflects how well the initial spatial feature describes the appearance of the drainage outlets in the validation set. The model would then fine-tune the parameters within the convolutional neural network until the loss function trends toward a positive direction, indicating that the spatial feature description of the drainage outlets is becoming more accurate, finishing a round of training. Figure 5-3-7 shows an example of the labeling of drainage outlets with rectangular boxes.

Figure 5-3-7: Labeling of outlets with rectangular boxes

For training of the drainage outlets, 1000 round of training is performed, which produces a spatial feature of the drainage outlets with a loss function value that indicates a satisfactory matching probability of the model's perception of drainage outlets compared to the labeled outlets in the validation sets. The spatial feature of the drainage outlets from machine learning is then input into the detection model of YOLOv8 to search for detection boxes of drainage outlets in each frame of the video.

With the detection box information, the approximate spatial ranges of drainage outlets in each frame are obtained. However, the center point location of each detection box does not necessarily represent the precise location of each drainage outlet. One reason for the inaccuracy originates from the manual labeling in the machine learning process. Further, as far as the detection model is concerned, it merely detects an object with a white center and a dark background. These two reasons lead to inaccuracy in detection box center locations and inconsistency of sizes of the same detection boxes from frame to frame, which produces errors in revealing the accurate locations of drainage outlets in different frames.

This inaccuracy can be improved by incorporating keypoint detection within each detection box. By adding a manually marked keypoint located at the center of each drainage outlet in the labeling stage using LabelMe during the machine learning process, the detection model could produce a more accurate result that reflects the coordinates of the outlets in each frame. Figure 5-3-8 shows the labeling of outlets with keypoints within rectangular boxes and the detection result.

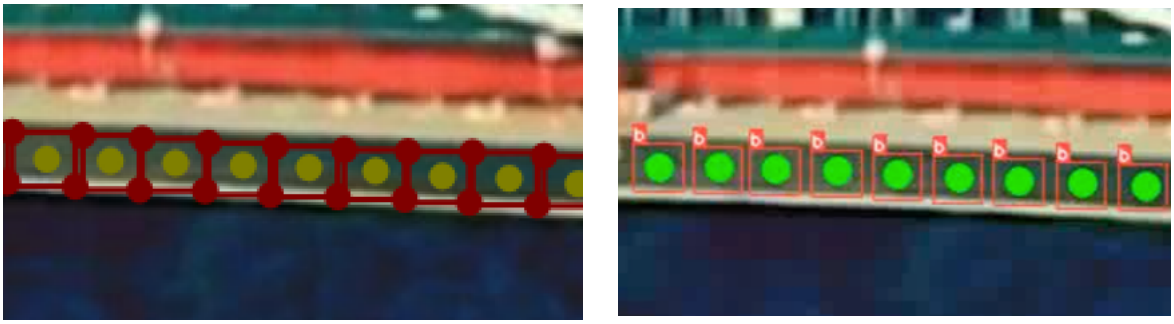

(a) Labeling **(b) Detection**

Figure 5-3-8: Labeling and detection with keypoints and rectangular boxes

For the detection of drainage outlets with keypoint and detection box, the detection box would first provide an approximate range in which the outlet is located, then the keypoint would give more accurate coordinates of the center of the outlet in the frame that could yield more reliable results for VIV dynamic characteristics determination.

5.3.2.1.2 Tracking of target objects

With the drainage outlets detected using detection boxes and keypoints, the next step is to track the movements of each drainage outlet in the video. An open-source algorithm named ByteTrack is used for object tracking in this framework.

ByteTrack assigns a unique ID for all detection boxes in the first frame of the video, then utilizes the Kalman filter [126] and the Hungarian algorithm [127] to maintain the same unique box ID for each box throughout the duration of the video. The Kalman filter extracts the temporal feature of a detection box or a keypoint and predicts their coordinates in the following frame, then uses the Hungarian algorithm to calculate and compare the IOU value based on the predicted location of the detection box and the location of all detection boxes in the following frame to identify the same detection box, thus maintaining the same unique ID for the box from frame to frame. Each keypoint in the detection box inherits the same unique ID from the detection box.

The tracking of detection boxes and keypoints is robust and adaptive to temporary blockage and graphical interference, such as lighting condition change, sudden blurriness, and change of color tone of the video, making it ideal for real-time monitoring, which is prone to environmental interference, as shown in Figure 5-3-9.

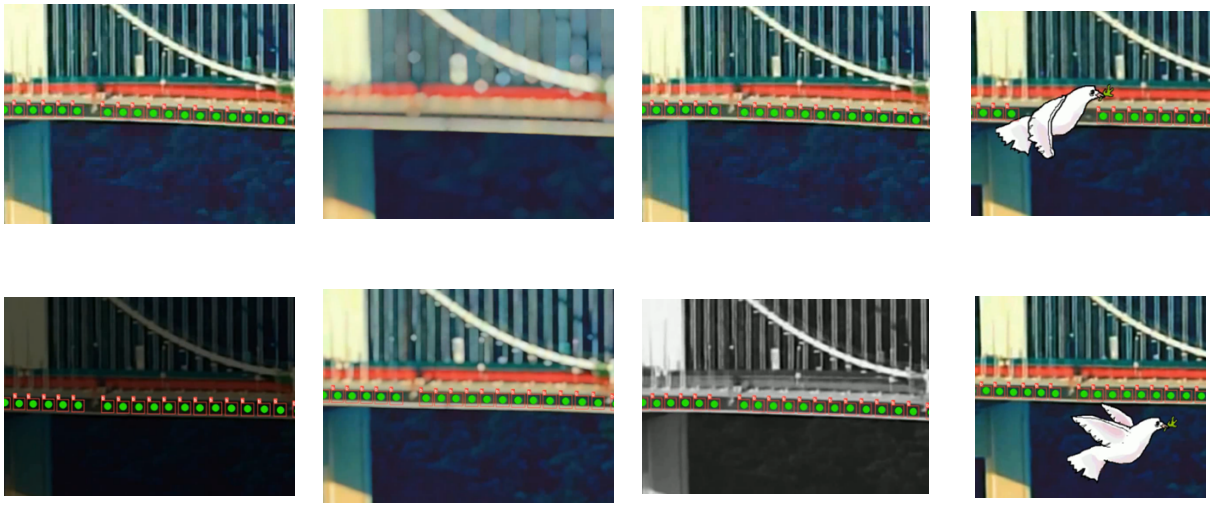

(a) Lower brightness **(b) Blurriness** **(c) Color tone change** **(d) Blockage**

Figure 5-3-9: Interference robustness of the tracking method

As seen In Figure 5-3-9(a), the detection boxes remain consistent when the lighting condition changes. In Figure 5-3-9(b), when a sudden blurriness occurs for the video, the detection boxes would recover quickly after the definition of the video recovers. In Figure 5-3-9(c), the detection boxes remain consistent when the color tone changes from color to black-and-white. In Figure 5-3-9(d), when the detection boxes are temporarily blocked, the detection boxes would recover quickly after the blockage.

5.3.2.2 VIV monitoring based on uncalibrated real bridge video

With the detection and tracking of drainage outlets introduced in the previous section, the time history of the two-dimensional coordinates of each drainage outlet throughout the duration of the video can be obtained. By extracting the coordinates of the detected keypoints in each frame,

the VIV shape of the bridge can be visualized, as shown in Figure 5-3-10.

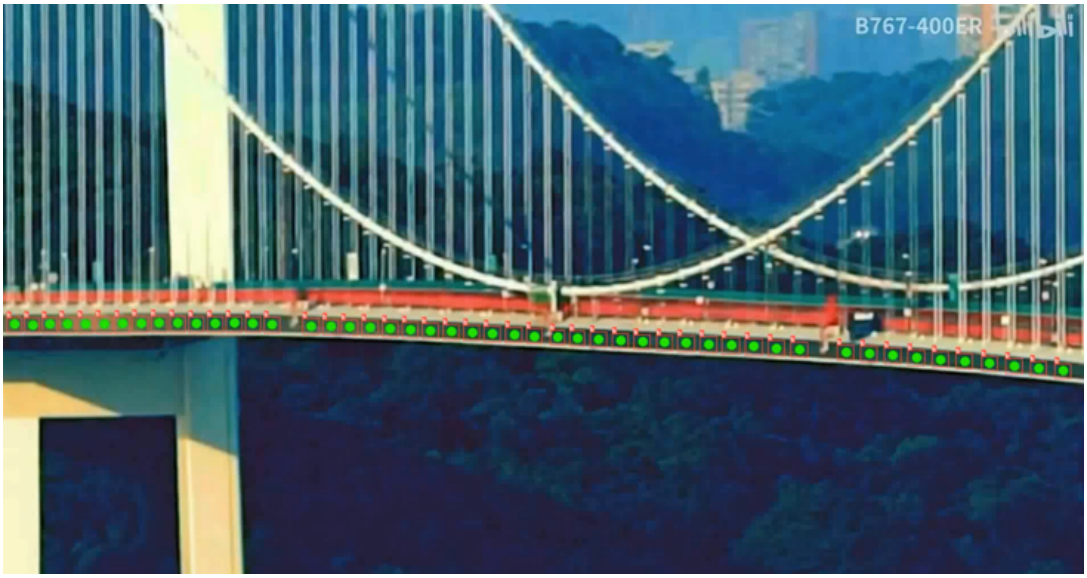

(a) Keypoint tracking

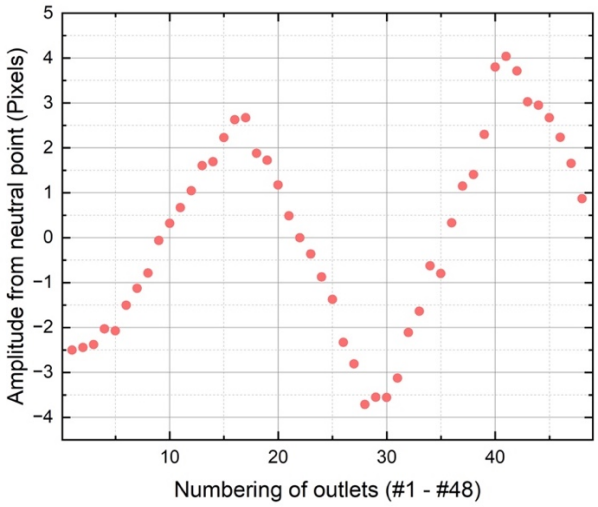

(b) Extracted results in MATLAB

Figure 5-3-10: Bridge VIV visualization

With further post-processing conducted in MATLAB [114], the coordinates of drainage

outlets can be used to reflect the VIV dynamic characteristics of the bridge, such as frequency, amplitude, and mode shape. On bridges where drainage outlets are not visible or installed, other structural/non-structural components such as roadside lamps, hangers, and crash barriers can be used as the target objects.

5.3.2.2.1 Distance-based conversion

As seen in Figure 7(a), the video is taken from an angle respective to the plane of the side of the girder. Based on the geometric perspective principle, the drainage outlets that oscillate with the same amplitude at different distances from the camera exhibit different object dimensions and amplitude. The ratio of this zooming effect follows a linear relationship with respect to the outlets' distances from the camera.

To adapt the zooming effect for videos taken from an angle, the zooming ratios of different outlets in the video need to be calculated. To calculate the zooming ratio of the drainage outlets located from the left to right side of the video, the distances between adjacent keypoints on the x-direction are extracted where the distances are normalized respective to the x-direction distance between the two keypoint furthest to the right of the video. Eq. 5-3-2 indicates the calculation of the zooming ratio.

$$R_n = \frac{x_{n+1} - x_n}{x_{48} - x_{47}} \qquad \textbf{Eq. 5-3-2}$$

where R_n indicates the zooming ratio around the n^{th} outlet in a frame, x_n is the median x-coordinate of the n^{th} outlet, x_{47} and x_{48} are the median x-coordinate of the two rightmost outlets.

The zooming ratio can be used to normalize the oscillation amplitude of all drainage outlets to a unified scale in the video. A schematic comparison between the ununified coordinates directly from the keypoints detection and the coordinates from the unified scale keypoint detection on the y-direction is shown in Figure 5-3-11.

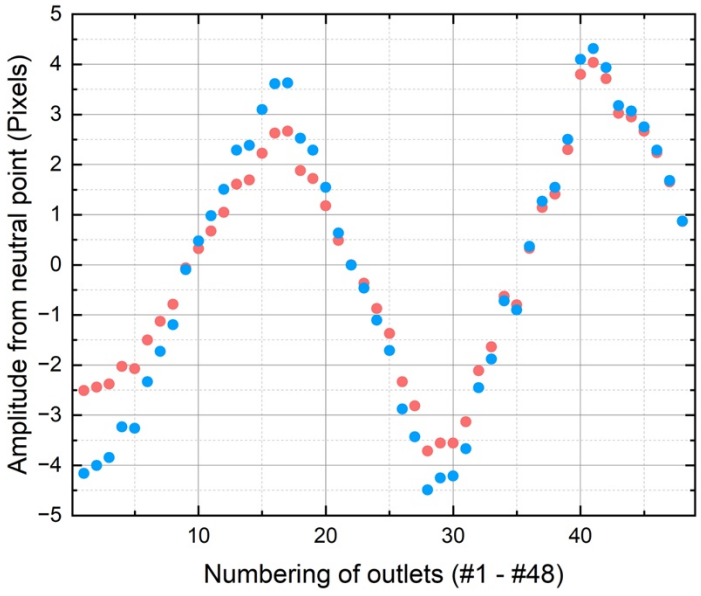

Figure 5-3-11: Keypoints coordinates from unified and ununified keypoint detection

From the unified scale, the oscillation amplitude in the world coordinate system can be calculated with Eq. 5-3-3.

$$y_{n,w} = \frac{y_{n,v}}{R_n} \times \frac{d}{x_{48} - x_{47}} \qquad \textbf{Eq. 5-3-3}$$

where $y_{n,w}$ is the y-direction amplitude of the n^{th} outlet in the world coordinate system, $y_{n,v}$ is the y-direction amplitude of the n^{th} outlet in the video coordinate system, d is the spacing between

drainage outlets in the world coordinate system, which equals to 12 m.

The VIV dynamic characteristics can be calculated with the keypoint coordinates from the world coordinate system.

5.3.2.2.2 Frequency determination

With the time histories of the y-direction movements of all keypoints detected, it is possible to calculate the VIV frequency of the girder section. The most straightforward method for such calculation is converting the time histories of y-direction movements into the frequency domain with the Fast Fourier Transformation (FFT) method. The predominant frequency of the keypoints movements is the VIV frequency of the girder. However, since the video analyzed has a short duration, the sample size for FFT is limited, and the direct result is that the frequency distribution (x-axis of the FFT) is relatively coarse. With the 33.8-second video duration and 60 fps frame rate, the FFT calculation yields a frequency step size of 0.0296 Hz. Conducting FFT calculations for movements of all 48 detected keypoints, the predominant frequencies are 0.3550 Hz for all keypoints detected, indicating that the frequencies for each keypoint all fall within the 0.0296 Hz range around the 0.3550 Hz frequency. Therefore, the FFT calculation is unsuitable for calculating accurate VIV frequency results based on videos with short durations.

To solve such inaccuracy in the VIV frequency calculation, this framework proposes a statistical method with peak-to-peak and trough-to-trough time duration measurement. Figure 5-3-12 shows how the peak-to-peak and trough-to-trough time durations are measured. Eq. 5-3-4

shows the calculation method.

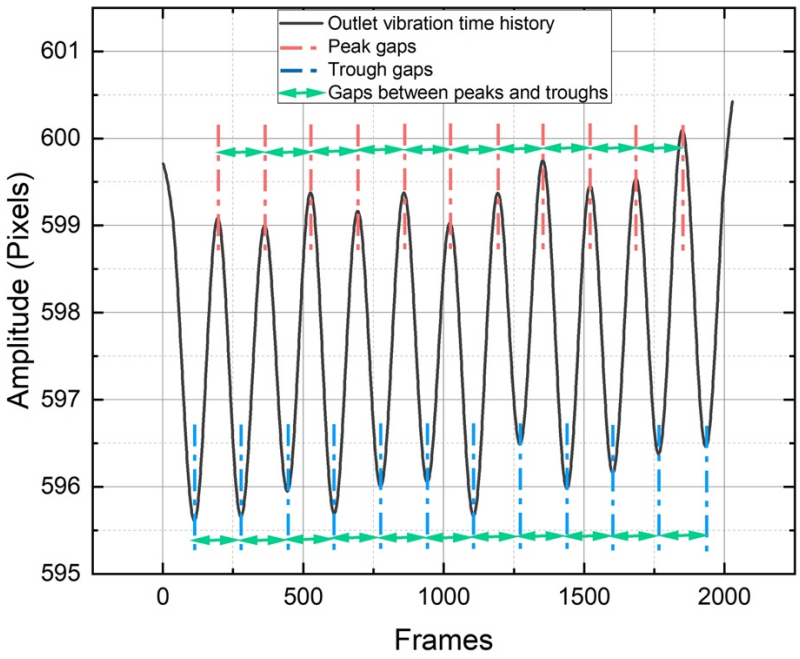

Figure 5-3-12: Schematic for peak/trough time durations

$$\begin{cases} g_{p,n} = t_{p,n+1} - t_{p,n} \\ g_{t,n} = t_{t,n+1} - t_{t,n} \end{cases} \quad \textbf{Eq. 5-3-4}$$

where $g_{p,n}$ and $g_{t,n}$ are the gap between n^{th} and $n+1^{th}$ peaks and between n^{th} and $n+1^{th}$ troughs, $t_{p,n}$ and $t_{t,n}$ are the time point where the n^{th} peak or trough occurs in the y-direction oscillation time history for a drainage outlet.

By gathering statistics on the time durations between adjacent peaks/troughs from the movement time history of all detected outlets, it is observed that the distribution of the time durations follows a normal distribution, as shown in Figure 5-3-13.

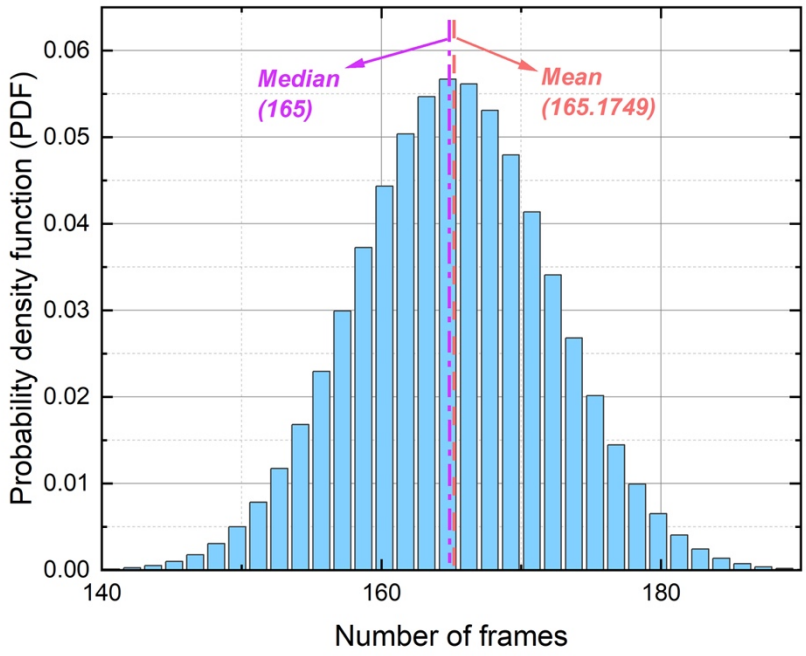

Figure 5-3-13: Distribution of adjacent peak and trough time duration

In Figure 10, 989 samples are included. The adjacent peak/trough time durations distribution is a relatively tight normal distribution with a small kurtosis value and slight negative skewness, indicating light tails and approximate symmetry on the normal distribution. The mean value of the peak/trough time duration is 165.175 frames, the median value is 165 frames, and the standard deviation is 7.023 frames. The 95% confidence interval is [164.737, 165.613]. The frequency of the VIV can be calculated with the frame values using Eq. 5-3-5.

$$f = \frac{fps}{n_{frame}} \qquad \textbf{Eq. 5-3-5}$$

where f is the frequency in Hz, fps is the frame-per-second value of the video, which is 60 fps,

n_{frame} is the time duration frame value.

The calculated frequency information based on the adjacent peak and trough time duration frame values and the comparable frequencies determined by Li et al. [140] and Zhao et al. [141] for the same VIV event is summarized in Table 5-3-2.

Table 5-3-2: VIV frequency based on adjacent peak and trough time durations

	Mean	Median	95% CI	Std. Dev.
Frequency (Hz)	0.3633	0.3636	[0.3623, 0.3642]	0.0154
Li et al. [140] (Hz)	0.3650		-	
Zhao et al. [141] (Hz)	0.3682		-	

Based on the mean value of the distribution of adjacent peaks and troughs, this research determines the VIV frequency to be 0.3633 Hz. Since the time duration distribution is discrete, and the frame-per-second value for the video is 60 fps, the precision of the VIV frequency is determined to be ±0.0083 Hz.

5.3.2.2.3 Amplitude determination

The time history of the y-direction movement of a detected keypoint is shown in Figure 5-3-14.

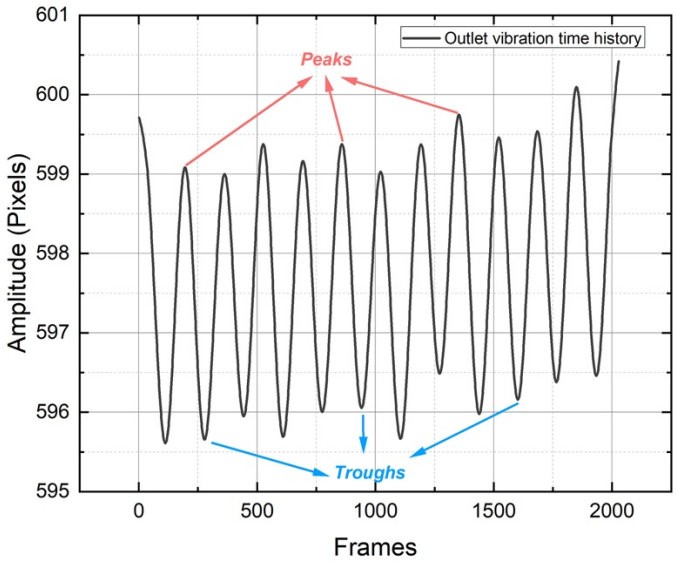

Figure 5-3-14: Time history of y-direction movement of keypoint #20

As seen in Figure 5-3-14, there is a clear upward trend of the oscillation movement of the keypoint over time. The trend is potentially due to the video's camera movement originating from the recording's hand-held nature. To minimize the effect of the camera movement on the calculation for VIV amplitude, a statistical method with peak-to-tough distance is proposed. Figure 5-3-15 shows a schematic for such a method.

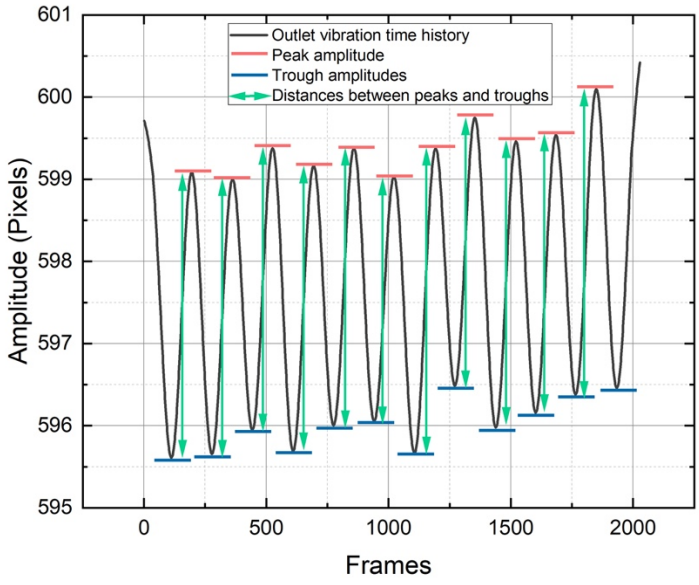

Figure 5-3-15: Peak-to-trough method

By measuring the y-direction distance between the adjacent peaks and troughs and gathering the statistics, the amplitude distribution for all detected keypoints can be calculated. Figure 5-3-16 shows the maximum amplitude of all keypoints detected in the world coordinate system.

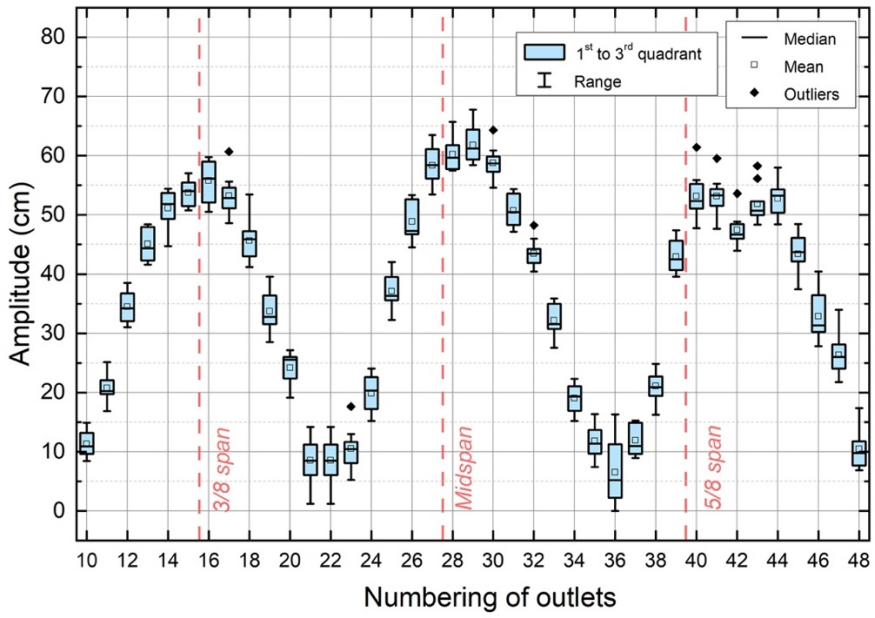

Figure 5-3-16: Maximum amplitude distribution for all keypoints

In Figure 13, the amplitude distribution of each keypoint detected over time is presented in a box plot format. The figure shows that the maximum amplitude occurs to the right of the mid-span. Near the 3/8 span and 5/8 span, there are two clear peaks as well. The maximum amplitude result of the VIV is summarized in Table 5-3-3.

Table 5-3-3: maximum amplitude for keypoints detected

Detection target	Location	Value (cm)
Amplitude (cm)	6 m to the right of 3/8 span	55.77
	18 m to the right of Mid-span	60.21
	6 m to the right of 5/8 spam	53.12

As summarized in Table 5-3-3, the maximum amplitude occurred at keypoint #29, 18 m to the right of the mid-span of the bridge, and has a value of 60.21 cm. The y-direction definition of the video (1080 pixels) controls the precision of the amplitude, and the value is determined to be ±3.54 cm.

5.3.2.2.4 Mode recognition

Based on the time history of the overall bridge vibration shape, the mode of the VIV can be determined by counting the number of peaks and troughs and comparing it with that from the dynamic characteristics determination from the bridge's FEM model. It is determined from the tracking result that there are three peaks and two troughs during the VIV of the bridge based on the video. By comparing the obtained mode shape from the detection with the mode shapes from the FEM modeling result of the bridge by Zhao et al. [141], the mode is determined as the 3rd order vertical bending mode. The mode shape from numerical analysis by Zhao et al. [141] is shown in Figure 5-3-17.

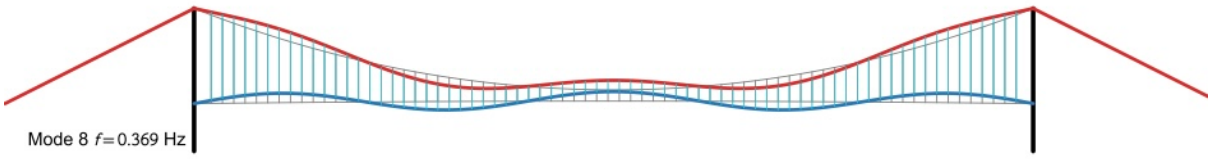

Figure 5-3-17: 3rd order vertical bending mode shape by Zhao et al. [141]

5.3.3 3D reconstruction based on a single camera and homographic conversion

5.3.3.1 Single-camera 3D reconstruction

The distance-based conversion method introduced in the previous section provided sufficient accuracy when camera setup information is unavailable. To further improve the conversion accuracy between the video coordinates system and the world coordinate system when camera setup information is available, a three-dimensional reconstruction (3D reconstruction) technique with a single camera setup is implemented in this framework.

The 3D reconstruction technique utilized in this framework is single-camera calibration with intrinsic and extrinsic matrices, which associates the coordinates of pixels in a video with the coordinates of their counterparts in the real world. Three coordinate systems are used in this technique, including the video coordinate system (VCS), the camera coordinate system (CCS), and the world coordinate system (WCS). A schematic of the single camera calibration is shown in Figure 5-3-17.

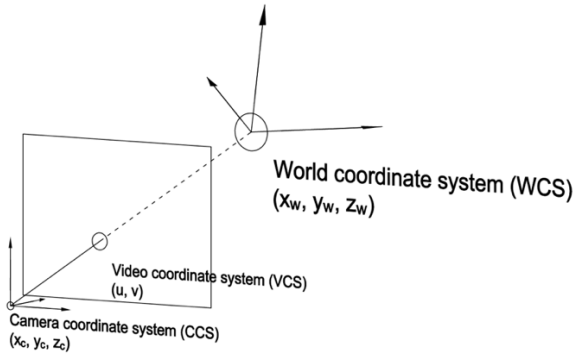

Figure 5-3-17: Single camera calibration

As seen in Figure 14, the WCS is at an angle and a distance compared to the CCS. To convert the object's coordinates from the WCS to the CCS, an extrinsic matrix including nine rotation terms and three translation terms is implemented, as shown in Eq. 5-3-6.

$$\begin{bmatrix} x_c \\ y_c \\ 1 \end{bmatrix} = \begin{bmatrix} r_1 & r_2 & r_3 & t_1 \\ r_4 & r_5 & r_6 & t_2 \\ r_7 & r_8 & r_9 & t_3 \end{bmatrix} \begin{bmatrix} X \\ Y \\ Z \\ 1 \end{bmatrix} \quad \textbf{Eq. 5-3-6}$$

where x_c and y_c are the point's coordinates in the CCS, X, Y, and Z are the point's coordinates in the WCS, the *r terms* are the rotation components in the extrinsic matrix, and the *t terms* are the translation components in the extrinsic matrix.

By multiplying the coordinates of the object in the WCS by the extrinsic matrix, they are converted to the CCS. An intrinsic matrix is used to convert the object's coordinates from the CCS to the VCS. Eq. 5-3-7 shows the intrinsic matrix for a camera in which the optical axis and sensor axis are aligned.

$$\begin{bmatrix} x \\ y \\ 1 \end{bmatrix} = \begin{bmatrix} f_x & 0 & c_x \\ 0 & f_y & c_y \\ 0 & 0 & 0 \end{bmatrix} \begin{bmatrix} x_c/Z_c \\ y_c/Z_c \\ 1 \end{bmatrix} \quad \textbf{Eq. 5-3-7}$$

where x and y are the point's coordinates in the VCS, Z_c is the z-direction distance between the point in the WCS and the CCS, f_x and f_y are the focal length of the camera on the x and y-direction, c_x and c_y are the coordinates of optical center in the VCS.

Combining the extrinsic matrix and the intrinsic matrix, the conversion of coordinates of a point from the WCS to the VCS is shown in Eq. 5-3-8.

$$Z_c \begin{bmatrix} x \\ y \\ 1 \end{bmatrix} = \begin{bmatrix} f_x & 0 & c_x \\ 0 & f_y & c_y \\ 0 & 0 & 0 \end{bmatrix} \begin{bmatrix} r_1 & r_2 & r_3 & t_1 \\ r_4 & r_5 & r_6 & t_2 \\ r_7 & r_8 & r_9 & t_3 \end{bmatrix} \begin{bmatrix} X \\ Y \\ Z \\ 1 \end{bmatrix} \quad \textbf{Eq. 5-3-8}$$

After the multiplication of extrinsic and intrinsic matrices, there are a total of eleven unknown parameters. Therefore, it requires six pairs of known coordinates from the WCS and the VCS to solve. However, in the cases of drainage outlet movement detection in this research, all drainage outlets are located in the same plane in the WCS. Therefore, the conversion can be simplified by setting the value of *Z* to zero in Eq. 5-3-8. The result of this simplification is the homography matrix conversion, as shown in Eq. 5-3-9.

$$Z_c \begin{bmatrix} x \\ y \\ 1 \end{bmatrix} = \begin{bmatrix} f_x & 0 & c_x \\ 0 & f_y & c_y \\ 0 & 0 & 0 \end{bmatrix} \begin{bmatrix} r_1 & r_2 & t_1 \\ r_3 & r_4 & t_2 \\ r_5 & r_6 & t_3 \end{bmatrix} \begin{bmatrix} X \\ Y \\ 1 \end{bmatrix} \quad \textbf{Eq. 5-3-9}$$

After multiplying extrinsic and intrinsic matrices in the homography matrix conversion, there are seven unknown parameters, and it requires only four pairs of known coordinates from the WCS and the VCS to solve. The conversion accuracy by the homography matrix can be further improved by utilizing the least square method with more than four known coordinates.

In the previous section, the distance-based conversion provides sufficient conversion functionality between the WCS and the VCS for the purpose of this research. While the homography matrix conversion requires additional information on the camera setup, including focal length and width/height of the video as well as at least four pairs of known coordinates from the world and video, it provides a more accurate, reliable, and systematic way for camera

calibration, which is beneficial for accurate real-time monitoring application of bridge VIV dynamic characteristics determination.

5.3.3.2 Bridge VIV animation detection verification

To demonstrate the application of the homography matrix conversion and distance-based conversion on bridge VIV monitoring, an animation for a bridge under the influence of VIV is created in Blender [150]. The bridge in the animation is a suspension bridge with a span of 1000 m, vibrating with a 100 m wavelength at a frequency of 0.5 Hz and an amplitude of 2 m. Circular shapes that are similar to the shape of the drainage outlets are attached to the side of the girder at a spacing of 20 m to represent the outlets and to serve as the target objects being detected. A chessboard with nine pairs of known coordinates is added to the same z-direction plane of the target objects to serve as the basis for camera calibration with homography matrix conversion. The focal length of the virtual camera that captures the bridge VIV movements and the chessboard is 50 mm on both the x and y-direction and is used for the intrinsic matrix calculation. The 20 m distance between the outlets is used to calculate the zooming ratios for the distance-based conversion. The animation setup is shown in Figure 5-3-18, and a snapshot of the captured video is shown in Figure 5-3-19.

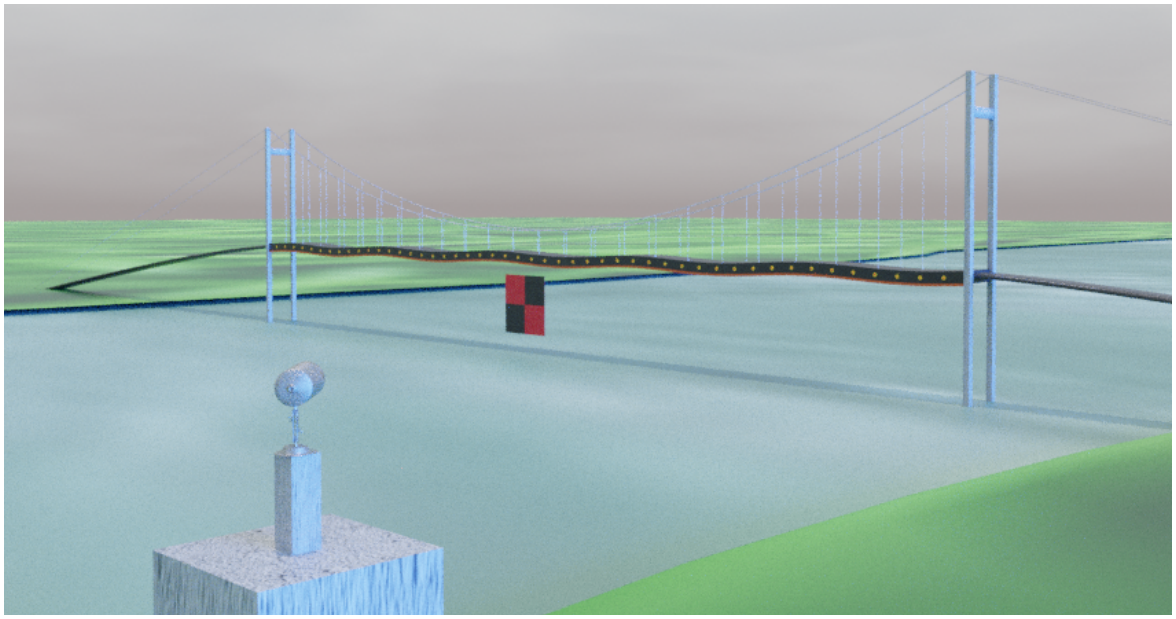

Figure 5-3-18: Animation setup

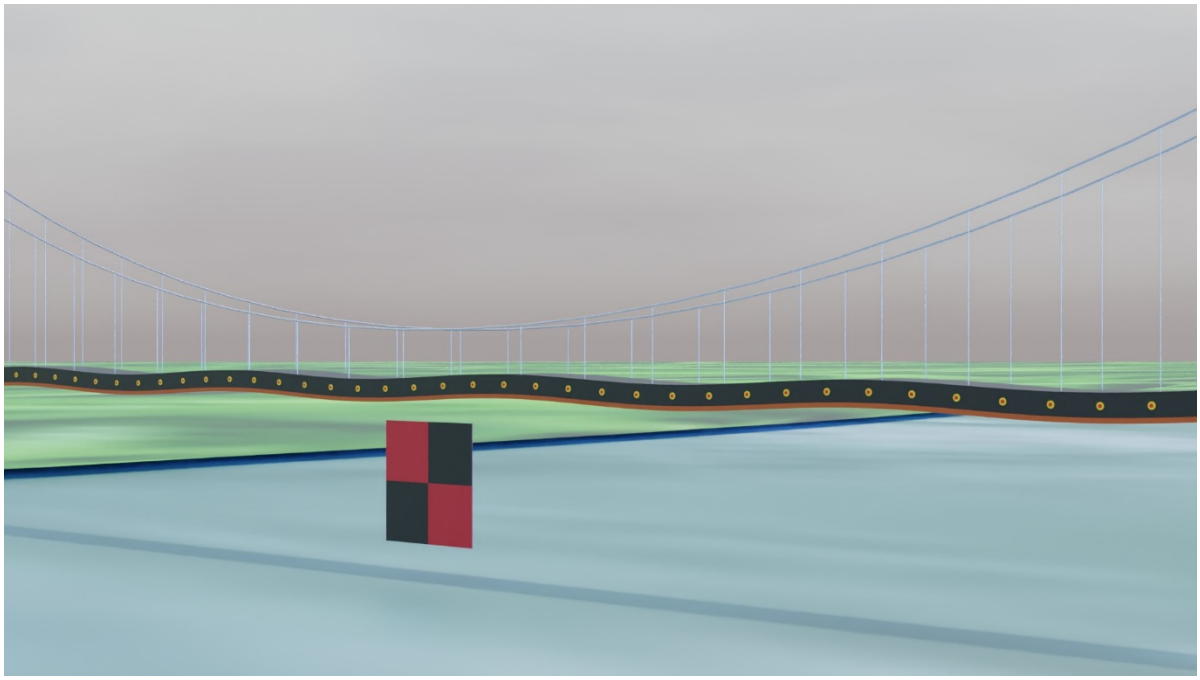

Figure 5-3-19: A snapshot of the captured video

The video is recorded, and the drainage outlets on the side of the girder (target objects), as

well as the chessboard, are put through the detection and tracking process introduced in the previous sections. For realistic purposes, blurriness is added to the video to simulate real-bridge monitoring conditions. Figure 5-3-20 shows a schematic for the labeling of the drainage outlets and the chessboard with rectangular boxes and keypoints.

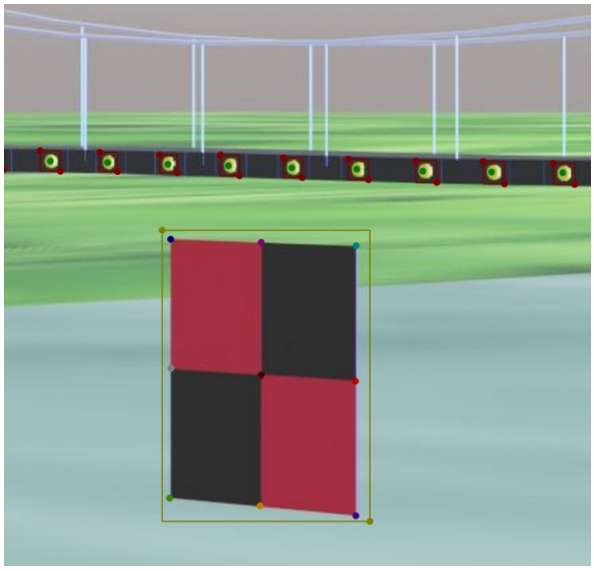

Figure 5-3-20: Labeling of outlets and chessboard

A schematic of the tracking result of the outlets in the animation is shown in Figure 5-3-21.

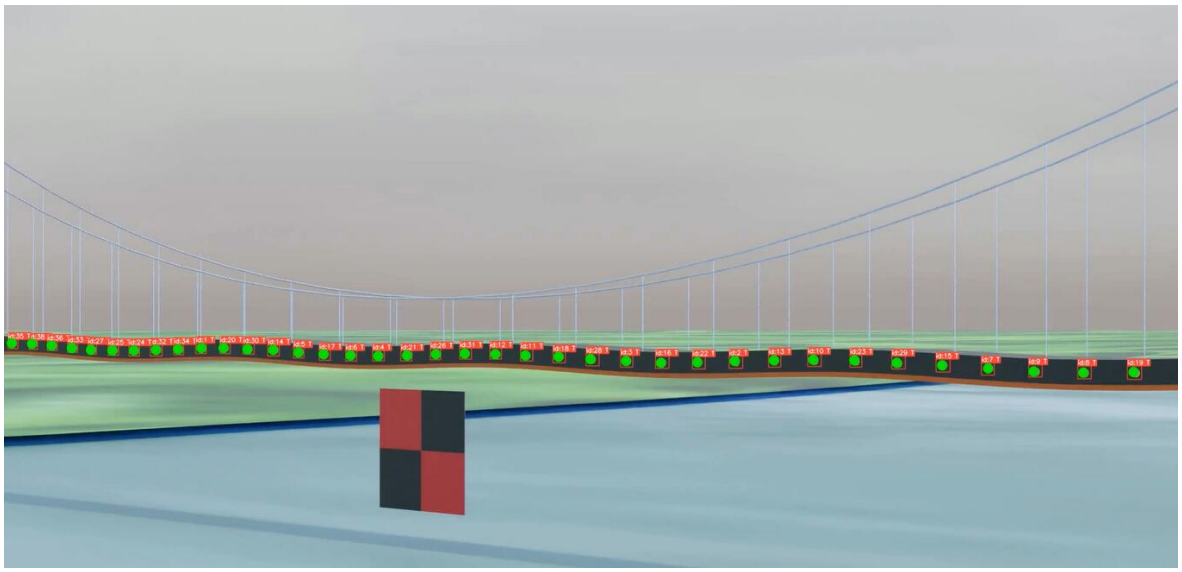

Figure 5-3-21: Tracking of the outlets

The frequency and the amplitude of the VIV are calculated using the methods introduced in previous sections. Homography matrix conversion and distance-based conversion are used in the camera calibration process of the calculation. The result is shown in Table 5-3-4.

Table 5-3-4: Result comparison

	Animation value	Homography matrix/95% CI	Distance-based/95% CI
Frequency (Hz)	0.4774	0.4768/±0.0009	0.4762/±0.0011
Amplitude (m)	2.0000	2.0027/±0.0266	1.9878/±0.0221

As seen in Table 5-3-4, the AI-based detection and tracking method results with the homography matrix conversion and the distance-based conversion match the actual VIV dynamic characteristics well. The calculation based on homography matrix conversion provided more accurate results as compared to the distance-based conversion method. However, both methods provided reliable results with small errors for the VIV frequency calculation (0.13% for

homography matrix conversion and 0.25% for distance-based conversion) and the VIV amplitude calculation (0.14% for homography matrix conversion and 0.61% for distance-based conversion). Based on the calculation results, it is concluded that when the camera setup is known, and prior camera calibration is possible, the homography matrix conversion provides better accuracy and reliability. In situations where these conditions are not met, such as for a dynamic characteristics determination for a bridge VIV event with an arbitrarily recorded video or a fast-response on-site measuring of a bridge VIV event, the distance-based conversion could provide reliable results as well.

5.4 Chapter Summary

In the first part of this chapter, several mechanical VIV mitigation measures are proposed and tested on a FEM model of the prototypical long-span suspension bridge with 1st order vertical bending VIV (0.4311m/0.1098 Hz) for their effectiveness. The mitigation measures include damping cables installed on the main cables, viscous damping devices installed at the midspan of the main span, bearing support damping devices, and longitudinal and rotational damping devices on hangers.

By comparing the effectiveness of various mechanical mitigation measures, damping devices installed on the bridge's main cables are the most effective option among all other options. Then, variations of damping devices installed on the bridge's main cables are further explored. A V-shaped cable connecting the main cables on the main span and side span with a rotational

damping device located at the tower-girder intersection is the most effective variation. With the V-shaped cable installed, the VIV amplitude of the bridge is reduced by as high as 58.71% (with 500 KN · s/m damping coefficients at the rotational damping device). The V-shaped cable VIV mitigation measure is tested on higher-order modes of VIV on the bridge, and its effectiveness increases as the order of the vibration mode increases. The equivalent damping effect of the girder-end bearing supports friction is discussed. The friction force is verified to improve the damping capability of the bridge and could potentially be an effective mitigation VIV measure as well.

In the second part of this chapter, an AI-based VIV detection method based on the machine learning and object-tracking method developed in Chapter 3 is first introduced. The method tracks the coordinates of target objects on the main span of bridges in a surveillance monitor video on the longitudinal direction of the bridge and converts the two-dimensional coordinates of the lamps on the video to a three-dimensional space with the geometric perspective technique to reveal the amplitude, frequency, and mode shape of the VIV.

To further promote the monitoring accuracy of the method, an innovative framework for bridge VIV dynamic characteristics monitoring with AI-based machine-learning target object detection and tracking with keypoint detection is proposed. Due to its machine-learning nature, this framework exhibits robustness and flexibility in the presence of external interferences, such as temporary blockage and bridge environmental variations affecting target objects. For videos taken from an angle and a distance from the target objects, camera calibration with homography matrix conversion is implemented when camera setup information is available to provide accurate

monitoring results. For videos without camera setup information, a distance-based conversion method with known spacing between target objects is proposed and yields satisfactory results as well. To improve the accuracy of VIV dynamic analysis recognition for videos with short durations, a peak/trough-based statistical method for calculating VIV frequency and amplitude is proposed. The framework is verified on a video recording of a real-bridge VIV event without camera setup information, as well as an animation of bridge VIV with camera setup information. Accurate detection is achieved in both cases. The VIV dynamic characteristics monitoring framework with AI-based machine-learning target object detection and tracking is promising in real-bridge VIV monitoring. Real-time VIV monitoring can be achieved with a single camera setup in the vicinity of the bridge and with an on-site or remote Python-supported device.

Chapter 6 Conclusions and Future Work

This research explored the initiation mechanism, comfort level, and magnitude control of VIV on box girder suspension bridges utilizing methods of girder section wind tunnel experiment, bridge FEM modeling in ANSYS Workbench, flow field CFD analysis in ANSYS Fluent, and data analysis using MATLAB and Pycharm. A suspension bridge currently under construction with a main span of 1760 m is used as the prototypical bridge for this research. The conclusions from this research are summarized in this chapter.

6.1 Initiation mechanism of VIV for box girder sections with various aerodynamic shapes

To analyze the initiation mechanisms of VIV on suspension bridges with box girders, this research starts by analyzing the most generic box girder section shape, the rectangular box girder sections. Further, on the basis of the rectangular girder sections analysis, triangular wind noses are installed on the two ends of the rectangular girder sections, and the rectangular box girder section with wind noses is studied. The analysis of the rectangular girder sections with wind noses takes one step closer to the streamlined girder section shape that most box girder bridges adopt. Finally, a streamlined box girder section from the design of the prototypical long-span suspension bridge is analyzed to reveal the actual mechanism of VIV around the box girder section on real long-span suspension bridges. The analyses mentioned above are discussed in Chapter 2 and Chapter 3.

Chapter 2 focuses on exploring the initiation mechanism of VIV for rectangular girder sections and rectangular girder sections with wind noses installed. Girder sections of interest are first tested in wind tunnel experiments for their dynamic VIV responses and then simulated in CFD analyses to monitor the flow field characteristics around the girders.

From the wind tunnel experiments, it is observed that there exist two lock-in ranges for both the vertical bending mode and rotational mode of the 1:6 and 1:7.875 rectangular girder section. When wind noses are installed on the rectangular sections, there only exists one obvious lock-in range for both modes of the 1:6 and 1:7.875 rectangular girder sections with wind noses.

A vortex recognition and path tracking method is proposed based on mass monitoring points setup (MPF-track). By tracking the path of vortexes around the rectangular girder sections, a vortex merging pattern that reduces the number of vortexes on the upwind side of the girder to its half on the downwind side of the girder is observed. It is concluded that this decrease in the number of vortexes on the upwind and downwind sides of the girder is the cause for the two VIV lock-in range phenomena.

For rectangular girder sections with wind noses installed, similar to that of rectangular girder sections, there also exist several vortex shedding mechanisms on the upwind side and downwind side of the girder, which would lead to the multi-order lock-in ranges phenomenon. However, for both the vertical bending mode and the rotational mode, there is one lock-in range with a significantly smaller lift force (rotational moment) when compared to the other one. Therefore, although there are still two lock-in ranges for each mode, one is smaller than the other,

leading to only one obvious VIV lock-in range in these types of scenarios.

Chapter 3 focuses on exploring the initiation mechanism of VIV for a streamlined girder section and its VIV performance with various aerodynamic VIV mitigation measures installed. A 1:50 streamlined girder section model with and without the aerodynamic measures installed is first tested in wind tunnel experiments for their dynamic VIV responses and effectiveness of aerodynamic measures and then simulated in CFD analyses to monitor the flow filed characteristics around the girders to explore the VIV mechanisms of the girder section. To evaluate the influence of the Reynolds number effect for wind tunnel experiments with different scaling factors, a 1:20 streamlined girder section model is tested in wind tunnel experiments.

The original section is tested in the 1:50 streamlined girder section wind tunnel experiments, and two vertical bending VIV lock-in ranges and one rotational mode VIV lock-in range are observed. The streamlined girder section is then tested with various aerodynamic VIV mitigation measures installed, among which the 0.67 m central stabilizing board and the 1.35 m horizontal stabilizing board are the most effective. When the two measures are installed as a combination on the streamlined girder section, the VIV response of vertical bending and rotational modes are effectively reduced.

Since the flow field is more complex for streamlined girder sections when compared to the flow fields around the rectangular girder sections with or without wind noses discussed in the previous chapter, especially when aerodynamic measures and accessory non-structural components are installed, a visual vortex recognition and tracking method based on Convolutional

Neural Network (CNN) and machine learning (YOLOv5/DeepSORT) is utilized in this chapter for easier and less time-consuming vortex tracking. The method uses weight files obtained from two separate machine learning processes that contain the spatial and temporal features of vortexes to recognize and track the development of vortexes. The initial spatial feature weight file is optimized in accordance with the visual characteristics of the vortexes to increase recognition machine learning efficiency. The tracking process is capable of tracking the merging processes of vortexes as it utilizes the Kalman filter and the Hungarian Algorithm.

CFD analyses revealed different frequencies of total lift force and rotational moment on the girder. By utilizing the AI-based vortex tracking method, it is revealed that the vortex shedding frequency on the upwind side is approximately twice that on the downwind side. By inspection, when compared to the rectangular box girder section with wind noses, the upper half of the wind noses on the streamlined girder section has a steeper inclination, which led to vortexes with higher magnitude, thus causing the two VIV lock-in range to appear in the vertical bending mode. The wind noses appear to have reduced the influencing range of the vortexes and, therefore, decreased the moment arm of the vortex mechanisms on the upwind side, showing only one obvious VIV lock-in range for the rotational mode.

By comparing the result from the 1:50 and the 1:20 streamlined girder section wind tunnel experiments, the influence of different Reynolds number conditions in wind tunnel experiments is discussed. It is found that when compared to that under the high Reynolds number condition, the girder section under the low Reynolds number condition is more critical as it experiences more

VIV lock-in ranges and higher unified amplitude in both modes considered.

6.2 Comfort level for drivers and passengers in vehicles on bridge under VIV

During VIV events on long-span suspension bridges, the movements of the main girders could cause discomfort for drivers and passengers in vehicles traveling on bridges, which is a potential safety hazard. This part of the research proposes a methodology for determining the comfort level of drivers and passengers on suspension bridges under VIV based on the vibrational serviceability of the human body via wind-traffic-bridge (WTB) coupled vibration analysis.

In Chapter 4, a wind-traffic-bridge (WTB) coupling vibration model is established. Based on the coupling vibration model, the displacement, velocity, and acceleration that vehicles and pedestrians experience on the bridge during different modes of VIV can be calculated. With the dynamic responses of vehicles and pedestrians on a bridge under VIV, the OVTV and MSI index can be calculated using a proposed Fast Fourier Transform Convolution method to evaluate the comfort level experienced by the drivers, passengers, and pedestrians. The calculation is performed on the prototypical long-span suspension bridge of this research for verification. The main conclusion of Chapter 4 is summarized as follows:

1. In cases where no road surface roughness is present on a bridge, the dynamic response of the bridge girder is a good indicator of the dynamic response experienced by the vehicle.

2. The comfort level represented by OVTV is not significantly influenced by VIV events

because the common frequency ranges of VIVs (0-0.5 Hz) do not fall within the applicable frequency range of OVTV (0.5-80 Hz).

3. VIV mainly influences comfort level represented by the MSI index. Vibration amplitude, length of vibration, and frequency of vibration are the main influencing factors, while factors such as wind speed and road surface roughness do not contribute much to the MSI index.

6.3 Mechanical measures and AI-based detection method for VIV on long-span suspension bridges

In Chapter 3, several aerodynamic VIV mitigation measures installed on the streamlined girder section are proposed and tested for effectiveness. Although these aerodynamic measures effectively reduce the magnitude of VIV displacement for the streamlined girder section, the VIV response is not entirely mitigated, and their applicability to girder sections of other shapes is not verified. Chapter 5 focuses on developing mechanical VIV mitigation measures that supplement the aerodynamic mitigation measures and are effective for wider application on other long-span suspension bridges regardless of the aerodynamic shapes of their box girder sections.

In Chapter 5, several mechanical VIV mitigation measures are proposed and tested on a FEM model of the prototypical long-span suspension bridge with vertical bending VIV for their effectiveness. The mitigation measures tested include damping cables installed on the main cables, viscous damping devices installed at the midspan of the main span, bearing support damping

devices, and longitudinal and rotational damping devices on hangers.

By comparing the effectiveness of various mechanical mitigation measures, damping devices installed on the bridge's main cables are the most effective option among all other options. Then, variations of damping devices installed on the bridge's main cables are further explored. A V-shaped damping cable connecting the main cables on the main span and side span with a rotational damping device located at the tower-girder intersection is the most effective variation. With the V-shaped damping cable installed, the VIV amplitude of the bridge is reduced by as high as 58.71% (with 500 KN·s/m damping coefficients at the rotational damping device). The V-shaped cable VIV mitigation measure is tested on higher-order VIV on the bridge, and the results are satisfactory. The equivalent damping effect of the girder-end bearing supports friction is discussed. The friction force is verified to improve the damping capability of the bridge and could potentially be an effective mitigation VIV measure as well.

An innovative framework for bridge VIV dynamic characteristics monitoring with AI-based machine-learning target object detection and tracking with keypoint detection is proposed in Chapter 5. Accurate frequency, amplitude, and mode shape detections of the bridge VIV are achieved with a video of a bridge VIV event and a simulation animation video of bridge VIV.

6.4 Future Work

Regarding the mechanism of the VIV of various box girder sections, this research focused

on exploring the initiation mechanism. After obtaining the dynamic response of the girder sections from separate wind tunnel experiments, research efforts are aimed at the flow field characteristics around stationery girder sections in CFD analyses. Therefore, the research on flow field characteristics around dynamic girder sections and the VIV mechanism during the lock-in ranges is lacking. Further effort should be taken on this topic.

One possible first step is utilizing machine learning and visual tracking methods of vortexes around the dynamic girder section introduced in Chapter 3 for the dynamic girder section during VIV in CFD analyses. In present studies, scholars have mostly focused on time-average flow field characteristics around stationary and dynamic girder sections to study the VIV mechanisms. In this research, the studies for VIV mechanisms rely more on tracking individual vortexes, and functionalities such as vortex recognition, vortex tracking, and vortex merging detection are developed based on machine learning and visual recognition. For the dynamic girder section CFD analysis, these functionalities can be further developed and used to study the lock-in phenomenon of VIV by tracking vortexes as well as the girder movements during the VIV.

The Reynolds number effect is another topic that could be further studied from this research. Chapter 3 briefly discussed the Reynolds number effect by comparing the VIV response wind speed range and displacement amplitude of a 1:20 streamlined girder section model and a 1:50 streamlined girder section model. The 1:20 model has a higher Reynolds number and exhibited fewer VIV lock-in ranges and smaller VIV amplitude for both the vertical bending mode and the rotational mode compared to the VIV response of the 1:50 model, which has a lower Reynolds

number. Further studies can be carried out on this topic as discussed as follows.

The Reynolds number is generally considered to measure how turbulent the flow field around a girder section is. The lower the Reynolds number, the less turbulent the flow field is. For sections with a pointy leading edge (such as the wind nose on the streamlined girder section), the Reynolds number effect is commonly disregarded as the wind nose serves as a distinctive separation point for the incoming flow. However, for the streamlined girder section, the turning corner between the wind noses and the road surface is another location influencing the Reynolds number effect. The flow field is less turbulent for the smaller 1:50 girder section with the lower Reynolds number. Therefore, the vortexes generated at the turning corner between the wind nose and the road surface can potentially travel differently compared to those generated at the same location on the 1:20 girder section, which has the higher Reynolds number. Their reattachment locations could also be different. As a starting point, the vortex recognition and tracking method based on machine learning can be utilized here to track how the vortexes travel and reattach to the girder surface under different scaling factors and Reynolds number conditions.

Another application of machine learning and visual recognition is detecting and monitoring VIV incidents on bridges and their respective amplitude and mode shapes based on surveillance monitoring videos. Present studies mainly utilized the Digital Image Correlation (DIC) method. The DIC method tracks the movement of the same pixels in two adjacent video frames to detect deformation and movements of the bridge deck for VIV amplitude and mode shapes. However, since the method relies heavily on the consistency of the same pixels, the recognition is easily

influenced by lighting, background change, pedestrians and vehicles passing by, etc. To overcome the said technical difficulties, this research proposes a VIV dynamic characteristics monitoring framework utilizing AI-based machine-learning target object detection and tracking with keypoint tracking. The framework uses drainage outlets on the side of the main girder as the object and provides accurate frequency, amplitude, and mode shape monitoring results for a video of a bridge VIV event as well as a simulation animation of a bridge with VIV. The VIV dynamic characteristics monitoring framework with AI-based machine-learning target object detection and tracking is promising in real-bridge VIV monitoring. The next step is to implement the real-time bridge VIV monitoring application of this framework with a single camera setup in the vicinity of the bridge and with an on-site or remote Python-supported device. Other applications of the framework such as girder section models monitoring during wind tunnel experiments should be looked into as well, as this framework is an applicable non-contact alternative to the current wind tunnel experiments monitoring system based on LASER transducers often installed close to the models. The monitoring device can be placed on the downwind side of the models to avoid flow field interference for the experiment, which is crucial in obtaining accurate and reliable results.

Chapter 7 Appendices

Appendix I. Selected aerodynamic measures from 1:50 girder section model

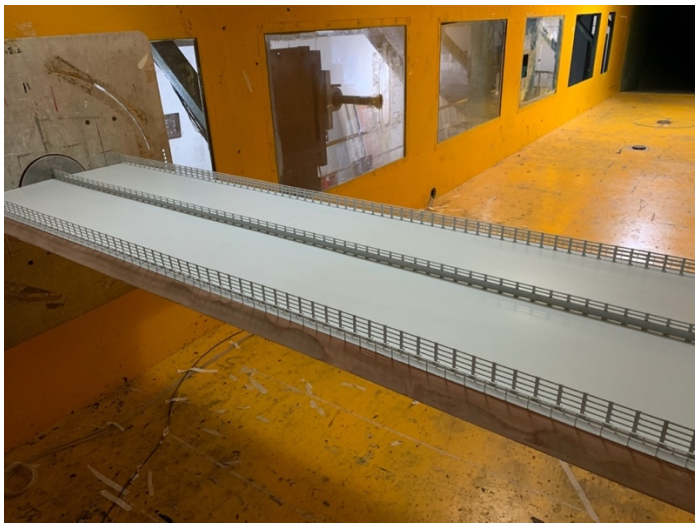

A- 1: 0.67m central stabilizing boards

A- 2: 1.02m central stabilizing board

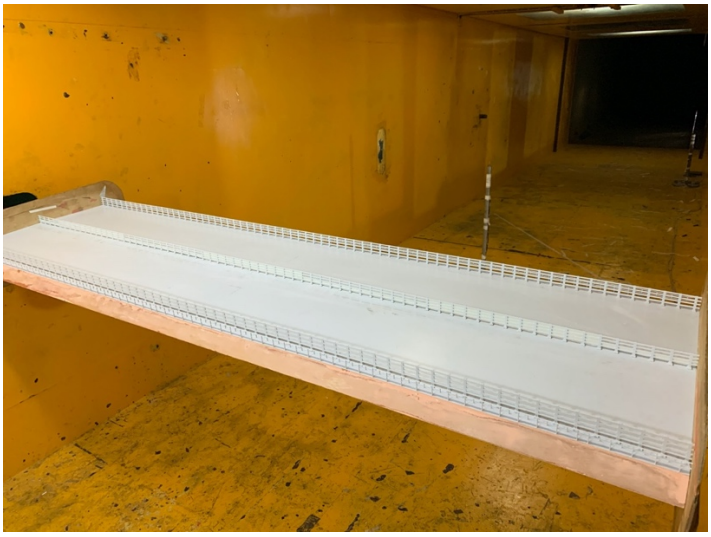

A- 3: Varying height stabilizing board on upwind side

A- 4: Varying height stabilizing board on the downwind side

A- 5: T-top central stabilizing board

A- 6: Bottom central stabilizing board

Appendix II. Mode shapes from FEM analysis

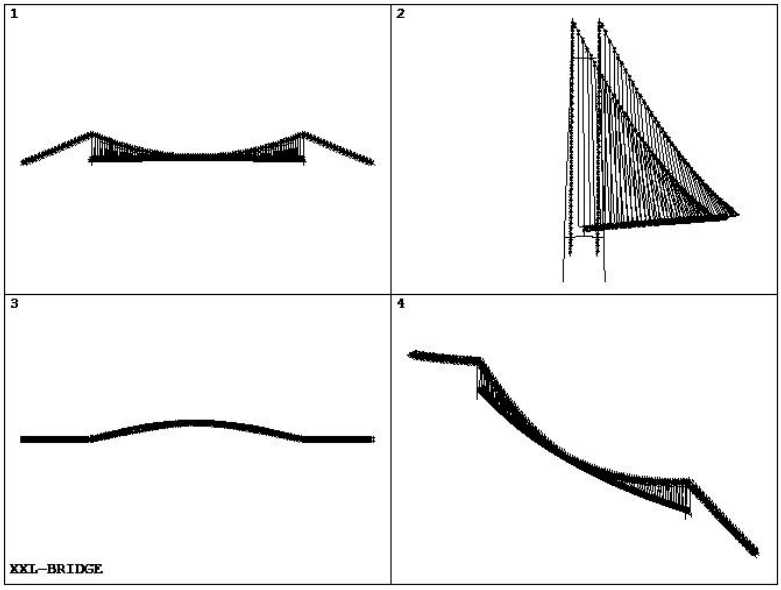

A- 7: Mode 1 shape

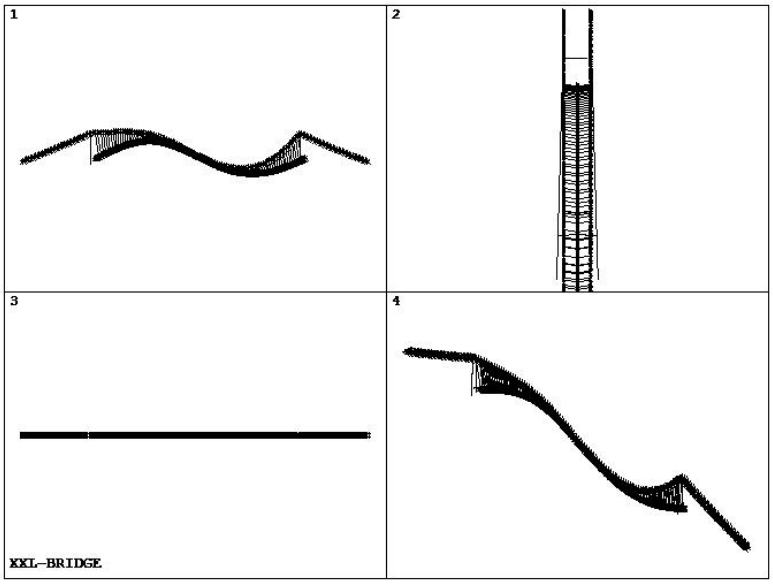

A- 8: Mode 2 shape

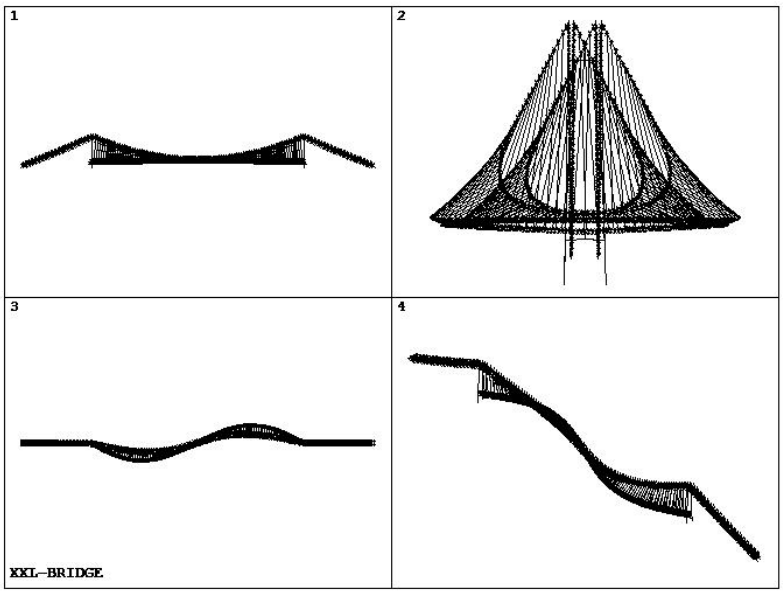

A- 9: Mode 3 shape

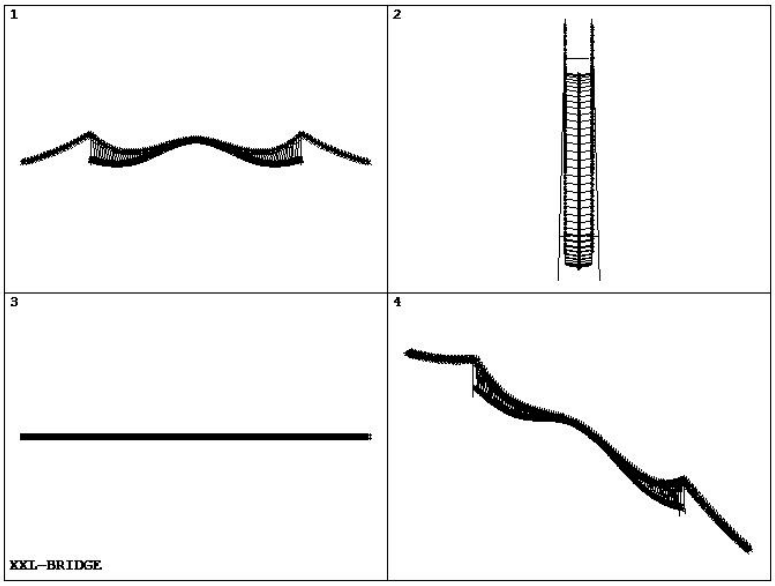

A- 10: Mode 4 shape

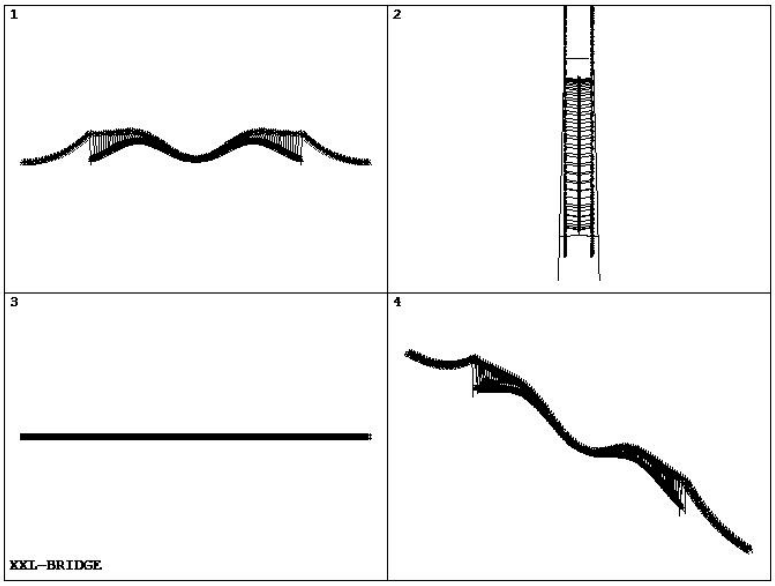

A- 11: Mode 5 shape

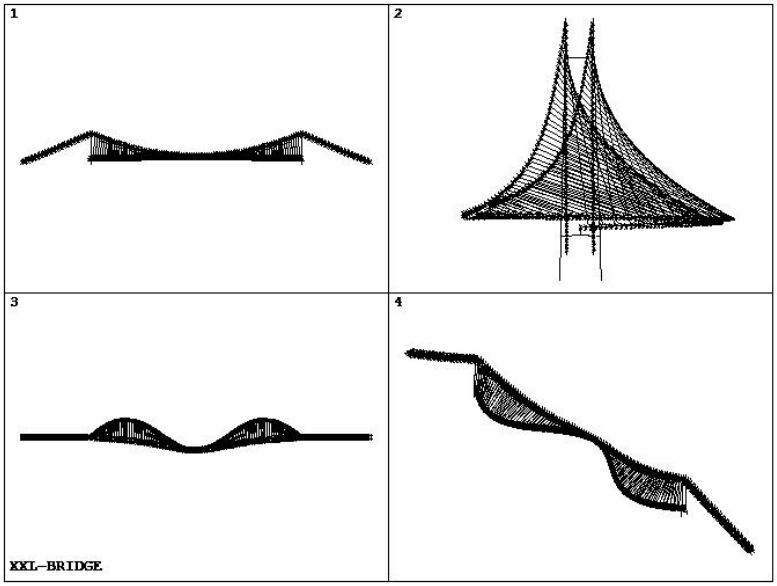

A- 12: Mode 6 shape

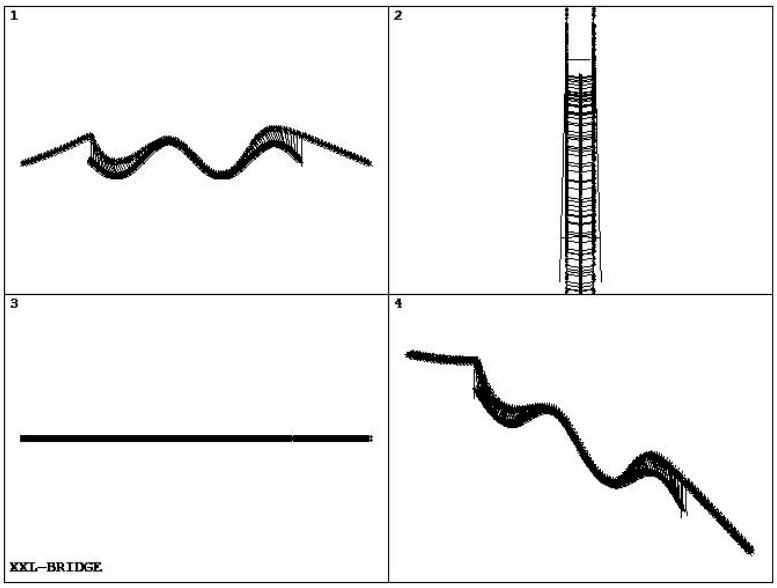

A- 13: Mode 7 shape

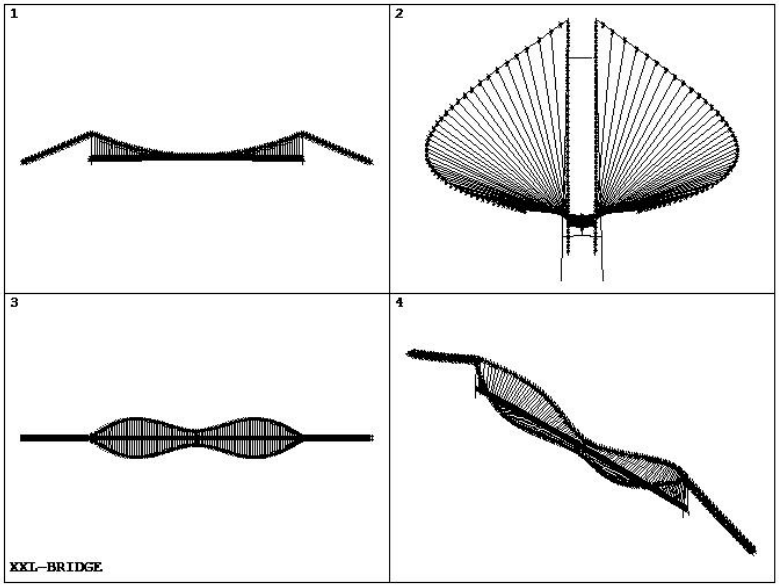

A- 14: Mode 8 shape

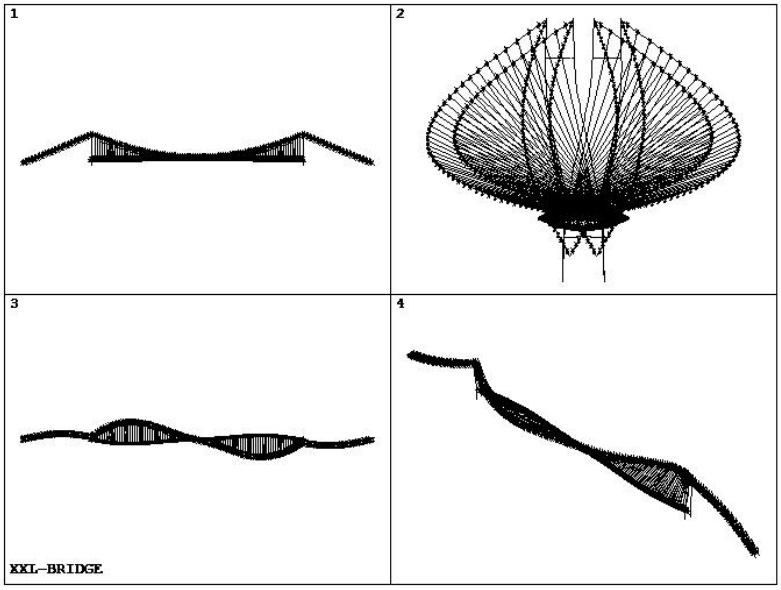

A- 15: Mode 9 shape

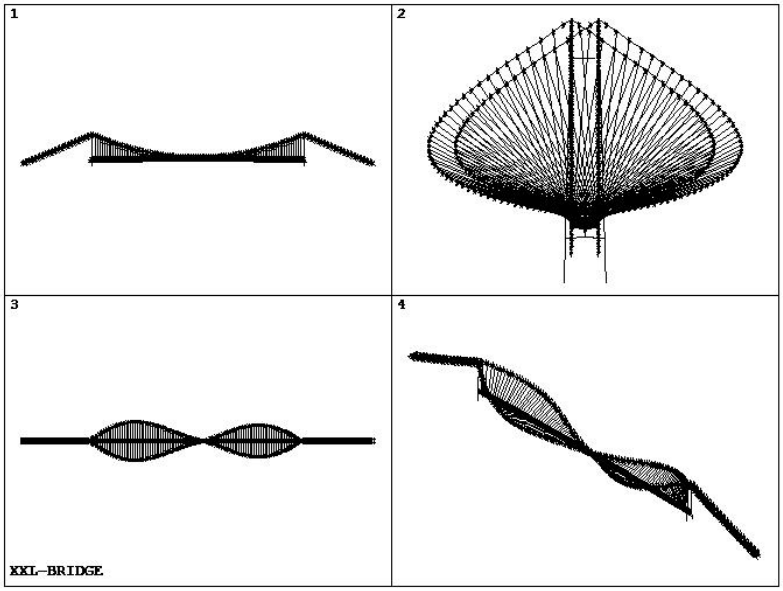

A- 16: Mode 10 shape

Appendix III. Selected aerodynamic measures from 1:20 girder section model

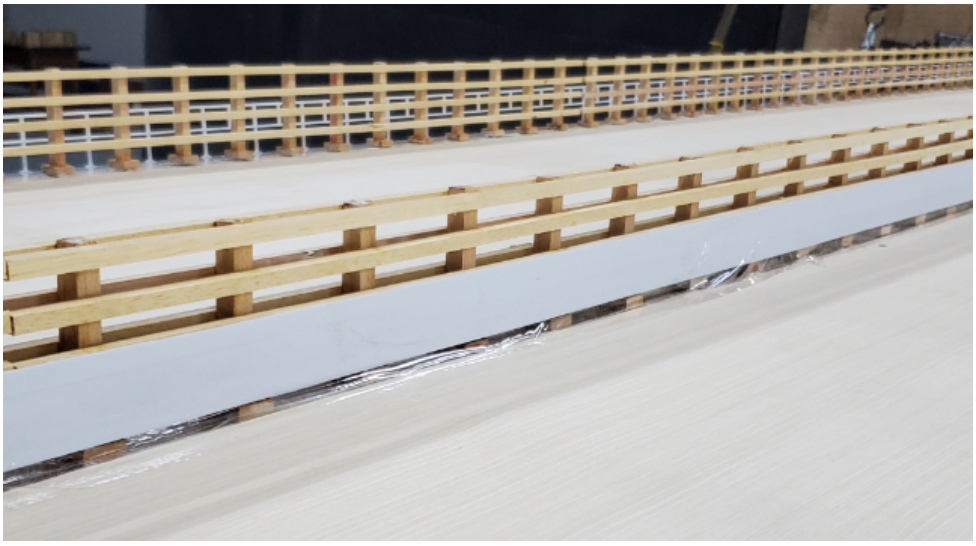

A- 17: 0.67m central stabilizing board

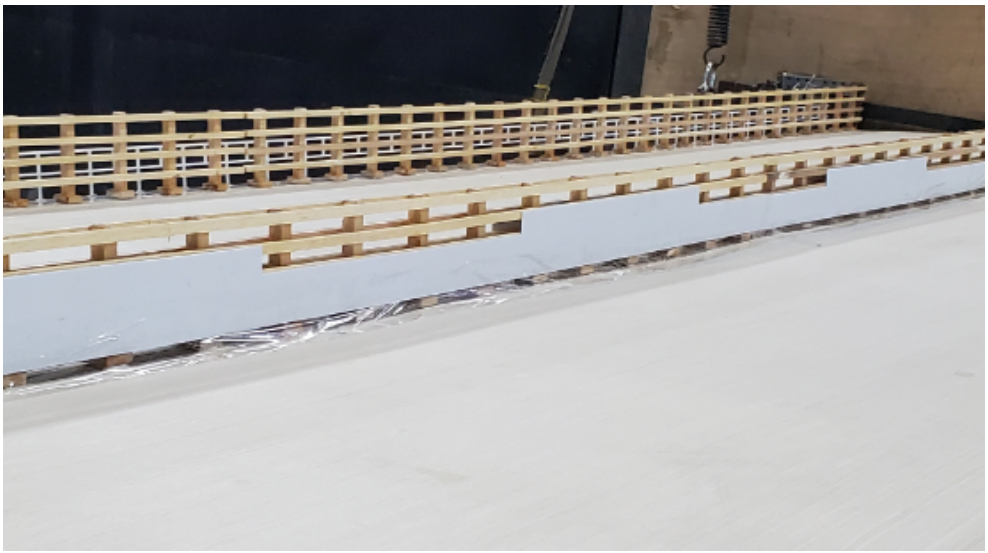

A- 18: Varying height central stabilizing board

A- 19: Step shape horizontal stabilizing board

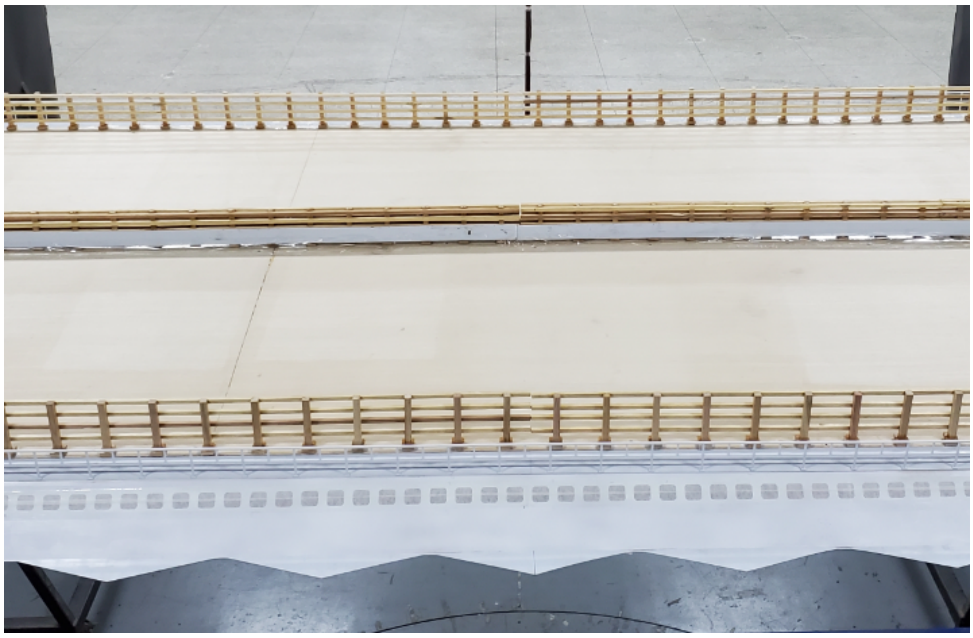

A- 20: Triangle horizontal stabilizing board

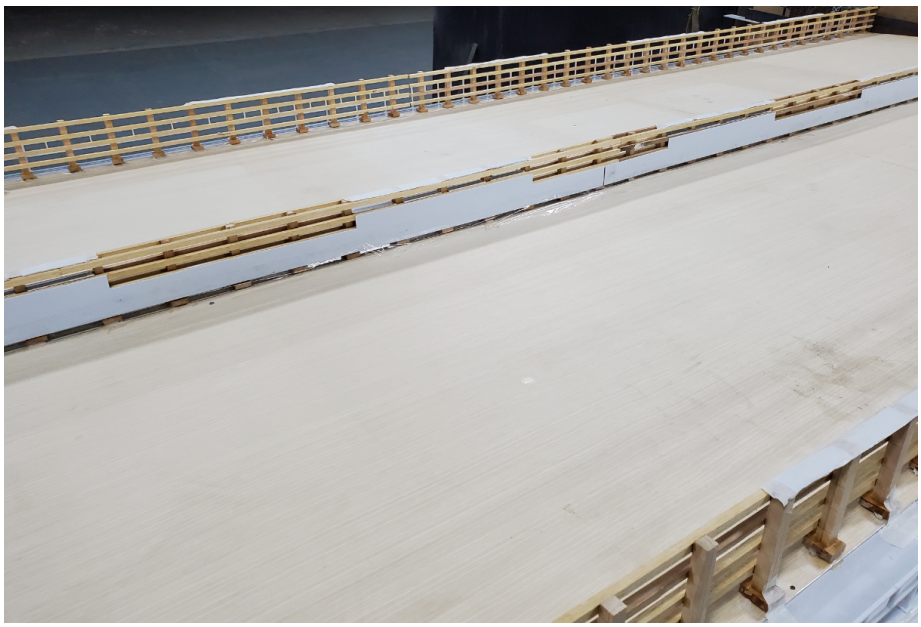

A- 21: Barrier boards with space in addition to varying height board

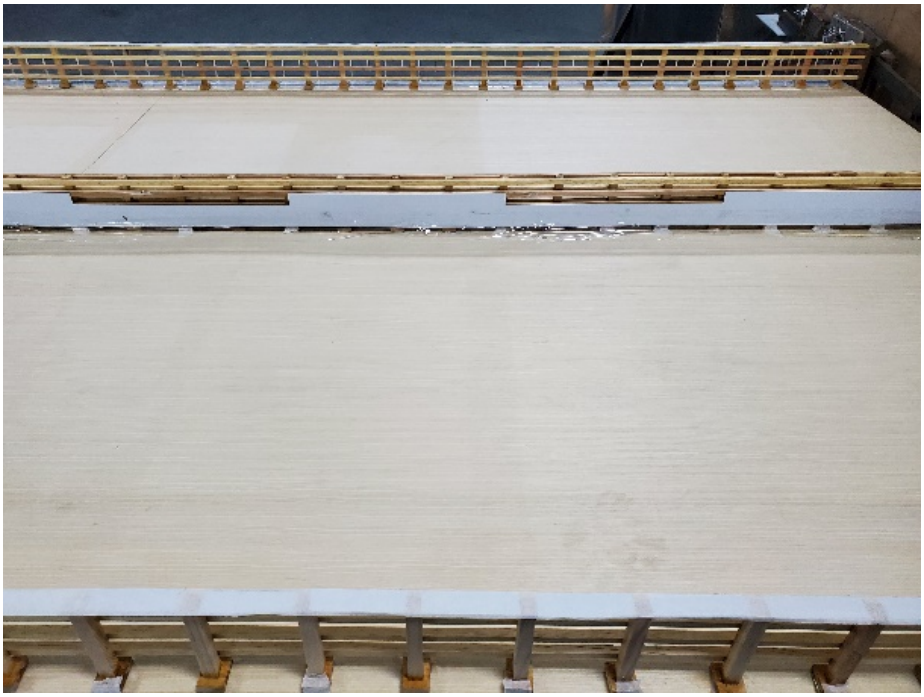

A- 22: Barrier boards with no space in addition to varying height board

Chapter 8 Bibliography

[1] A. Larsen, "Aerodynamic Aspects of the Final Design of the 1624m Suspension Bridge Across the Great Belt," *Journal of Wind Engineering and Industrial Aerodynamics,* vol. 48, no. 2, pp. 261-285, 1993.

[2] A. Nasr, E. Kjellström and I. Björnsson, "Bridges in a changing climate: a study of the potential impacts of climate change on bridges and their possible adaptations," *Structure and Infrastructure Engineering,* vol. 16, no. 4, pp. 738-749, 2020.

[3] Y. J. Ge, L. Zhao and K. Xu, "Review and Reflection on Vortex-induced Vibration of Main Girders of Long-span Bridges," *China Journal of Highway Transportation,* vol. 32, no. 10, 2019.

[4] D. H. Dan and H. J. Li, "Monitoring, intelligent perception, and early warning of vortex-induced vibration of suspension bridge," *The journal of the International Association for Structural Control and Monitoring,* vol. 29, no. 5, 2022.

[5] D. L. Gao, Z. Deng, W. H. Yang and W. L. Chen, "Review of the excitation mechanism and aerodynamic flow control of vortex-induced vibration of the main

girder for long-span bridges: A vortex-dynamics approach," *Journal of Fluids and Structures,* vol. 105, no. 103348, 2021.

[6] Y. Nakamura, "Unsteady lifts and Wakes of Oscillating Rectangular Prisms," *Journal of the Engineering Mechanics Division,* 1975.

[7] R. Fail, J. A. Lawford and R. C. W. Eyre, Low Speed Experiments on the Wake Characteristics of Flat Plates Normal to an Air Stream, London: HM Stationery Office, 1959.

[8] S. Komatsu and H. Kobayashi, "Vortex-induced Oscillation of Bluff Cylinders," *Journal of Wind Engineering and Industrial Aerodynamics,* 1980.

[9] N. Shiraishi and M. Matsumoto, "On Classification of Vortex-induced Oscillation and Its Application for Bridge Structures," *Journal of Wind Engineering and Industrial Aerodynamics,* 1983.

[10] M. C. Welsh and R. Parker, "Effects of sound on flow separation from blunt flat plates," *International Journal of Heat & Fluid Flow,* vol. 4, no. 2, pp. 113-127, 1983.

[11] Y. Nakamura, Y. Ohya and H. Tsuruta, "Experiments on vortex shedding from flat plates with square leading and trailing edges," *Journal of Fluid Mechanics,* vol. 222, pp. 437-447, 1991.

[12] M. P. Paidoussis, S. J. Price and E. De Langre, Fluid-Structure Interactions:

Cross-flow-induced Instabilities, Cambridge: Cambridge University Press, 2010.

[13] G. Bartoli, L. Bruno, G. Buresti, F. Ricciardelli, M. V. Salvetti and A. Zasso., "Benchmark on the Aerodynamics of a Rectangular 5:1 Cylinder: An overview after the first four years of activity," *Journal of Wind Engineering and Industrial Aerodynamics,* vol. 126, pp. 97-106, 2014.

[14] A. M. Marra, C. Mannini and G. Bartoli, "Measurements and Improved Model of Vortex-induced Vibrations for and Elongated Rectangular Cylinder," *Journal of Wind Engineering & Industrial Aerodynamics,* pp. 358-367, 2015.

[15] C. Mannini, A. Soda and G. Schewe, "Unsteady RANS modeling of flow past a rectangular cylinder: Investigation of Reynolds number effects," *Computers and Fluids,* vol. 39, no. 9, pp. 1609-1624, 2010.

[16] C. Mannini, A. Soda and G. Schewe, "Numerical investigation on the three-dimensional unsteady flow past a 5:1 rectangular cylinder," *Journal of Wind Engineering and Industrial Aerodynamics,* vol. 99, no. 4, pp. 469-482, 2011.

[17] L. Bruno, D. Fransos and N. Coste, "3D flow around a rectangular cylinder: A computational study," *Journal of Wind Engineering and Industrial Aerodynamics,* vol. 98, no. 6, pp. 253-276, 2010.

[18] J. A. Witteveen, P. S. Omrani and A. Mariotti, "Uncertainty quantification of a rectangular 5:1 cylinder," in *AIAA Non-deterministic Approaches Conference*,

2015.

[19] A. Mariotti, M. V. Salvetti and P. S. Omrani, "Stochastic analysis of the impact of freestream conditions on the aerodynamics of a rectangular 5:1 cylinder," *Computers and Fluids,* vol. 136, pp. 170-192, 2016.

[20] C. Mannini, A. M. Marra and L. Pigolotti, "The effects of free-stream turbulence and angle of attack on the aerodynamics of a cylinder with rectangular 5:1 cross section," *Journal of Wind Engineering and Industrial Aerodynamics,* vol. 161, pp. 42-58, 2017.

[21] D. T. Nguyen, D. M. Hargreaves and J. S. Owen, "Vortex-induced vibration of a 5:1 rectangular cylinder: A comparison of wind tunnel sectional model tests and computational simulations," *Journal of Wind Engineering and Industrial Aerodynamics,* vol. 175, pp. 1-16, 2018.

[22] L. Bruno, M. V. Salvetti and F. Ricciardelli, "Benchmark on the Aerodynamics of a Rectangular 5:1 Cylinder: An overview after the first four years of activity," *Journal of Wind Engineering and Industrial Aerodynamics,* vol. 6, pp. 87-106, 2014.

[23] G. Gao, L. Zhu and J. Li, "Modelling nonlinear aerodynamic damping during transverse aerodynamic instabilities for slender rectangular prisms with typical side ratios," *Journal of Wind Engineering and Industrial Aerodynamics,* vol.

197, p. 104064, 2020.

[24] M. Zhang, F. Xu and O. Oiseth, "Aerodynamic damping models for vortex-induced vibration of a rectangular 4:1 cylinder: Comparison of modeling schemes," *Journal of Wind Engineering and Industrial Aerodynamics,* vol. 205, no. 104321, 2020.

[25] A. Larsen and G. L. Larose, "Dynamic Wind Effects on Suspension and Cable-stayed Bridges," *Journal of Sound and Vibration,* 2015.

[26] A. Larsen, M. Savage and A. Lafreniere, "Investigation of Vortex Response of a Twin Box Bridge Section at High and Low Reynolds Numbers," *Journal of Wind Engineering and Industrial Aerodynamics,* 2008.

[27] S. Laima, H. Li and W. L. Chen, "Investigation and Control of Vortex-induced Vibration of Twin Box Girders," *Journal of Fluids and Structures,* 2013.

[28] K. C. S. Kwok, X. R. Qin and C. H. Fok, "Wind-induced Pressures Around a Sectional Twin-deck Bridge Model," *Journal of Wind Engineering and Industrial Aerodynamics,* 2012.

[29] C. X. Hu, L. Zhao and Y. J. Ge, "Time-frequency Evolutionary Characteristics of Aerodynamic Forces Around a Streamlined Close-box Girder During Vortex-induced Vibration," *Journal of Wind Engineering and Industrial Aerodynamics,* 2018.

[30] F. Nagao, H. Utsunomiya and E. Yioshioka, "Effects of Handrails on Separated Sehar Flow and Vortex-induced Oscillation," *Journal of Wind Engineering & Industrial Aerodynamics,* pp. 819-827, 1997.

[31] Q. H. Guan, J. W. Li and T. Zhao, "Effects of Railings on Vortex-induced Vibration of a Bridge Deck Section," *Journal of Vibration and Shock,* pp. 150-156, 2014.

[32] S. Laima, H. Li and W. L. Chen, "Effects of Attachments on Aerodynamic Characteristics and Vortex-induced Vibration of Twin-box Girder," *Journal of Fluids and Structures,* pp. 115-133, 2018.

[33] Y. X. Yang, R. Zhou and Y. J. Ge, "Experimental Studies on VIV Performance and Countermeasures for Twin-box Girder Bridges with Various Slot Width Ratios," *Journal of Fluids and Structures,* pp. 476-489, 2016.

[34] P. H. Hallack, "Aerodynamic behavior analysis of Rio-Niterói bridge by means of computational fluid dynamics," *Engineering Structures,* pp. 935-944, 2013.

[35] A. Larsen, "Dynamic Wind Effects on Suspension and Cable-stayed Bridges," *Journal of Sound and Vibration,* pp. 2-28, 2015.

[36] G. Schewe, "Reynolds Number Effects in Flow Around More-or-less Bluff Bodies," *Journal of Wind Engineering & Industrial Aerodynamics,* pp. 1267-1289,

2001.

[37] M. Kawatani, H. Kim and H. Uejima, "Effects of turbulent flows on vortex-induced oscillation of bridge girders with basic sections," *Journal of Wind Engineering and Industrial Aerodynamics,* pp. 477-486, 1993.

[38] M. Matsumoto, N. Shiraishi and H. Shirato, "Mechanism of and Turbulence Effect on Vortex-induced Oscillations for Bridge Box Girders," *Journal of Wind Engineering and Industrial Aerodynamics,* pp. 467-476, 1993.

[39] S. Manzoor, P. Hemon and X. Amandolese, "Vortex Induced Vibrations of a Square Cylinder in a Wind Tunnel," in *ASME 3rd Fluids Engineering Summer Meeting*, Quebec, 2010.

[40] L. D. Zhu, "Mass Simulation and Amplitude Conversion of Bridge Sectional Model Test for Vortex-excited Resonance," *Engineering Mechanics,* pp. 204-208, 2005.

[41] R. Xian, H. L. Liao and M. S. Li, "Application of Scanlan's Nonlinear Model to Describe Spanwise Vortex-induced Vibration of a Long-span Bridge Girder," *Journal of Vibration and Shock,* pp. 54-58, 2009.

[42] A. Larsen, "Investigation of vortex response of a twin box bridge section at high and low Reynolds numbers," *Journal of Wind Engineering and Industrial Aerodynamics,* vol. 96, no. 6, pp. 934-944, 2008.

[43] W. Y. Yuan, S. Laima and W. L. Chen, "Investigation on the vortex-and-wake-induced vibration of a separated-box bridge girder," *Journal of Fluid and Structures,* vol. 70, pp. 145-161, 2017.

[44] B. Wu, L. L. Zhang and Y. Yang, "Investigation and control of VIVs with multi lock-in regions on the wide flat box girders," *Journal of Control Science and Engineering,* pp. 1-17, 2017.

[45] Y. Tamura and G. Matsui, "Wake-oscillator model of vortex-induced oscillation of circular cylinder," in *5th International conference on wind engineering*, Fort Collins, 1979.

[46] M. Matsumoto, "Vortex shedding of bluff bodies: a review," *Journal of Fluids and Structures,* vol. 13, no. 1, pp. 791-811, 1999.

[47] T. Wu and A. Kareem, "An overview of vortex-induced vibration (VIV) of bridge decks," *Frontiers of Structural and Civil Engineering,* vol. 6, no. 4, pp. 335-347, 2012.

[48] L. Huang, S. Zhou and P. Liang, "Numerical simulation for two separate vortex-induced vibration lock-in intervals of bridge sections," *Journal of Vibration and Shock,* vol. 35, no. 11, pp. 47-53, 2016.

[49] C. X. Hu, L. Zhao and Y. J. Ge, "Multiple-order vertical vortex-induced vibration mechanism of a typical streamlined closed-box girder," *Journal of Wind*

Engineering and Industrial Aerodynamics, vol. 227, pp. 1-17, 2022.

[50] S. W. Li, S. J. Laima and H. Li, "Data-driven Modeling of Vortex-induced Vibration of a Long-span Suspension Bridge Using Decision Tree Learning and Support Vector Regression," *Journal of Wind Engineering and Industrial Aerodynamics,* 2018.

[51] M. Raissi, Z. C. Wang and M. S. Triantafyllou, "Deep Learning of Vortex-induced Vibrations," *Journal of Fluid Mechanics,* 2019.

[52] S. Y. Wei, X. W. Jin and H. Li, "General Solutions for Nonlinear Differential Equation: A Rule-based Self-learning Approach Using Deep Reinforcement Learning," *Computational Mechanics,* 2019.

[53] H. Barhoush, A. H. Namini and R. A. Skop, "Vortex Shedding Analysis by Finite Elements," *Journal of Sound and Vibration,* pp. 111-127, 1995.

[54] R. Lewandowski, Application of Semi-empirical model to Analysis of Vortex-excited Vibrations of Beams near Synchronisation Region, New York: Civil-Comp Press, 2000.

[55] F. Ehsan and R. H. Scanlan, "Modeling Spanwise Correlation Effects in the Vortex-Induced Response of Flexible Bridges," *Journal of Wind Engineering & Industrial Aerodynamics,* pp. 1105-1114, 1990.

[56] Z. T. Zhang and Z. Q. Chen, "Similarity of Amplitude of Sectional model to

that of Full Bridge in the Case of Vortex-induced Resonance," *China Civil Engineering Journal,* pp. 77-82, 2011.

[57] R. Xian, H. L. Liao and M. S. LI, "Calculation of Spanwise Vortex-induced Vibration Responses of Long-span Bridge Girder," *Journal of Southwest Jiaotong University,* pp. 740-746, 2008.

[58] Y. G. Sun, The Analytical Approach and Application Study of Vortex-induced Vibration of Long-span Bridge Based on Partial Correlation, Chengdu: Southwest Jiaotong University, 2013.

[59] X. L. Meng, Nonlinear Behavior and Mechanism of Vertical Vortex-induced Vibration of Long Span Steel-box-deck Bridges, Shanghai: Tongji University, 2013.

[60] R. H. Scanlan and E. Simiu, Wind Effects on Structures. 2nd Edition, New York, 1986.

[61] A. Larsen, "A Generalized Model for Assessment of Vortex Induced Vibrations of Flexible Structures," *Journal of Wind Engineering and Industrial Aerodynamics,* pp. 281-294, 1995.

[62] R. Hartlen and I. Currie, "Lift-Oscillator Model of Vortex-Induced Vibration," *Journal of the Engineering Mechanics Division,* vol. 96, no. 5, 1970.

[63] I. Goswami, R. H. Scanlan and N. P. Jones, "Vortex-induced Vibrations of Circular Cylinders. II: New Model," *Journal of Engineering Mechanics,* pp. 2288-

2302, 1993.

[64] K. Xu, Y. J. Ge and L. Zhao, "Calculating Vortex-induced Vibration of Bridge Decks at Different Mass-damping Conditions," *Journal of Bridge Engineering,* 2018.

[65] M. Mashnad and P. Jones, "A Model for Vortex-induced Vibration Analysis of Long-span Bridges," *Journal of Wind Engineering & Industrial Aerodynamics,* pp. 96-108, 2014.

[66] G. Dianna, F. Resta and M. Belloli, "On the Vortex Shedding Forcing on Suspension Bridge Deck," *Journal of Wind Engineering & Industrial Aerodynamics,* pp. 341-363, 2006.

[67] L. D. Zhu, H. Sun and Q. Zhu, "Displacement-based Parameter Identification Method of the Nonlinear Model for Vortex-induced Force," *China Journal of Highway Transportation,* 2019.

[68] A. Larsen, "Storebelt Suspension Bridge Vortex Shedding Excitation and Mitigation by Guide Vans," *Journal of Wind Engineering & Industry Aerodynamics,* pp. 283-296, 2000.

[69] W. Q. Tao, Numerical Heat Transfer, XJTU Press, 2001.

[70] ANSYS, ANSYS Fluent theory guide, ANSYS Inc., 2007.

[71] S. Heinz, "A review of hybrid RANS-LES methods for turbulent flows:

Concepts and applications," *Progress in Aerospace Sciences,* vol. 114, no. 100597, 2020.

[72] P. R. Spalart, "Detached-Eddy Simulation," *Annual Review on Fluid Mechanics,* vol. 41, pp. 91-202, 2009.

[73] P. R. Spalart, S. Deck and M. L. Shur, "A New Version of Detached-Eddy Simulation, Resistant to Ambiguous Grid Densities," *Theoretical and Computational Fluid Dynamics,* vol. 20, no. 3, p. 181, 2006.

[74] A. Chatterjee, "An introduction to the proper orthogonal decomposition," *Current Science,* vol. 78, no. 7, pp. 808-817, 2000.

[75] P. J. Schmid, "Dynamic mode decomposition of numerical and experimental data," *Journal of Fluid Mechanics,* vol. 656, pp. 5-28, 2010.

[76] Y. Q. Wang and N. Gui, "A review of the third-generation vortex identification method and its applications," *Chinese Journal of Hydrodynamics,* vol. 34, no. 4, pp. 413-429, 2019.

[77] C. Liu, "Liutex-third generation of vortex definition and identification methods," *ACTA Aerodynamica Sinica,* vol. 38, no. 3, pp. 413-431, 2020.

[78] E. Simiu and D. Yeo, Wind effects on structures: modern structural design for wind, Hoboken, NJ.: John Wiley & Sons, 2019.

[79] Y. Tamura and A. Kareem, Advanced Structural Wind Engineering, 1 ed.,

Tokyo: Springer Japan, 2013.

[80] Y. Hwang, S. Kim and H. Kim, "Cause investigation of high-mode vortex-induced vibration in a long-span suspension bridge," *Structure and Infrastructure Engineering,* vol. 16, pp. 84-93, 2020.

[81] Y. Xu, Wind effects on cable-supported bridges, 1 ed., Singapore: John Wiley & Sons Singapore, 2013.

[82] R. Battista and M. Pfeil, "Reduction of vortex-induced oscillations of Rio–Niterói bridge by dynamic control devices," *Journal of Wind Engineering and Industrial Aerodynamics,* vol. 84, pp. 273-288, 2000.

[83] A. Larsen, S. Esdahl, J. Andersen and T. Vejrum, "Storebælt suspension bridge – vortex shedding excitation and mitigation by guide vanes.," *Journal of Wind Engineering and Industrial Aerodynamics,* vol. 88, pp. 283-296, 2000.

[84] Y. X. Yang, T. T. Ma and Y. J. Ge, "Evaluation on bridge dynamic properties and vortex induced vibration performance based on wind tunnel test and field measurement," *Wind and Structures,* vol. 20, pp. 719-737, 2015.

[85] T. Argentini, D. Rocchi and A. Zasso, "Aerodynamic interference and vortex-induced vibrations on parallel bridges: The Ewijk bridge during different stages of refurbishment," *Journal of Wind Engineering and Industrial Aerodynamics,* vol. 147, pp. 276-282, 2015.

[86] J. Macdonald, P. Irwin and M. Fletcher, "Vortex-induced vibrations of the Second Severn Crossing cable-stayed bridge - full-scale and wind tunnel measurements," in *Proceedings of the ICE - Structures and Buildings*, 2002.

[87] F. Weber and M. Maślanka, "Frequency and damping adaptation of a TMD with controlled MR damper," *Smart Materials and Structures,* vol. 21, no. 055011, 2012.

[88] H. Zhao, Y. Ding, A. Li, X. C. B. Liu and J. Lu, "Evaluation and Early Warning of Vortex-Induced Vibration of Existed Long-Span Suspension Bridge Using Multisource Monitoring Data," *Journal of Performance of Constructed Facilities,* vol. 35, no. 04021007, 2021.

[89] J. Zhang, L. Zhou, Y. Tian, S. Yu, W. Zhao and Y. Cheng, "Vortex-induced vibration measurement of a long-span suspension bridge through noncontact sensing strategies," *Computer-Aided Civil and Infrastructure Engineering,* 2021.

[90] L. Zhao, C. Liu and Y. Ge, "Vortex-induced vibration sensitivity of bridge girder structures," *Acta Aerodynamica Sinica,* vol. 38, pp. 694-704, 2020.

[91] J. Zhu, Z. Xiong, H. Xiang, X. Huang and Y. Li, "Ride comfort evaluation of stochastic traffic flow crossing long-span suspension bridge experiencing vortex-induced vibration," *Journal of Wind Engineering and Industrial Aerodynamics,* vol. 219, no. 104794, 2021.

[92] D. Dan, X. Yu, F. Han and B. Xu, "Research on dynamic behavior and traffic management decision-making of suspension bridge after vortex-induced vibration event," *Structural Health Monitoring,* pp. 1-15, 2021.

[93] AASHTO, AASHTO LRFD: Bridge design specifications, Washington, DC.: AASHTO, 2020.

[94] BSI, Steel, concrete and composite bridges—Part 2: Specification for loads, London: British Standards Institution, 2006, p. 98.

[95] JTG/T-3360-01-2018, Wind-Resistant Design Specification for Highway Bridges, Beijing: China Communications Press, 2019.

[96] H. Sato, "Wind-resistant design manual for highway bridges in Japan," *Journal of Wind Engineering and Industrial Aerodynamics,* vol. 91, pp. 1499-1509, 2003.

[97] A. Azizinamini, K. Barth, R. Dexter and C. Rubeiz, " High performance steel: research front—historical account of research activities," *Journal of Bridge Engineering,* vol. 9, pp. 212-217, 2004.

[98] K. Nguyen, A. Camara, O. Rio and L. Sparowitz, "Dynamic effects of turbulent crosswind on the serviceability state of vibrations of a slender arch bridge including wind–vehicle–bridge interaction," *Journal of Bridge Engineering,* vol. 22, no. 06017005, 2017.

[99] M. Griffin, Handbook of human vibration, San Diego, CA.: Academic Press Inc., 1990.

[100] H. Moghimi and H. Ronagh, "Development of a numerical model for bridge–vehicle interaction and human response to traffic-induced vibration," *Engineering Structures,* vol. 30, pp. 3808-3819, 2008.

[101] K. Nguyen, B. Freytag, M. Ralbovsky and O. Rio, "Assessment of serviceability limit state of vibrations in the UHPFRC-Wild bridge through an updated FEM using vehicle-bridge interaction," *Computers & Structures ,* vol. 156, pp. 29-41, 2015.

[102] ISO, Mechanical vibration and shock-evaluation of human exposure to whole body vibrations, Geneva: International Organization for Standardization, 1997, p. 31.

[103] BSI, Guide to measurement and evaluation of human exposure to whole-body mechanical vibration and repeated shock, London: British Standards Institution, 2012.

[104] Y. Xu and W. Guo, "Effects of bridge motion and crosswind on ride comfort of road vehicles," *Journal of Wind Engineering and Industrial Aerodynamics,* vol. 92, pp. 641-662, 2004.

[105] J. Zhu, W. Zhang and M. Wu, "Evaluation of ride comfort and driving safety

for moving vehicles on slender coastal bridges," *Journal of Vibration and Acoustics,* vol. 140, p. 051012, 2018.

[106] A. Camara, I. Kavrakov, K. Nguyen and G. Morgenthal, "Complete framework of wind-vehicle-bridge interaction with random road surfaces," *Journal of Sound and Vibration,* vol. 458, pp. 197-217, 2019.

[107] S. Chen and J. Wu, "Modeling stochastic live load for long-span bridge based on microscopic traffic flow simulation," *Computers & Structures ,* vol. 89, pp. 813-824, 2011.

[108] Y. Liu, X. Yin, D. L. F and C. Cai, "Ride comfort of the bridge-traffic-wind coupled system considering bridge surface deterioration," *Wind and Structures,* vol. 23, pp. 19-42, 2016.

[109] X. Yin, Y. Liu, L. Deng and C. Cai, "Impact factors of bridges in service under stochastic traffic flow and road surface progressive deterioration," *Advances in Structural Engineering,* vol. 19, pp. 38-52, 2016.

[110] Y. Zhou and S. Chen, "Vehicle ride comfort analysis with whole-body vibration on long-span bridges subjected to crosswind," *Journal of Wind Engineering and Industrial Aerodynamics,* vol. 155, pp. 126-140, 2016.

[111] H. Yu, B. Wang, G. Zhang, Y. Li and X. Chen, "Ride comfort assessment of road vehicle running on long-span bridge subjected to vortex-induced vibration,"

Wind and Structures, vol. 31, pp. 393-402, 2020.

[112] H. F. Xiang and Y. J. Ge, "Wind Resistance Challenges and Fundamental Research on Long-span Bridges," *Engineering Science,* vol. 13, no. 9, pp. 8-12, 2011.

[113] Ansys, Ansys Student 2022 R2, Ansys, Inc..

[114] MATLAB, 9.7.0.1190202 (R2019b), Natick, Massachusetts: The MathWorks Inc., 2018.

[115] Pycharm, ver. 2022.3, JetBrains, 2022.

[116] EN 1998-1, Eurocode 8: Design of Structure for Earthquake Resistance. 1st ed., Brussels: BSi, 2004.

[117] D. M. Siringoringo and Y. Fujino, "System identification of suspension bridge from ambient vibration response," *Engineering Structures,* vol. 30, no. 2, pp. 462-477, 2008.

[118] C. Cerretelli and C. H. K. Williamson, "The physical mechanism for vortex merging," *Journal of Fluid Mechanics,* vol. 475, pp. 41-77, 2003.

[119] Y. Wang, P. Liu, T. Hu and Q. Qu, "Investigation of co-rotating vortex merger in ground proximity," *Aerospace Science and Technology,* vol. 53, pp. 116-127, 2016.

[120] G. Jocher, *ultralytics/yolov5: v5.0 - YOLOv5-P6 1280 models, AWS, Supervise.ly and YouTube integrations,* Zenodo, 2020.

[121] N. Wojke, A. Bewley and D. Paulus, "Simple Online and Realtime Tracking with a Deep Association Metric," in *2017 IEEE International Conference on Image Processing (ICIP)*, 2017.

[122] N. Wojke and A. Bewley, "Deep Cosine Metric Learning for Person Re-identification," in *2018 IEEE Winter Conference on Applications of Computer Vision (WACV)*, 2018.

[123] Anaconda, Vers. 2-2.4.0., Anaconda Software Distribution, 2016.

[124] A. Paszke, S. Gross, S. Chintala, G. Chanan, E. Yang, Z. DeVito, Z. M. Lin, A. Desmaison, L. Antiga and A. Lerer, "Automatic differentiation in PyTorch," in *NISP 2017 Workshop Autodiff*, Long beach, 2017.

[125] Y. J. Ma, D. H. Yu, T. Wu and H. F. Wang, "PaddlePaddle: An Open-Source Deep Learning Platform from Industrial Practice," *Frontiers of Data and Computing,* vol. 1, no. 1, pp. 105-115, 2019.

[126] R. Kalman, "A New Approach to Linear Filtering and Prediction Problems," *ASME Journal of Basic Engineering,* vol. 82, pp. 35-45, 1960.

[127] H. W. Kuhn, "The Hungarian Method for the assignment problem," *Naval Research Logistics Quarterly,* vol. 2, pp. 83-97, 1955.

[128] W. Zhang, Z. Wei, Y. X. Yang and Y. J. Ge, "Comparison and analysis of vortex induced vibration for twin-box bridge sections based on experiments in different Reynolds numbers," *Journal of Tongji University (Natural Science),* vol. 36, no. 1, pp. 6-11, 2008.

[129] G. L. Larose, S. Larsen, A. Larsen, M. Hui and A. G. Jensen, "Sectional model experiments at high Reynolds number for the deck of a 1018 m span cable-stayed bridge," in *Proceedings of the 11th International Conference on Wind Engineering*, Lubbock, Texas, 2003.

[130] C. Hu, L. Zhao, H. Chen, Z. Zhou and Y. Ge, "Reynolds number effects on aerodynamic forces of a streamlined close-box girder during vortex-induced vibrations," *Journal of Vibration and Shock,* vol. 38, no. 12, pp. 118-125, 2019.

[131] A. Larsen and G. Schewe, "Reynolds number effects in the flow around a bluff bridge cross section," *Journal of Wind Engineering and Industrial Aerodynamics,* vol. 74/76, pp. 829-838, 1998.

[132] H. Li, S. Laima and H. Jing, "Reynolds number effects on aerodynamic characteristics and vortex-induced vibration of a twin-box girder," *Journal of Fluids and Structures,* vol. 50, pp. 358-375, 2014.

[133] X. Cui, J. Li and F. Chen, "Reynolds number effect on vortex resonance of streamline-like bridge deck section," *Journal of Chang'an University (Natural*

Science Edition), vol. 31, pp. 47-51, 2011.

[134] J. Li, Z. Lin and T. Jin, "The application of pressure integration method in the study of Reynolds number effects on bridge sections," *Journal of Vibration Engineering,* vol. 19, pp. 505-508, 2006.

[135] B. Spencer, V. Hoskere and Y. Narazaki, "Advances in Computer Vision-Based Civil Infrastructure Inspection and Monitoring," *Engineering,* vol. 5, no. 2, pp. 199-222, 2019.

[136] Y. Zhuang, W. Chen, T. Jin, B. Chen, H. Zhang and W. Zhang, "A Review of Computer Vision-Based Structural Deformation Monitoring in Field Environments," *Sensors,* vol. 22, no. 10, p. 3789, 2022.

[137] K. Luo, X. Kong, J. Zhang, J. Hu and J. Li, "Computer Vision-Based Bridge Inspection and Monitoring: A Review," *Sensors,* vol. 23, no. 18, p. 7863, 2023.

[138] B. Pan, L. Tian and X. Song, "Real-time, non-contact and targetless measurement of vertical deflection of bridges using off-axis digital image correlation," *NDT & E International,* vol. 79, pp. 73-80, 2016.

[139] C. Dong, X. Ye and T. Jin, "Identification of structural dynamic characteristics based on machine vision technology," *Measurement,* vol. 126, pp. 405-416, 2018.

[140] D. Li, W. Chen, B. Peng and B. Yan, "Rapid DIC Deformation Measurement

Technology and Engineering Application," 25 6 2021. [Online]. Available: http://www.zbl.cn/index.php?m=content&c=index&a=show&catid=14&id=725. [Accessed 26 9 2023].

[141] L. Zhao, W. Cui, X. Shen, S. Xu, Y. Ding and Y. Ge, "A fast on-site measure-analyze-suppress response to control vortex-induced-vibration of a long-span bridge," *Structures,* vol. 35, pp. 192-201, 2022.

[142] G. Lin, W. Li and Z. Lu, "Output-only modal analysis of the Humen Bridge from video measurement," in *14th International Conference on Damage Assessment of Structures*, Online, 2022.

[143] M. Wang, W. Ao, J. Bownjohn and F. Xu, "Completely non-contact modal testing of full-scale bridge in challenging conditions using vision sensing systems," *Engineering Structures,* vol. 282, no. 114994, 2022.

[144] Y. Shao, L. Li, J. Li, Q. Li, S. An and H. Hao, "Monocular vision based 3D vibration displacement measurement for civil engineering structures," *Engineering Structures,* vol. 293, no. 116661, 2023.

[145] L. Zhao and Y. Ge, "Emergency Measures for Vortex-induced Vibration of Humen Bridge," in *The 2020 World Congress on Advances in Civil, Environmental, & Materials Research (ACEM20)*, Seoul, Korea, 2020.

[146] G. Jocher, A. Chaurasia and J. Qiu, *YOLO by Ultralytics (Version 8.0.0)*

[Computer software]. https://github.com/ultralytics/ultralytics, 2023.

[147] Y. Zhang, P. Sun, Y. Jiang, D. Yu, F. Weng, Z. Yuan, P. Luo, W. Liu and X. Wang, "ByteTrack: Multi-Object Tracking by Associating Every Detection Box," in *ECCV 2022*, Tel Aviv, 2022.

[148] B767-400ER, "VIV of Humen Bridge on 2020/5/5," Bilibili, 5 5 2020. [Online]. Available: https://www.bilibili.com/video/BV1Nt4y1178T/?spm_id_from=333.337.search-card.all.click&vd_source=96a4900b6cb39e77593852dc8ff59455. [Accessed 26 9 2023].

[149] W. Kentaro, "Labelme: Image Polygonal Annotation with Python," [Online]. Available: https://github.com/wkentaro/labelme.

[150] Blender Foundation, Blender, Amsterdam: Blender.org, 2023.

[151] Y. Zhou and S. Chen, "Investigation of the live-load effects on long-span bridges under traffic flows," *Journal of Bridge Engineering,* vol. 23, no. 04018021, 2018.

[152] C. X. Hu and Y. J. Ge, "Mechanism of suppression of vortex-induced vibrations of a streamlined closed-box girder using additional small-scale components," *Journal of Wind Engineering and Industrial Aerodynamics,* vol. 189, pp. 314-331, 2019.

[153] Y. J. Ge, L. Zhao and J. X. Cao, "Case study of vortex-induced vibration and mitigation mechanism for a long-span suspension bridge," *Journal of Wind Engineering and Industrial Aerodynamics,* vol. 220, no. 104866, 2022.

[154] E. Cheynet, J. B. Jakobsen and J. Snabjorssen, "Full-scale Observation of the Flow Downstream of a Suspension Bridge Deck," *Journal of Wind Engineering and Industrial Aerodynamics,* 2005.

[155] J. B. Frandsen, "Simultaneous Pressure and Accelerations Measured Full-scale on the Great Belt East Suspension Bridge," *Journal of Wind Engineering and Industrial Aerodynamics,* 2001.

[156] H. Li, S. J. Laima and J. P. Ou, "Investigation of Vortex-induced Vibration of a Suspension Bridge with Two Separated Steel Box Girders Based on Field Measurements," *Engineering Structures,* 2011.

[157] R. H. Scanlan, "FHWA-RD-80-50 Final Report [R]," FHWA, Washington DC, 1981.

[158] B. Vickery and R. Basu, "Across-wind Vibrations of Structures of Circular Cross-section. Part I. Development of a Mathematical Model for Two-dimensional Conditions," *Journal of Wind Engineering & Industrial Aerodynamics,* pp. 49-73, 1983.